

**Encapsulation of Scorodite Particles with Phosphate
Coatings**

By

Felipe Lagno

Department of Mining, Metals and Materials Engineering

McGill University

Montreal

Canada

September 2005

A thesis submitted to McGill University in partial fulfillment of
the requirements of the degree of Doctor of Philosophy

© Felipe Lagno, 2005



Library and
Archives Canada

Bibliothèque et
Archives Canada

Published Heritage
Branch

Direction du
Patrimoine de l'édition

395 Wellington Street
Ottawa ON K1A 0N4
Canada

395, rue Wellington
Ottawa ON K1A 0N4
Canada

Your file *Votre référence*
ISBN: 978-0-494-21666-8
Our file *Notre référence*
ISBN: 978-0-494-21666-8

NOTICE:

The author has granted a non-exclusive license allowing Library and Archives Canada to reproduce, publish, archive, preserve, conserve, communicate to the public by telecommunication or on the Internet, loan, distribute and sell theses worldwide, for commercial or non-commercial purposes, in microform, paper, electronic and/or any other formats.

The author retains copyright ownership and moral rights in this thesis. Neither the thesis nor substantial extracts from it may be printed or otherwise reproduced without the author's permission.

AVIS:

L'auteur a accordé une licence non exclusive permettant à la Bibliothèque et Archives Canada de reproduire, publier, archiver, sauvegarder, conserver, transmettre au public par télécommunication ou par l'Internet, prêter, distribuer et vendre des thèses partout dans le monde, à des fins commerciales ou autres, sur support microforme, papier, électronique et/ou autres formats.

L'auteur conserve la propriété du droit d'auteur et des droits moraux qui protègent cette thèse. Ni la thèse ni des extraits substantiels de celle-ci ne doivent être imprimés ou autrement reproduits sans son autorisation.

In compliance with the Canadian Privacy Act some supporting forms may have been removed from this thesis.

Conformément à la loi canadienne sur la protection de la vie privée, quelques formulaires secondaires ont été enlevés de cette thèse.

While these forms may be included in the document page count, their removal does not represent any loss of content from the thesis.

Bien que ces formulaires aient inclus dans la pagination, il n'y aura aucun contenu manquant.


Canada

To Maria de los Angeles and Fernanda

Abstract

Arsenic disposal is one of the most important environmental issues the mining and metallurgical industries are faced with. This problem has worsened in recent years because of the increasing arsenic content of the low-grade and complex ores currently processed by the mining industry and the introduction of stricter environmental regulations.

This Ph.D. thesis sought to develop a novel concept for arsenic fixation suitable for the long-term safe disposal of arsenic generated and disposed by the minerals industry. In particular this research project investigates the encapsulation of scorodite, a well characterized Fe(III)-As(V) compound having the following formula $\text{FeAsO}_4 \cdot 2\text{H}_2\text{O}$, with phosphate coatings, materials potentially not prone to reductive decomposition. Reductive decomposition is known to be responsible for the release of arsenic into the environment from arsenate solids such as scorodite.

The subject matter of this thesis is the application of heterogeneous crystallisation techniques to produce stable phosphate coatings on scorodite particles. The experimental work reported in this thesis involved three different types of studies, namely (1) production of a number of synthetic minerals; (2) evaluation of their stability; and (3) encapsulation of scorodite with two of these synthetic minerals. The synthesis work involved the production of aluminium and calcium phosphates via homogeneous, heterogeneous and seeded crystallisation. The stability work involved the study of the dissolution of hydrated aluminium phosphate ($\text{AlPO}_4 \cdot 1.5\text{H}_2\text{O}$), dicalcium phosphate dihydrate ($\text{CaHPO}_4 \cdot 2\text{H}_2\text{O}$), and calcium-deficient hydroxyapatite ($\text{Ca}_{10-x}(\text{HPO}_4)_x(\text{PO}_4)_{6-x}(\text{OH})_{2-x}$, $x < 2$). Finally, the encapsulation work involved the deposition of hydrated aluminium phosphate and calcium-deficient hydroxyapatite on scorodite particles and the evaluation of their stability in simulated oxic and anoxic environments.

The directed deposition of phosphate on scorodite particles was achieved via the control of supersaturation. For the directed deposition of aluminium phosphate, the supersaturation was controlled via pH adjustment. On the other hand, for the controlled deposition of calcium-deficient hydroxyapatite on scorodite particles supersaturation was controlled via regulated mixing of two Ca(II) and P(V) solutions at constant pH. Both encapsulation techniques appeared to enhance scorodite stability under simulated oxic and anoxic environments by reducing the arsenic release rate up to one order of magnitude.

Abrégé

Le rejet de l'arsenic dans l'environnement est l'un des principaux problèmes rencontrés par les industries minières et métallurgiques. Ce problème s'est accru ces dernières années du fait de l'augmentation de la teneur en arsenic dans les minerais couramment utilisées par les industries minières et également par de nouvelles normes environnementales plus strictes.

L'objectif de cette thèse de doctorat est de développer un nouveau concept de fixation pour l'arsenic pour permettre une déposition sécuritaire à long terme de l'arsenic. En particulier, ce projet de recherche se focalise sur l'encapsulation de la scorodite, un composé Fe(III)-As(V) bien connu de formule $\text{FeAsO}_4 \cdot 2\text{H}_2\text{O}$, par un minéral phosphaté, type de matériaux qui ne sont pas enclin à présenter une décomposition réductrice. Ce type de décomposition est connu pour être responsable du relargage de l'arsenic dans l'environnement sous forme d'arsenate solide comme la scorodite.

Le principal axe de recherche de cette thèse est l'étude détaillée des techniques de cristallisation hétérogène et leurs applications de façon à produire par déposition directe un revêtement phosphaté stable sur des particules de scorodite. Le travail présenté dans cette thèse est décomposé en trois grandes parties : (1) la production de plusieurs minéraux synthétiques, (2) l'étude de leur stabilité, et (3) l'encapsulation de la scorodite par deux de ses matériaux. Le travail de synthèse consiste en la production de phosphates d'aluminium et de calcium par cristallisation homogène, hétérogène ou cristallisation utilisant un précurseur. L'étude de la stabilité se focalise sur la dissolution de plusieurs composés : phosphate d'aluminium hydraté ($\text{AlPO}_4 \cdot 1.5\text{H}_2\text{O}$), phosphate de dicalcique dihydraté ($\text{CaHPO}_4 \cdot 2\text{H}_2\text{O}$) et d'hydroxyapatite déficiente en calcium ($\text{Ca}_{10-x}(\text{HPO}_4)_x(\text{PO}_4)_{6-x}(\text{OH})_{2-x}$, $x < 2$). Enfin le travail d'encapsulation consiste en la déposition de phosphate d'aluminium hydraté ou d'hydroxyapatite déficiente en calcium sur les

particules de scorodite et il consiste également en l'évaluation de leur stabilité en milieu oxygène et anoxygène.

Le dépôt direct de minéraux phosphatés sur des particules de scorodite fut réalisé par le contrôle de la supersaturation. Pour le dépôt direct de phosphate d'aluminium, la supersaturation fut obtenue par le contrôle du pH. De cette façon, l'expansion cristalline et la nucléation hétérogène furent favorisées par rapport à la nucléation homogène. Par ailleurs, pour le contrôle du dépôt d'hydroxyapatite déficiente en calcium sur les particules de scorodite, la supersaturation fut obtenue par un mélange réglé de solutions de Ca(II) et de P(V) à pH constant. Toutes ces techniques de recouvrements, permettent d'augmenter la stabilité de la scorodite, même si celle-ci est confrontée à des environnements oxygènes ou anoxygènes. Cette stabilité se traduit par une diminution, d'un ordre de grandeur, de l'arsenic relargué.

Acknowledgements

First, and foremost, I would like to express my most sincere thanks to Professor George P. Demopoulos, my supervisor, for giving me an opportunity to carry out research under his supervision, for his advice and for his intellectual generosity.

My thanks go to Dr. John Mahoney for the support he provided with solution modelling and to Dr. Stephen Chryssoulis for evaluating aluminium phosphate coated scorodite using SEM-EDX, TOF-SIMS and TOF-LIMS.

I am also grateful to all members of Hydromet Group at McGill: My thanks go particularly to Seref for being great colleague and for his friendship, to Vincent (from New Caledonia), Cinziana, Georgiana, and Marie-Claude who made my stay at McGill more enjoyable. Jean François for helping me with the VP-SEM microscope. A big thank you to Ed Silauskas for his help with ICP.

The support of this work by Natural Sciences and Engineering Research Council of Canada (NSERC) via a strategic project grant is gratefully acknowledged, as is the sponsorship of Hatch, COGEMA Resources Inc., Barrick Gold and Placer Dome. The Institute for Innovation in Mining and Metallurgy (IM2 - CODELCO Chile Subsidiary) is greatly thanked for giving me the opportunity of taking three years leave of absence to pursue my studies in Canada. The Government of Canada is also acknowledged for the financial help provided in the form of a full graduate scholarship.

Last, but certainly not least, I like to dedicate this thesis to my wife María de los Angeles, who has supported me, encouraged me, and comfort me during these three years. I am particularly indebted to her for leaving everything else behind and joining me in this journey. Thank you!

Table of Contents

Abstract	i
Abrégé	ii
Acknowledgements	v
Table of Contents	vi
List of Figures	x
List of Tables	xxii
List of Symbols	xxiii
Chapter 1. Introduction	1
References	4
Chapter 2. Literature review and theory	6
2.1 The Arsenic problem	6
2.2 Arsenic removal and fixation	8
2.2.1 Processing options	8
2.2.2 Formation of scorodite and related compounds	11
2.3 Crystallisation theory	12
2.3.1 Supersaturation	13
2.3.2 Nucleation	15

2.3.3	Crystal growth.....	24
2.3.4	Phase transformations.....	28
2.4	Phosphate minerals.....	30
2.4.1	Aluminium phosphates.....	31
2.4.2	Calcium phosphates.....	34
2.5	Review of coating technologies in aqueous media.....	38
	References.....	39
Chapter 3. Experimental.....		57
3.1	Introduction.....	57
3.2	Crystallisation reactor and procedure.....	57
3.3	Chemicals and materials used.....	59
3.4	Chemical analysis and reproducibility.....	60
3.5	Characterisation.....	60
3.6	Preparation of scorodite.....	62
	References.....	64
Chapter 4. Synthesis and stability of hydrated aluminium phosphate.....		66
4.1	Introduction.....	66
4.2	Synthesis.....	66
4.2.1	Materials and methods.....	66
4.2.2	Metastable zone for aluminium phosphate precipitation.....	68
4.2.3	Seed-assisted precipitation of hydrated aluminium phosphate.....	70
4.3	Stability.....	72
4.3.1	Methods.....	72
4.3.2	Thermodynamic considerations.....	74
4.3.3	Experimental data.....	77
4.3.4	Determination of the solubility product.....	80
4.3.5	Evaluation of the dissolution mechanism with PHREEQC.....	81

4.4	Conclusions	84
	References	85
Chapter 5. Synthesis and stability of selected calcium phosphates		88
5.1	Introduction	88
5.2	Synthesis	88
5.2.1	Materials and methods	88
5.2.2	Metastable region of calcium phosphate precipitation	91
5.2.3	Crystallisation of dicalcium phosphate dihydrate	93
5.2.4	Crystallisation of calcium-deficient hydroxyapatite	95
5.2.5	Product characterisation	98
5.3	Stability	104
5.3.1	Methods	104
5.3.2	Thermodynamic considerations	106
5.3.3	Experimental data	107
5.3.4	Evaluation of the dissolution mechanism with PHREEQC	113
5.4	Conclusions	119
	References	120
Chapter 6. Scorodite encapsulation with phosphate coatings		125
6.1	Introduction	125
6.2	Encapsulation with aluminium phosphate	125
6.2.1	Materials and methods	125
6.2.2	Deposition kinetics	126
6.2.3	Heterogeneous nucleation mechanism	131
6.2.4	Characterisation of the coating	136
6.3	Encapsulation with calcium phosphate	144
6.3.1	Materials and methods	144
6.3.2	Deposition kinetics	146

6.3.3	Analysis of the deposition process using SEM	159
6.4	Stability	159
6.4.1	Materials and methods.....	159
6.4.2	Stability in oxic environment	163
6.4.3	Stability in anoxic environment	168
6.4.4	Analysis of the coating stability with SEM.....	170
6.5	Conclusions	172
	References.....	173
Chapter 7.	Synopsis.....	175
7.1	Global conclusions	175
7.2	Claims to originality	176
7.3	Recommendations for future work	177
Appendix A.	Deposition of $\text{CaHPO}_4 \cdot 2\text{H}_2\text{O}$	179

List of Figures

Figure 2.1.	Summary of industrial operating practice as of year 2000/2001 based on 48 operations reported in reference [21].	10
Figure 2.2.	Supersaturation control area for atmospheric precipitation of scorodite at 95°C from Fe(III)-As(V)-SO ₄ solution (reproduced from [41]).	13
Figure 2.3.	Solubility-supersaturation diagram explaining the stable metastable and labile zones for a salt with inverse solubility (adapted from [60]).	14
Figure 2.4.	Classification of nucleation mechanism (adapted from [63]).	16
Figure 2.5.	Overall free energy change resulting from an embryo nucleating homogeneously from solution, according to equation (2.4) (reproduced from [54]).	18
Figure 2.6.	Heterogeneous nucleation: a embryo (<i>e</i>) nucleating on catalytic foreign smooth surface (<i>s</i>) in liquid (<i>l</i>) (reproduced from [69]).	20
Figure 2.7.	Nucleation on a foreign particle for different wetting angles θ (reproduced from [69]).	20
Figure 2.8.	Generalised nucleation rate diagram showing the dominant areas for homogeneous, heterogeneous and surface nucleation (reproduced from [66]).	23
Figure 2.9.	Simplified illustration of primary and secondary crystal growth.	25
Figure 2.10.	Concentration variation in the fluid adjacent to the growing crystal surface (adapted from [62]).	26

Figure 2.11.	Growth sites at a crystal surface showing the movement of solvated solute molecule. The interplanar distance in the crystal lattice, d , is indicated (adapted from [54]).....	27
Figure 2.12.	Classification of three epitaxy growth modes (reproduced from [87]).	29
Figure 2.13.	Solubility isotherms of calcium phosphate phases in the ternary system $\text{Ca}^{2+}\text{-PO}_4^{3-}\text{-H}_2\text{O}$ at 25 °C. Calculated with the aid of PHREEQC for solutions in which Ca to P molar ratio is given by the stoichiometry of each phase. One phase each time was considered and no carbonates were present.	36
Figure 3.1.	Crystallisation reactor set-up.....	58
Figure 3.2	XRD pattern of $\text{FeAsO}_4\cdot 2\text{H}_2\text{O}$ produced by atmospheric precipitation.	63
Figure 3.3.	Scanning electron micrographs of scorodite substrate material.....	63
Figure 3.4.	Particle size distribution of scorodite produced by atmospheric precipitation. median = 22.8 μm , mean = 26.4 μm , and mode = 21.3 μm . 64	
Figure 3.5.	Back-scattered electron image of scorodite precipitated under atmospheric conditions.	64
Figure 4.1.	Metastable zone width for the $\text{Al}_2(\text{SO}_4)_3\text{-H}_3\text{PO}_4\text{-NaOH}$ system at 95 °C. Symbols: \square Initial point – Critical concentration for homogeneous nucleation; \odot Final point - pseudo-solubility.....	68
Figure 4.2.	XRD pattern of product obtained by homogeneous precipitation (relative intensity); solids produced from a solution with $[\text{P(III)}]_0 = 0.2$ mol/L and $\text{Al:P} = 1$; $\text{AlPO}_4\text{-H}_3$ pattern from reference [3].....	69

Figure 4.3.	Scanning electron micrographs of hydrated aluminium phosphate produced by homogeneous precipitation.....	69
Figure 4.4.	Particle size distribution of hydrated aluminium phosphate produced by homogeneous precipitation. Median = 3.3 μm , mean = 3.6 μm , and mode = 4.2 μm	70
Figure 4.5.	One-stage aluminium phosphate precipitation with pH control using homogeneously produced seed (Seed concentration, 30 g/L); NaOH as base; 95 $^{\circ}\text{C}$; precipitation pH 1.70.	71
Figure 4.6.	Scanning electron micrographs of hydrated aluminium phosphate produced by seed-assisted precipitation after three recycles.	71
Figure 4.7.	Particle size distribution of hydrated aluminium phosphate produced by seed-assisted precipitation. median = 16.8 μm , mean = 16.7 μm and mode = 18.6 μm	72
Figure 4.8.	XRD pattern of product obtained by seed-assisted precipitation ($\text{AlPO}_4\text{-H}_3$ pattern from reference [3])......	73
Figure 4.9.	TGA Analysis of hydrated aluminium phosphate produced by seed-assisted precipitation; heating rate 10 $^{\circ}\text{C}\cdot\text{min}^{-1}$	73
Figure 4.10.	P(V) and Al(III) concentrations and pH as a function of time at 22 $^{\circ}\text{C}$. (a) final pH of 2.43; (b) final pH of 3.62 (c) final pH of 3.79;. (d) final pH of 4.18; (e) final pH of 6.44 and (f) final pH of 8.80. (Symbols \square Al(III); \blacksquare P(V); \circ pH).....	78
Figure 4.11.	Experimental solubility determined for $\text{AlPO}_4\cdot 1.5\text{H}_2\text{O}$ at 22 $^{\circ}\text{C}$ (equilibration time 30 d).....	79
Figure 4.12.	Al(III) to P(V) molar ratio in solution after 30 d of dissolution.	79

Figure 4.13.	XRD pattern of solids before and after equilibrium at various pH compared to synthetic $\text{Al}(\text{OH})_3$ (Gibbsite), $\text{Al}_3(\text{OH})_3(\text{PO}_4)_2 \cdot 9\text{H}_2\text{O}$ (Kingite), $\text{AlPO}_4 \cdot 1.5\text{H}_2\text{O}$ and $\text{AlPO}_4 \cdot 2\text{H}_2\text{O}$ (Variscite).....	80
Figure 4.14.	Ion activity product for aluminium (oxy)hydroxides during the dissolution of $\text{AlPO}_4 \cdot 1.5\text{H}_2\text{O}$ as a function of time at 22 °C at different equilibration pHs. Log K_{sp} for (1) $\text{Al}(\text{OH})_3$ (amorphous) (2) $\text{Al}(\text{OH})_3$ (gibbsite), and (3) AlOOH (diaspore) are shown (broken lines) as well.	82
Figure 4.15.	Ion activity product of $\text{AlPO}_4 \cdot 1.5\text{H}_2\text{O}$ as a function of time at 22 °C at different equilibration pHs. Log K_{sp} for $\text{AlPO}_4 \cdot 1.5\text{H}_2\text{O}$ is also shown (broken lines).	83
Figure 5.1.	Metastable zone width for the $\text{CaCl}_2\text{-H}_3\text{PO}_4\text{-NaOH}$ system at 22 °C: (a) Ca:P = 1; (b) Ca:P = 1.67.....	92
Figure 5.2.	Generalised precipitation diagram for the synthesis of calcium phosphate phases. DCPD: $\text{CaHPO}_4 \cdot 2\text{H}_2\text{O}$; OCP: $\text{Ca}_8(\text{HPO}_4)_2(\text{PO}_4)_4 \cdot 5\text{H}_2\text{O}$; and HAP: $\text{Ca}_{10}(\text{PO}_4)_6(\text{OH})_2$	93
Figure 5.3.	One-stage dicalcium phosphate dihydrate crystallisation. (a) Homogeneous precipitation (precipitation pH 5.4); (b) Seed-assisted precipitation using homogeneously produced seed (precipitation pH 5.0 and seed concentration, 10 [g/L]); NaOH as base.....	95
Figure 5.4.	Homogeneous precipitation (spontaneous) of hydroxyapatite: LaMer diagram (left); evolution of calcium to phosphorus molar ratio (right).....	96
Figure 5.5.	Semi-batch seed-assisted precipitation of (calcium-deficient) hydroxyapatite. Concentration of phosphorus in solution (left); evolution of calcium to phosphorus molar ratio (right). Reagent solution addition rate 40 mL/h.....	97

Figure 5.6.	Semi-batch seed-assisted precipitation of (calcium-deficient) hydroxyapatite. Concentration of phosphorus in solution (left); evolution of calcium to phosphorus molar ratio (right). Reagent solution addition rate 80 mL/h.	98
Figure 5.7.	Scanning electron micrographs of dicalcium phosphate dihydrate produced by homogeneous precipitation (left) and seed-assisted precipitation (right).....	99
Figure 5.8.	XRD pattern of products obtained by homogeneous precipitation and seed-assisted precipitation compared to $\text{CaHPO}_4 \cdot 2\text{H}_2\text{O}$ (brushite).	99
Figure 5.9.	Scanning electron micrographs of hydroxyapatite produced by homogeneous precipitation.	100
Figure 5.10.	Scanning electron micrographs of hydroxyapatite produced by seed-assisted precipitation.	100
Figure 5.11.	XRD patterns of hydroxyapatites produced with different precipitation strategies compared to $\text{Ca}_{10}(\text{PO}_4)_3(\text{OH})_2$ (hydroxyapatite).....	101
Figure 5.12.	IR spectra of calcium-deficient hydroxyapatites. (a) homogeneous precipitation product; (b) seed-assisted precipitation product (40 mL/h); (c) seed-assisted precipitation product (80 mL/h).	103
Figure 5.13.	P(V) and Ca(II) concentrations and pH as a function of time at 22 °C. (a) initial pH of 4.5; (b) initial pH of 5.50 (c) initial pH of 6.70.	108
Figure 5.14.	Experimental solubility determined for $\text{CaHPO}_4 \cdot 2\text{H}_2\text{O}$ at 22 °C. (equilibration time 20 d). Final concentrations of Ca(II) and P(V) as a function of pH (left). Calcium to Phosphorus molar ratio in solution	

	after 20 d of dissolution (right).....	109
Figure 5.15.	XRD pattern of solids before and after equilibration at various pH compared to $\text{CaHPO}_4 \cdot 2\text{H}_2\text{O}$	109
Figure 5.16.	Ca(II) to P(V) molar ratio during solids preparation steps; (step 0 was performed at pH = 7.0).....	110
Figure 5.17.	P(V) and Ca(II) concentrations and pH as a function of time at 22 °C. (a) initial pH of 5.0; (b) initial pH of 6.0; (c) initial pH of 7.0; (d) initial pH of 8.0; (e) initial pH of 9.0.	111
Figure 5.18.	Experimental solubility determined for calcium-deficient hydroxyapatite at 22 ° C (equilibration time 30 d).	112
Figure 5.19.	Calcium to phosphorus molar ratio in solution after 30 d of dissolution.	112
Figure 5.20.	XRD pattern of solids before and after equilibrium at various pH compared to $\text{Ca}_8(\text{HPO}_4)_2(\text{PO}_4)_4 \cdot 5\text{H}_2\text{O}$; $\beta\text{-Ca}_3(\text{PO}_4)_2$ and $\text{Ca}_{10}(\text{PO}_4)_3(\text{OH})_2$ (hydroxyapatite).	113
Figure 5.21.	Ion activity product of $\text{CaHPO}_4 \cdot 2\text{H}_2\text{O}$ as a function of time at 22 °C at different equilibration pHs. Ion activity product expressed as equation (5.4).	114
Figure 5.22.	Ion activity product of $\text{Ca}_{10}(\text{PO}_4)_3(\text{OH})_2$ as a function of time at 22 °C at different equilibration pHs. Ion activity product expressed as equation (5.7).	116
Figure 5.23.	Final Ion activity product (expressed as hydroxyapatite) versus final pH.	117

Figure 5.24.	Potential lines of hydroxyapatite, octacalcium phosphate; β -tricalcium phosphate, and dicalcium phosphate dihydrate in the system $\text{Ca}(\text{OH})_2 + \text{H}_3\text{PO}_4 + \text{H}_2\text{O}$ at 22°C. Points represent experimental data after 30 d of equilibration. (Final pHs are shown in bracket).	118
Figure 5.25.	Ca and P concentrations in solution vs. pore size membrane used.....	119
Figure 6.1.	Controlled deposition of aluminium phosphate on scorodite. (a) Variation of P(V) and Al(III) with time; (b) Variation of As(V) and Fe(III) with time. Experimental conditions: P(V)= 0.16 mol/L, Al:P =1, T=95 °C, precipitation pH 1.7.	127
Figure 6.2.	Quantity of aluminium and phosphorus removed and arsenic release as a function of 1.5 h periods during controlled crystallisation-deposition of $\text{AlPO}_4 \cdot x\text{H}_2\text{O}$ on scorodite particles.	128
Figure 6.3.	Controlled crystallisation-deposition of aluminium phosphate on scorodite followed by two recycles. Experimental conditions: P(V)= 0.16 mol/L, Al:P =1, T=95 °C, precipitation pH 1.7.	129
Figure 6.4.	Quantity of aluminium and phosphorus removed and arsenic release as a function of 1.5 h periods during controlled crystallisation-deposition of $\text{AlPO}_4 \cdot x\text{H}_2\text{O}$ on previously coated scorodite particles. (a) One recycle; (b) two recycles.	130
Figure 6.5.	Effect of base on the precipitation kinetics. (a) Variation of P(V) with time; (b) Variation of As(V) with time. Experimental conditions: P(V)= 0.16 mol/L, Al:P =1, T=95 °C, precipitation pH 1.7.	131
Figure 6.6.	"Ion exchange" between scorodite and PO_4 -containing solution. (a) Variation of P(V) with time; (b) Variation of As(V) with time. Experimental conditions: P(V)= 0.16 mol/L, Al:P =0 in "ion exchange"	

	test, Al:P=1 in standard test, T=95 °C, precipitation pH 1.7.	132
Figure 6.7.	Distribution of phosphate complexes (at 25 °C) as a function of pH. (a) In the presence of Al ³⁺ ions, (b) in a solution without Al ³⁺ ions.....	133
Figure 6.8.	Deposition of aluminium phosphate on scorodite following "ion exchange". (a) Variation of P(V) with time; (b) Variation of As(V) with time. Experimental conditions: P(V)= 0.16 mol/L, Al:P =1, T=95 °C, precipitation pH 1.7.	134
Figure 6.9.	Effect of substrate material on the precipitation kinetics of aluminium phosphate Experimental conditions: P(V)= 0.16 mol/L, Al:P =1, T=95 °C, precipitation pH 1.7. (CaSO ₄ ·2H ₂ O 50 g/L).....	135
Figure 6.10.	Scanning electron micrograph of hydrated aluminium phosphate precipitated heterogeneously on gypsum crystals.....	135
Figure 6.11.	Back-scattered electron (BSE) image of a scorodite particle coated with aluminium phosphate material (left) and elemental X-ray maps.	136
Figure 6.12.	Back-scattered electron (BSE) images of encapsulated scorodite particles of different size fractions.....	137
Figure 6.13.	Cross section scanning electron micrographs of scorodite particles coated with aluminium phosphate material after one-, two-, and three-deposition cycles.	138
Figure 6.14.	Back-scattered electron images of a scorodite particles coated with aluminium phosphate material. The particle on the left was obtained by deposition using NaOH as base, while the particle on the right was obtained with MgO as base.	139
Figure 6.15.	XRD pattern of product obtained by directed deposition of aluminium	

phosphate after two consecutive recycles. Scorodite substrate (Chapter 3) and $\text{AlPO}_4 \cdot 1.5\text{H}_2\text{O}$ produced by seed-assisted precipitation (Chapter 4) are also shown. The $\text{AlPO}_4 \cdot \text{H}_3$ pattern is from reference [3]. 140

Figure 6.16.	Backscattered electron image of a scorodite particle coated with aluminium phosphate material after the bulk of the coating was dislodged.....	141
Figure 6.17.	SEM-EDX radial compositional analysis of coated scorodite particle shown in Figure 6.16.....	141
Figure 6.18.	Depth Profiling through the encapsulated scorodite by TOF-LIMS.....	142
Figure 6.19.	In depth profiling through AlPO_4 coated scorodite. Scatterplot of positive ion (+ve, left) and negative ion (-ve, right). TOF-LIMS data collected at moderate ablator laser energies. Symbols: \square Core, \blacktriangle Subsurface, and \odot Surface.....	143
Figure 6.20.	Spatial distribution of Al and Fe after various ablation times.....	144
Figure 6.21.	Batch precipitation of (Ca-deficient) hydroxyapatite at controlled pH on scorodite particles (10 g/L); NaOH as base; precipitation pH 7.60. a) Variation of P(V), Ca(II), and As(V) with time; (b) Variation of Ca:P molar ratio in solution with time.	147
Figure 6.22.	Batch precipitation of (Ca-deficient) hydroxyapatite at controlled pH on scorodite previously equilibrated at pH 7.6 (10 g/L); NaOH as base; precipitation pH 7.60. a) Variation of P(V), Ca(II), and As(V) with time; (b) Variation of Ca:P molar ratio in solution with time.	148
Figure 6.23.	Quantity of calcium and phosphorus removal and arsenic release after	

	30 min of batch deposition of Ca-deficient hydroxyapatite on scorodite with and without pre-equilibration at pH 7.6.....	149
Figure 6.24.	Evolution of the saturation index for some crystalline calcium arsenate compounds as a function of time during batch precipitation. (a) Using pre-equilibrated scorodite at pH 7.6 particles as substrate; (b) using "as is" scorodite particles as substrate.	151
Figure 6.25.	Evolution of the saturation index for some crystalline calcium carbonate compounds as a function of time during batch precipitation. (a) Using pre-equilibrated scorodite at pH 7.6 particles as substrate; (b) using "as is" scorodite particles as substrate.....	151
Figure 6.26.	Semi-batch crystallisation of Ca-deficient hydroxyapatite using scorodite particles as substrate (10 g/L) (a) Concentration of P and As in solution; (b) Ca:P molar ratio. Reagent solution addition rate 6 mL/h.....	153
Figure 6.27.	Semi-batch crystallisation of Ca-deficient hydroxyapatite using scorodite particles as substrate (10 g/L) (a) Concentration of P and As in solution; (b) Ca:P molar ratio. Reagent solution addition rate 10 mL/h.....	153
Figure 6.28.	Semi-batch crystallisation of Ca-deficient hydroxyapatite using scorodite particles as substrate (10 g/L) (a) Concentration of P and As in solution; (b) Ca:P molar ratio. Reagent solution addition rate 20 mL/h.....	154
Figure 6.29.	Calculated calcium to phosphate molar ratio in the precipitated product during the course of the semi-batch precipitation of Ca-deficient hydroxyapatite in the presence of scorodite substrate.	156

Figure 6.30.	Ion activity product for $\text{Ca}_3(\text{PO}_4)_2$ during the semi-batch precipitation of Ca-deficient hydroxyapatite in presence of scorodite particles as a function of time. (a). Reagent solution addition rate 20 mL/h; (b). Reagent addition rate 10 mL/h; and (c). Reagent addition rate 6 mL/h. (Critical <i>IAP</i> is shown in broken lines).....	158
Figure 6.31.	Back-scattered electron images of scorodite particles coated with calcium phosphate material. (a),(b) Reagent addition rate 20 mL/h; (c),(d). Reagent addition rate 10 mL/h; and (e),(f) Reagent addition rate 6 mL/h.	160
Figure 6.32.	Back-scattered electron image of a scorodite particle coated with calcium phosphate material produced under reagent addition rate 6 mL/h(left). X-ray maps confirming the presence of CaPO_4 -material deposited on scorodite (right).	161
Figure 6.33.	Dissolution kinetics of Arsenic(V) versus time at different equilibration pH at oxic conditions. Symbols: \square Scorodite substrate; \bullet AIP(1); \diamond AIP(2); and Δ AIP(3).	163
Figure 6.34.	Arsenic concentration in solution after 10 d of dissolution for scorodite particles coated with an aluminium phosphate material.	164
Figure 6.35.	Concentration after 10 d of equilibration compared to respective solubilities.(a) phosphorus concentration; (b) aluminium concentration.....	164
Figure 6.36.	Dissolution kinetics of As(V) versus time at different equilibration pH at oxic conditions. Symbols: \square Scorodite substrate; \diamond dHAP(low); and Δ dHAP(med).....	165
Figure 6.37.	Arsenic concentration after 10 d of equilibration for scorodite particles	

	coated with a calcium phosphate material.	166
Figure 6.38.	Concentration after 10 d of equilibration compared to respective solubilities.(a) phosphorus concentration; (b) calcium concentration.....	166
Figure 6.39.	Dissolution kinetics of As(V), P(V) and Ca(II) versus time at pH 6.0. (a) dHAP(low); (b) dHAP(med).....	167
Figure 6.40.	Ca:P and Ca:(P+As) in solution as a function of time at pH 6. (a) dHAP(low); (b) dHAP(med).	168
Figure 6.41.	Dissolution kinetics of total arsenic(left) and total iron(right) versus equilibration time at under chemically generated anoxic conditions. Symbols: □ Scorodite substrate; ● AIP(1); △ AIP(3); and ◇ dHAP(low).....	169
Figure 6.42.	Final concentration levels of elements from anoxic dissolution of scorodite substrate, AIP(1), AIP(3) and dHAP(low) at pH 7, E _h 100 mV, and 22 °C (equilibration time 6 weeks).....	169
Figure 6.43.	Daily average values of pH and E _h during anoxic stability test. (a) E _h variation; (b) pH variation. Set-point values are also shown in broken lines.	170
Figure 6.44.	Dissolution kinetics and speciation of scorodite dissolution under chemically generated anoxic conditions. Arsenic speciation (left); iron speciation (right).....	171
Figure 6.45.	Back-scattered electron images of scorodite particles coated with calcium and aluminium phosphate before and after oxic and anoxic stability tests.....	171

List of Tables

Table 3.1.	List of Chemical reagents used.....	59
Table 4.1.	Equilibria and constants considered in the present PHREEQC study.	76
Table 4.2.	Solubility data and solubility product estimates using PHREEQC	81
Table 5.1.	Equilibria and constants considered in the present PHREEQC study	94
Table 5.2.	Lattice parameters and stoichiometry of produced solids	102
Table 5.3.	Solubility data, K_{sp} , and ion activity product estimates using PHREEQC for the dissolution of $\text{CaHPO}_4 \cdot 2\text{H}_2\text{O}$	115
Table 6.1.	Equilibria and constants considered in the present PHREEQC study.	150
Table 6.2.	Calculated and measured stoichiometry of produced coated solids	156

List of Symbols

a	Activity of ionic species, [mol·m ⁻³] or [mol·L ⁻¹]
a_{eq}	Activity of ionic species at solubility, [mol·m ⁻³] or [mol·L ⁻¹]
a_c	Volumetric crystal surface, [m ² ·m ⁻³]
a_m	Surface area of a crystal, [m ²]
a, b, c	parameters for unit cell of crystal: three vectors (a, b, c) that form the edges of a parallelepiped
B	Full width at half maximum of a X-ray diffraction peak, [rad]
C	Bulk concentration, [mol·m ⁻³] or [mol·L ⁻¹]
C_{eq}	Equilibrium concentration at solubility, [mol·m ⁻³] or [mol·L ⁻¹]
C_{∞}	Equilibrium concentration or solubility of an infinite size crystal, [mol·m ⁻³] or [mol·L ⁻¹]
d	Interplanar distance in the crystal lattice, [m]
d_m	Molecular diameter, [m]
D	Molecular diffusivity of the solute, [m ² ·s ⁻¹]
E	Detachment probability of surface nuclei
G	Growth rate, [m·s ⁻¹]
$\Delta G_{f,0}$	Gibbs free energy of formation, [J·mol ⁻¹]
IAP	Ion activity product
I	Ionic strength, [mol·m ⁻³]
J	Nucleation rate, [#·m ⁻³ ·s ⁻¹]
k_B	Boltzmann constant, $1.380 \cdot 10^{-23}$ [J·K ⁻¹]
k_d	Mass transfer coefficient, [m·s ⁻¹]
k_r	Growth rate constant, [m·s ⁻¹]
k_1	Surface solute absorption growth rate constant, [m·s ⁻¹]
k_2	Surface spiral growth rate constant, [m·s ⁻¹]

k_e	Surface nucleation (polynuclear) growth rate constant, [$\text{m}\cdot\text{s}^{-1}$]
K_e	Exponential constant for Surface nucleation (polynuclear) growth
K_{sp}	Solubility product
L	Crystal size as equivalent diameter, [m]
N_A	Avogadro's number, $6.0221\cdot 10^{23}$ [mol^{-1}]
r	Radius of the crystal, [m]; growth order
r_{cr}	Critical nucleus size, [m]
S	Saturation ratio
SI	Saturation index
T	Temperature, [K] or [$^{\circ}\text{C}$]
t	average crystallite size, [nm]
v_m	Molar volume of the crystal, [$\text{m}^3\cdot\text{mol}^{-1}$]
w_B	mass fraction of B, [$\text{kg}\cdot\text{kg}^{-1}$]
$W(r)$	Work to form an embryo of radius r , [J]
z	valency

Greek Letters

δ	Thickness of diffusion layer, [m]
ϕ	Heterogeneous nucleation factor
γ	Activity coefficient
γ_{el}	Interfacial free energy (embryo-liquid), [$\text{J}\cdot\text{m}^{-2}$]
γ_{sl}	Interfacial free energy (solid-liquid), [$\text{J}\cdot\text{m}^{-2}$]
γ_{se}	Interfacial free energy between the substrate surface and the embryo, [$\text{J}\cdot\text{m}^{-2}$]
γ_e	Edge energy per unit length, [$\text{J}\cdot\text{m}^{-1}$]
$\Delta\gamma$	Wetting condition, [$\text{J}\cdot\text{m}^{-2}$]
λ	root-mean displacement, [m]; λ is the wavelength of the X-rays, [nm]
$\Delta\mu$	chemical potential difference for transition from liquid to solid state, [J]
$\Delta\mu_v$	chemical potential difference for transition from liquid to solid state per molecular volume $\Delta\mu_v = \Delta\mu/v_m$, [$\text{J}\cdot\text{m}^{-3}$]

θ	Contact angle, [rad]; Bragg's diffraction angle, [rad or °]
τ	Induction time, [s] or [min]
ρ	Crystal density, [kg·m ⁻³]
Ω	Pre- exponential term, [s ⁻¹ m ⁻³] or [s ⁻¹ m ⁻²]

Subscripts and superscripts

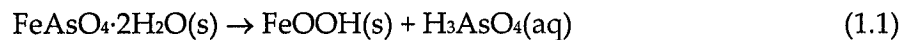
<i>A</i>	Cation of an electrolyte
<i>B</i>	Anion of an electrolyte
<i>aq</i>	aqueous phase
<i>cr</i>	Critical
<i>eq</i>	value at equilibrium
<i>homo</i>	Homogeneous nucleation
<i>het</i>	Heterogeneous nucleation
<i>s</i>	solid phase
<i>surf</i>	Surface nucleation

Chapter 1. Introduction

Arsenic is a major contaminant in the non-ferrous extractive metallurgical industry and its disposal is one of the most important environmental issues for the mining and metallurgical industries. This problem has worsened in recent years because of the increasing arsenic content of the low-grade or complex ores currently processed by the mining industry and the introduction of stricter environmental regulations [1,2].

Its removal and immobilisation from process effluents typically involves lime neutralisation and coprecipitation with ferric iron. The resulting precipitate is considered to be relatively stable provided that the Fe(III) to As(V) ratio is 4 or higher [3]. In the case, though, of arsenic-rich and iron-deficient effluents, such as acid plant effluents, the need to use a large excess of iron (a costly operation when dealing with large amounts of arsenic), the production of crystalline scorodite ($\text{FeAsO}_4 \cdot 2\text{H}_2\text{O}$) is advocated as a better alternative. This mineral is not only widely accepted as being one of the most stable forms of arsenic for disposal, but scorodite dewateres much easier and is more compact than the amorphous sludge generally produced by coprecipitation [4,5].

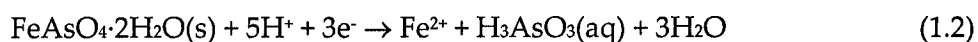
However, questions have been raised, mostly based on thermodynamic grounds, with reference to the long term stability of scorodite. Thus, scorodite may decompose under oxic conditions according to thermodynamics at $\text{pH} > 4$ (different pH have been reported by different investigations) converting to goethite, releasing then arsenic into solution [6,7,8,9,10]:



A recently completed scorodite stability study revealed that no goethite forms even when scorodite is equilibrated at 75 °C for several months. Instead, the formation of a nano-crystalline ferrihydrite phase appears to block further breakdown of scorodite. But

even in this case arsenic solubility in the order of 5 mg/L (at 22 °C) was determined for scorodite at pH 7 increasing to higher values in the alkaline region [5,11]. Tailings pore waters in general should not, according to certain environmental regulations, exceed 1 mg/L [8,12]. Hence, scorodite despite meeting currently the EPA TCLP criterion (< 5 mg/L of arsenic after 20 h extraction period at pH 5.0) may not be able to meet stricter environmental regulations in the future.

Notwithstanding the limited stability of scorodite under oxic conditions the major concern with the disposal of arsenic in the form of scorodite is its documented instability under anoxic conditions. Thus, according to Rochette et al. [13] scorodite undergoes reductive decomposition to Fe(II) and As(III) when E_h decreases below ~ 100 mV. In this manner, scorodite would dissolve releasing arsenious acid according to:



As a number of mining operations practice the method of sub-aqueous deposition of tailings reductive decomposition of scorodite might occur, releasing arsenic into the environment. It has been reported that crystalline ferric sulphoarsenate (resembling scorodite) produced in an autoclave (190°C) and stored in an impounded pond has undergone reductive dissolution releasing As(III) (and Fe(II)) at the Campbell Mine of Placer Dome [14]. This was attributed to the presence of soluble organic carbon in the aqueous environment. Additionally, as reported in literature [15] below about 2 m depth, aqueous environments can become anaerobic; hence, under such conditions the possibility of reactive metal sulphides acting as reductants cannot be ruled out [1].

The main objective of this work is to investigate the development of a novel method of arsenic fixation based on the encapsulation of scorodite particles via direct crystallisation on them of stable phosphate coatings not prone to oxic and anoxic decomposition.

In more specific terms, the objectives of this research study are:

- i. To prepare crystalline aluminium and calcium phosphates by controlled

homogeneous and seeded crystallisation, under ambient pressure conditions and subject them to dissolution studies and thermodynamic modelling.

- ii. To design and describe novel encapsulation processes by coating scorodite particles with the above synthetic phosphate minerals.
- iii. To evaluate the stability of encapsulated scorodite under simulated anoxic (anaerobic) and oxic (aerobic) environments.
- iv. To investigate phases, layers, and cohesion between the scorodite particles and the phosphate materials via a variety of characterisation tools, including: XRD (X-ray diffraction); FT-IR (Fourier Transform Infrared Spectroscopy), TOF-SIMS and TOF-LIMS (time of flight secondary ion mass spectrometer and laser ionisation mass spectrometer respectively), SEM-EDX (scanning electron microscope equipped with an energy dispersive X-ray analyser) and TGA (thermo gravimetric analysis).

The present work has been organised into a number of chapters as follows: Chapter 1 and Chapter 2 are the introduction and an extensive literature survey of the subject matter of the thesis. Chapter 2 includes the current status of arsenic fixation and disposal in the metallurgical industry along with a review of the formation of scorodite and related compounds and some aspects of crystallisation theory of precipitation. Finally, a review of the chemistry and synthesis of aluminium and calcium phosphates is presented.

Chapter 3 describes the experimental equipment and procedures used to achieve the proposed objectives as well as the analytical methods employed. In Chapters 4 and 5, the synthesis and stability of aluminium and calcium phosphates are investigated experimentally and via thermodynamic modelling with the aid of PHREEQC.

In Chapter 6, the controlled deposition of aluminium phosphate and calcium phosphate onto scorodite particles is investigated, including the testing of the encapsulated solids

in oxic and anoxic chemical environments. Finally, Chapter 7 provides a global summary of the major findings of this work, states the contributions made to knowledge, and gives a brief outline of how this work can be continued in the future.

References

- 1 Harris, G.B. The removal and stabilization of arsenic from aqueous process solutions: Past, present and future. In *Minor Elements 2000: Processing and Environmental Aspects of As, Sb, Se, Te and Bi*; Young, C.A., Ed.; Society for Mining Metallurgy and Exploration: Littleton, CO, 2000, pp. 3-20.
- 2 Riveros, P.A.; Dutrizac, J.E.; Spencer, P. Arsenic disposal practices in the metallurgical industry. *Canadian Metallurgical Quarterly*, 2001, 40(4), 395-420.
- 3 Harris, G.B. The removal of arsenic from process solutions: Theory and industrial practice. In *Hydrometallurgy 2003: Electrometallurgy and Environmental Hydrometallurgy*; Young, C.A.; Alfantazi, A.M.; Anderson, C.G.; Dreisinger, D.B.; Harris, B.; James, A., Eds.; The Minerals, Metals & Materials Society: Warrendale, PA, 2003, Volume 2, pp. 1889-1902.
- 4 Demopoulos, G.P.; Lagno, F.; Wang Q.; Singhania, S. The atmospheric scorodite process. In *Copper 2003-Cobre 2003, Hydrometallurgy of Copper*; Riveros, P.A.; Dixon, D.; Dreisinger D.B.; Menacho J., Eds.; The Canadian Institute of Mining, Metallurgy and Petroleum (CIM): Montreal, QC, 2003, Book 2, pp. 597-616.
- 5 Demopoulos, G.P. On the preparation and stability of scorodite. In *Arsenic Metallurgy*; Reddy, R.G.; Ramachandran, V.; Eds.; The Minerals, Metals & Materials Society Warrendale, PA, 2005, pp. 25-50.
- 6 Krause, E.; Ettl, V.A. Solubility and stability of scorodite. $\text{FeAsO}_4 \cdot 2\text{H}_2\text{O}$: New data and further discussion. *American Mineralogist*, 1988, 73, 850-854.
- 7 Robins, R.G. The stability and solubility of ferric arsenate: An update. In *EPD Congress 1990*; Gaskell, D.R., Ed.; The Minerals, Metals & Materials Society: Warrendale, PA, 1990, pp. 93-104.
- 8 Langmuir, D.; Mahoney, J.; MacDonald, A.; Rowson, J. Predicting arsenic

- concentrations in the porewaters of buried uranium mill tailings. *Geochimica et Cosmochimica Acta*, **1999**, 63(19-20), 3379-3394.
- 9 Welham, N. J.; Malatt, K. A.; Vukcevic, S. The stability of iron phases presently used for disposal from metallurgical systems - A review. *Minerals Engineering*, **2000**, 13(8-9), 911-931.
- 10 Bluteau, M-C.; Demopoulos, G.P. Fixation of arsenic in the form of scorodite. A solubility study. In *Waste Processing and Recycling in Mineral and Metallurgical Industries V*; Rao, S.R.; Harrison, F.W.; Kozinski, J.A.; Amaratunga, L.M.; Cheng, T.C.; Richards, G.G.; Pickles, C.A., Eds.; Canadian Institute of Mining, Metallurgy and Petroleum(CIM): Montreal, QC, **2004**, pp. 439-452.
- 11 Bluteau, M-C. The incongruent dissolution of scorodite- solubilities, kinetics and mechanisms. *M.Eng. Thesis*, McGill University, QC, **2004**.
- 12 Environment Canada. Status report on water pollution prevention and control in the Canadian, metal mining industry 2001; Minerals and Metals Division: Ottawa, ON, **2003**, <http://www.ec.gc.ca/nopp/docs/rpt/waterpollution/mining2001/en/toc.cfm>
- 13 Rochette, E.A.; Li, G.C.; Fendorf, S.E. Stability of arsenate minerals in soil under biotically generated reducing conditions. *Soil Science Society America Journal*, **62**, **1998**, 1530-1537.
- 14 McCreadie, H.; Jambor, J.L., Blowes, D.W.; Hiller, D. Geochemical behaviour of autoclave-produced ferric arsenates and jarosite in a gold-mine tailings impoundment. In *Waste Characterization and Treatment*; Petruk, W., Ed.; Society for Mining Metallurgy and Exploration: Littleton, CO, **1998**, pp. 61-78.
- 15 Hopkin, W. The problem of arsenic disposal in non-ferrous metals production. *Environmental Geochemical and Health*, **1989**, 11(3-4), 101-112.

Chapter 2. Literature review and theory

In this chapter, the technical literature is reviewed starting with an overview of the problem and options of arsenic removal and disposal in the metallurgical industry along with the formation of scorodite in aqueous solution. Afterwards, a review of the basic principles of aqueous crystallisation theory is given with the objective of defining the underlying theoretical foundations on which the present work is based. In particular, emphasis is given on the definition and role of supersaturation in controlling the crystallisation process. The chapter concludes with a brief review of coating technologies in aqueous media and the chemistry and synthesis of aluminium and calcium phosphates in aqueous media.

2.1 The Arsenic problem

Arsenic as a result of weathering processing of arseniferous minerals reports to water in the form of As(III) or As(V) state causing a number of diseases to those drinking arsenic-containing water. Among the diseases reported (in addition to its widely known poisoning properties) are keratosis (skin pigmentation) and cancer [1]. The drinking-water arsenic contamination produced in Bangladesh and West Bengal, India is now well documented and environmental activities are moving to implement stricter standards. This is exemplified with the new EPA standard for drinking water at 0.01 mg/L (10 μ g/L) for arsenic to be entered as of January 2006 [2].

The mining industry must deal with soluble arsenic because of the presence of arsenic in many ores and concentrates. Common minerals include the two sulphides realgar (As_4S_4) and orpiment (As_2S_3) and the oxidised form arsenolite (As_2O_3). The arsenides and the mixed arsenides-sulphides of iron, cobalt, copper, and nickel such as arsenopyrite (FeAsS), cobaltite (CoAsS), enargite (Cu_3AsS_4), and gersdorffite (NiAsS) [3,4].

Clearly, if some of the arsenic present in the above minerals entered any metallurgical circuit it would increase the production costs due to arsenic interference with metal extraction, deterioration of the product purity, but more important increased environmental risk and tailings disposal problems [5,6].

In hydrometallurgical operations, arsenic-containing ores are leached and soluble arsenic species of As(III) and/or As(V) are produced. In those cases where autoclaves are used, as in the processing of pyritic gold ores by pressure oxidation, arsenic is reported to be fixed by the formation of stable scorodite-type precipitates [5]. During bacterial leaching of pyritic gold ores or concentrates, the arsenic leached is coprecipitated downstream with iron as a ferric arsenate at the final neutralisation stage [7].

In pyrometallurgical operations such as roasting, smelting, and conversion, considerable amounts of arsenic are volatilised as As_2O_3 or As_2S_3 , depending upon the overall temperature and oxygen potential of the respective process, which have to be captured in electrostatic precipitators as an arsenic-bearing flue-dust [8]. A normal industrial practice is the continuous recycling of arsenic-rich flue dust within the pyrometallurgical operations. However, this practice causes an increase of arsenic in the copper anode destined for electrorefining [5]. Several hydrometallurgical processes have been proposed to treat the flue-dust and some were implemented. These processes are based on either acidic or alkaline leaching in order to remove arsenic and other impurities from arsenic-bearing dust [9]. Flue dust can also be upgrade in order to remove base metals and produce As_2O_3 [10].

Modern smelters normally employ acid plants to control SO_2 emissions from smelting and converting operations. Gases entering the acid plants are pre-cleaned, in gas scrubbing and cooling systems to remove dust, SO_3 , and metals, for efficient acid plant operation and production of sulphuric acid. The solution generated, so-called weak acid effluent, contains, among other base metals, dissolved trivalent arsenic at high concentrations, approximately 2 up to 20 g/L [11].

The arsenic present in this effluent must be removed from solution and fixed in a storable, insoluble, and stable form. This is generally achieved by coprecipitation with Fe(III) [12,13], by precipitation of As_2S_3 , which must be suitably stockpiled [14]; or by precipitation with lime, which leads to the formation of several calcium arsenate compounds [15]. The latter method is not considered viable over the long term because of the gradual formation of calcium carbonate and concomitant release of arsenic [16]. In the case of As_2O_3 flue dusts, stockpiling in protected dry areas has been historically practiced as well [17].

During the electrolytic refining of copper anodes arsenic level is kept at a concentration less than about 15 g/L by withdrawing a bleed stream of the circulating electrolyte [18]. The electrolyte bleed stream after partial decopperising is advanced to a set of electrowinning cells -so-called liberator cells- to remove copper and arsenic as an arsenical sludge [19,20].

The amount of arsenic generated by the metallurgical industry is several times higher than the arsenic demand. On the other hand, the arsenic demand is shrinking because of enforcement of legislation while the arsenic generation has increased because of the increasing arsenic content of the low-grade and complex ores, currently processed by the mining industry, and the introduction of stricter environmental regulations [5,13]. Since, the imbalance in the arsenic "supply and demand" the majority of the arsenic generated/mobilised by metallurgical operations necessitates being disposed as a waste.

2.2 Arsenic removal and fixation

2.2.1 Processing options

The removal and fixation of arsenic by precipitation and, particularly, the solubility and stability of the resulting precipitates is of considerable importance to the metallurgical industry, as is illustrated by the increasing number of publications dealing with this problem as early as the 1950s [21].

Coprecipitation of arsenic with iron at high Fe(III):As(V) molar ratio is one the most widely applied methods for disposing of arsenic in effluent streams [13]. This technology is the United States EPA "Best Demonstrated Available Technology" (BDAT) for the removal of dissolved arsenic [22]. The resulting precipitate is considered to be relatively stable provided that the Fe(III):As(V) ratio is 4 or higher [21]. According to the majority of investigations arsenic was retained in the precipitated via adsorption on ferrihydrite [23]. However, recent research has revealed that at least in the case of arsenic concentrated arsenic solutions, that the coprecipitate is comprised of two arsenic phases: amorphous ferric arsenate $\text{FeAsO}_4 \cdot x\text{H}_2\text{O}$ ($x > 2$) and ferrihydrite with adsorbed arsenate [24].

Arsenic fixation in autoclaves becomes economically attractive only if arsenic stabilisation is operated co-currently with the processing of valuable concentrates. This concept is reflected in the widely practised oxygen pressure leaching of refractory gold concentrates as a pre-treatment procedure, and also in the proposed aqueous pressure process for treatment of arsenic-rich roaster waste and other arsenical sulphide minerals with metal values [25]. In these processes, most of the arsenic reports in a stable scorodite-type precipitate.

More complex compounds, such as the apatite structured calcium phosphate arsenate have recently been reported to be of low solubility and appropriate stability for disposal considerations [26]. The produced compound is stable only at $\text{pH} > 9.5$; hence, it requires special storage conditions. Precipitation of mimetite (Pb(II) chloroarsenate, $\text{Pb}_5(\text{AsO}_4)_3\text{Cl}$) has been studied in detail [27]; however, because of the complexing of lead by acetate mimetite does not pass EPA's TCLP [28].

Some efforts have been given to solidification/stabilisation [29,30], also known as encapsulation or fixation, with a summary of the various methods used and investigated published by Leads et al. [31]. Most of these methods include high temperature fixation of ceramic-type materials [32] or fixation with cement and lime [33]; however, the long-

term stability of this material has not been convincingly demonstrated

The encapsulation of arsenical solid wastes using pyrometallurgical slags has also been investigated by Twidwell [34] and more recently by Riveros and Utigard [35]. This process has been rejected due to the rapid decomposition of the arsenate-arsenite at the operating temperatures (higher than 900 °C), and difficulties in injecting powdered arsenate-arsenite into the slag. Combining arsenic wastes with polymers such as HDPE has been reported for encapsulation of As_2O_3 [36]. Nevertheless, the processing temperatures employed approach the sublimation temperature of As_2O_3 , and the process was both inefficient and hazardous.

A summary of the current methods used for the bulk removal and disposal of arsenic was conducted recently by Harris [21]. The methods currently being applied for the removal and fixation of arsenic can be classified in: (i) iron-arsenic coprecipitates; (ii) high temperature iron arsenates; (iii) lime neutralisation-calcium arsenate (arsenite); (iv) copper arsenate; (v) arsenic sulphide; and (vi) arsenic trioxide. In Figure 2.1 a distribution of the industrial operating practices is shown.

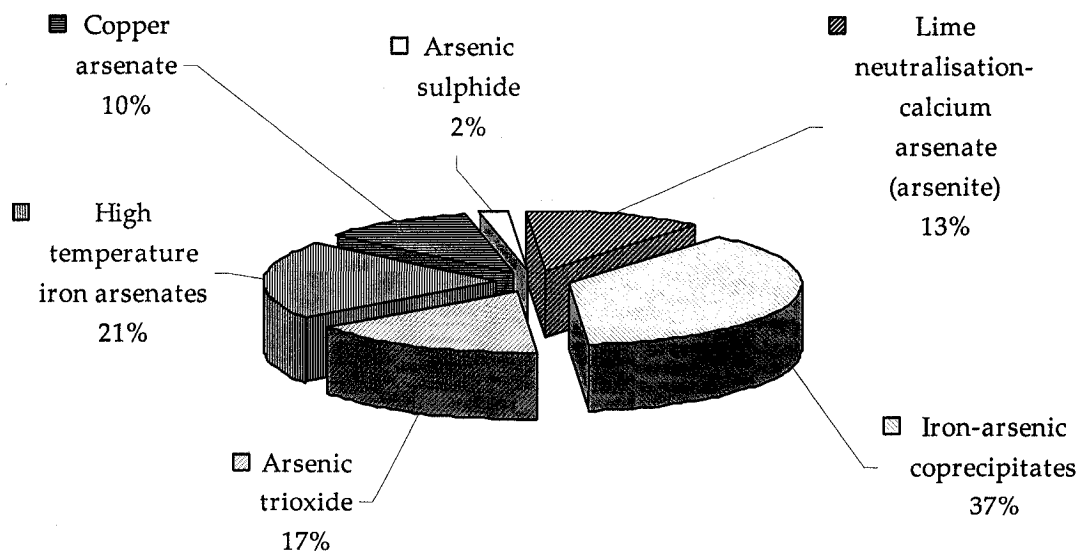


Figure 2.1. Summary of industrial operating practice as of year 2000/2001 based on 48 operations reported in reference [21].

It can be seen from Figure 2.1 that still some operations practice simple lime

neutralisation. Chiefly, they are located in extremely arid climates (e.g. the Atacama Desert in the north of Chile), where it rarely rains.

For the treatment of arsenic-rich and iron-deficient waste solutions or solids, the fixation of arsenic in the form of scorodite (a crystalline ferric arsenate, $\text{FeAsO}_4 \cdot 2\text{H}_2\text{O}$), clearly shows several operational advantages. Among those are its low solubility (typically <1 mg/L of As at $\text{pH} = 5$ [37,38,39]) compliance with environmental regulations [40]. Scorodite has a high arsenic content (25-30%), good thickening and filtration properties, compact volume, and low water retention. Typical waste solutions or solids that can be treated for the production of crystalline scorodite are: acid plant effluents, Cu-ER electrolyte bleed streams, As_2O_3 flue dusts, and arsenic-contaminated soils [41,42].

2.2.2 Formation of scorodite and related compounds

The formation of crystalline scorodite has been reported by various researchers from a number of different chemical environments: from Fe(III)-As(V)- NO_3 solution under hydrothermal conditions ($>150^\circ\text{C}$) [43] and from Fe(III)-As(V)- SO_4 solution over the temperature range of 150 to 200°C [44]. In addition to scorodite, two other types of ferric arsenate compounds could be precipitated out of the solution, depending on the initial Fe(III):As(V) molar ratio in the solution and precipitation temperature [44]. Type I, with approximate composition $\text{Fe}_2(\text{HAsO}_4)_3 \cdot x\text{H}_2\text{O}$ ($x < 4$), forms when the initial Fe to As molar ratio in solution is ~ 1.0 , and the temperature higher than 150°C . At temperatures above 200°C and for Fe to As molar ratios of 1.5 or higher, Type II becomes predominant and its formula can be generalised as $\text{Fe}_4(\text{AsO}_4)_3(\text{OH})_x(\text{SO}_4)_y$ ($x+2y=3$) [19,45]. It has been reported that Type II shows solubility levels as low as scorodite [38].

Papangelakis and Demopoulos [46] also reported the formation of scorodite during acid pressure oxidation (140 - 190°C) of arsenopyrite in a 0.5 mol/L H_2SO_4 medium. Finally Van Weert and Droppert reported the production of scorodite via the hydrothermal processing of As_2O_3 in the presence of HNO_3 solutions [47]. The formation conditions in

all these cases relate to the use of autoclaves, which are considered to being capital-intensive.

It has been demonstrated that crystalline scorodite can also be formed at ambient pressure. Controlled crystallisation of scorodite from arsenic-rich waste acid solutions under atmospheric pressure conditions based on the concept of supersaturation control that favours the attainment of crystallinity was experimentally demonstrated by Demopoulos and co-workers [41,48,49,50,51,52]. This research program was successful in determining the conditions for atmospheric precipitation of crystalline scorodite. This was first demonstrated in the case of chloride solutions [53] and subsequently in the case of sulphate media [48]. Before this study, precipitation of crystalline scorodite was possible only via autoclave processes [44].

The ambient-pressure precipitation and fixation of arsenic in the form of scorodite by a supersaturation-controlled approach is described schematically in Figure 2.2. This figure shows the experimentally determined values of critical arsenic concentration C_{cr} and the equilibrium concentration C_{eq} in sulphate solutions of molar ratio Fe(III) to As(V) equal to 1.0 at 95°C.

The region between the two lines defines the operating window for the precipitation of crystalline scorodite in the presence of seed. Stepwise increase of pH as shown on the figure ensures operation within the crystallisation zone.

2.3 Crystallisation theory

Crystallisation is an important separation and purification technique employed in a variety of industries to produce a wide-variety of materials in the chemical, metallurgical, and pharmaceutical industries. In medicine and biology, precipitation plays an important role in normal and pathological mineralisation (for example the formation of bones, teeth, or shell) [54]. Crystallisation (including precipitation) is of economic importance in the hydrometallurgical industry for the separation and/or

production of inorganic metal compounds in the form of good quality crystals, both in terms of purity and size [55].

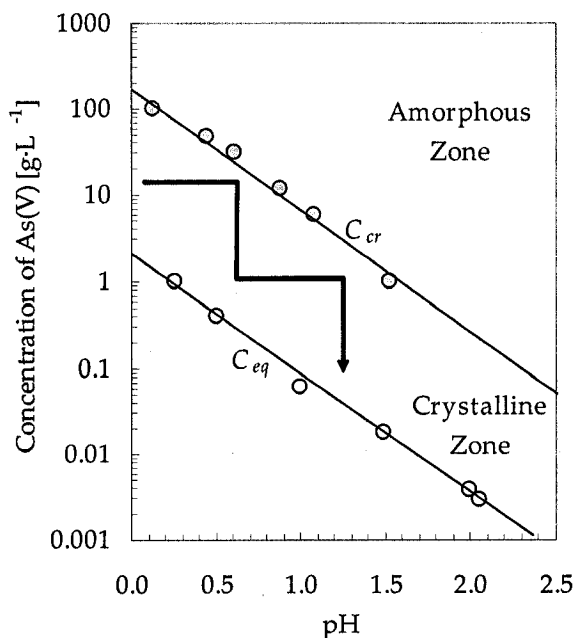


Figure 2.2. Supersaturation control area for atmospheric precipitation of scorodite at 95°C from Fe(III)-As(V)-SO₄ solution (reproduced from [41]).

2.3.1 Supersaturation

Crystallisation is a rate process; this means that the time required for the formation of a crystal depends on some driving force. In the case of crystallisation, the driving force is called *Supersaturation*. Supersaturation is the essential variable in any precipitation system and the level of supersaturation in the precipitation solution rules the rates of simultaneous processes, such as nucleation, growth, and Ostwald ripening [56,57].

Supersaturation can be measured by means of the saturation ratio S that is defined as the concentration of component ions in excess of the equilibrium concentration. It is expressed, in simple terms, as the ratio of the actual concentration to the equilibrium concentration [58].

$$S = \frac{C}{C_{eq}} \quad (2.1)$$

C being the bulk solute concentration and C_{eq} the equilibrium concentration (solubility) of the solute at given temperature and pressure of the system. If $S > 1$, the solution is supersaturated.

More strictly speaking, supersaturation for sparingly soluble salt $A_\alpha B_\beta$ is defined as [58]:

$$S = \left(\frac{a(A)^\alpha \cdot a(B)^\beta}{a(A)_{eq}^\alpha \cdot a(B)_{eq}^\beta} \right) = \left(\frac{IAP}{K_{sp}} \right) \approx \left(\frac{C(A)^\alpha \cdot C(B)^\beta}{C(A)_{eq}^\alpha \cdot C(B)_{eq}^\beta} \right) \quad (2.2)$$

Where subscript *eq* refers to equilibrium conditions, a denotes the activities of the respective ions, IAP is the ion activity product in the supersaturated solution and K_{sp} is the solubility product.

Supersaturation can be seen as a measure of the deviation of a dissolved salt from its equilibrium value. Figure 2.3 shows a solubility diagram for a soluble salt with inverse solubility (its equilibrium concentration in solution decreases with increasing temperature). At the point A the solid salt is in equilibrium with the solute, this equilibrium might be upset by: increasing the solution concentration at constant temperature (line AB), increasing the temperature (line AC), or varying concentration and temperature (line AD).

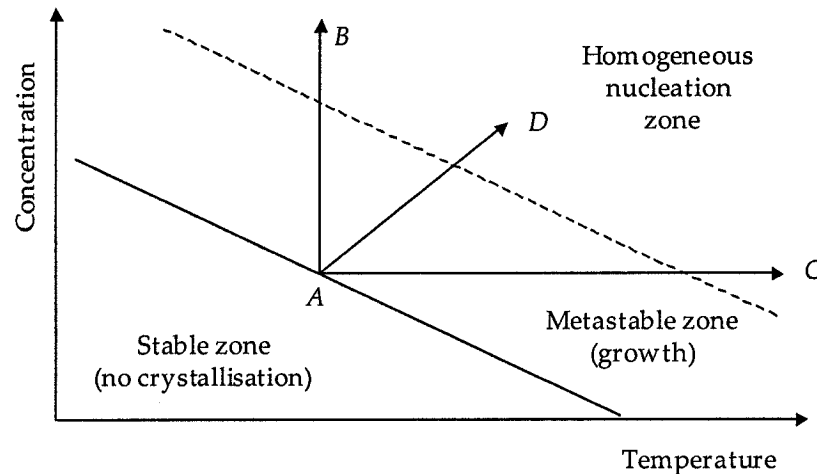


Figure 2.3. Solubility-supersaturation diagram explaining the stable metastable and labile zones for a salt with inverse solubility (adapted from [60]).

Nevertheless, there is a limit in the extent of deviation from equilibrium marked by the

dashed line in Figure 2.3. Once, this line is reached, spontaneous precipitation occurs. This range of supersaturation defines the homogeneous nucleation zone (also called labile zone) and the broken line is known as the critical homogeneous nucleation line [59,60].

Below the solubility line, precipitation cannot take place. On the contrary, since in this range the solution is undersaturated dissolution takes place. The metastable zone is important information for designing and operating a precipitation process, since, industrial crystallisers are operated, in general, in the metastable zone for producing a desired product quality with respect to crystallinity, median size, particle size distribution, shape, and purity [61].

Supersaturation in solution can be developed in many ways including temperature fluctuation, metal complexation and dissociation, solids dissolution, or pH change. Any of these methods may be used to generate a particular solid phase. However, the most common method used in hydrometallurgical systems is pH change [55].

2.3.2 Nucleation

The formation of a crystal in liquid solutions begins with nucleation. Once a critical supersaturation level has been reached nucleation takes place.

Nucleation can be caused by various mechanisms. In the case of a crystal-free solution that contains no foreign particles, nuclei are formed by primary homogeneous nucleation. If nucleation takes place on the surface of foreign particles, primary heterogeneous nucleation is the mechanism. The difference from primary nucleation and secondary nucleation is that the latter is caused by the presence of the same material that is being nucleated. The presence of seed crystals is essential in this nucleation process; however, when the secondary nuclei do not come from the seed, i.e., its formation is due to external forces (apparent or contact) the mechanism is called non-activated secondary nucleation [58,62,63]. Figure 2.4 gives an overview of the different types of nucleation.

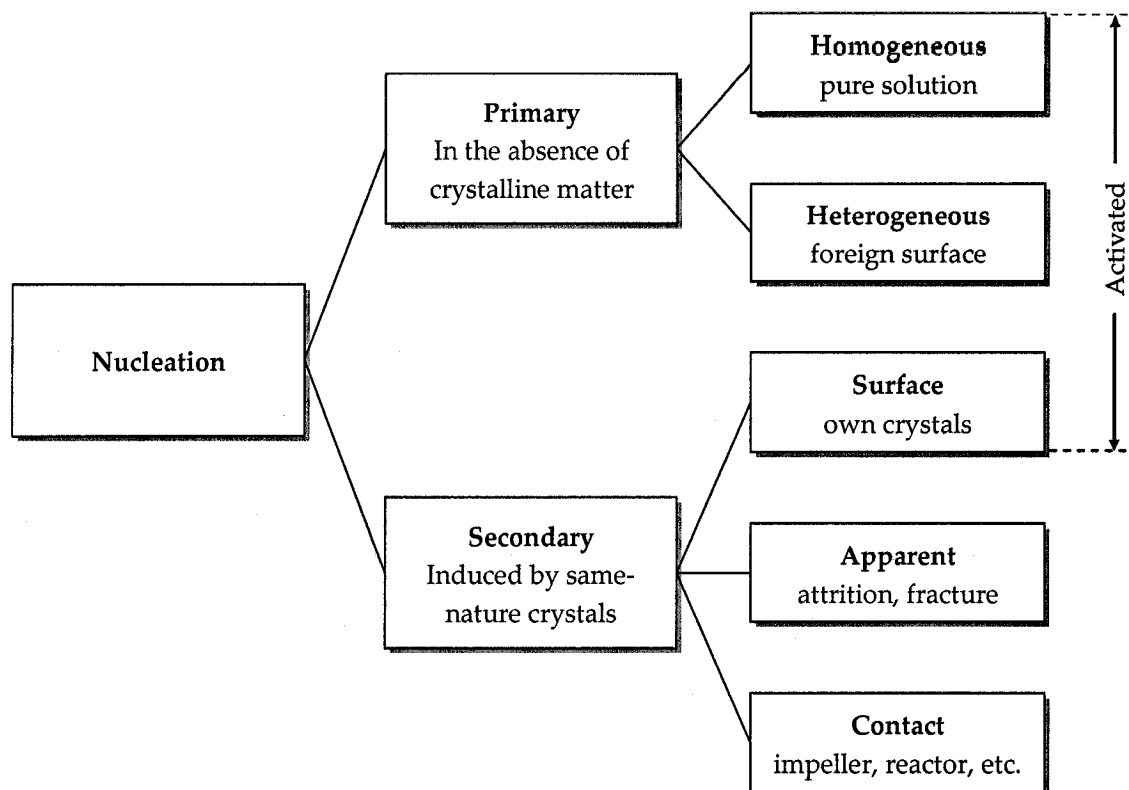
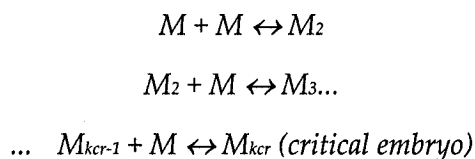


Figure 2.4. Classification of nucleation mechanism (adapted from [63]).

Primary homogeneous nucleation: This occurs in the absence of a solid surface. With supersaturation as the driving force, molecules or ion pairs form embryos or clusters of 10-1000 units, which grow to form stable nuclei as soon as they are above a minimum critical size, r_{cr} . It is presumed that in supersaturated solutions, solute embryos are constantly forming and dispersing but only those exceeding size r_{cr} result in viable nuclei [64]. Accordingly, the embryo formation can be schematised as [58,65]:



Where M_k is embryo made of k molecules or ions ($k=2, 3, \dots, k_{cr-1}, k_{cr}$), and the M_{kcr} corresponds to an embryo with a critical size.

The work, W , to form an embryo of size r in a supersaturated solution is defined as the difference between the free energy of the system in its final and initial states, i.e., after

and before the embryo formation [64]. Considering the embryo having molar volume, v_m , and surface area, a_m , the overall free energy change resulting from an embryo nucleating homogeneously from solution is given by [54]:

$$W = v_m \cdot \Delta\mu_v + a_m \cdot \gamma_{el} \quad (2.3)$$

where $\Delta\mu_v = \Delta\mu/v_m$, is the chemical potential difference for transition from liquid to solid state per molecular volume of the solid phase and γ_{el} is the interfacial free energy embryo-solution (assumed to be independent of embryo size). In every supersaturated solution $\Delta\mu_v$ is a negative quantity, proportional to the nucleus volume and is a function of the saturation ratio ($\Delta\mu = -k_B T \cdot \text{Ln} S$, k_B is the Boltzmann constant and T the absolute temperature). In Eq. (2.3) both terms depend on the embryo size. Introducing the assumption that the embryo being a sphere of radius r , Eq. (2.3) can be written as [66]:

$$W(r) = \frac{4\pi r^3}{3v_m} \Delta\mu + 4\pi r^2 \gamma_{sl} = -\frac{4\pi r^3}{3v_m} k_B T \cdot \text{Ln} S + 4\pi r^2 \gamma_{sl} \quad (2.4)$$

The molecular volume can be calculated from $v_m = M/\rho \cdot N_A$ (M is the crystal molecular weight, ρ is the crystal density, N_A is Avogadro's number), and the interfacial free energy embryo-solution is considered such as an average of the specific surface energies of the crystal faces present in the equilibrium form of the crystal ($\gamma_{el} \sim \gamma_{sl}$) [64].

In Figure 2.5 the nucleation to form an embryo is plotted. It can be seen that the negative *volume-term* (free energy gain) and the positive *surface-term* (free energy loss) in equation (2.4) result in a maximum of W_{cr} at $r = r_{cr}$. Physically, the embryo of size r_{cr} is the critical nucleus, and $W_{cr} = W(r_{cr})$ is the nucleation work. These two basic quantities in the theory of nucleation are obtained from equation (2.4) with the help of the condition $\partial W/\partial r = 0$ at $r=r_{cr}$ for maximum:

$$r_{cr} = -\frac{2\gamma_{sl}}{\Delta\mu_v} = \frac{2\gamma_{sl} v_m}{k_B T \cdot \text{Ln} S} \quad (2.5)$$

$$W_{cr} = \frac{16\pi\gamma_{sl}^3}{3} \left[\frac{v_m}{k_B T \cdot \text{Ln} S} \right]^2 \quad (2.6)$$

The critical nuclei size decreases and the number of nuclei increases as S increases. Thus,

at high S a large population of ultra fine colloidal particles will form at a very fast rate. The critical nuclei size is usually between 40 and 200 Å and is a function of supersaturation. In practical terms then a high degree of supersaturation is expected to yield a large population of ultra-fine particles [55].

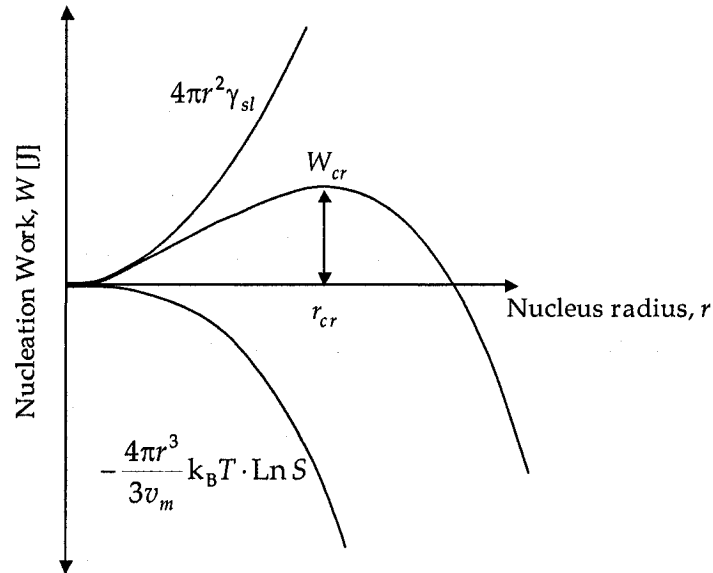


Figure 2.5. Overall free energy change resulting from an embryo nucleating homogeneously from solution, according to equation (2.4) (reproduced from [54]).

Considering primary homogeneous nucleation as an activated process, the nucleation rate, J_{homo} , can be expressed as an Arrhenius-type equation [66]:

$$J_{homo} = \Omega_{homo} \exp\left[-\frac{W_{cr}}{k_B T}\right] \quad (2.7)$$

The pre-exponential term (Ω_{homo}) in equation (2.7) can be estimated for primary homogeneous nucleation by using Einstein's equation for the relation between time, t , the root-mean-square displacement, λ , and the diffusion coefficient, D (i.e. $\lambda/2t = D$), and assuming equilibrium exists among all embryos. This yields $\Omega_{homo} = 2D/d^5$ where d is the interplanar distance in the crystal lattice [67]. The theoretical estimation of Ω_{homo} is $10^{39\pm3}$ [$s^{-1}\cdot m^{-3}$] while the experimental values obtained from nucleation of slightly soluble salts (of which, a homogeneous nucleation is expected) range widely between 10^{25} and 10^{56} [68].

Combining equations (2.6) and (2.7) results in the expression [66]:

$$J_{hom} = \Omega_{hom} \cdot \exp \left[-\frac{16}{3} \left(\frac{\gamma_{sl}}{k_B T} \right)^3 \left(\frac{v_m}{\ln S} \right)^2 \right] \quad (2.8)$$

Equation (2.8) indicates that three main variables govern the rate of nucleation: temperature; saturation ratio S ; and interfacial free energy, γ_{sl} .

Primary heterogeneous nucleation: This is induced by surfaces of a different material than the one that is precipitated (for instance a foreign solid). Nucleation is induced due to the lower surface energy of these surfaces than that of a newly forming particle. Thus, nucleation takes place at supersaturation levels that are lower than the critical supersaturation for homogeneous nucleation. The overall free energy change or nucleation work associated with the formation of a critical nucleus under heterogeneous conditions, W_{cr}^{het} , is less than, W_{cr} , associated with homogeneous nucleation, or [64]:

$$W_{cr}^{het} = \phi \cdot W_{cr} \quad (2.9)$$

where the factor ϕ , less than unity, can be expressed as

$$\phi = \frac{(2 + \cos \theta)(1 + \cos \theta)^2}{4} \quad (2.10)$$

In the above equation, θ is the contact angle formed between the embryo and the foreign surface, which corresponds to the angle of wetting in a liquid-solid system and is given by Young's equation (see Figure 2.6).

$$\gamma_{le} \cos \theta = \gamma_{sl} - \gamma_{se} \quad (2.11)$$

where γ_{sl} and γ_{el} represent the interfacial free energies between the liquid phase (l) and the surface (s) and the embryo (e) respectively, and γ_{se} the interfacial free energy between the substrate surface and the embryo.

In Young's equation, see Figure 2.7, at the limit $\theta \rightarrow \pi$ there is a complete mismatch between the crystalline lattices of the substrate and that of the embryo; while at $\theta \rightarrow 0$ a

perfect match is implied [69].

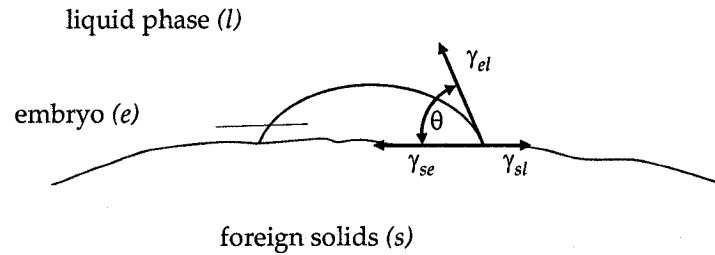


Figure 2.6. Heterogeneous nucleation: a embryo (e) nucleating on catalytic foreign smooth surface (s) in liquid (l) (reproduced from [69]).

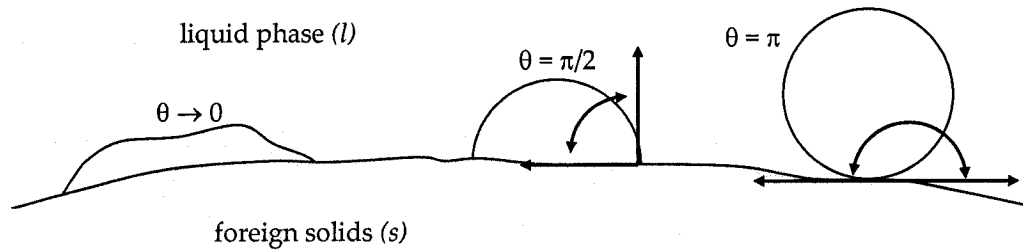


Figure 2.7. Nucleation on a foreign particle for different wetting angles θ (reproduced from [69]).

Similarly to homogeneous nucleation, the rate of heterogeneous nucleation can be estimated from:

$$J_{het} = \Omega_{het} \cdot \exp\left[-\frac{W_{cr}^{het}}{k_B T}\right] \quad (2.12)$$

where the pre-exponential factor $\Omega_{het} < \Omega_{homo}$ [66].

Secondary nucleation: This is related to the growth rate of existing crystals. This is the most likely source of new crystals in continuous stirred crystallisers or seeded batch crystallisers in the crystal suspension itself. This occurs at a much lower supersaturation than that needed for primary nucleation [66]. The seed crystals facilitate surface nucleation of newly deposited material due to lower activation energy barriers [70].

According to Nielsen [67], the formation of a surface (2-D) nucleus is similar to the formation of 3-D nucleus in a supersaturated medium. The adsorbed ions on the crystal surface move randomly and collide among each other. Finally, these collisions lead to

the formation of a critical 2-D embryo with radius r in metastable equilibrium. The nucleation work for the formation of a cylindrical 2-D is [66]:

$$W(r) = \frac{\pi r^2 d}{v_m} \Delta\mu + 2\pi r \gamma_e \quad (2.13)$$

where γ_e represents the edge energy per unit length, $\gamma_e = \gamma_{el} d$ and d is the interplanar distance in the crystal lattice ($d \sim (v_m)^{1/3}$). Analogously, with the theory of primary nucleation the critical size associated with the formation of a critical 2-D embryo on the crystal surface is [66]:

$$r_{cr}^{surf} = -\frac{\gamma_e}{d\Delta\mu_v} = \frac{\gamma_{el} v_m}{k_B T \cdot \text{Ln } S} \quad (2.14)$$

And the nucleation work associated with this embryo, W_{cr}^{surf} , is [66]:

$$W_{cr}^{surf} = \pi \gamma_{sl}^2 \left[\frac{v_m}{k_B T \cdot \text{Ln } S} \right] \quad (2.15)$$

The rate of crystal growth due to surface (two-dimensional) nucleation is given in the same form as that of homogeneous nucleation except in different units ($\# \text{ m}^{-2} \text{ s}^{-1}$):

$$j_{surf} = \Omega_{surf} \cdot \exp \left[-\frac{W_{cr}^{surf}}{k_B T} \right] \quad (2.16)$$

where $\Omega_{surf} = D/d^4$ [66]. Mersmann [71], in order to convert the surface rate from crystal surface units to volume of solution units, proposed the following relation:

$$J_{surf} = E \cdot j_{surf} \cdot a_c \quad (2.17)$$

where a_c represents the volumetric crystal surface (m^2/m^3), and E the detachment probability of surface nuclei. At the limit $E \rightarrow 1$ every new surface nucleus will be detached from the surface. While on the contrary, when $E \rightarrow 0$, results in $J_{surf} \rightarrow 0$ and in this case the surface nucleation only contributes to the growth of the crystals (see section 2.3.3).

Two more secondary nucleation mechanisms have been reported in literature, apparent secondary nucleation, and contact secondary nucleation.

Apparent secondary nucleation takes place when the contact between crystals and crystal-crystalliser results in the formation of cracks on the crystal contacted. In industrial crystallisers, an enormous number of attrition (or fracture) fragments are generated [69], these fragments have the ability to grow and to become active nuclei. Attrition and fracture become an important issue for crystals above 100 μm . In the case of reactive crystallisation (precipitation) this phenomena is neglected [72].

Contact secondary nucleation occurs when a growing particle collides with, the walls of the reactor, the stirrer, the pump impeller, or with each other, thus generating new residual solute particles [73].

These mechanisms are of non-activated nature, i.e., the generation of a new nucleus is due to external (mechanical) forces instead of activation energy associated driving forces.

Induction time: Establishment of supersaturated conditions in the solution satisfies the thermodynamic prerequisite for crystal formation. However, after the initial moment of supersaturating the solution, a certain induction time, τ , might elapse preceding the formation of a detectable amount of the new phase. This time (experimentally observable) is a measure of the "ability" of the solution to remain in metastable equilibrium [65]. The length of the induction time may vary from a fraction of a second to a few years. This time is influenced by several important operating variables such as supersaturation, temperature, pH, agitation speed, and impurities [74,75,76,77,78]. The induction time may be considered as the sum of the time intervals required for the achievement of the steady state of the nucleus distribution, τ_d , the formation of the critical nucleus, τ_n , and the growth of the critical nucleus to detectable size, τ_g [54].

$$\tau = \tau_d + \tau_n + \tau_g \quad (2.18)$$

Induction time depends on both nucleation and growth components. However, a simplifying assumption is made that τ is essentially related to nucleation rate according to [79]:

$$\tau \propto \frac{1}{J} \quad (2.19)$$

This equation is valid only if the transient period, the time intervals required for the achievement of the steady state of the nucleus distribution (τ_d), is negligible and can be ignored. Söhnel and Mullin [80] suggest that non-steady state nucleation is unimportant during the formation of crystalline salts from aqueous solution, no matter whether the nucleation is homogeneous or heterogeneous.

Supersaturation control: Another critical feature of the dependency of the nucleation rate on saturation ratio is the fact that nucleation starts only when a critical S value (S_{cr}) is exceeded. In Figure 2.8 a generalised nucleation rate diagram is shown. It can be seen that there is a critical value of the saturation ratio, S_{cr} , for homogeneous, heterogeneous, and surface nucleation and once this value is reached nucleation starts and propagates quickly. These critical saturation ratios are presented in increasing order, as follows:

$$S_{cr,surf} < S_{cr,heter} < S_{cr,homo} \quad (2.20)$$

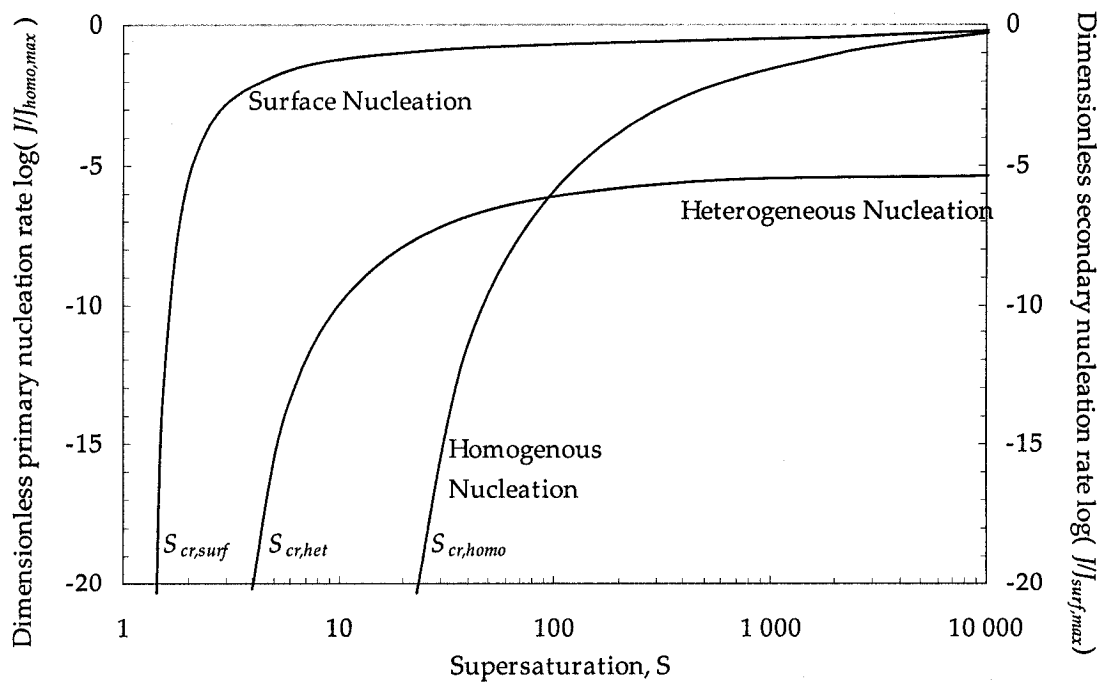


Figure 2.8. Generalised nucleation rate diagram showing the dominant areas for homogeneous, heterogeneous and surface nucleation (reproduced from [66]).

At low supersaturation surface nucleation on own crystals dominates ($J \approx J_{surf}$) whereas at very high supersaturation the rate is equal to J_{homo} , i.e. homogeneous nucleation dominates. The rate of heterogeneous nucleation often prevails at medium supersaturation and depends on the specific surface area of foreign particles and on the contact angle (θ) of a nucleus on the foreign surface [71]. In general, the rate of activated nucleation can be composed of the three contributions according to:

$$J = J_{hom} + J_{het} + J_{surf} \quad (2.21)$$

In this work, heterogeneous nucleation is the route by which a phosphate-coating material has to be deposited on the surface of scorodite particles. Heterogeneous nucleation occurs at a lower critical value of S , $S_{cr,het}$, than homogeneous nucleation, i.e., $S_{cr,het} < S_{cr,homo}$.

The importance of supersaturation control in scorodite encapsulation is evident: an increase in either pH or concentration will result in high supersaturation favouring homogeneous nucleation; hence, precipitation of phosphate phases will not occur on the surface of the scorodite substrate material [57]. Consequently, the encapsulation of scorodite must be done in a way that avoids surpassing the critical supersaturation level that corresponds to $S_{cr,homo}$. On the other hand, for scorodite encapsulation, the supersaturation has to be kept higher than the critical value of S for heterogeneous nucleation, i.e., $S_{cr,het} < S < S_{cr,homo}$.

2.3.3 Crystal growth

Nucleation is followed by the growth of the nuclei. The crystal growth rate along with nucleation controls the final particle size distribution, product purity, and crystal habit. Moreover, primary growth and secondary growth are responsible for the resultant shape of the final crystallites. Figure 2.9 shows the characteristic differences between these two growth mechanisms. Primary growth means that the increase in particle size is due to a new layer being continuously deposited onto an individual particle. Whereas, during

secondary growth, a larger particle is formed by the collision and joining together of two or more particles. This mode of growth, known as agglomeration, results in an irregular morphology for the particle [61].

These two mechanisms often occur simultaneously, where at lower supersaturation values primary growth dominates and at higher supersaturation values secondary becomes the dominant mechanism [55].

Primary crystal growth: The classical approach to crystal growth considers the overall growth rate as being determined by the relative magnitudes of two resistances in series, namely, the bulk diffusion step in which, the transport of growth units (molecules, atoms, or ions) from the bulk solution to the crystal surface, followed by the "integration" step in which the growth units build into the crystal lattice [81].

One or more of elementary processes controls the rate of crystal growth. Thus, the determination of growth kinetics is important in the evaluation of the rate-determining mechanism. However, if the crystals are sparingly soluble, quite small $<5 \mu\text{m}$, or are in a well-mixed suspension, the diffusion of material to the surface will be rapid, and the surface integration is likely to be the controlling step [82].

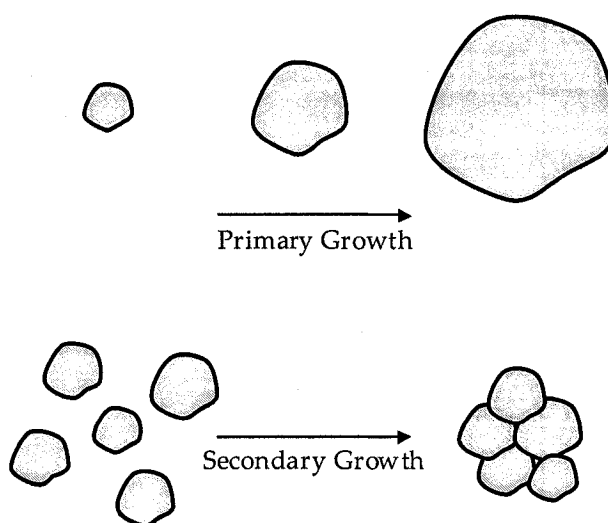


Figure 2.9. Simplified illustration of primary and secondary crystal growth.

Transport controlled growth: If the transport of growth units through the bulk medium controls the growth rate, their diffusion as illustrated in Figure 2.10 may be considered. In this case, the growth of particles is characterised by [82].

$$G = \frac{dL}{dt} = \frac{v_m D}{\delta} (C - C_{eq}) = k_d (S - 1) \quad (2.22)$$

where D is the diffusion coefficient, C is the solute concentration, C_{eq} is its solubility, k_d is the mass transfer coefficient and L is the size of the crystallites.

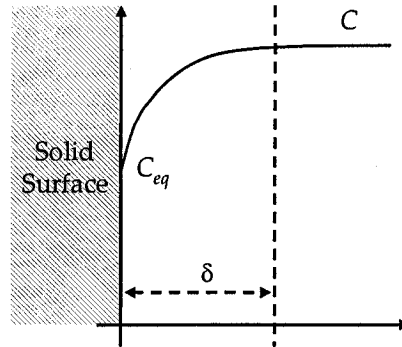


Figure 2.10. Concentration variation in the fluid adjacent to the growing crystal surface (adapted from [62]).

Surface integration controlled growth: The surface integration processes may compromise adsorption of growth units on the crystal surface (terrace), the diffusion of hydrated or dehydrated ions along the surface, the formation of 2-D surface nuclei, and the integration of growth units into the energetically favourable growth sites (kinks or steps on the crystal face, see Figure 2.11).

The equation representing the surface integration step is essentially an empirical equation that allows for all processes, but bulk diffusion, that are involved in the growth process and so enables growth data to be correlated without having to postulate any specific physical mechanism for this "surface integration" step [61]:

$$G = \frac{dL}{dt} = k_r (S - 1)^r \quad (2.23)$$

where k_r is the growth constant and r the growth order. The kinetic order and constant have no physical significance; they depend on the possible surface integration

mechanisms. Surface adsorption, spiral growth, and surface nucleation (polynuclear) are most commonly proposed as controlling mechanisms [54,61,62,66,82,83].

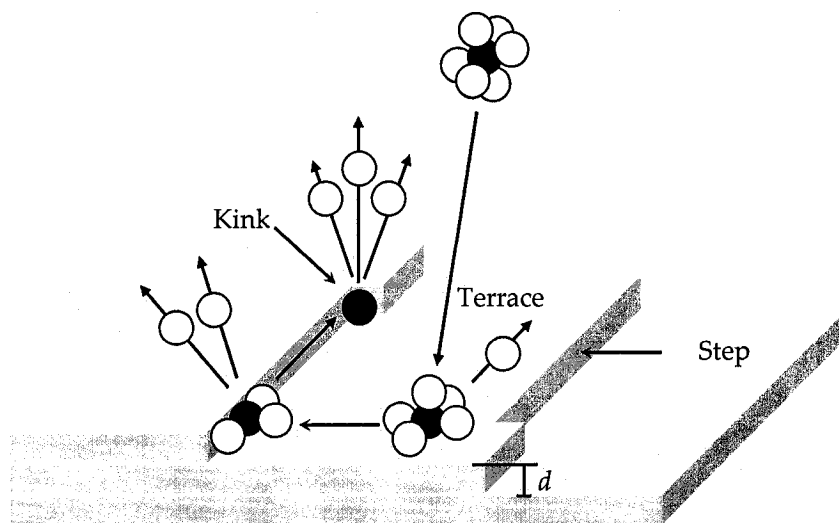


Figure 2.11. Growth sites at a crystal surface showing the movement of solvated solute molecule. The interplanar distance in the crystal lattice, d , is indicated (adapted from [54]).

Secondary crystal growth: Two types of secondary growth of particles can be differentiated according to the intensity of interparticle force: aggregation for weak force such as van der Waals forces and agglomeration for strong forces such as chemical bond[84].

During aggregation particles collide among each other to form a cohesive mass or cluster; the resultant structure is called an aggregate. Aggregation is favoured as the population density of colloid increases. High shear forces (agitation) tend to promote the formation of compact aggregates. Batch reactors are associated with extensive aggregation [55]. Agglomeration similarly to aggregation is a collection of two or more particles, agglomeration may alter the particle size, physical properties, and surface properties [61].

Primary crystal growth on a foreign surface: In the case of heterogeneous nucleation, the structural compatibility (lattice matching, crystal structure and lattice constant) as well as the chemical compatibility (chemical bonding) have a marked effect on deposit

morphology [85].

From a thermodynamic point of view, the growth morphology is controlled by the interfacial energy of the substrate (γ_{sl}), the embryo (γ_{el}) and the interfacial free energy between the substrate surface and the embryo (γ_{se}). The wetting condition in the growth of an embryo e on a surface s requires that [86]:

$$\Delta\gamma = (\gamma_{el} + \gamma_{es}) - \gamma_{sl} < 0 \quad (2.24)$$

The deposit morphology is strongly related with the sign of $\Delta\gamma$ in equation (2.24). Growth modes are placed in three mechanisms according to the resulting deposit morphology [85,86,87] (see Figure 2.12):

- **The Frank-van der Merwe (layer-by-layer):** growth takes place when the deposit units are more strongly attracted to the substrate than they are to themselves, in this case $\Delta\gamma < 0$ the energy balance will favour "wetting" of the surface by the deposited film, and layer-by-layer growth is expected.
- **Volmer-Weber (3D islands):** occurs when deposit units are more strongly attracted to themselves than to the substrate, that is, when γ_{al} is sufficiently in excess of γ_{bl} that equation (2.24) is never fulfilled even for a strong attractive interaction between a and b and little strain ($\gamma_{ab} < 0$) and,
- **Stranski-Krastanov (layer-plus-island):** in this mode, the most common one, layers form first then misfit strain energy contributions can modify γ_{es} with increasing film thickness, $\gamma_{el} + \gamma_{es}$ exceeds γ_{sl} and the growth mode transforms from 2D layer-by-layer to 3D islands.

2.3.4 Phase transformations

When reactive crystallisation in aqueous solution is carried out at either low temperature or in the absence of supersaturation control (or both), the solids formed are often either poorly crystalline or metastable phases, which upon ageing are converted to crystalline

stable compounds [55].

Early in 1897, Ostwald [as cited in ref. 88] formulated his so-called step rule, which states that "...the phase which is precipitating first is not the thermodynamically stable but rather a metastable phase" [88]. Later on, Stranski and Totomanow [as cited in ref. 89] studied this rule and claimed, "...the least stable phase nucleates first, because the interfacial energy requirements are less stringent" [89].

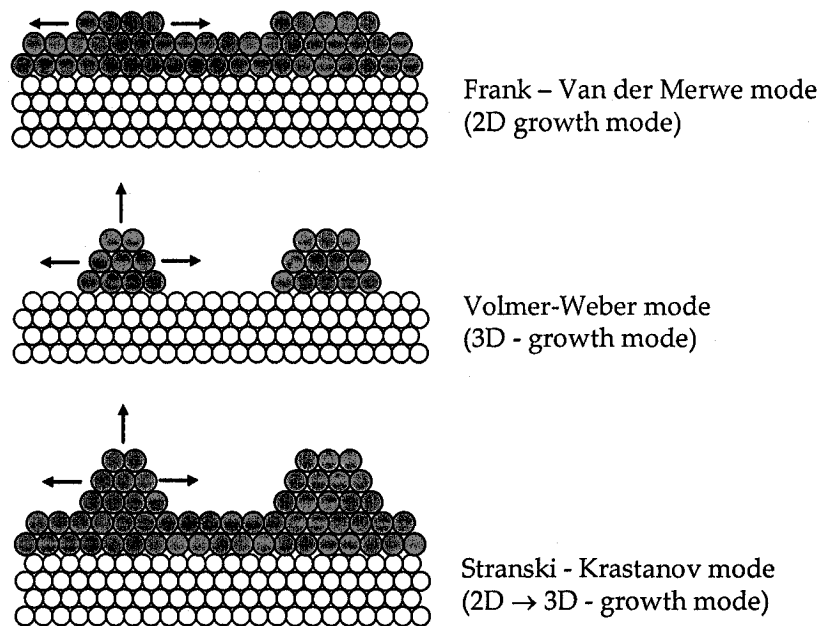


Figure 2.12. Classification of three epitaxy growth modes (reproduced from [87]).

A clear demonstration of Stranski or Ostwald step rule is the hydrolysis of Al(III) salts at high supersaturation which begins with the formation of the least stable amorphous aluminium hydroxide phase that later transforms to a poorly-crystalline form of boehmite, sometimes called pseudoboehmite, followed by its transition to the more stable intermediate crystal phase (α -Al(OH)₃, bayerite) and finally to the stable crystal phase (γ -Al(OH)₃ (gibbsite)) [90,91].

Another manifestation of this rule is in calcium phosphate precipitation process, where, the formation of precursor phases, such as dicalcium phosphate dihydrate, CaHPO₄·2H₂O, or octacalcium phosphate, Ca₈(HPO₄)₂(PO₄)₄·5H₂O, depending on the experimental conditions, precedes the formation of the most stable phase

hydroxyapatite, $\text{Ca}_{10}(\text{PO}_4)_6(\text{OH})_2$ [92]. This type of phase transformation reaction in aqueous media has been shown to proceed mainly through stepwise dissolution and re-precipitation [88,92].

There is a special case of phase transformation called Ostwald ripening. This process is not a phase transformation itself; although it produces a change in the crystal size of the precipitates. This usually takes place in batch crystallisation systems, where, as the supersaturation decreases because of the crystallisation process itself, the nucleation barrier and the critical nucleus size increase (equations (2.5) and (2.6)). Having as a result, the dissolution of small particles and the growth of large particles. As a consequence of this the average particle size over time increases while the number of particles in a system decreases [93,94].

2.4 Phosphate minerals

Phosphate minerals are found under a wide range of environmental conditions such as silicate melts, natural soils and ocean floors. In naturally occurring minerals phosphorus is pentavalent (phosphate, PO_4), although, trivalent, tetravalent, and hexavalent phosphorus compounds can be synthesised [95]. The crystallisation of inorganic phosphate salts is of great importance because of its involvement in areas such as biological mineralisation, the removal of phosphate from wastewaters, and in the formation of lake and ocean sediments [96]. Moreover, the increase in phosphate concentrations in water bodies, such as lakes, estuaries, or slow-moving streams near heavily populated areas are directly responsible for eutrophication (accelerated growth of algae as a result of excess nutrients in water [97]). Therefore, the precipitation and dissolution of phosphate minerals are of great environmental interest [98].

In this section, two phosphate salts are reviewed in detail, namely aluminium phosphate and calcium phosphate, with the purpose of highlighting the nucleation and growth characteristics of these salts in aqueous media.

2.4.1 Aluminium phosphates

Aluminium phosphates are of interest from both environmental as well as technological points of views. With reference to the former, the formation of aluminium phosphates helps remove phosphate from wastewaters or in other instances their dissolution helps regulate the release of phosphate in acidic soils [95,99]. In terms of technological relevance aluminium phosphates are important in the area of catalysis, due to their surface acidity and thermal stability [100,101,102].

Few well-crystallised aluminium phosphates, with an Al_2O_3 to P_2O_5 molar ratio of 1, have been observed in nature [95]. These include anhydrous aluminium phosphate; berlinite, the quartz form of AlPO_4 ; tridymite; and cristobalite; and two hydrated aluminium phosphates, variscite and metavariscite, both compositionally $\text{AlPO}_4 \cdot 2\text{H}_2\text{O}$ [103,104]. Variscite is orthorhombic; $2/m2/m2/m$ whereas metavariscite is monoclinic; $2/m$.

In addition to the naturally occurring aluminium phosphates a number of synthetic hydrated aluminium phosphates have been reported, so called $\text{AlPO}_4\text{-H}_i$ (i : 1,2,3,4). $\text{AlPO}_4\text{-H}_1$ and H_2 exhibit properties of molecular sieves, however, $\text{AlPO}_4\text{-H}_3$ and H_4 do not represent microporous materials, although $\text{AlPO}_4\text{-H}_3$ shows some prominent water adsorption characteristics [105]. According to McCusker and co-workers [106], $\text{AlPO}_4\text{-H}_1$ is hexagonal having a molecular formula $\text{Al}_{18}\text{P}_{18}\text{O}_{72} \cdot 42\text{H}_2\text{O}$ ($\text{AlPO}_4 \cdot 2.33\text{H}_2\text{O}$), $\text{AlPO}_4\text{-H}_2$ structure is orthorhombic and its molecular formula is $\text{Al}_6\text{P}_6\text{O}_{24} \cdot 4\text{H}_2\text{O}$ ($\text{AlPO}_4 \cdot 0.67\text{H}_2\text{O}$) [107]. The crystal structure of $\text{AlPO}_4\text{-H}_3$, as determined by Pluth and Smith [108], is orthorhombic with a chemical formula $\text{Al}_{16}\text{P}_{16}\text{O}_{64} \cdot 24\text{H}_2\text{O}$ ($\text{AlPO}_4 \cdot 1.5\text{H}_2\text{O}$). The crystal and molecular structure of $\text{AlPO}_4\text{-H}_4$ was recently determined by Poojary et al. [109] to be monoclinic with composition $\text{AlPO}_4 \cdot \text{H}_2\text{O}$. Variscite, metavariscite and the hydrates of $\text{AlPO}_4\text{-H}_1\text{-H}_4$ show important structural differences. In variscite and metavariscite all the aluminium atoms are $\text{AlO}_4(\text{H}_2\text{O})_2$ octahedral [103,104]; in $\text{AlPO}_4\text{-H}_1$ and $\text{AlPO}_4\text{-H}_2$, 33.3% of the framework aluminium atoms are $\text{AlO}_4(\text{H}_2\text{O})_2$ octahedral and 66.7% of Al atoms

are tetrahedrally (AlO_4) coordinated [110,111]. On the other hand, $\text{AlPO}_4\text{-H}_3$ and $\text{AlPO}_4\text{-H}_4$ contain equal amounts of AlO_4 tetrahedral and $\text{AlO}_4(\text{H}_2\text{O})_2$ octahedral [108,109].

Several synthesis methods have been described in the literature in the production of one or more of these aluminium phosphate phases. These methods can be classified in two main routes: the first one involving crystallisation of aluminophosphate gels and the second one involving homogeneous precipitation of amorphous aluminium phosphate solids followed by their conversion to crystalline phases via ageing. In both routes chloride and nitrate solutions were used. d'Yvoire was the first one that reported the synthesis of $\text{AlPO}_4\text{-H}_i$ (i : 1,2,3,4) along with variscite and metavariscite [112] using aluminophosphate gels ($\text{Al}_2\text{O}_3:\text{P}_2\text{O}_5 = 2.73$) heated at temperature around $100\text{ }^\circ\text{C}$ and subsequent refluxing. According to this procedure different hydrated aluminium phosphates are obtained by varying the amount of Al(III) and P(V) in solution. Thus, concentrated solutions ($[\text{Al(III)}] = 1.96\text{ mol/L}$ and $[\text{P(V)}] = 5.35\text{ mol/L}$) were found to produce metavariscite, while dilute solutions ($[\text{Al(III)}] = 0.0032\text{ mol/L}$ and $[\text{P(V)}] = 0.0089\text{ mol/L}$) were found to produce variscite. However, for solutions of intermediate concentration d'Yvoire observed the formation of metastable $\text{AlPO}_4\text{-H}_i$ hydrates that upon prolonged equilibration converted to variscite or a mixture of variscite and metavariscite. d'Yvoire, though, was not able to isolate $\text{AlPO}_4\text{-H}_1$, H_2 , H_3 , or H_4 as single pure phases.

Duncan et al. [105] reinvestigated the synthesis of these metastable hydrated aluminium phosphates, H_1 through H_4 , by working at hydrothermal conditions. Thus, they were able to produce highly crystalline $\text{AlPO}_4\text{-H}_1$ and $\text{AlPO}_4\text{-H}_4$ by reacting gels of different molar amounts of Al_2O_3 , P_2O_5 and HCl ($\text{Al}_2\text{O}_3:n\text{P}_2\text{O}_5:m\text{HCl}:50\text{H}_2\text{O}$ $n=0.6,0.8,1.0,1.2$ and $m=0,0.5,1.0,1.5,2.0$) at $140\text{ }^\circ\text{C}$. It was reported that $\text{AlPO}_4\text{-H}_1$ crystallised as a pure phase within four hours followed by its transformation to $\text{AlPO}_4\text{-H}_4$ after extended period of time (18 h). They were not able to isolate pure $\text{AlPO}_4\text{-H}_2$ material but they managed to produce pure $\text{AlPO}_4\text{-H}_3$ phase using an aluminophosphate gel system with the following additions $1.0\text{Al}_2\text{O}_3:1.2\text{P}_2\text{O}_5:1.0\text{HCl}:50.0\text{H}_2\text{O}$ at $140\text{ }^\circ\text{C}$ after 4 h.

García-Carmona et al. [111] reported the synthesis of aluminium phosphate hydrates following the aluminophosphate gel route again but using a quaternary ammonium template. This template appears to control the structure of the synthesised material [113]. Their synthesis method involved reacting gels at controlled pH of composition n -dipropylamine: P_2O_5 : Al_2O_3 : $40H_2O$ at the solution boiling point and atmospheric pressure. The reaction products varied with pH: (1) at pH 3.5-3.8 variscite was the predominant phase, (2) in the pH intervals 3.8-5.2 and 5.4-5.7 $AlPO_4-H_3$ was the major phase, and (3) at pH 5.2-5.4 $AlPO_4-H_1$ and H_2 were obtained.

More recently Kunii et al. [114] reported the synthesis of $AlPO_4-H_1$ - H_2 -and H_3 via this time of microwave heating of aluminophosphate gels made up of different kinds of aluminium sources, namely amorphous aluminium hydroxide, gibbsite, and boehmite. More specifically, the authors were able to produce pure $AlPO_4-H_1$, $-H_2$, and $-H_3$, by crystallising gels at 125, 118, and 90 °C containing aluminium hydroxide, gibbsite, and boehmite respectively.

The second synthesis route involving homogeneous precipitation of amorphous aluminium phosphates followed by their conversion to crystalline phases via ageing has been limited to the preparation of variscite. Thus, Cole and Jackson [115] reported that upon addition of 0.1 M sodium hydroxide to slightly acid solutions of aluminium chloride containing a 2:1 excess of phosphate (as KH_2PO_4 or NaH_2PO_4) an amorphous aluminium phosphate precipitated, which after ageing at 90 °C from 8 h to 2 days yielded variscite, $AlPO_4 \cdot 2H_2O$, contaminated with small amounts of sterrettite, $Al_6(PO_4)_4(OH)_6 \cdot 5H_2O$.

Similarly, Bache [116] reported the synthesis of variscite by mixing dilute solutions of $AlCl_3$ and NaH_2PO_4 in the molar ratio Al(III) to P(V) equal to 0.4 with the precipitation pH adjusted to 4.0 and ageing at 90°C for 14 days. Finally, Matijević and co-workers [117,118] reported the production of colloidal crystalline variscite of several morphologies by ageing at elevated temperatures of 80 to 98°C acidified solutions

containing $\text{Al}(\text{NO})_3$, and K_2HPO_4 at $\text{pH} < 2.2$ for a t least 3 days.

All the methods described above require either temperature over the boiling point of water or long ageing times in chloride or nitrate media. Moreover, in many instances the yield of these reactions was low as dilute solutions were used or simply no pure hydrates were obtained. Finally, no synthesis method starting from sulphate solutions has been reported.

2.4.2 Calcium phosphates

Crystallisation of calcium phosphate minerals has attracted the interest of researchers in different fields due to its significance: (a) in municipal wastewater treatment processes [119,120], (b) in the field of water system scale control [121,122], (c) in the development and manufacture of biomaterials [123,124], and finally (d) in the study of biological processes as bone and tooth mineralisation [125,126].

Calcium phosphate phases: In the ternary system $\text{Ca-PO}_4\text{-H}_2\text{O}$, there are ten well-known crystalline calcium phosphates, with calcium to phosphate molar ratios ranging from 0.5 to 2 [127]. Monocalcium phosphate monohydrate (MCPM, $\text{Ca}(\text{H}_2\text{PO}_4)_2 \cdot \text{H}_2\text{O}$), monocalcium phosphate anhydrous (MCPA, $\text{Ca}(\text{H}_2\text{PO}_4)_2$), dicalcium phosphate dihydrate (DCPD, $\text{CaHPO}_4 \cdot 2\text{H}_2\text{O}$), dicalcium phosphate anhydrous (DCPA, CaHPO_4), octacalcium phosphate (OCP, $\text{Ca}_8(\text{HPO}_4)_2(\text{PO}_4)_4 \cdot 5\text{H}_2\text{O}$), β -tricalcium phosphate (β -TCP, $\beta\text{-Ca}_3(\text{PO}_4)_2$), two forms of α -tricalcium phosphate (α -TCP, $\alpha\text{-Ca}_3(\text{PO}_4)_2$), hydroxyapatite (HAP, $\text{Ca}_{10}(\text{PO}_4)_3(\text{OH})_2$), and tetracalcium phosphate (TTCP, $\text{Ca}_4(\text{PO}_4)_2\text{O}$). Besides, those well-crystalline calcium phosphate phases, another two poorly crystalline calcium phosphate phases have been reported in literature, namely amorphous calcium phosphate (ACP, $\sim \text{Ca}_9(\text{PO}_4)_6 \cdot n\text{H}_2\text{O}$; $n=9\sim 14$; 15-20% H_2O), and calcium-deficient hydroxyapatite (CDHAP, $\text{Ca}_{10-x}(\text{HPO}_4)_x(\text{PO}_4)_{6-x}(\text{OH})_{2-x}$, $x < 2$).

The phases reported above can be classified, for practical purposes, in two different categories: (1) calcium phosphates obtained by reactive crystallisation in aqueous

solution at temperatures below the boiling point of water (low-temperature calcium phosphates), and (2) calcium phosphates obtained by a thermal reaction (high temperature calcium phosphates) [128].

Based on the former classification, high temperature calcium phosphates are monocalcium phosphate, α and β tricalcium phosphate (exactly the same chemical composition but with a different crystallographic structure), hydroxyapatite, oxyapatite, and tetracalcium phosphate. All the traditional calcium phosphates used in medicine are high-temperature calcium phosphates, principally β -tricalcium phosphate, hydroxyapatite, and β -TCP+HAP composites called bicalcium phosphates (BCP) [128].

Among the low-temperature calcium phosphates are monocalcium phosphate monohydrate, amorphous calcium phosphate, dicalcium phosphate dihydrate, octacalcium phosphate, and calcium-deficient hydroxyapatite. The discovery of calcium phosphate cements (mixture of Ca-PO_4 powders and water that hardens with time at room temperature [128]) has led to a much wider use of low-temperature calcium phosphates in the field of biomaterials and, in particular, as bone and tooth substitutes [129]. A brief description of the synthesis of low-temperature calcium phosphates is given below.

Calcium phosphate synthesis: The formation of calcium phosphates is contingent upon pH, temperature, and supersaturation [130]. The solubility isotherms for some calcium phosphate phases shown in Figure 2.13 were calculated with the aid of PHREEEQC [131]. Solubility products, dissociation constants, and ion pair formation constants used to calculate these solubility isotherms are those reported by Brown and co-workers [132,133,134,135]. It can be seen from Figure 2.13 that above pH 4.0 hydroxyapatite is the most stable phase followed by (in terms of solubility) β -tricalcium phosphate, octacalcium phosphate and dicalcium phosphate dihydrate. Therefore, all of the calcium phosphates listed above might be converted into hydroxyapatite at a pH higher than 4.0 [130].

Monocalcium phosphate monohydrate, (MCPM, $\text{Ca}(\text{H}_2\text{PO}_4)_2 \cdot \text{H}_2\text{O}$) is the most acidic and highest in solubility of all calcium phosphates. It has been found to precipitate from highly acidic solutions that are normally found in the industrial production of phosphorus-bearing fertiliser (triple super-phosphate) [136].

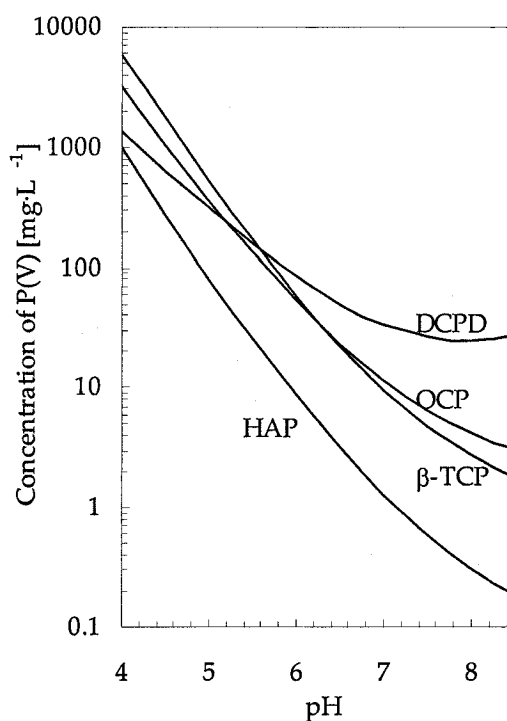


Figure 2.13. Solubility isotherms of calcium phosphate phases in the ternary system Ca^{2+} - PO_4^{3-} - H_2O at 25 °C. Calculated with the aid of PHREEQC for solutions in which Ca to P molar ratio is given by the stoichiometry of each phase. One phase each time was considered and no carbonates were present.

Dicalcium phosphate dihydrate (DCPD or brushite) with the formula $\text{CaHPO}_4 \cdot 2\text{H}_2\text{O}$ and dicalcium phosphate anhydrous (DCPA) with the formula CaHPO_4 are stable phases at a pH lower than 4.0 at 25°C [137]. Dicalcium phosphate dihydrate can be easily crystallised from aqueous chloride solutions at 25 °C under a great variety of conditions, such as concentration of calcium and phosphate ranging from 0.005 mol/L to 0.5 mol/L and pH from 3.0 to 6.0 via homogeneous nucleation conditions [138,139]. High temperature above 80°C, and $\text{pH} < 4.0$, favour the precipitation of dicalcium phosphate anhydrous [140].

Octacalcium phosphate ($\text{Ca}_8(\text{HPO}_4)_2(\text{PO}_4)_4 \cdot 5\text{H}_2\text{O}$) is reported as an intermediate phase during the precipitation of hydroxyapatite from aqueous solutions. According to Fernández et al. [141] octacalcium phosphate can be precipitated by homogeneous nucleation at temperatures as low as 40 °C when the pH is kept between 5.5 and 7.5. On the other hand, at higher temperature a lower pH range is required for the formation of octacalcium phosphate, for example, at 70 °C the optimal precipitation range is $4.5 < \text{pH} < 5.5$.

Amorphous calcium phosphate (ACP) is frequently found during homogeneous precipitation of calcium phosphate salts. This phase is characterised by the absence of peaks in the powder X-ray diffraction pattern. It consists of spherical $\text{Ca}_9(\text{PO}_4)_6$ clusters close-packed to form the larger spherical particles with water being held in the interstices [142]. Meyer and Eanes [143,144] reported that at pH 7.6 and 25 °C this material has a lifetime of less than 60 min after which octacalcium phosphate and then calcium-deficient hydroxyapatite crystallised. These transformations are considered solution-mediated rather than hydrolysis, hence, one phase disappearing with the development of the next.

Calcium-deficient hydroxyapatite chemistry is very complex. This material can have a Ca:P molar ratio from 1.50 to 1.67 [145]. Calcium-deficient hydroxyapatite has been reported during seeded growth experiments with the precipitation pH determining the final Ca:P molar ratio. More specifically, the calcium to phosphate molar ratio has ranged from 1.49 to 1.65 as the pH changed from 6.0 to 9.0 [146].

Calcium-deficient hydroxyapatite with Ca:P=1.50 ($\text{Ca}_9\text{HPO}_4(\text{PO}_4)_5\text{OH}$) has been referred to erroneously as β -tricalcium phosphate which has almost the same chemical composition, but a different crystalline structure. The name apatitic tricalcium phosphate has been also reported [147].

In general, the aqueous precipitation of calcium phosphate salts at $\text{pH} > 6.0$ end up in the formation of calcium-deficient-hydroxyapatite. However, the degree of Ca-deficiency

has been found to relate with supersaturation, temperature, and precipitation pH [148,149].

Thus, stoichiometric hydroxyapatite is expected if the precipitation is carried out at either low supersaturation [150], to prevent the formation of less stable calcium phosphates, or at high pH and high temperature to accelerate the transformation of such calcium phosphate phases to hydroxyapatite [151].

2.5 Review of coating technologies in aqueous media

As was mentioned earlier, this work seeks to encapsulate scorodite with phosphate mineral coatings. Evangelou and co-workers [152,153,154] have developed a similar concept for the purpose of preventing pyrite-pyrrhotite oxidation and acid production in pyritic waste. Their first encapsulation methodology involved coating pyrite with an iron phosphate coating. This was done by reacting pyrite with a solution composed of low but critical concentrations of H_2O_2 , KH_2PO_4 , and a pH buffer [152]. A second encapsulation methodology involved the formation of an iron oxide coating. H_2O_2 was used to oxidise pyrite and produce an iron oxide coating on its surface. This oxide coating was not as effective as the phosphate coating [153]. A third coating methodology is that of an iron-oxide-silica coating [154]. This was done by leaching pyritic waste with a solution composed of H_2O_2 and silica at pH 5 adjusted with sodium acetate (NaOAc). Compared to iron phosphate or oxide coatings, the silica coating was found to be more resistant to the acid environment.

Another coating procedure has been developed by Paraskeva et al. [155] in order to prevent sand reentrainment during oil production from unconsolidated or poorly consolidated reservoir formations. Consolidation was conducted through in situ precipitation of calcium phosphate on the grain surfaces, forming uniform coatings. The grains were gradually *cemented* with bridges of calcium phosphate crystallites and to form a consolidated and porous structure.

In the field of wastewater treatment, the removal and recovery of phosphorus (and ammonia) by heterogeneous precipitation of struvite ($\text{NH}_4\text{MgPO}_4 \cdot 6\text{H}_2\text{O}$) or hydroxyapatite ($\text{Ca}_5(\text{PO}_4)_3\text{OH}$) has been reported [156,157,158]. This technology after successfully piloting is used commercially in Europe and elsewhere [159]. Several crystal seed materials such as phosphate rocks [159], bone charcoal [159], calcium silicate hydrate [159], sands [160] and calcite [161] have been reported. Similarly, the deposition of CaCO_3 on sand pellets has been done in the Netherlands for water softening [162].

Hydroxyapatite $\text{Ca}_5(\text{PO}_4)_3(\text{OH})$, which is the major constituent of bone and teeth, is an important biomaterial [163,164,165]. Especially, the formation of a hydroxyapatite coating on other substances has received much attention in the application as biocompatible materials. Investigations on heterogeneous precipitation of calcium phosphates from aqueous "synthetic body fluid" (SBF) solutions, containing urea (H_2NCONH_2) have been investigated onto the surface of another calcium phosphate [166,167], onto chitosan [168], TiO_2 surfaces [169], silicate glasses [170,171,172], silica [173], cellulose [174], and onto protein films [175].

References

- 1 Bissen, M.; Frimmel, F.H. Arsenic - a review. Part I: Occurrence, toxicity, speciation, mobility. *Acta hydrochimica et hydrobiologica*, **2003**, 31(1), 9-18,
- 2 U.S. Environmental Protection Agency. National primary drinking water regulations; arsenic and clarifications to compliance and new source contaminants monitoring; Final rule. *U.S. Federal Register*, **2001**, 66(14), pp. 6975-7066. http://www.epa.gov/safewater/ars/arsenic_finalrule.pdf
- 3 Escobar-Gonzalez, V.L.; Monhemius, A.J. The mineralogy of arsenates relating to arsenic impurity control. In *Arsenic Metallurgy: Fundamentals and Applications*; Reddy, R.G.; Hendrix, J.L.; Queaneu, P.B., Eds.; The Minerals, Metals & Materials Society: Warrendale, PA, **1988**, pp. 405-453.
- 4 Greenwood, N.N.; Earnshaw, A. *Chemistry of the Elements*, 2nd ed.; Butterworth-

- Heinemann: Oxford, UK, 1997; Chapter 13, pp. 547-553.
- 5 Riveros, P.A.; Dutrizac, J.E.; Spencer, P. Arsenic disposal practices in the metallurgical industry. *Canadian Metallurgical Quarterly*, 2001, 40(4), 395-420.
 - 6 Piret, N.L.; Melin, A.E. An engineering approach to the arsenic problem in the extraction of non-ferrous metals. In *Productivity and Technology in the Metallurgical Industries*; Koch M.; Taylor, J.C., Eds.; The Minerals, Metals & Materials Society: Warrendale, PA, 1989, pp. 735-814.
 - 7 Spencer P.A.; Budden J.R.; Rhodes M.K. Bacterial oxidation technology - A viable process for refractory gold ores and base metals recovery. *Minerals Engineering*, 1991, 4(7-11), 1143-1152.
 - 8 A. Valenzuela, K. Fytas and M. Sánchez, Arsenic management in pyrometallurgical processes. Part I: Distribution in smelting-converting. In *Fifth International Conference on Clean Technologies for the Mining Industry*; Sánchez, M.A.; Vergara, F.; Castro, S.H., Eds.; Universidad de Concepción: Concepción, Chile, 2000, pp. 95-105.
 - 9 Twidwell L.G.; Mehta, A.K. Disposal of arsenic bearing copper smelter flue dust. *Nuclear and chemical waste management*, 1985, 5(4), 297-303.
 - 10 Piret, N.L. The removal and safe disposal of arsenic in copper processing. *JOM-Journal of Metals*, 1999, 51(9), 16-17.
 - 11 Dalewski, F. Removing arsenic from copper smelter gases. *JOM-Journal of Metals*, 1999, 51(9), 24-26.
 - 12 Harris, G.B.; Krause, E. The disposal of arsenic from metallurgical processes: its status regarding ferric arsenate. In *Extractive Metallurgy of Copper, Nickel and Cobalt*; Reddy R.G.; Weizenbach R.N., Eds.; The Minerals, Metals & Materials Society: Warrendale, PA, 1993, Volume I, pp. 1221-1237.
 - 13 Harris, G.B. The removal and stabilization of arsenic from aqueous process solutions: Past, present and future. In *Minor Elements 2000: Processing and Environmental Aspects of As, Sb, Se, Te and Bi*; Young, C.A., Ed.; Society for Mining Metallurgy and Exploration: Littleton, CO, 2000, pp. 3-20.

- 14 Tomita, M.; Higashi, M.; Oto, S.; Okamoto, H. Hydrometallurgical process of copper converter dust at the Saganoseki Smelter & Refinery. In *Residues and Effluents Processing and Environmental Considerations*; Reddy, R.G.; Imrie W.P.; Queneau, P.B., Eds.; The Minerals, Metals & Materials Society: Warrendale, PA, 1991, pp. 283-293.
- 15 Castro S.H.; Muñoz, P. Removal of Arsenic(III) in solution by co-precipitation of calcium arsenite and calcium hydroxide. In *Fifth International Conference on Clean Technologies for the Mining Industry*; Sánchez, M.A.; Vergara, F.; Castro, S.H., Eds.; Universidad de Concepción: Concepción, Chile, 2000, pp. 121-129.
- 16 Nishimura, T.; Itoh, C.T.; Tozawa, K.; Robins, R.G. Stabilities and solubilities of metal arsenites and arsenates in water and effect of sulphate and carbonate ions on their solubilities. In *Arsenic Metallurgy: Fundamentals and Applications*; Reddy, R.G.; Hendrix, J.L.; Queaneu, P.B., Eds.; The Minerals, Metals & Materials Society: Warrendale, PA, 1988, pp. 77-98.
- 17 Cullen, W.R.; Reimer, K.J.; Koch, I.; Ollson, C.A. Arsenic in Yellowknife, Canada. In *Arsenic Metallurgy*; Reddy, R.G.; Ramachandran, V.; Eds.; The Minerals, Metals & Materials Society Warrendale, PA, 2005, pp. 149-167.
- 18 Hoffmann, J.E. The purification of copper refinery electrolyte. *JOM-Journal of Metals*, 2004, 56(6), 30-33.
- 19 Monhemius, A.J.; Swash, P.M. Removing and stabilizing As from copper refining circuits by hydrothermal processing. *JOM-Journal of Metals*, 1999, 51(9), 30-33.
- 20 Wang, S. Impurity control and removal in copper tankhouse operations, *JOM-Journal of Metals*, 2004; 56(7), 34-37.
- 21 Harris, G.B. The removal of arsenic from process solutions: Theory and industrial practice. In *Hydrometallurgy 2003*; Young, C.A.; Alfantazi, A.M.; Anderson, C.G.; Dreisinger, D.B.; Harris, B.; James, A., Eds.; The Minerals, Metals & Materials Society: Warrendale, PA, 2003, Volume 2, Electrometallurgy and Environmental Hydrometallurgy, pp. 1889-1902.
- 22 Rosengrant, L.; Fargo, L. *Final Best Demonstrated Available Technology (BDAT)*

- Background Document for K031, K084, K101, K102, Characteristic As Waste (D004); Characteristic Se Wastes (D010), and P and U Wastes Containing As and Se Listing Constituents; Report EPA/530-SW-90/059A; United States EPA: Washington, DC, 1990.*
- 23 Twidwell, L.G.; Robins, R.G.; Hohn, J.W. The removal of arsenic from aqueous solution by coprecipitation with iron(III). In *Arsenic Metallurgy*; Reddy, R.G.; Ramachandran, V.; Eds.; The Minerals, Metals & Materials Society Warrendale, PA, 2005, pp. 3-24.
- 24 Jia, Y.F.; Demopoulos, G.P.; Chen, N.; Cutler, J.N. and Jiang, D.T. Preparation, characterization and solubilities of adsorbed and co-precipitated Iron(III)-Arsenate solids. In *Hydrometallurgy 2003*; Young, C.A.; Alfantazi, A.M.; Anderson, C.G.; Dreisinger, D.B.; Harris, G.B.; James, A., Eds.; The Minerals, Metals & Materials Society: Warrendale, PA, 2003, Volume 2: Electrometallurgy and Environmental Hydrometallurgy, pp. 1923-1935.
- 25 Geldart, J.; Williamson, R.; Maltby, P. Aqueous pressure oxidation as a waste treatment process-stabilizing roaster wastes. *Hydrometallurgy*, 1992, 30, 29-44.
- 26 Twidwell, L.G.; McCloskey, J.; Lee, M.G.; Saran, J. Arsenic removal from mine and process waters by lime/phosphate. In *Arsenic Metallurgy*; Reddy, R.G.; Ramachandran, V.; Eds.; The Minerals, Metals & Materials Society Warrendale, PA, 2005, pp. 71-88.
- 27 Comba, P. G.; Dahnke, D. R.; Twidwell, L.G. Arsenic removal from process and wastewaters. In *Arsenic Metallurgy: Fundamentals and Applications*; Reddy, R.G.; Hendrix, J.L.; Queaneu, P.B., Eds.; The Minerals, Metals & Materials Society: Warrendale, PA, 1988, pp. 305-319.
- 28 Twidwell, L.G.; Plessas, K.O.; Comba, P.G.; Dahnke, D.R. Removal of arsenic from wastewaters and stabilization of arsenic bearing waste solids: Summary of experimental studies. *Journal of Hazardous Materials*, 1994, 36(1), 69-80.
- 29 Palfy, P.; Vircikova, E.; Molnar, L. Processing of arsenic waste by precipitation and solidification. *Waste Management*, 1999, 19(1), 55-59.

- 30 Dutré V.; Vandecasteele, C. Solidification/Stabilization of hazardous arsenic containing waste from a copper refining process. *Journal of Hazardous Materials*, 1995, 40(1), 55-68.
- 31 Leist, M.; Casey, R.J.; Caridi, D. The management of arsenic wastes: Problems and Prospects. *Journal of Hazardous Materials*, 2000, 76(1), 125-138.
- 32 White, T.; Toor, I. Stabilizing Toxic Metal Concentrates by Using SMITE. *JOM-Journal of Metals*, 1996, 48(3), 54-58.
- 33 Dutré, V.; Vandecasteele, C. Immobilization Mechanism of Arsenic in Waste Solidified Using Cement and Lime. *Environmental Science and Technology*, 1998, 32(18), 2782-2787.
- 34 Twidwell, L.G. Fixations of arsenic in smelter flue dust by dissolution in smelter slags. *Journal of Hazardous Materials*, 1983, 8(1), 85-90.
- 35 Riveros, G.; Utigard, T.A. Disposal of arsenic in copper discharge slags. *Journal of Hazardous Materials*, 2000, 77(1&3), 241-252.
- 36 Carter, M.; Baker N.; Burford, R. Polymer encapsulation of arsenic-containing waste. *Journal of Applied Polymer Science*, 1995, 58(1), 2039-2046.
- 37 Krause, E.; Ettel, V.A. Solubility and stability of scorodite, $\text{FeAsO}_4 \cdot 2\text{H}_2\text{O}$: New data and further discussion. *American Mineralogist*, 1988, 73, 850-854.
- 38 Swash, P.M.; Monhemius, A.J.; Schaekers, J.M. Solubilities of process residues from biological oxidation pretreatments of refractory gold ore. In *Minor Elements 2000: Processing and Environmental Aspects of As, Sb, Se, Te and Bi*; Young, C.A., Ed.; Society for Mining Metallurgy and Exploration: Littleton, CO, 2000, pp. 115-123.
- 39 Bluteau, M-C.; Demopoulos, G.P. Fixation of arsenic in the form of scorodite. A solubility study. In *Waste Processing and Recycling in Mineral and Metallurgical Industries V*; Rao, S.R.; Harrison, F.W.; Kozinski, J.A.; Amaratunga, L.M.; Cheng, T.C.; Richards, G.G.; Pickles, C.A., Eds.; Canadian Institute of Mining, Metallurgy and Petroleum(CIM): Montreal, QC, 2004, pp. 439-452.
- 40 Swash, P.M.; Monhemius, A.J. The scorodite process: A technology for the

- disposal of Arsenic in the 21st century. In *Effluent Treatment in the Mining Industry*; Sánchez, M.A.; Vergara, F.; Castro, S.H., Eds., Universidad de Concepción: Concepción, Chile, 1998, pp. 119-161.
- 41 Demopoulos, G.P.; Lagno, F.; Wang Q.; Singhania, S. The atmospheric scorodite process. In *Copper 2003-Cobre 2003, Hydrometallurgy of Copper*; Riveros, P.A.; Dixon, D.; Dreisinger D.B.; Menacho J., Eds.; The Canadian Institute of Mining, Metallurgy and Petroleum (CIM): Montreal, QC, 2003, Book 2, pp. 597-616.
- 42 Demopoulos, G.P. On the preparation and stability of scorodite. In *Arsenic Metallurgy*; Reddy, R.G.; Ramachandran, V.; Eds.; The Minerals, Metals & Materials Society Warrendale, PA, 2005, pp. 25-50.
- 43 Dutrizac J.E.; Jambor, J.L. The synthesis of crystalline scorodite: FeAsO₄·2H₂O. *Hydrometallurgy*, 1988, 19, 377-384.
- 44 Swash P.M.; Monhemius, A.J. Hydrothermal precipitation from aqueous solutions containing Iron(III), arsenate and sulphate. In *Hydrometallurgy '94*; Chapman and Hall: London, UK, 1994, pp. 177-190.
- 45 Ugarte, F.J.G.; Monhemius, A.J. Characterization of high temperature arsenic-containing residues from hydrometallurgical processes. *Hydrometallurgy*, 1992, 30, 69-86.
- 46 Papangelakis V.G.; Demopoulos, G.P. Acid pressure oxidation of arsenopyrite: Part I, Reaction chemistry. *Canadian Metallurgical Quarterly*, 1990, 29, 1-11.
- 47 Van Weert, G.; Droppert, D.J. Aqueous processing of arsenic trioxide to crystalline scorodite, *JOM-Journal of Metals*, 1994, 46(6), 36-38.
- 48 Droppert, D.J.; Demopoulos, G.P.; Harris, G.B. Ambient pressure production of crystalline scorodite from arsenic-rich metallurgical effluent solutions. In *EPD Congress 1996*; Warren, G.W., Ed.; The Minerals, Metals & Materials Society: Warrendale, PA, 1996, pp. 227-239.
- 49 Filippou, D.; Demopoulos, G.P. Arsenic immobilization by controlled scorodite precipitation. *JOM- Journal of Metals*, 1997, 49(12), 52-55.
- 50 Wang, Q.; Demopoulos, G.P.; Harris, G.B. Arsenic fixation in metallurgical plant

- effluents in the form of crystalline scorodite via a non-autoclave oxidation-precipitation process. In *Minor Elements 2000: Processing and Environmental Aspects of As, Sb, Se, Te and Bi*; Young, C.A., Ed.; Society for Mining Metallurgy and Exploration: Littleton, CO, 2000, pp 225-237.
- 51 Singhania, S.; Wang, Q.; Filippou, D.; Demopoulos, G.P. Temperature and seeding effects on the precipitation of scorodite from sulfate solutions under atmospheric-pressure conditions. *Metallurgical and Materials Transactions B*, 2005, 36B, 327-333.
- 52 Singhania, S.; Wang, Q.; Filippou, D.; Demopoulos, G.P. Acidity, valency and third-ion effects on the precipitation of scorodite from mixed sulfate solutions under atmospheric-pressure conditions. *Metallurgical and Materials Transactions B*, 2005, (in press)
- 53 Demopoulos, G.P., Droppert, D.J.; Van Weert. G. Precipitation of crystalline scorodite ($\text{FeAsO}_4 \cdot 2\text{H}_2\text{O}$) from chloride solutions. *Hydrometallurgy*, 1995, 38, 245-261.
- 54 Brečević, L.; Kralj, D. Kinetics and mechanisms of crystal growth in aqueous systems. In *Interfacial Dynamics, Surfactant Science Series (88)*; Kallay, N., Ed.; Marcel Dekker: New York, NJ, 2000, pp. 435-474.
- 55 Demopoulos, G.P. Aqueous precipitation and crystallisation for the production of particulate solids with desired properties. *Hydrometallurgy*, 2005 (in press).
- 56 Schawtz, A.M; Myerson, A.S. Solutions and solutions properties. In *Handbook of Industrial Crystallization*; Myerson, A.S.; Joseph, J.; Jacobs V.J., Eds.; Butterworth-Heinemann: Oxford, UK, 2002, pp. 1-32.
- 57 Karpinski, P.H.; Wey, J.S. Precipitation processes. In *Handbook of Industrial Crystallization*; Myerson, A.S.; Joseph, J.; Jacobs V.J., Eds.; Butterworth-Heinemann: Oxford, UK, 2002, pp. 141-159.
- 58 Mullin, J.W. *Crystallization*; 3rd ed., Butterworth-Heinemann: Oxford, UK, 1993.
- 59 Koutsoukos, P.G. Growth of calcium phosphates on different substrates: Epitaxial considerations. In *Calcium Phosphates in Biological and Industrial Systems*;

- Amjad, Z; Ed., Kluwer Academic: Boston, MA, 1998, pp. 41-66.
- 60 Koutsoukos, P.G. Current knowledge of calcium phosphate chemistry and in particular solid surface-water interface interactions. In *Second International Conference on the Recovery of Phosphorus from Sewage and Animal Wastes*; Holland, NL, 2001. <http://www.nhm.ac.uk/research-curation/departments/mineralogy/research-groups/phosphate-recovery/Nordwijkerhout/Koutsoukos.pdf>
- 61 Tai, C.Y.; Chien, W-C. Chen, P-C. Particle nucleation and growth. In *Encyclopedia of Surface and Colloid Science*; Somasundaran, P., Ed.; Marcel Dekker: New York, NJ, 2002, pp. 3903-3918.
- 62 Brečević, L. Crystal growth, kinetics and mechanisms. In *Encyclopedia of Surface and Colloid Science*; Somasundaran, P., Ed.; Marcel Dekker: New York, NJ, 2002, pp. 1289-1299.
- 63 Garside, J. Industrial crystallization from solution. *Chemical Engineering Science*, 1985, 40, 3-26.
- 64 Kashchiev, D. *Nucleation: Basic Theory with Application*; Butterworth-Heinemann: Oxford, UK, 2000.
- 65 Kashchiev, D.; Van Rosmalen, G.M. Review: Nucleation in solutions revisited. *Crystal Research and Technology*, 2003, 38(7-8), 555-574.
- 66 Dirksen, J.A.; Ring, T.A. Fundamentals of crystallization: Kinetic effects on particle size distributions and morphology. *Chemical Engineering Science*, 1991, 46(10), 2389-2427.
- 67 Nielsen, A.E. *Kinetics of Precipitation*; Pergamon Press: New York, NJ, 1964.
- 68 Söhnel, O.; Garside, J. *Precipitation: Basic principles and industrial applications*; Butterworth-Heinemann: Oxford, UK, 1992.
- 69 Mersmann, A.; Braun, B.; Löffelmann, M. Prediction of crystallization coefficients of the population balance. *Chemical Engineering Science*, 2002, 57, 4267-4275.
- 70 Strickland-Constable, R.F. *Kinetics and Mechanism of Crystallization*; Academic Press: London, UK, 1968.
- 71 Mersmann, A. Supersaturation and nucleation. *Chemical Engineering Research and*

- Design*, 1996, 74(A), 812-820.
- 72 Mersmann, A.; Löffelmann, M. Crystallization and precipitation: The optimal supersaturation. *Chemical Engineering and Technology*, 2000, 23(1), 11-15.
- 73 Denk E.G.; Botsaris, G.D. Mechanism of contact nucleation. *Journal of Crystal Growth*, 1972, 15(1), 57-60.
- 74 Söhnel, O.; Mullin, J.W. A method for the determination of precipitation induction periods. *Journal of Crystal Growth*, 1978, 44(4), 377-382.
- 75 Söhnel, O.; Mullin, J.W. Precipitation of calcium carbonate. *Journal of Crystal Growth*, 1982, 60(2), 239-250.
- 76 Gómez-Morales, J.; Torrent-Burgués, J.; Rodríguez-Clemente, R. Nucleation of calcium carbonate at different initial pH conditions. *Journal of Crystal Growth*, 1996, 169, 331-338.
- 77 Joshi, M.S.; Antony, A.V. Nucleation in supersaturated potassium dihydrogen orthophosphate solutions. *Journal of Crystal Growth*, 1979, 46(1), 7-9.
- 78 Mullin, J.W.; Szaček, S. The precipitation of potassium aluminium sulphate from aqueous solution. *Journal of Crystal Growth*, 1981, 53(3), 515-518.
- 79 Wu, W.; Nancollas, G.H. Determination of interfacial tension from crystallization and dissolution data: A comparison with other methods. *Advances in Colloid and Interfaces Science*, 1999, 79, 229-279.
- 80 Söhnel, O.; Mullin, J.W. Interpretation of crystallization induction periods. *Journal of Colloid and Interface Science*, 1988, 123(1), 43-50.
- 81 Garside, J.; Mullin, J.W.; Das, S.N. Growth and dissolution kinetics of potassium sulphate crystals in an agitated vessel. *Industrial and Engineering Chemistry Fundamentals*, 1974, 13(4), 299-305.
- 82 Nielsen, A.E. Mechanism and rate laws in electrolyte crystal growth from aqueous solutions. In *Geochemical Processes at Mineral Surfaces*; Davis, J.A.; Hayes, K.F., Eds.; ACS Symposium Series 323; American Chemical Society: Washington, DC, 1986, pp. 600-614.
- 83 Collier A.P.; Hounslow, M.J. Growth and aggregation rates for calcite and

- calcium oxalate monohydrate. *AIChE Journal*, **1999**, 45(11), 2298-2305.
- 84 Randolph, A.D.; Larson, M.A. *Theory of Particulate Processes: Analysis and Techniques of Continuous Crystallization*; Academic Press: London, UK, **1988**.
- 85 Chambers, S.A. Epitaxial growth and properties of thin film oxides. *Surface Science Reports*, **2000**, 39(5&6), 105-180.
- 86 Pashley, D.W. Epitaxy growth mechanisms. *Materials Science and Technology*, **1999**, 15(1), 2-8.
- 87 Lorenz, W.J.; Staikov, G. 2D and 3D thin film formation and growth mechanisms in metal electrocrystallization - an atomistic view by in situ STM, *Surface Science*, **1995**, 335, 32-43
- 88 Feenstra, T.P.; De Bruyn, P.L. The Ostwald rule of stages in precipitation from highly supersaturated solutions: a model and its application to the formation of the nonstoichiometric amorphous calcium phosphate precursor phase. *Journal of Colloid and Interface Science*, **1981**, 84(1), 66-72 .
- 89 Blesa, M.A.; Matijević E. Phase transformations of iron oxides, oxohydroxides, and hydrous oxides in aqueous media. *Advances in Colloid and Interfaces Science*, **1989**, 29(3-4), 173-221.
- 90 Van Straten, H.A.; Holtkamp, B.T.W.; de Bruyn, P.L. Precipitation from supersaturated aluminate solutions: I. Nucleation and growth of solid phases at room temperature. *Journal of Colloid and Interface Science*, **1984**, 98(2), 342-362.
- 91 Van Straten, H.A.; De Bruyn, P.L. Precipitation from supersaturated aluminate solutions: II. Role of temperature. *Journal of Colloid and Interface Science*, **1984**, 102(1), 260-277.
- 92 Wu, W.; Nancollas, G.H. The dissolution and growth of sparingly soluble inorganic salts: A kinetics and surface energy approach. *Pure and Applied Chemistry*, **1998**, 70, 1867-1872.
- 93 Marqusee, J.A.; Ross, J. Kinetics of phase transitions: Theory of Ostwald ripening. *Journal of Chemical Physics*, **1983**, 79, 373-378.
- 94 Madras, G.; McCoy, B.J. Transition from nucleation and growth to Ostwald

- ripening, *Chemical Engineering Science*, **2002**, 57, 3809-3818.
- 95 Lindsay, W.L.; Vlek, P.L.G.; Chien, S.H. Phosphate minerals. In *Minerals in soil environment*, 2nd ed.; Dixon, J.B; Weed, S.B.; Eds.; Soil Science Society of America: Madison, WI, **1989**, pp. 1089-1130.
- 96 Nancollas, G.H. The nucleation and growth of phosphate minerals. In *Phosphate Minerals*; Nriagu, J.O.; Moore, P.B.; Eds.; Springer Verlag: Berlin, **1984**, pp 137-154.
- 97 de-Bashana, L.E.; Bashana, Y. Recent advances in removing phosphorus from wastewater and its future use as fertilizer (1997–2003). *Water Research*, **2004**, 38, 4222-4246.
- 98 Pierri, E.; Tsamouras, D.; Dalas, E. Ferric phosphate precipitation in aqueous media. *Journal of Crystal Growth*, **2000**, 213, 93-98.
- 99 Hsu, P.H. Crystallization of variscite at room temperature. *Soil Science*, **1982**, 133, 305-313.
- 100 Ishikawa, T. Metal phosphates and apatites. In *Fine Particles: Synthesis, Characterization and Mechanism of Growth*; Sugimoto, T., Ed.; Marcel Dekker: New York, NJ, **2000**, pp. 350-385.
- 101 Szostak R. Synthesis of Molecular Sieve Phosphates. In *Molecular Sieves: Science and Technology*; Karge, H.G.; Weitkamp, J., Eds.; Springer-Verlag: Berlin, **1998**, Vol. I, pp. 157-158.
- 102 Martens, J.A.; Jacobs, P.A. Phosphate-based zeolites and molecular sieves. In *Catalysis and Zeolites: Fundamentals and Applications*; Weitkamp, J.; Puppe L. Eds.; Springer-Verlag: Berlin, **1999**, pp. 53-80.
- 103 Kniep, R.; Mootz, D.; Vega, A. Variscite. *Acta Crystallographica B*, **1977**, 33, 263-265.
- 104 Kniep, R. and Mootz, D. Metavariscite: A redetermination of its crystal structure. *Acta Crystallographica B*, **1973**, 29, 2292-2294.
- 105 Duncan, B.; Stocker, M.; Gwinup, D.; Szostak, R.; Vinje, K. Template-Free Synthesis of the Aluminophosphates H₁ through H₄. *Bulletin de la Société Chimique*

- de France*, 1992, 129, 98-110.
- 106 McCusker, L.B.; Baerlocher, Ch.; Jahn, E.; Bülow, M. The triple helix inside the large-pore aluminophosphate molecular sieve VPI-5. *Zeolites*, 1991, 11, 308-313
- 107 Li, H-X; Davis, M.E. Further studies on aluminophosphate molecular sieves. Part 1. $\text{AlPO}_4\text{-H}_2$: A Hydrated Aluminophosphate Molecular Sieve. *Journal of the Chemical Society-Faraday Transactions*, 1993, 89(6), 951-965.
- 108 Pluth, J.J.; Smith, J.V. Hydrated aluminophosphate ($\text{AlPO}_4\cdot 1.5\text{H}_2\text{O}$) with PO_4 , AlO_4 and $\text{AlO}_4(\text{H}_2\text{O})_2$ groups and encapsulated water. *Acta Crystallographica C*, 1986, 42, 1118-1120.
- 109 Poojary, D.M.; Balkus, Jr., K.J.; Riley, S.J.; Gnade, B.E.; Clearfield, A. Synthesis and *ab initio* structure determination of $\text{AlPO}_4\text{-H}_2\text{O-H}_4$ from powder diffraction data. *Microporous Materials*, 1994, 2(4), 245-250.
- 110 Martens, J. A.; Jacobs, P.A. Crystalline microporous phosphates: A family of versatile catalysts and adsorbents. In *Advanced Zeolite Science and Applications: Studies in Surface Science and Catalysis*; Jansen J.C.; Stocker M., Karge H.G., Weitkamp J., Eds.; Elsevier: Amsterdam, 1994, Vol. 85, pp. 653-685.
- 111 García-Carmona, J.; Rodríguez-Clemente, R.; Gómez-Morales, J. Directed crystallization of selected aluminophosphates hydrates by pH control. *Advanced Materials*, 1998, 10(1), 46-49.
- 112 d'Yvoire, F. Étude des Phosphates d'aluminium et de fer trivalent. l'orthophosphate Neutre d'aluminium. *Bulletin de la Société Chimique de France*, 1961, 372, 1762-1776.
- 113 Lok, B.M.; Cannan, T.R.; Messina, C.A. The role of organic molecules in molecular sieve synthesis. *Zeolites*, 1983, 3(4), 282-291.
- 114 Kunii, K., Narahara, K.; Yamanaka S. Template-free synthesis of $\text{AlPO}_4\text{-H}_1$, -H_2 , and -H_3 by microwave heating. *Microporous and Mesoporous Materials*, 2002, 52(3), 159-167.
- 115 Cole, C.V.; Jackson, M. L. Colloidal dihydroxy dihydrogen phosphates of aluminum and iron with crystalline character established by electron and x-ray

- diffraction. *Journal of Physical Chemistry*, 1950, 54(1), 128-142.
- 116 Bache, B.W. Aluminum and iron phosphate studies relating to soils: I. Solution and hydrolysis of variscite and strengite. *Journal of Soil Science*, 1963, 14(1), 113-123.
- 117 Katsanis, E.P.; Matijević, E. Preparation and properties of uniform colloidal aluminium phosphate particles. *Colloid and Surfaces*, 1982, 5(1), 43-53.
- 118 Gómez-Morales, J.; Rodríguez-Clemente, R.; Matijević, E. The mechanism of precipitation of colloidal variscite ($\text{AlPO}_4 \cdot 2\text{H}_2\text{O}$) particles. *Journal of Colloid and Interface Science*, 1992, 151, 555-562.
- 119 Wiechers, H.N.S. Chemical phosphate removal from municipal wastewaters: current practice and recent innovation. *Water SA*, 1986, 12(4), 197-202.
- 120 Woods, N.C.; Sock, S.M.; Daigger, G.T. Phosphorus recovery technology modeling and feasibility evaluation for municipal wastewater treatment plants. *Environmental Technology*, 1999, 20, 663-679.
- 121 Perez, L.A. Mechanism of calcium phosphate scale formation and inhibition in cooling systems. In *Calcium Phosphates in Biological and Industrial Systems*; Amjad, Z; Ed., Kluwer Academic: Boston, MA, 1998, pp. 395-415.
- 122 Perez, L.A.; Kessler, S.M. Novel calcium phosphate scale inhibitor. In *Water Soluble Polymers Solution Properties and Applications*; Amjad, Z; Ed., Kluwer Academic: Boston, MA, 2002, pp. 149-161.
- 123 Burg, K.J.L.; Porter, S.; Kellam, J.F. Biomaterials developments for bone tissue engineering. *Biomaterials*, 2000, 21, 2347-2359.
- 124 Elliott, J.C. Recent studies of apatites and other calcium orthophosphates. In *Calcium Phosphate Materials: Fundamentals*; Bres, E.; Hardouin, P.; Eds.; Sauramps edical: Montpellier, VT, 1998, pp. 25-66.
- 125 Paule, W.J.; Bernick, S.; Strates, B.; Nimni, M.E. Calcification of implanted vascular tissues associated with elastin in an experimental animal-model *Journal of Biomedical Materials Research*, 1992, 26(9), 1169-1177.
- 126 Engelhardt, G.R.; Harless, J.D.; Wefel, J.S.; Stanford, C.M.; Keller, J.C. Dissolution

- characteristics of hydroxyapatite-coated surfaces. *Journal of Dental Research*, 1996, 75: 398.
- 127 Tung, M.S. Calcium phosphates: Structure, composition, solubility, and stability. In *Calcium Phosphates in Biological and Industrial Systems*; Amjad, Z; Ed., Kluwer Academic: Boston, MA, 1998, pp. 1-19.
- 128 Bohner, M. Calcium orthophosphates in medicine: from ceramics to calcium phosphate cements. *Injury*, 2000, 31(Suppl.4), 37-47.
- 129 Chow, L.; Takagi, S.; Sugawara, A.; Eanes, E.D.; Heywood, B. Setting reactions and compressive strengths of calcium-phosphate cements. *Journal of Dental Research*, 1990, 69(12), 1852-1856.
- 130 House, W.A. The physico-chemical conditions for the precipitation of phosphate with calcium. *Environmental Technology*, 1999, 20, 727-733.
- 131 Parkhurst, D. L.; Appelo, C. A. J. *User's Guide to PHREEQC (Version 2)-A Computer Program for Speciation, Batch-Reaction, One-Dimensional Transport, and Inverse Geochemical Calculations*; Water-Resources Investigations Report 99-4259; U.S. Geological Survey: Reston, VA, 1999; <http://wwwbrr.cr.usgs.gov/>.
- 132 Moreno, E.C.; Gregory, T.M.; Brown, W.E. Solubility of $\text{CaHPO}_4 \cdot 2\text{H}_2\text{O}$ and formation of ion pairs in the system $\text{Ca}(\text{OH})_2\text{-H}_3\text{PO}_4\text{-H}_2\text{O}$ at 5, 15, 25, and 37 °C. *Journal of Research of the National Bureau of Standards*, 1970, 74A(4), 461-475.
- 133 Gregory, T.M.; Moreno, E.C.; Patel, J.M.; Brown, W.E. Solubility of $\beta\text{-Ca}_3(\text{PO}_4)_2$ in the system $\text{Ca}(\text{OH})_2\text{-H}_3\text{PO}_4\text{-H}_2\text{O}$ at 5, 15, 25, and 37 °C. *Journal of Research of the National Bureau of Standards*, 1974, 78A(6), 667-674.
- 134 McDowell, H.; Gregory, T.M.; Brown, W.E. Solubility of $\text{Ca}_5(\text{PO}_4)_3\text{OH}$ in the system $\text{Ca}(\text{OH})_2\text{-H}_3\text{PO}_4\text{-H}_2\text{O}$ at 5, 15, 25, and 37 °C. *Journal of Research of the National Bureau of Standards*, 1977, 81A, 273-281.
- 135 Tung, M.S.; Eidelman, N.; Sieck, B.; Brown, W.E. Octacalcium Phosphate Solubility Product from 4 to 37 °C. *Journal of Research of the National Bureau of Standards*, 1988, 95(3), 613-624.
- 136 Dorozhkin, S.V., Epple, M.; Biological and medical significance of calcium

- phosphates, *Angewandte Chemie International Edition*, **2002**, 41(17), 3130-3146.
- 137 Vereecke, G.; Lemaitre, J. Calculation of the solubility diagrams in the system $\text{Ca}(\text{OH})_2\text{-H}_3\text{PO}_4\text{-KOH-HNO}_3\text{-CO}_2\text{-H}_2\text{O}$. *Journal of Crystal Growth*, **1990**, 104(4), 820-832.
- 138 Arifuzzaman, S.M.; Rohani, S. Experimental study of brushite precipitation. *Journal of Crystal Growth*, **2004**, 267(3-4), 624-634.
- 139 Abbonaa, F.; Christensson, F.; Franchini-Angela, M.; Lundager-Madsen, H.E. Crystal habit and growth conditions of brushite, $\text{CaHPO}_4\cdot 2\text{H}_2\text{O}$, *Journal of Crystal Growth*, **1993**, 131, 331-346.
- 140 Freche, M.; Heughebaert, J.C. Calcium phosphate precipitation in the 60-80°C range. *Journal of Crystal Growth*, **1989**, 94, 947-954.
- 141 Fernández, E.; Gil, F.J.; Ginebra, M.P.; Driessens, F.C.M.; Planell, J.A.; Best SM. Calcium phosphate bone cements for clinical applications - Part II: Precipitate formation during setting reactions. *Journal of Materials Science: Materials In Medicine*, **1999**, 10(3), 177-183.
- 142 Posner, A.S.; Betts, F. Synthetic amorphous calcium phosphate and its relation to bone mineral structure. *Accounts of Chemical Research*, **1975**, 8, 273-281.
- 143 Meyer, J.L.; Eanes, E.D. Thermodynamic analysis of amorphous to crystalline calcium phosphate transformation. *Calcified Tissue Research*, **1978**, 25(1), 59-68.
- 144 Meyer, J.L.; Eanes, E.D. Thermodynamic analysis of secondary transition in spontaneous precipitation of calcium phosphate. *Calcified Tissue Research*, **1978**, 25(3), 209-216.
- 145 Brown, P.W.; Martin, R.I. An analysis of hydroxyapatite surface layer formation. *Journal of Physical Chemistry B*, **1999**, 103(10), 1671-1675.
- 146 Nancollas, G.H.; Lore, M.; Perez, L.; Richardson, C.; Zawacki S.J. Mineral phases of calcium phosphate. *The Anatomical Record*, **1989**, 224(2), 234-241.
- 147 Chair, H.; Heughebaert, J.C.; Heughebaert, M. Precipitation of stoichiometric tricalcium phosphate prepared by continuous process. *Journal of Materials Chemistry*, **1995**, 5(6), 895-899.

- 148 Heughebaert, J.C.; Zawacky, S.J.; Nancollas, G.H. The growth of nonstoichiometric apatite from aqueous solution at 37 °C. I. Methodology and Growth at pH 7.4. *Journal of Colloid and Interface Science*, **1990**, 135(1), 20-32.
- 149 Zawacky, S.J.; Heughebaert, J.C.; Nancollas, G.H. The growth of nonstoichiometric apatite from aqueous solution at 37 °C. II. Effects of pH upon the Precipitated Phase. *Journal of Colloid and Interface Science*, **1990**, 135(1), 33-44.
- 150 Nancollas, G.H.; Koutsoukos, P.G. Calcium phosphate nucleation and growth in solution. *Progress in Crystal Growth and Characterization*, **1980**, 3(1), 77-102.
- 151 Rodríguez-Lorenzo, L.M.; Vallet-Regí, M. Controlled crystallization of calcium phosphate apatites. *Chemistry of Materials*, **2000**, 12, 2460-2465.
- 152 Evangelou, V.P. Potential microencapsulation of pyrite by artificial inducement of ferric phosphate coatings. *Journal of Environmental Quality*, **1995**, 24(3), 535-542.
- 153 Zhang, Y.L.; Evangelou, V.P. Influence of iron oxide forming conditions on pyrite oxidation. *Soil Science*, **1996**, 161(12), 852-864.
- 154 Zhang, Y.L.; Evangelou, V.P. Formation of ferric hydroxide-silica coatings on pyrite and its oxidation behavior. *Soil Science*, **1998**, 163(1), 53-62.
- 155 Paraskeva, C.A.; Charalambous, P.; Stokka, L-E. ; Klepetsanis, P.G.; Koutsoukos, P.G.; Read, P.; Payatakes, C. Sandbed consolidation with mineral precipitation. *Journal of Colloid and Interface Science*, **2000**, 232(2), 326-339.
- 156 Momberg, G.A.; Oellermann, R.A. The removal of phosphate by hydroxyapatite and struvite crystallisation in South Africa. *Water Science and Technology*, **1992**, 26, 987-996.
- 157 Williams, S. Struvite precipitation in sludge stream at sludge wastewater treatment plant and opportunities for phosphorus recovery. *Environmental Technology*, **1999**, 20, 743-747.
- 158 Schipper, W.J.; Klapwijk, A.; Potjer, B.; Rulkens, W.H.; Temmink, B.G.; Kiestra, F.D.G.; Lijmbach, A.C.M. Phosphate recycling in the phosphorus industry. *Environmental Technology*, **2001**, 22, 1337-1345.
- 159 Moriyama, K.; Kojima, T.; Minawa, Y.; Matsumoto, S.; Nakamachi, K.

- Development of artificial seed crystal for crystallization of calcium phosphate. *Environmental Technology*, 2001, 22, 1245-1252.
- 160 Giesen, A. Crystallisation process enables environmental friendly phosphate removal at low costs. *Environmental Technology*, 1999, 20, 769-775.
- 161 Donnert, D.; Salecker, M. Elimination of phosphorus from wastewater by crystallization. *Environmental Technology*, 1999, 20, 735-742.
- 162 Sijstermans, L.F.J. Pellet production from concentrated solutions with a pellet reactor. *M.Eng. Thesis*, Delf University of Technology, The Netherlands, 1992.
- 163 Nancollas, G.H. The mechanism of biological mineralization. *Journal of Crystal Growth*, 1977, 42, 185-193.
- 164 Nancollas, G.H.; Koutsoukos, P.G. Calcium phosphate nucleation and growth in solution. *Progress in Crystal Growth and Characterization*, 1980, 3(1), 77-102.
- 165 Tamai, H.; Yasuda, H. Preparation of polymer particles coated with hydroxyapatite. *Journal of Colloid and Interface Science*, 1999, 212, 585-588.
- 166 Heughebaert, J-C.; De Rooij, J.F.; Nancollas, G.H. The growth of dicalcium phosphate dihydrate on octacalcium phosphate at 25°C. *Journal of Crystal Growth*, 1986, 76(1), 192-198.
- 167 Heughebaert, J-C.; Zawacki, S.J.; Nancollas, G.H. The growth of octacalcium phosphate on beta tricalcium phosphate. *Journal of Crystal Growth*, 1983, 63(1), 83-90.
- 168 Varma, H.K.; Yokogawa, Y.; Espinosa, F.F.; Kawamoto, Y.; Nishizawa, K.; Nagata, F.; Kameyama, T. Porous calcium phosphate coating over phosphorylated chitosan film by a biomimetic method. *Biomaterials*, 1999, 20, 879-88.
- 169 Wu, W.; Nancollas, G.H. Kinetics of heterogeneous nucleation of calcium phosphates on anatase and rutile surfaces. *Journal of Colloid and Interface Science*, 1998, 199(2), 206-211.
- 170 Tanahashi, M.; Yao, T.; Kokubo, T.; Minoda, M.; Miyamoto, T.; Nakamura, T.; Yamamuro, T. Apatite coating on organic polymers by a biomimetic process. *Journal of the American Ceramic Society*, 1994, 77(11), 2805-2808.

- 171 Izquierdo-Barba, I.; Salinas, A.J.; Vallet-Regi, M. In vitro calcium phosphate layer formation on sol-gel glasses of the CaO-SiO₂ system. *Journal of Biomedical Materials Research*, **1999**, 47(2), 243-250.
- 172 Takadama, H.; Kim, H.-M.; Kokubo, T.; Nakamura, T. Mechanism of biomineralization of apatite on a sodium silicate glass: TEM-EDX study in vitro. *Chemistry of Materials*, **2001**, 13(3), 1108-1113.
- 173 Ngankam, P.A.; Schaaf, P.; Voegel, J.C.; Cuisinier, F.J.G. Heterogeneous nucleation of calcium phosphate salts at a solid/liquid interface examined by scanning angle reflectometry. *Journal of Crystal Growth*, **1999**, 197(4), 927-938.
- 174 Rhee, S.-H.; Tanaka, J. Hydroxyapatite formation on cellulose cloth induced by citric acid. *Journal of Materials Science: Materials in Medicine*, **2000**, 11(7), 449-452.
- 175 Campbell, A.A.; Nancollas, G.H. The mineralization of calcium phosphate on separated salivary protein films. *Colloids and Surfaces*, **1991**, 54, 33-40.

Chapter 3. Experimental

3.1 Introduction

The experimental work reported in this thesis involved three different types of studies, namely: (1) production of a number of synthetic minerals; (2) evaluation of their solubility; and (3) encapsulation of scorodite with two of these synthetic minerals. The synthesis work involved the production of aluminium and calcium phosphates via homogeneous, heterogeneous and seeded crystallisation. The stability work involved the study of the dissolution of hydrated aluminium phosphate ($\text{AlPO}_4 \cdot 1.5\text{H}_2\text{O}$), dicalcium phosphate dihydrate ($\text{CaHPO}_4 \cdot 2\text{H}_2\text{O}$), and calcium-deficient hydroxyapatite ($\text{Ca}_{10-x}(\text{HPO}_4)_x(\text{PO}_4)_{6-x}(\text{OH})_{2-x}$, $x < 2$). Finally, the encapsulation work involved the deposition of hydrated aluminium phosphate and calcium-deficient hydroxyapatite on scorodite particles and the assessment of their stability.

Although, a separate experimental section with specific information is included in each chapter, some common features as the experimental set-up and analytical characterisation methods are described here. In this chapter also a description of the procedure used to prepare the scorodite material used in the encapsulation studies is included.

3.2 Crystallisation reactor and procedure

The experiments were carried out in a 3 L Applikon® bioreactor adapted for inorganic precipitation research (Figure 3.1). The system was configured to measure and control pH, temperature, and agitation speed.

The pH was controlled by the ADI 1010 BioController. When pH deviates above or below the set point, the controller activates a peristaltic pump, which introduces a base

(NaOH = 1 mol/L or 0.1 mol/L) or acid (H_2SO_4 0.5 mol/L, HCl 0.1 mol/L) to either Al(III)- $\text{PO}_4\text{-SO}_4$ or Ca(II)- $\text{PO}_4\text{-Cl}$ containing solution through a "triple inlet assembly" located in the bioreactor headplate. Two 0.5 L reagent addition bottles were used for these additions. For high temperature reactions, the solution temperature (95 °C) was maintained with a circulating oil bath. All process parameters were controlled using PID (Proportional, Integral, Derivative) functions. BioXpert software was used to log data and to perform supervisory control.

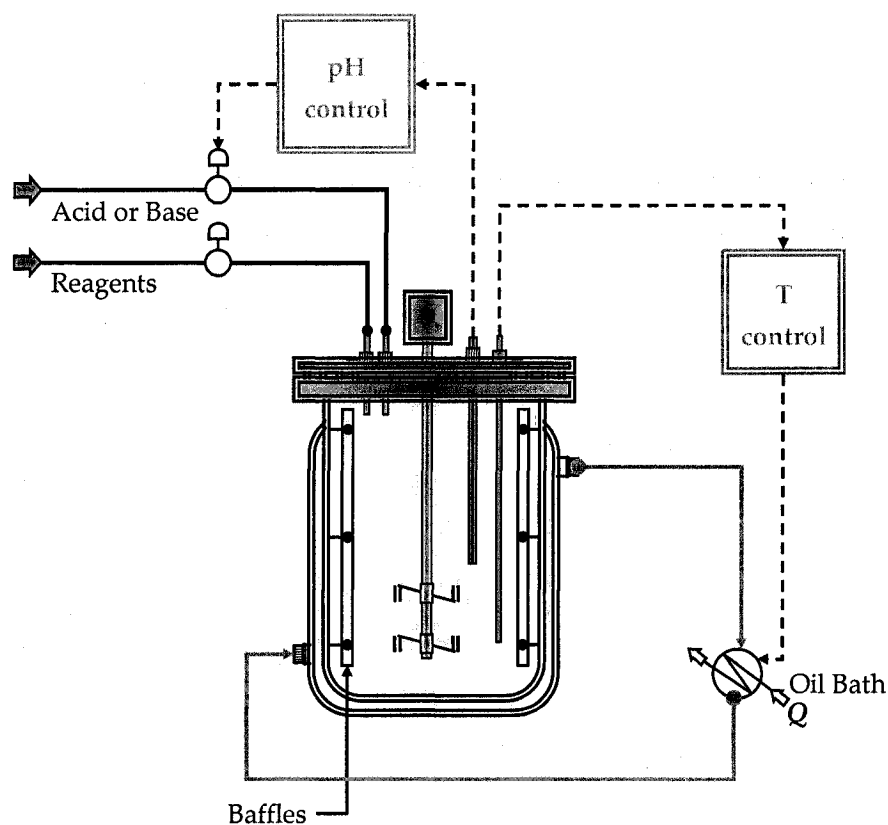


Figure 3.1. Crystallisation reactor set-up.

During the course of the precipitation process, samples of slurry were taken at regular time intervals, were filtered through membrane filters (GE Osmonics Cameo 0.22 μm for precipitation conducted at 95 °C or Corning 0.25 μm for tests carried out at room temperature) and diluted with acidified ($w_{\text{HNO}_3} \sim 5\%$) deionised water. At the end of each test, the entire suspension was filtered.

The final filtrate together with the filtrates of the intermediate samples were analysed by

inductive coupled plasma atomic emission spectrophotometry (ICP-AES) for P, As, Ca, and Al. The final slurry was filtered and the solids washed by repulping 3 times with 1000 mL of deionised acidified hot water (60 °C). All experiments were carried out with deionised water prepared via a dual ion exchange system consisting of a Cole Parmer ion exchanger type 1506-25 "universal" and an ion exchanger type 1506-35 "Research". All experiments were carried out in duplicate runs.

3.3 Chemicals and materials used

The chemicals used are listed below in Table 3.1

Table 3.1. List of Chemical reagents used.

Name	Formula	Supplier	Grade
Aluminium Sulphate Octadecahydrate	$Al_2(SO_4)_3 \cdot 18H_2O$	Fisher	Reagent (A.C.S)
Sodium Phosphate Monobasic Monohydrate	$NaH_2PO_4 \cdot H_2O$	Fisher	Reagent (A.C.S)
Calcium chloride dihydrate	$CaCl_2 \cdot 2H_2O$	Fisher	Reagent (A.C.S)
Ferric Sulphate Pentahydrate	$Fe_2(SO_4)_3 \cdot 5H_2O$	Aldrich	Reagent (A.C.S)
Arsenic Pentoxide Trihydrate	$As_2O_5 \cdot 3H_2O$	Aldrich	Reagent (A.C.S)
Sodium Sulphate	Na_2SO_4	Fisher	Reagent (A.C.S)
Sulphuric Acid	H_2SO_4	Fisher	Reagent (A.C.S)
Nitric Acid	HNO_3	Fisher	Reagent (A.C.S)
Hydrochloric Acid	HCl	Fisher	Reagent (A.C.S)
Phosphoric Acid	H_3PO_4	Fisher	Reagent (A.C.S)
Sodium Hydroxide	$NaOH$	Fisher	Reagent (A.C.S)
Magnesium Oxide	MgO	Fisher	Reagent (A.C.S)
Gypsum	$CaSO_4 \cdot 2H_2O$	Aldrich	Reagent (A.C.S)
Sodium hydrosulphide hydrate	$NaHS \cdot H_2O$	Aldrich	Reagent (A.C.S)

3.4 Chemical analysis and reproducibility

The calcium, aluminium, iron, arsenic, and phosphorus contents in solution were determined by inductive coupled plasma atomic emission spectrophotometry (ICP-AES). Calibration was performed using 0, 5, 10, 50, and 100 mg/L solutions of Ca, Al, Fe, As, and P. All standards were prepared from ICP grade standards of 1000 mg/L.

The analysis of Arsenic(III) and Iron(II) in solution was conducted using standard oxidation-reduction titration methods. The concentration of Fe(II) was determined by titration against potassium dichromate ($K_2Cr_2O_7$) with sodium diphenylamine-4-sulphonate as indicator. Determination of As(III) was made by a method involving separation of As(III) with the aid of a cation exchange resin (Dowex 50W-X8) as reported elsewhere [1]. Titration of the purified solution was conducted with $KBrO_3$ and methyl orange was used as indicator. As(III) was found not to interfere with the titration of Fe(II).

The data presented and plotted in this work were expressed as the average of duplicate runs; then, the uncertainty reported was equal to the positive difference of the two measurements divided by two. Error bars are plotted along with the data and they are not visible when smaller than the symbol size. Chemical analysis of solids was performed by dissolving 0.5 g of material in triplicate and the uncertainty in this case is estimated as the two standard deviations associated with the mean value. For data estimated by calculations such as solubility products, the errors are estimated as two standard deviations as well.

3.5 Characterisation

The solids were characterised via a series of techniques. For X-ray Diffraction (XRD) analysis, a Rigaku Rotaflex D-Max diffractometer equipped with a rotative anode and a copper target ($K\alpha_1$ Copper with $K\alpha = 0.15406$ nm) was used. Chemical analysis of solids was performed by dissolving 0.5 g of material in very strong HCl solution (~5 mol/L),

followed by adjustment of concentration <100 mg/L and then determination by ICP-AES. The final solids were also observed with a JEOL 840A scanning electron microscope (SEM). The samples were gold-coated prior to examination. The size of particles and their mode of distribution were determined using a Horiba LA-920 Laser scattering particle-size distribution analyser. Thermogravimetric analysis (TGA Perkin-Elmer thermogravimetric analyser) was performed to determine the number of crystallisation waters. For infrared spectroscopy analysis, the powder was pressed into pellets of KBr and the spectra recorded with a Bruker Optics IFS66 FT-IR spectrometer in the range 400 to 4000 cm^{-1} .

In addition, secondary electron microscopy analysis and elemental mapping were also obtained using a variable pressure scanning electron microscope (SEM type Hitachi S-3000N). Grains were mounted in epoxy and polished to create grain mounts similar to those used for reflected light microscopy.

Surface composition analysis and depth-profile of the encapsulated scorodite particles were investigated at AMTEL Ltd. Several microbeam techniques were applied, such as SEM-EDX (Scanning Electron Microscope equipped with an energy dispersive X-ray analyser), TOF-SIMS (Time of Flight Secondary Ion Mass Spectrometer), and TOF-LIMS (Time of Flight Laser Ionisation Mass Spectrometer) [2]. For surface analysis TOF-SIMS was operated in "static" SIMS mode, so, only top monolayers of the sample surface were analysed. For depth profiling the operation was in "dynamic" SIMS mode, i.e., a higher energy primary ion beam ablated the sample surface and depth profiles were acquired.

Prior to TOF-LIMS the solids sample was prescreened at 40 μm and 20 μm to obtain coarser particles more desirable for this technique. The process of screening the sample was conducted in deionised water, using fine nylon screens of 40 μm and 20 μm gauge. Screening was facilitated with the use of manual agitation of the pulp, and with a water jet from a wash bottle.

For the analysis of particles via TOF-SIMS and TOF-LIMS scorodite particles were

randomly selected from the +40 μm fraction and mounted on indium foil. Indium is a soft metal with reasonable conductance that prevents charge accumulation during analysis. One row of grains was used for each of TOF-SIMS and TOF-LIMS analysis, SEM-EDX, TOF-LIMS and TOF-SIMS.

3.6 Preparation of scorodite

The scorodite substrate material used in the encapsulation studies was produced via atmospheric precipitation as per the method previously developed at the McGill Hydrometallurgy laboratory [3,4,5]. A brief description of the basic principles on which this method is based was given in Section 2.2.2 of Chapter 2. In this procedure 1.5 L of As(V)–Fe(III)–H₂SO₄ solution was first prepared from analytical-grade arsenic pentoxide (As₂O₅), ferric sulphate pentahydrate (Fe₂(SO₄)₃·5H₂O) and sulphuric acid (H₂SO₄). The solution was then placed in the reactor (Figure 3.1) and heated to 95 °C while stirring. Slaked magnesium oxide ($w_{\text{MgO}} \sim 10\%$) was added slowly to reach the precipitation pH [3] at which seed was introduced into the solution. In the presence of seed, precipitation started and was allowed to continue for 2 h. The solution pH was monitored continuously throughout the experiment, and slurry samples were taken at regular time intervals. The pH was not controlled during precipitation since it has no impact on the arsenic removal efficiency [5].

The sample was subjected to XRD analysis that confirmed it to be scorodite, with good crystallinity (Figure 3.2). This precipitate was also characterised by Scanning Electron Microscopy (SEM); Figure 3.3 shows SEM images at different magnifications. It can be seen that the material consisted of dense agglomerated particles with size in the order of 25 μm . Particle size analysis (Figure 3.4) confirmed the SEM visual examination results.

Chemical composition analysis of the solids also confirmed that the material was scorodite. The mass fraction of As and Fe ($w_{\text{As}} = 32.4\%$ and $w_{\text{Fe}} = 23.6\%$) are in agreement with the theoretical values of As and Fe in scorodite ($w_{\text{As}} = 32.5\%$ and $w_{\text{Fe}} = 24.2\%$). A

minor amount of SO_4^{2-} (mass fraction of 2.6%) was also found to be incorporated in the scorodite reflecting the fact that synthesis took place in a sulphate-based system [5].

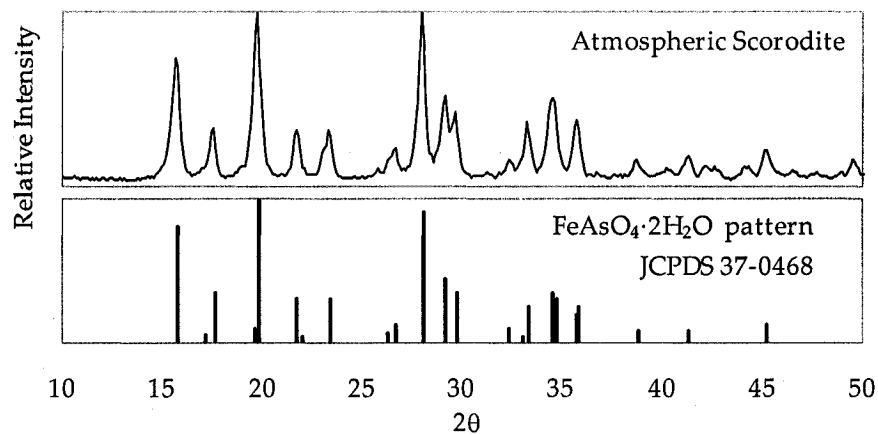


Figure 3.2 XRD pattern of $\text{FeAsO}_4 \cdot 2\text{H}_2\text{O}$ produced by atmospheric precipitation.

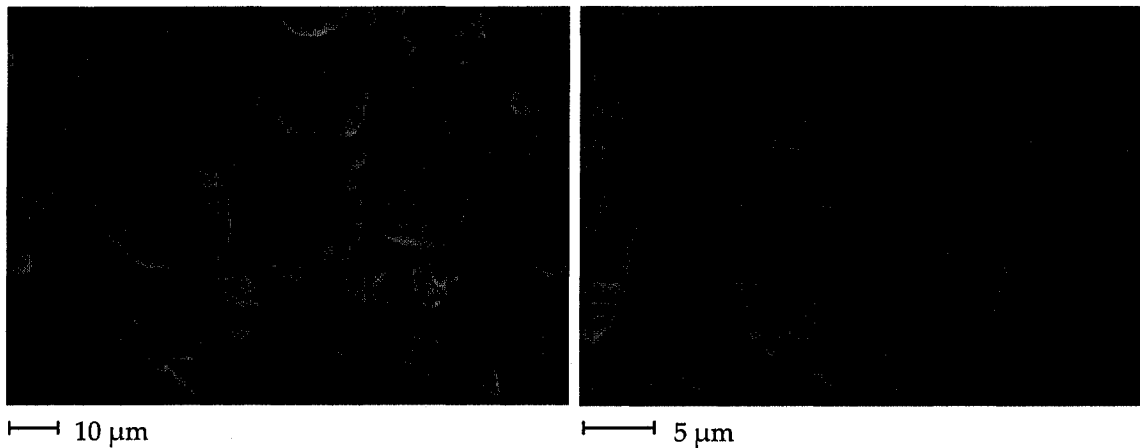


Figure 3.3. Scanning electron micrographs of scorodite substrate material.

A typical back-scattered electron image of the atmospheric scorodite is shown in Figure 3.5. It is revealed that the particles have grown through surface deposition, i.e., epitaxial growth. The lighter core observed from Figure 3.5 reflected that the original substrate for this synthesis was scorodite produced using a nitrate solution based on the autoclave described by Dutrizac and Jambor [6].

Finally, scorodite solids were stirred at $\text{pH}=2$ for 24 h three times in order to remove any amorphous material prior to their encapsulation. At the end of each step, the slurry was filtered and the solids washed by repulping 3 times with 1000 mL of acidified deionised hot water ($\text{pH} \sim 3$, 60°C). The freshly cleaned scorodite particles were subsequently used

for encapsulation with phosphate coatings (Refer to Chapter 6).

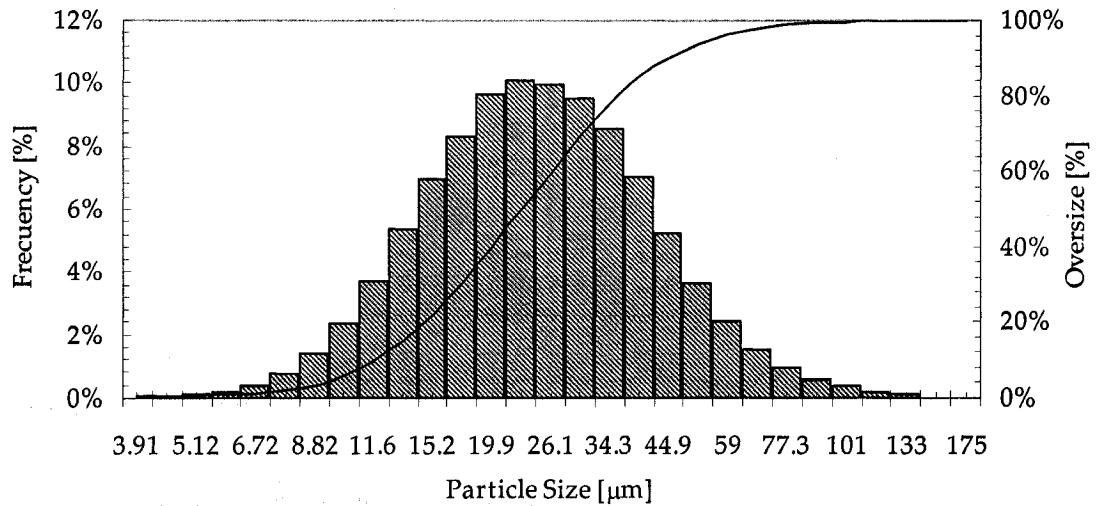


Figure 3.4. Particle size distribution of scorodite produced by atmospheric precipitation. median = 22.8 μm , mean = 26.4 μm , and mode = 21.3 μm .

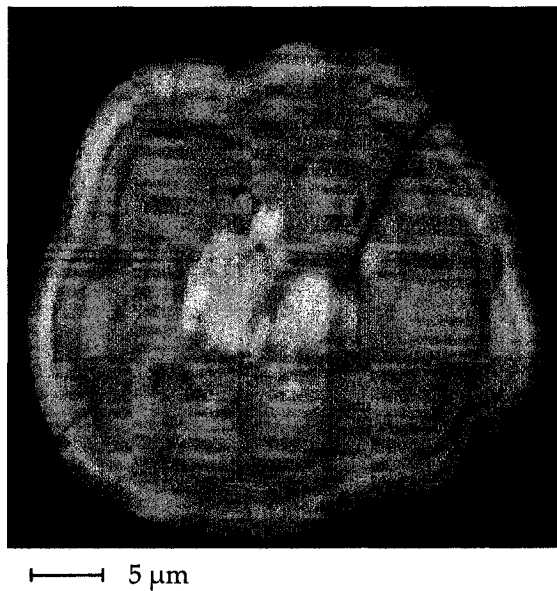


Figure 3.5. Back-scattered electron image of scorodite precipitated under atmospheric conditions.

References

- 1 Kondos, P.D. Pressure chloride leaching of a complex U/Ra/Ni/As ore: statistical modelling and solution chemistry, *Ph.D. Thesis*, McGill University, QC, 1988.

- 2 AMTEL Ltd. *Evaluation of scorodite reacted with Al-phosphate; AMTEL report 04/15 2004.*
- 3 Droppert, D.J.; Demopoulos, G.P.; Harris, G.B. Ambient pressure production of crystalline scorodite from arsenic-rich metallurgical effluent solutions. In *EPD Congress 1996*; Warren, G.W., Ed.; The Minerals, Metals & Materials Society: Warrendale, PA, 1996, pp. 227-239.
- 4 Singhanian, S.; Wang, Q.; Filippou, D.; Demopoulos, G.P. Temperature and seeding effects on the precipitation of scorodite from sulfate solutions under atmospheric-pressure conditions. *Metallurgical and Materials Transactions B*, 2005, 36B, 327-333.
- 5 Singhanian, S.; Wang, Q.; Filippou, D.; Demopoulos, G.P. Acidity, valency and third-ion effects on the precipitation of scorodite from mixed sulfate solutions under atmospheric-pressure conditions. *Metallurgical and Materials Transactions B*, 2005, (in press)
- 6 Dutrizac J.E.; Jambor, J.L. The synthesis of crystalline scorodite: $\text{FeAsO}_4 \cdot 2\text{H}_2\text{O}$. *Hydrometallurgy*, 1988, 19, 377-384.

Chapter 4. Synthesis and stability of hydrated aluminium phosphate

4.1 Introduction

This chapter is devoted to the synthesis by reactive crystallisation of hydrated aluminium phosphate ($\text{AlPO}_4 \cdot 1.5\text{H}_2\text{O}$) and testing its stability. The synthesis method developed here differs from the ones previously reported in the literature (refer to section 2.4.1 of Chapter 2) as it involves direct crystallisation from sulphate media rather than long-term ageing or hydrothermal routes in chloride or nitrate media. Following its synthesis the dissolution mechanism and stability of $\text{AlPO}_4 \cdot 1.5\text{H}_2\text{O}$ ($\text{AlPO}_4 \cdot \text{H}_3$) is reported at 22 °C over the pH range 2.4 to 8.8. Finally, the experimental results are analysed with the aid of PHREEQC [1] and the solubility product for $\text{AlPO}_4 \cdot 1.5\text{H}_2\text{O}$ is determined.

4.2 Synthesis

4.2.1 Materials and methods

Experimental set up: The experimental set-up used in this work was the same as the one described in Chapter 3 (Section 3.2).

Crystallisation tests: The precipitation of $\text{AlPO}_4 \cdot 1.5\text{H}_2\text{O}$ in sulphate media is described by the following reaction:



The precipitation process generates sulphuric acid; hence, it may be conducted with or without pH control. Moreover, the production of hydrated aluminium phosphate may

be done via homogeneous or seed-assisted precipitation. Both approaches were investigated in this chapter.

In a typical homogeneous precipitation test, 1.5 L of Al:P=1:1 solution, was first prepared from analytical-grade sodium phosphate monohydrate ($\text{NaH}_2\text{PO}_4 \cdot \text{H}_2\text{O}$), aluminium sulphate octadecahydrate ($\text{Al}_2(\text{SO}_4)_3 \cdot 18\text{H}_2\text{O}$) and sulphuric acid (H_2SO_4). The solution was then placed in the reactor and heated to the desired temperature while stirring. Sodium hydroxide (NaOH , 1 mol/L) was added slowly to raise the solution pH up to a critical level (critical supersaturation) signifying the onset of homogeneous nucleation (becoming evident by cloud formation) [2].

Once this point was reached, precipitation was allowed to continue for 24 h in a free drift-mode; after this period of time the pH was recorded and the solution was analysed for P and Al. The final solution composition was considered to represent a practical equilibrium for the system. Via this series of tests the metastable zone of $\text{AlPO}_4 \cdot 1.5\text{H}_2\text{O}$ was determined and used to design the seed-assisted crystallisation tests.

In a seed-assisted precipitation test, an acidic sulphate solution containing ~ 0.17 mol/L of P(V) and Al:P of 1:1 was heated to 95°C and then neutralised with 1 mol/L NaOH , until the precipitation pH of 1.7 was reached (just before the critical supersaturation level was attained); the solution was allowed to stabilise for 30 min, hence assuring uniform supersaturated conditions. At this point, 30 g/L of seed produced by homogeneous precipitation (the experimental procedure described above) was used to begin the precipitation process; the pH in this case (in contrast to the homogeneous precipitation test) was kept constant using NaOH (1 mol/L) as base, and after 4.5 h of precipitation the product was collected. During the course of the precipitation process, samples of slurry were taken at regular time intervals, and were filtered through membrane filter (GE Osmonics Cameo $0.22\ \mu\text{m}$) and diluted with acidified ($w_{\text{HNO}_3} \sim 5\%$) deionised water.

Characterisation and analysis: At the end of each test, the entire suspension was filtered. The final filtrate together with the filtrates of the intermediate samples were

analysed for P and Al. The final slurry was filtered and the solids washed by repulping 3 times with 1000 mL of acidified deionised hot water (60 °C). The final solids were subjected to a number of characterisation tests including X-ray Diffraction (XRD) analysis, chemical analysis by digestion, SEM examination and thermogravimetric analysis (more details on these techniques can be found in Chapter 3).

4.2.2 Metastable zone for aluminium phosphate precipitation

Critical supersaturation curves of aluminium phosphate as determined by the homogeneous precipitation experiments are shown in Figure 4.1. This figure shows the metastable zone width, which is defined by the critical concentration for homogeneous nucleation line and the pseudo-equilibrium line [2]. The precipitates obtained at the end of these experiments had a white colour. The precipitates were subjected to XRD analysis. A typical XRD pattern is shown in Figure 4.2. It can be seen from Figure 4.2 that the solids produced have good crystallinity and match the XRD pattern of hydrated aluminium phosphate H_3 , $(AlPO_4 \cdot 1.5H_2O)$ [3].

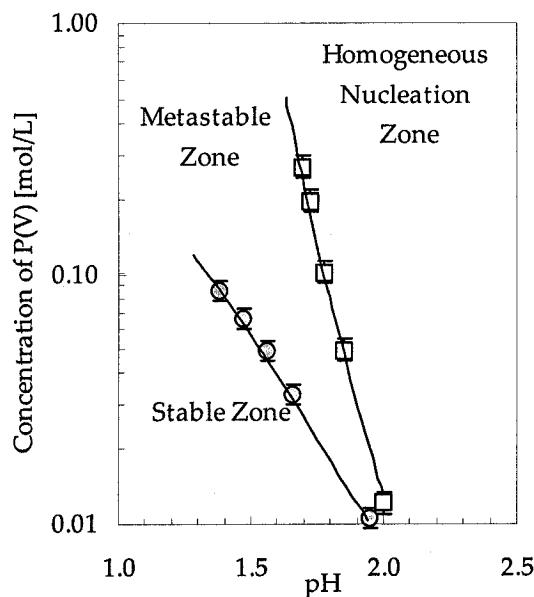


Figure 4.1. Metastable zone width for the $Al_2(SO_4)_3$ - H_3PO_4 - $NaOH$ system at 95 °C. Symbols: □ Initial point – Critical concentration for homogeneous nucleation; ○ Final point – pseudo-solubility.

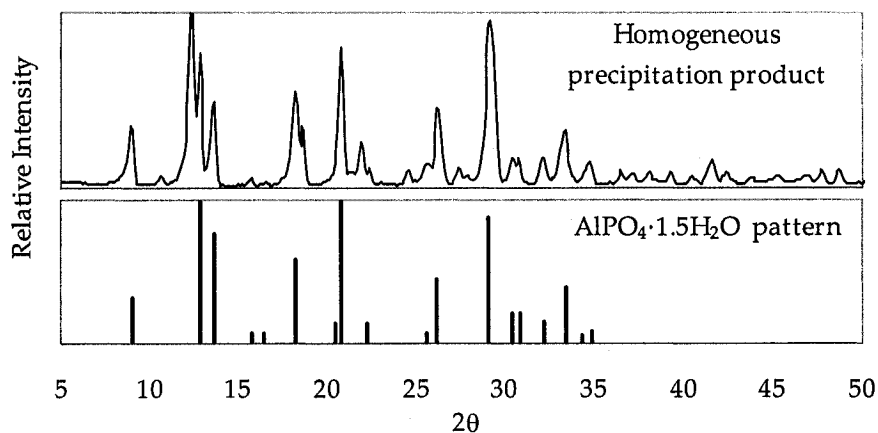


Figure 4.2. XRD pattern of product obtained by homogeneous precipitation (relative intensity); solids produced from a solution with $[\text{P(III)}]_0 = 0.2 \text{ mol/L}$ and $\text{Al:P} = 1$; $\text{AlPO}_4 \cdot 1.5\text{H}_2\text{O}$ pattern from reference [3].

Figure 4.3 shows SEM images of the produced material from an initial solution of $[\text{Al(III)}] = [\text{P(V)}] = 0.2 \text{ mol/L}$. It appears from this examination that the product consisted of irregularly shaped agglomerates of the order of $2\text{--}5 \mu\text{m}$ made up of primary crystallites smaller than $1 \mu\text{m}$. The particle size distribution of the produced hydrated aluminium phosphate is shown in Figure 4.4. It can be seen the median particle size to be $3.3 \mu\text{m}$ and distribution mode equal to $4.2 \mu\text{m}$.

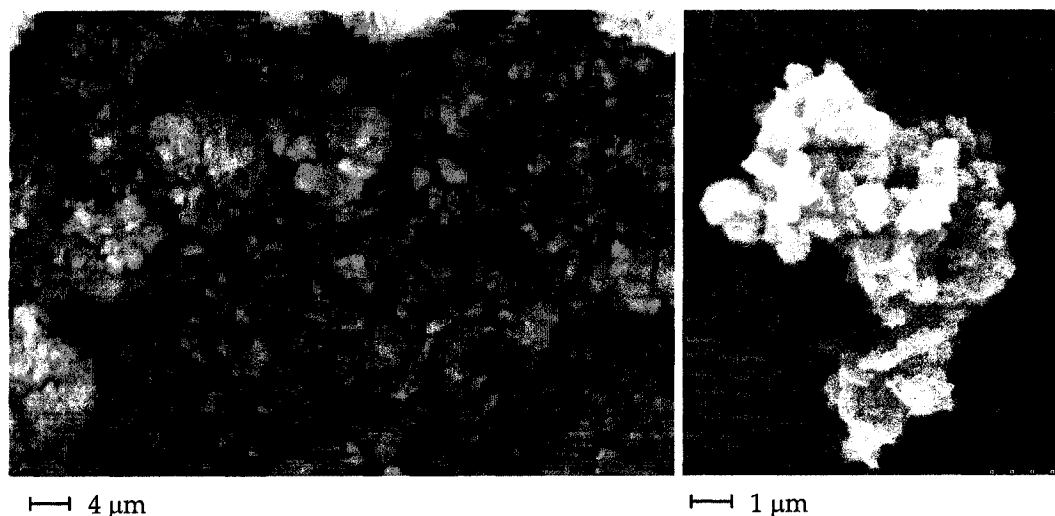


Figure 4.3. Scanning electron micrographs of hydrated aluminium phosphate produced by homogeneous precipitation.

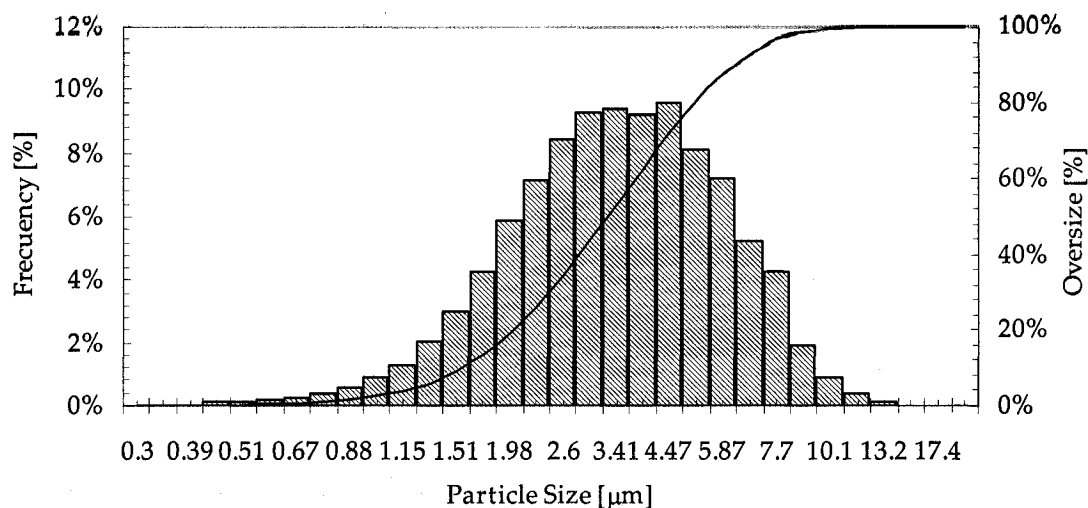


Figure 4.4. Particle size distribution of hydrated aluminium phosphate produced by homogeneous precipitation. Median = 3.3 μm , mean = 3.6 μm , and mode = 4.2 μm .

4.2.3 Seed-assisted precipitation of hydrated aluminium phosphate

Figure 4.5 shows the precipitation kinetics of a typical test run within the determined metastable zone in the presence of seed and at constant pH. Both the variation of Al(III) and P(V) are plotted. It can be seen that 80% of the Al and P were removed in ~ 2 h; moreover, aluminium and phosphorus precipitation proceeded at the same rate reflecting the stoichiometry of the reaction (Eq. (4.1)). This product was then recycled three times using a similar approach, i.e., 30 g/L of the product was used as seed in each recycle.

The final precipitate was characterised by scanning electron microscopy (SEM). Figure 4.6 shows SEM images at a magnification of 1800 (left) and of 4000 (right). It can be seen that the product was clearly coarser than the solids produced by homogeneous precipitation (Figure 4.4), with apparent particle size coarser than 10 μm . The SEM micrographs show that the crystals have grown through a combination of surface deposition and agglomeration. Figure 4.7 shows the particle size distribution of these solids. This analysis revealed the formation of small amount of particles with a size between 0.45 and 3.41 μm ; this might mean that either homogeneous nucleation was not

entirely prevented during precipitation or breakage (less likely) of the agglomerated solids took place during size distribution analysis.

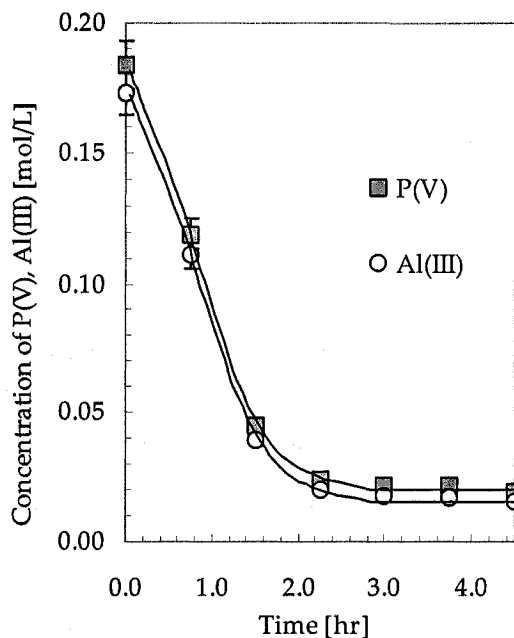


Figure 4.5. One-stage aluminium phosphate precipitation with pH control using homogeneously produced seed (Seed concentration, 30 g/L); NaOH as base; 95 °C; precipitation pH 1.70.

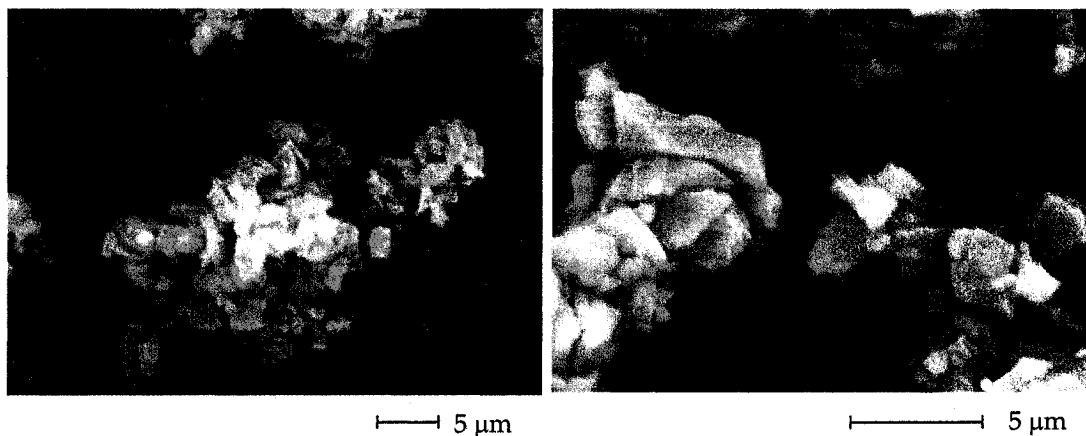


Figure 4.6. Scanning electron micrographs of hydrated aluminium phosphate produced by seed-assisted precipitation after three recycles.

The chemical make-up of the precipitate was determined via chemical analysis, XRD and TGA. For the chemical analysis, ~100 mg of precipitate was dissolved in 100 mL of strong HCl solution (~ 5 mol/L) by heating to about 70 °C. This analysis yielded a molar

ratio Al to P of 1.06 ± 0.08 . Moreover, the analysis revealed that small amount of SO_4^{2-} ($w_{\text{SO}_4} \sim 0.4\%$) was incorporated (not removable by extensive washing) into the crystal structure of the product most likely via substitution.

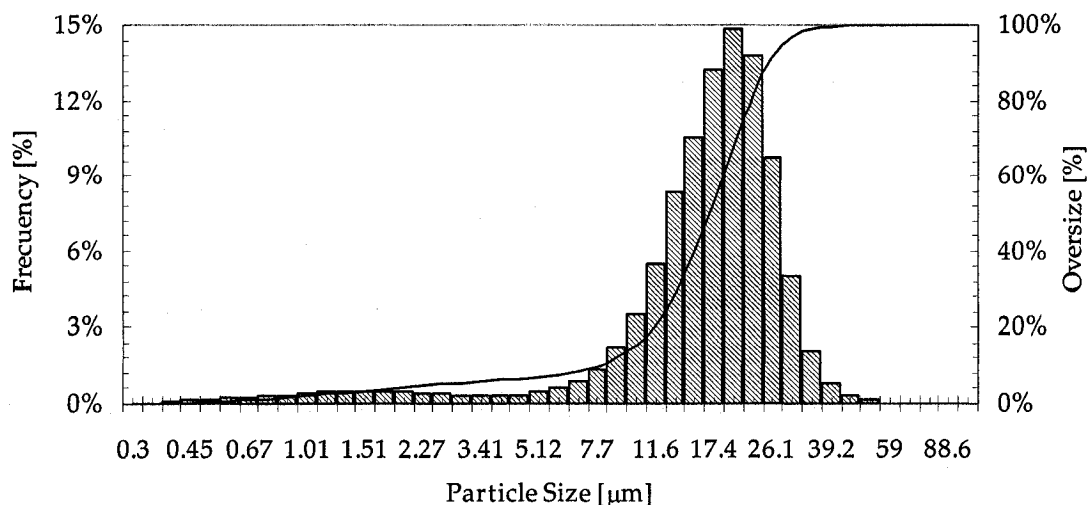


Figure 4.7. Particle size distribution of hydrated aluminium phosphate produced by seed-assisted precipitation. median = $16.8 \mu\text{m}$, mean = $16.7 \mu\text{m}$ and mode = $18.6 \mu\text{m}$.

XRD confirmed the presence of $\text{AlPO}_4 \cdot \text{H}_2\text{O}$ as the dominant phase, with good crystallinity (Figure 4.8) and TGA showed (Figure 4.9) that the weight loss for this material to occur between 80 and $130 \text{ }^\circ\text{C}$ and to amount to a reduction of 18.40% . This corresponds to a hydrated composition of $\text{AlPO}_4 \cdot 1.54\text{H}_2\text{O}$, which is in agreement with the formula $\text{AlPO}_4 \cdot 1.5\text{H}_2\text{O}$ reported by Pluth and Smith [4] for this material. The mass fraction of P and Al ($w_{\text{P}} = 18.7\%$ and $w_{\text{Al}} = 20.2\%$) were in agreement with the theoretical values of P and Al in a compound with molecular formula $\text{AlPO}_4 \cdot 1.5\text{H}_2\text{O}$ ($w_{\text{P}} = 18.1\%$ and $w_{\text{Al}} = 20.8\%$).

4.3 Stability

4.3.1 Methods

Solubility Measurements: The $\text{AlPO}_4 \cdot 1.5\text{H}_2\text{O}$ solids synthesised by the method just described were subjected to a special leaching procedure before actual solubility measurements were made in order to remove any soluble non-crystalline material that

could have distorted the measurements. This leaching procedure involved stirring 30 g of solids in 500 mL of 0.01 mol/L HNO_3 -containing solutions for 3 periods of 24 h each. At the end of each 24 h period, the slurry was filtered and the solids washed by repulping 3 times with 1000 mL of acidified hot water (pH~3, 60 °C) before proceeding with the subsequent 24 h leaching period.

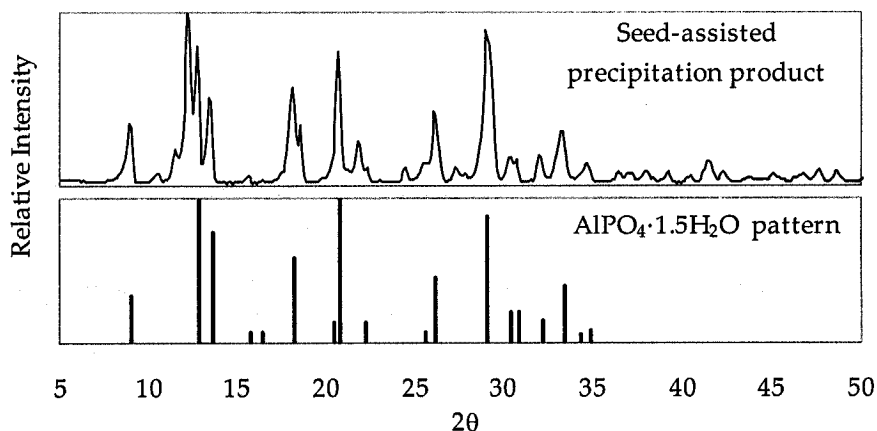


Figure 4.8. XRD pattern of product obtained by seed-assisted precipitation ($\text{AlPO}_4 \cdot 1.5\text{H}_2\text{O}$ pattern from reference [3]).

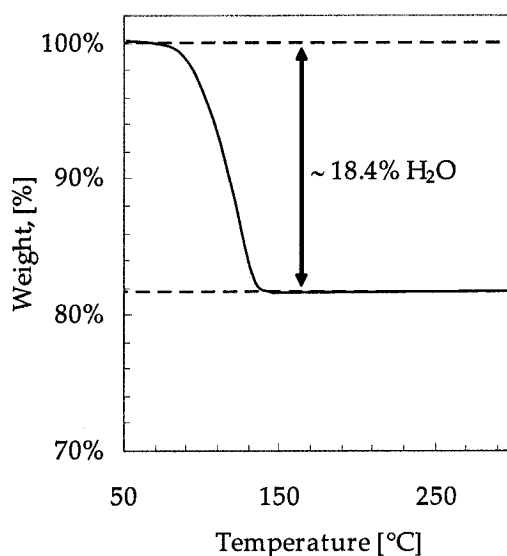


Figure 4.9. TGA Analysis of hydrated aluminium phosphate produced by seed-assisted precipitation; heating rate $10\text{ °C}\cdot\text{min}^{-1}$.

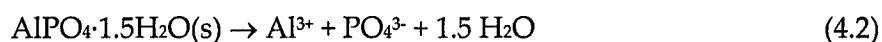
For the solubility tests, 200 mL of deionised water (prepared via a dual ion exchange system consisting of a Cole Parmer ion exchanger type 1506-25 "universal" and an ion

exchanger type 1506-35 "Research") was placed in 250 mL Erlenmeyer flasks, stoppered and agitated with magnetic stirrer. The experiments were performed at room temperature (22 °C). In each flask, 5 g of solids were added followed by pH adjustment. The pH of the slurry was measured and adjusted initially to 2.0 and 4.0 using HNO₃ solution and to pH values of 5.5, 6.5, 8.0 and 10.0 using NaOH solution. The pH was not adjusted during the dissolution test. At predetermined times, samples were taken, filtered using 0.025 µm pore size membranes, diluted with (5% HNO₃) solutions and analysed. The pH was measured using a Ross™ combination electrode with a reported accuracy of ±0.02 pH units (±4.5% in H⁺ activities). The pH electrode was standardised versus buffer pH solutions 4.0, 7.0 and 10.0. All experiments were carried out in duplicate runs.

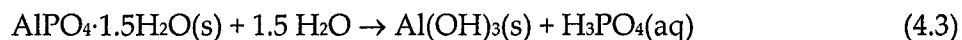
Characterisation and analysis: solutions and solids were characterised using the techniques described in 4.2.1.

4.3.2 Thermodynamic considerations

The dissolution process: The congruent dissolution reaction of AlPO₄·1.5H₂O is given by the following reaction:

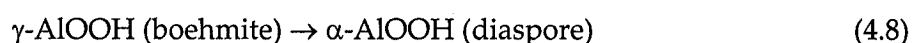
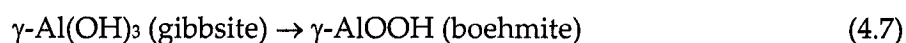
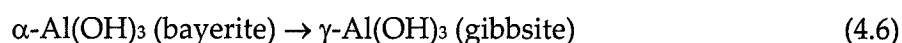
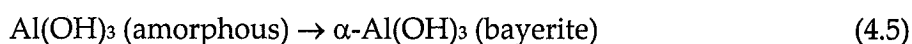


Alternatively AlPO₄·1.5H₂O may dissolve incongruently:



In this case the Al³⁺ concentration would be governed by the re-precipitation of Al³⁺ as one of the aluminium (oxy)hydroxide phases. Stranski's rule states that the least stable phase nucleates first, because the interfacial energy requirements are less stringent [5]. According to Lindsay and Walthall [6] the most soluble aluminium hydroxide material is Al(OH)₃(amorphous), followed by α-Al(OH)₃(bayerite), γ-AlOOH(boehmite), γ-Al(OH)₃(gibbsite), and α-AlOOH (diaspore). Some authors, however, have reported a different stability sequence, namely gibbsite < boehmite < diaspore [7,8]. Gibbsite is the most

common mineral found in weathered soils. Therefore, the formation of aluminium hydroxide phases, by re-precipitation, during the incongruent dissolution of $\text{AlPO}_4 \cdot 1.5\text{H}_2\text{O}$ is expected to proceed (at least in part) via the following phase transformation stages:

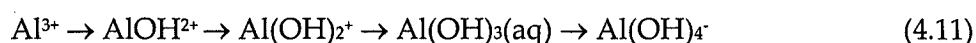


Ion activity product calculation: For the calculation of the ion activity product of $\text{AlPO}_4 \cdot 1.5\text{H}_2\text{O}$ ($IAP = a(\text{Al}^{3+}) \cdot a(\text{PO}_4^{3-})$) and Al(OH)_3 ($IAP = a(\text{Al}^{3+}) \cdot a(\text{OH}^-)^3$) all aqueous speciation equilibria need to be taken into account. Reactions (4.9) and (4.10) describe the formation of Al- PO_4 complexes.



According to Bohn and Peech [9] the $\text{Log}\beta$ values of the above reactions are 3.0 and 7.0 respectively. These values are in agreement with the data reported by Langmuir. [10] who independently reported values of 3.1 and 7.4, respectively. In this study the values of Langmuir are used.

The aluminium ion, Al^{3+} , exists as an octahedral hexahydrate ion, $\text{Al}(\text{H}_2\text{O})_6^{3+}$ in acidic solutions [11]. Hence, when the pH increases, the hexahydrate ion undergoes hydrolysis by four successive deprotonations, producing species with progressively increasing OH numbers as is shown in equation (4.11).



The thermodynamic constants for all the complexation and solubility equilibria

considered in the present study are listed in Table 4.1. The activity coefficients were calculated according to the Davies equation [12].

$$\text{Log } \gamma_k = -Az_k^2 \left(\frac{\sqrt{I}}{1 + \sqrt{I}} - 0.3I \right) \quad (4.12)$$

where γ_k is the activity coefficient of ion k , z_k its valency, I the ionic strength and A the Debye–Hückel constant.

Table 4.1. Equilibria and constants considered in the present PHREEQC study.

Reaction	Log K	Reference
$\text{H}_3\text{PO}_4 \leftrightarrow \text{H}_2\text{PO}_4^- + \text{H}^+$	-2.15	[13]
$\text{H}_2\text{PO}_4^- \leftrightarrow \text{HPO}_4^{2-} + \text{H}^+$	-7.20	[13]
$\text{HPO}_4^{2-} \leftrightarrow \text{PO}_4^{3-} + \text{H}^+$	-12.35	[13]
$\text{Al}^{3+} + \text{H}_2\text{O} \leftrightarrow \text{AlOH}^{2+} + \text{H}^+$	-5.00	[14]
$\text{Al}^{3+} + 2\text{H}_2\text{O} \leftrightarrow \text{Al}(\text{OH})_2^+ + 2\text{H}^+$	-10.1	[14]
$\text{Al}^{3+} + 3\text{H}_2\text{O} \leftrightarrow \text{Al}(\text{OH})_3(\text{aq}) + 3\text{H}^+$	-16.8	[14]
$\text{Al}^{3+} + 4\text{H}_2\text{O} \leftrightarrow \text{Al}(\text{OH})_4^+ + 4\text{H}^+$	-22.70	[14]
$\text{Al}^{3+} + \text{HPO}_4^{2-} \leftrightarrow \text{AlHPO}_4^+$	7.40	[10]
$\text{Al}^{3+} + \text{H}_2\text{PO}_4^- \leftrightarrow \text{AlH}_2\text{PO}_4^{2+}$	3.10	[10]
$\text{Al}(\text{OH})_3$ (amorphous) + $3\text{H}^+ \leftrightarrow \text{Al}^{3+} + 3\text{H}_2\text{O}$	10.80	[15]
$\text{Al}(\text{OH})_3$ (bayerite) + $3\text{H}^+ \leftrightarrow \text{Al}^{3+} + 3\text{H}_2\text{O}$	9.15	[7]
$\text{Al}(\text{OH})_3$ (gibbsite) + $3\text{H}^+ \leftrightarrow \text{Al}^{3+} + 3\text{H}_2\text{O}$	8.11	[7]
AlOOH (boehmite) + $3\text{H}^+ \leftrightarrow \text{Al}^{3+} + 2\text{H}_2\text{O}$	8.00	[7]
AlOOH (diaspore) + $3\text{H}^+ \leftrightarrow \text{Al}^{3+} + 2\text{H}_2\text{O}$	7.37	[7]

Note: Aluminium waters of hydration are omitted for simplicity

The potential role of phosphate sorption onto Al(III) (oxy)hydroxide is ignored since according to mass balance calculations only a small portion of the initial mass is

converted to Al(III) (oxy)hydroxide phases under the tested conditions (except for pH 8.8).

4.3.3 Experimental data

The variation of the solution concentration, in terms of Al(III) and P(V) along with pH, as a function of time for the experiments performed, is shown in Figure 4.10. It is observed that the aluminium concentration rose initially reaching a maximum after approximately 6 d, hereafter followed by a decrease before a steady state was attained. This suggests a certain supersaturation level being built up before the nucleation of aluminium hydroxide started taking place. On the other hand, the P(V) concentration rose gradually reaching a plateau with the exception of the test with final pH 4.18 (Figure 4.10(d)).

The final (after 30 d) Al(III) and P(V) concentrations are plotted as a function of equilibrium pH in Figure 4.11. A comparison of these values with the values published by Robins et al. for variscite (<0.03 mmol/L of P(V) at pH 4.0 [16]) revealed that $\text{AlPO}_4 \cdot 1.5\text{H}_2\text{O}$ is more soluble than the latter.

The data presented in Figure 4.10 and Figure 4.11 clearly indicate the dissolution process to be incongruent in nature. This is better seen if the data of Figure 4.11 are replotted as a final (i.e. equilibrium) Al(III) to P(V) molar ratio versus pH (Figure 4.12). According to this figure, the transition from congruent to incongruent dissolution takes place at around pH 3. Bache [17] reported the same incongruent point for variscite, but Robins et al. found the incongruent point for variscite to be at pH ~ 7.0 [16]. It is suspected that Bache's data are not correct because of the admission by the author that the starting variscite material "...perhaps contained a small amount of amorphous material"; hence, causing the incongruent point to shift to lower pH. On the other hand, Robins et al. provided limited information to allow for independent assessment of the accuracy of their results.

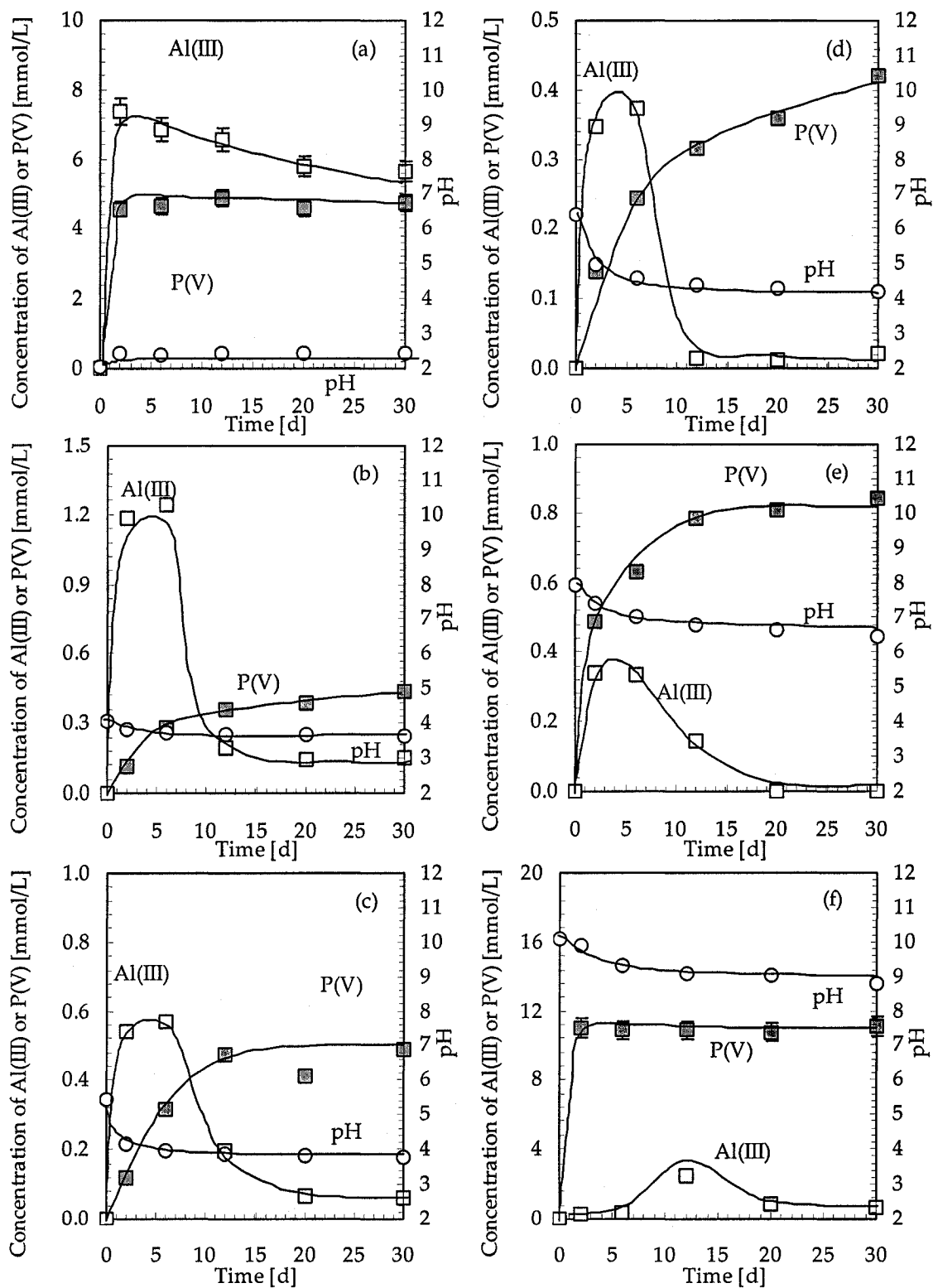


Figure 4.10. P(V) and Al(III) concentrations and pH as a function of time at 22 °C. (a) final pH of 2.43; (b) final pH of 3.62 (c) final pH of 3.79; (d) final pH of 4.18; (e) final pH of 6.44 and (f) final pH of 8.80. (Symbols \square Al(III); \blacksquare P(V); \diamond pH).

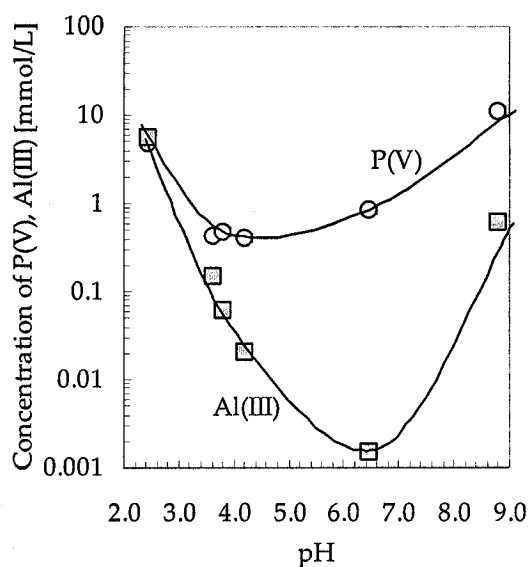


Figure 4.11. Experimental solubility determined for $\text{AlPO}_4 \cdot 1.5\text{H}_2\text{O}$ at 22 °C (equilibration time 30 d).

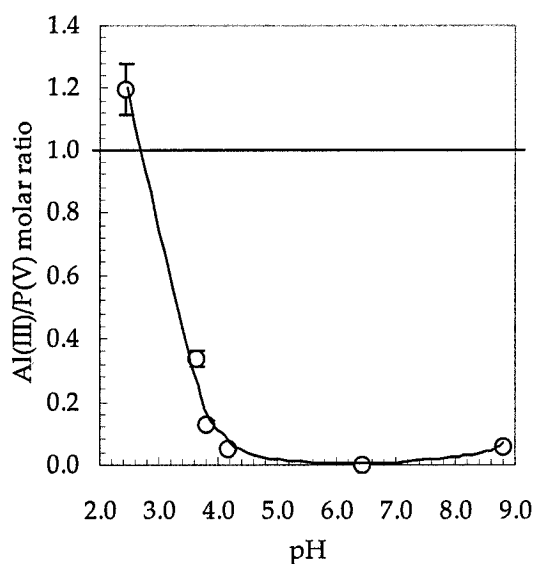


Figure 4.12. Al(III) to P(V) molar ratio in solution after 30 d of dissolution.

The equilibrated solids (after 30 d) were characterised by XRD in order to determine the type of aluminium (oxy)-hydroxide that had formed. The data are shown in Figure 4.13. The XRD analysis revealed the presence of gibbsite at elevated pHs (≥ 3.62), while for the intermediate pH range, the coexistence of a minor aluminium(III) basic phosphate (kingite) cannot be ruled out. Transformation to variscite was not detected.

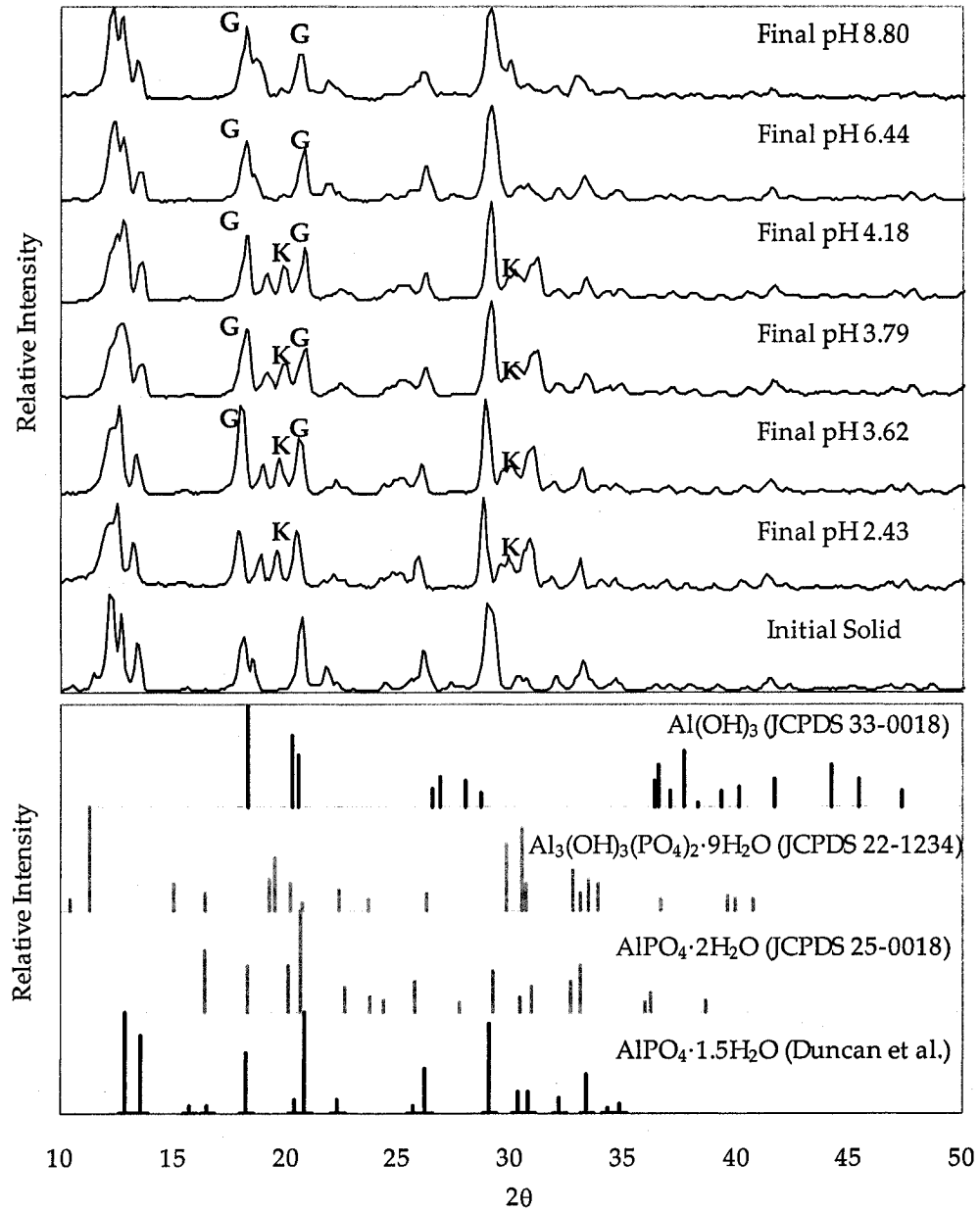


Figure 4.13. XRD pattern of solids before and after equilibrium at various pH compared to synthetic $\text{Al}(\text{OH})_3$ (Gibbsite), $\text{Al}_3(\text{OH})_3(\text{PO}_4)_2 \cdot 9\text{H}_2\text{O}$ (Kingite), $\text{AlPO}_4 \cdot 1.5\text{H}_2\text{O}$ and $\text{AlPO}_4 \cdot 2\text{H}_2\text{O}$ (Variscite).

4.3.4 Determination of the solubility product

Using the final solubility data along with the equilibrium and thermodynamic data listed in Table 4.1, the solubility product for $\text{AlPO}_4 \cdot 1.5\text{H}_2\text{O}$ was determined with the aid of PHREEQC (Table 4.2). It is interesting to note from the data of Table 4.2 that all

estimated K_{sp} values are reasonably close to each other over the whole pH range revealing that the estimation method is credible. From this calculation, the solubility product was determined to be $\text{Log}K_{sp} = -20.46 \pm 0.40$ (the data at pH 8.80 were excluded).

Table 4.2. Solubility data and solubility product estimates using PHREEQC

pH		Concentration [mmol·L ⁻¹]			Log K_{sp}
Initial	Final	Al(III)	P(V)		
2.00	2.43	5.659	4.733	-20.76	
4.00	3.62	0.148	0.439	-20.28	
5.50	3.79	0.063	0.490	-20.37	
6.50	4.18	0.021	0.422	-20.37	
8.00	6.44	0.001	0.841	-20.54	
10.00	8.80	0.632	11.106	-21.07	

The standard Gibbs free energy of formation ($\Delta G_{f,0}$) for $\text{AlPO}_4 \cdot 1.5\text{H}_2\text{O}$ was subsequently estimated using the determined solubility product and the following thermodynamic values: $\Delta G_{f,0} = -489.40 \pm 1.4 \text{ kJ}\cdot\text{mol}^{-1}$ for Al^{3+} [7], $\Delta G_{f,0} = -237.141 \pm 0.040 \text{ kJ}\cdot\text{mol}^{-1}$ for H_2O [15] and $\Delta G_{f,0} = -1018.24 \pm 1.5 \text{ kJ}\cdot\text{mol}^{-1}$ for PO_4^{3-} [18]. This calculation determined the standard Gibbs free energy of formation ($\Delta G_{f,0}$) for $\text{AlPO}_4 \cdot 1.5\text{H}_2\text{O}$ to be $-1980.5 \pm 4.3 \text{ kJ}\cdot\text{mol}^{-1}$. Upon comparison of these values to those reported for variscite $\text{Log}K_{sp} = -22.05$ [19] and $\Delta G_{f,0} = 2104.5 \text{ kJ}\cdot\text{mol}^{-1}$ [20] it becomes clear that $\text{AlPO}_4 \cdot 1.5\text{H}_2\text{O}$ is metastable versus variscite.

4.3.5 Evaluation of the dissolution mechanism with PHREEQC

Similarly to the calculation of the solubility product, the $\text{Log}(IAP)$ for aluminium phosphate and aluminium (oxy)hydroxide were estimated with the aid of PHREEQC as a function of time, so to better understand the $\text{AlPO}_4 \cdot 1.5\text{H}_2\text{O}$ dissolution mechanism. The respective $\text{Log}(IAP)$ calculated for each compound is presented in Figure 4.14 and Figure 4.15. On the same Figures, the $\text{Log}K_{sp}$ of the various aluminium (oxy)hydroxides phase

(Figure 4.14) and $\text{AlPO}_4 \cdot 1.5\text{H}_2\text{O}$ (Figure 4.15) are shown.

It can be seen from Figure 4.14(a) that the system is always undersaturated versus all aluminium (oxy)hydroxides confirming the congruent dissolution of $\text{AlPO}_4 \cdot 1.5\text{H}_2\text{O}$ at pH 2.43. However, as the pH increases (see Figure 4.14(b, c, d and e)), the system enters the incongruent region.

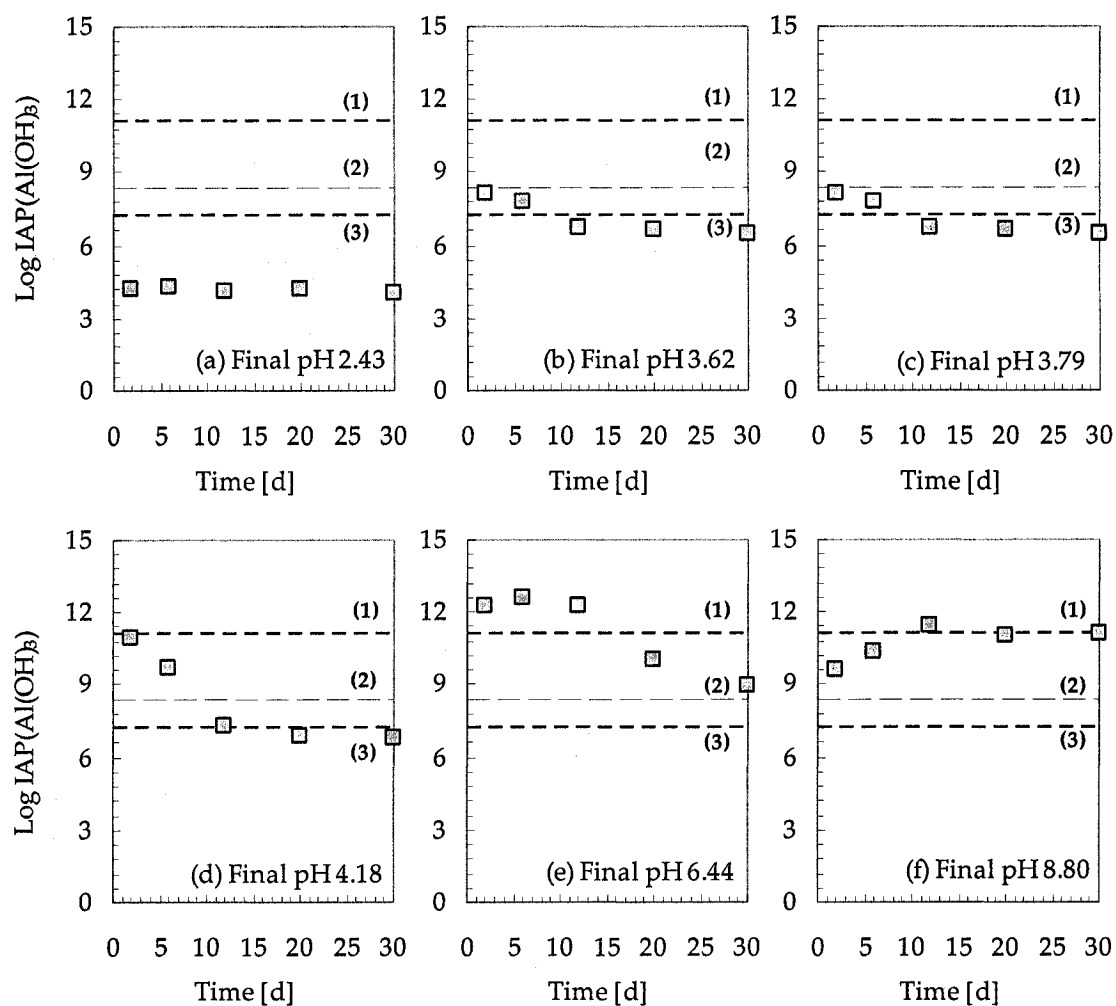


Figure 4.14. Ion activity product for aluminium (oxy)hydroxides during the dissolution of $\text{AlPO}_4 \cdot 1.5\text{H}_2\text{O}$ as a function of time at 22 °C at different equilibration pHs. Log K_{sp} for (1) $\text{Al}(\text{OH})_3$ (amorphous) (2) $\text{Al}(\text{OH})_3$ (gibbsite), and (3) AlOOH (diaspore) are shown (broken lines) as well.

According to the predicted data, the system is initially in equilibrium with an amorphous aluminium (oxy)hydroxide and supersaturated with reference to the more

stable crystalline phases. Diaspore rather than gibbsite is predicted to be the equilibrium aluminium (oxy)hydroxide phase after 30 d in the pH region 3.6 to 4.2 (Figure 4.14(b, c, and d)). This, however, was not confirmed by the XRD analysis (Figure 4.13), where the characteristic peak of gibbsite at $2\theta = 18.28^\circ$ was detected instead. This may in part reflect the quality of the solubility data used previously to determine the Gibbs free energy of formation of gibbsite. Thus, for example May et al.[21,22] had used 0.20 μm filters while Su and Harsh [7] used 0.1 μm membranes when they evaluated the solubility of gibbsite. In this study smaller filter sizes were used (0.02 μm) resulting in apparently lower solubility products.

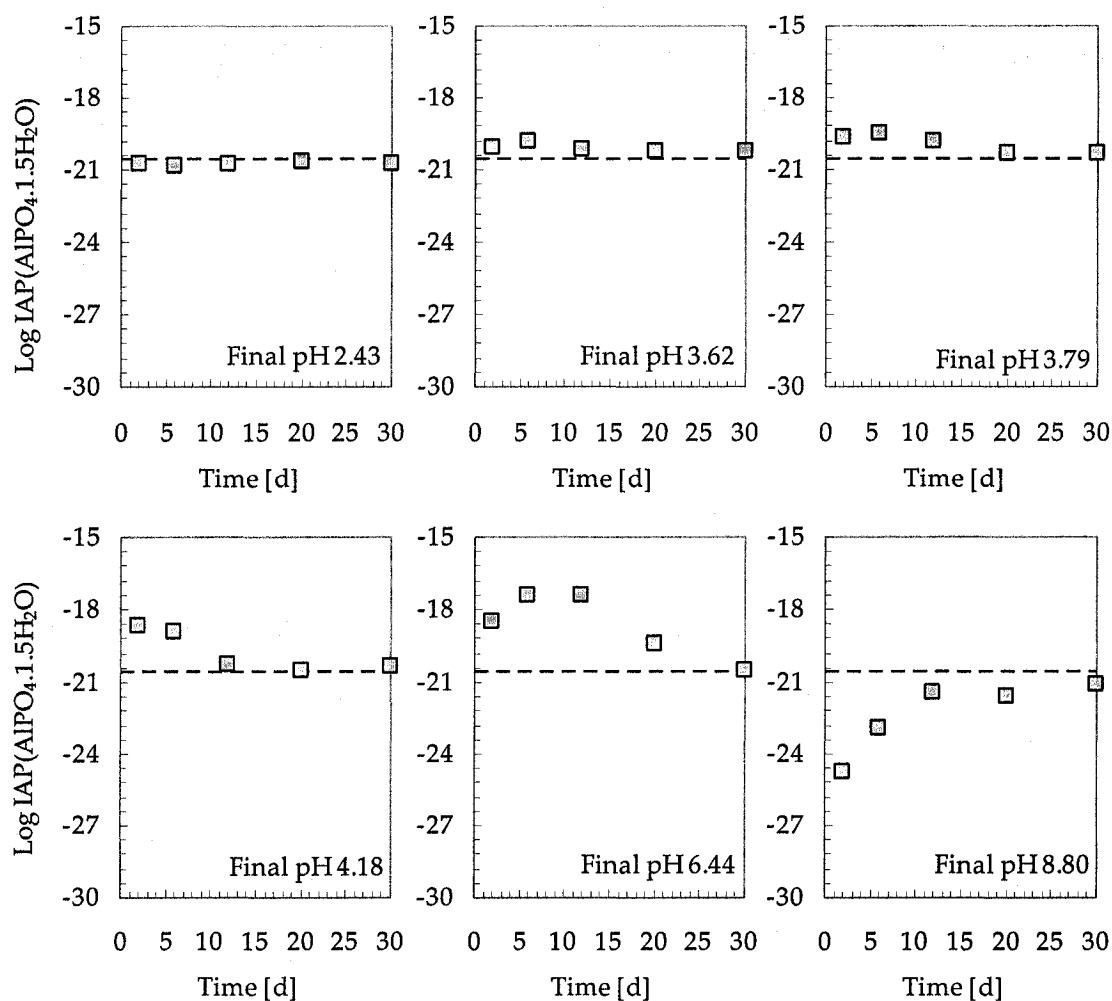


Figure 4.15. Ion activity product of AlPO₄·1.5H₂O as a function of time at 22 °C at different equilibration pHs. LogK_{sp} for AlPO₄·1.5H₂O is also shown (broken lines).

At higher pH the formation of a less stable $\text{Al}(\text{OH})_3$ phase like the amorphous one is predicted. This evolution of $\text{Al}(\text{OH})_3$ phases from amorphous in the early stages towards a more stable form (i.e. gibbsite, Figure 4.14(b,c, and d)) is in concordance with Stranski's rule [5]. Apparently, at elevated pH the phase transformation process that converts the amorphous $\text{Al}(\text{OH})_3$ phase to a crystalline (oxy)hydroxide is delayed.

As far as the Al-phosphate phase transformation is concerned it can be seen (Figure 4.15) that the system is in equilibrium with $\text{AlPO}_4 \cdot 1.5\text{H}_2\text{O}$ at pH 2.43 throughout the whole dissolution period (congruent dissolution), but slightly supersaturated during the initial stages of dissolution in the pH range 3.62 to 6.44. On the other hand, it is undersaturated in the early stages of dissolution at pH 8.8. Nevertheless, in all cases equilibrium was seen to be attained after 30 d.

4.4 Conclusions

A new synthesis method for hydrated aluminium phosphate $\text{AlPO}_4 \cdot 1.5\text{H}_2\text{O}$ ($\text{AlPO}_4\text{-H}_3$) was developed. The new method involved direct precipitation from a sulphate-matrix solution with aluminium to phosphorus molar ratio equal to one at 95 °C. For the initiation of homogeneous precipitation of crystalline material, supersaturation was increased to a critical level via pH adjustment. The critical pH at which homogeneous nucleation occurs is a function of solution composition.

The homogeneously produced material characterised by XRD and SEM analysis was found to be highly crystalline and to consist of aggregate particles of mean size $\sim 3.5 \mu\text{m}$. Use of seed and maintenance of supersaturation within the metastable zone via pH control (at 1.70) allowed the production of coarse aggregate particles of average size $\sim 16 \mu\text{m}$. Typically, 80% precipitation yield was obtained from a 5 g/L of Al(III) (Al:P = 1) over a period of 2 h equivalent to $0.07 \text{ mol} \cdot \text{L}^{-1} \cdot \text{h}^{-1}$.

The dissolution of $\text{AlPO}_4 \cdot 1.5\text{H}_2\text{O}$ was studied under the following experimental conditions: 22 °C, 30 d, 20 g/L and initial pH of 2.0, 4.0 5.5, 6.5, 8.0, and 10.0. It was

determined the dissolution to be congruent at initial pH 2.0 and becoming incongruent when initial pH was 4.0 or higher. It was observed that Al(III) concentration reached a critical level before the formation of Al(III) (oxy)hydroxide precipitates occurs. The sequence of formation of Al(III) (oxy)hydroxides phases, as determined by XRD analysis over the 30 d dissolution period was found to conform to Stranski's rule, i.e., the least stable phase forming first followed by its transformation to next stable Al(III) (oxy)hydroxide. This behaviour was confirmed with thermodynamic analysis of the dissolution process with the aid of PHREEQC. Finally, the K_{sp} of $\text{AlPO}_4 \cdot 1.5\text{H}_2\text{O}$ was determined to be $10^{-20.46 \pm 0.40}$ at 22 °C and 1 atm (101.325 kPa). The calculated standard Gibbs free energy of formation (ΔG_f°) for $\text{AlPO}_4 \cdot 1.5\text{H}_2\text{O}$ was $-1980.5 \pm 2.0 \text{ kJ} \cdot \text{mol}^{-1}$.

References

- 1 Parkhurst, D. L.; Appelo, C. A. J. *User's Guide to PHREEQC (Version 2)-A Computer Program for Speciation, Batch-Reaction, One-Dimensional Transport, and Inverse Geochemical Calculations; Water-Resources Investigations Report 99-4259; U.S. Geological Survey: Reston, VA, 1999; <http://wwwbr.cr.usgs.gov/>.*
- 2 Demopoulos, G.P. Aqueous precipitation and crystallization for the production of particulate solids with desired properties. *Hydrometallurgy*, 2005 (in press).
- 3 Duncan, B.; Stocker, M.; Gwinup, D.; Szostak, R.; Vinje, K. Template-Free Synthesis of the Aluminophosphates H₁ through H₄. *Bulletin de la Société Chimique de France*, 1992, 129, 98-110.
- 4 Pluth, J.J.; Smith, J.V. Hydrated aluminophosphate ($\text{AlPO}_4 \cdot 1.5\text{H}_2\text{O}$) with PO_4 , AlO_4 and $\text{AlO}_4(\text{H}_2\text{O})_2$ groups and encapsulated water. *Acta Crystallographica C*, 1986, 42, 1118-1120.
- 5 Blesa, M.A.; Matijević E. Phase transformations of iron oxides, oxohydroxides, and hydrous oxides in aqueous media. *Advances in Colloid and Interface Science*, 1989, 29(3-4), 173-221.
- 6 Lindsay, W.L.; Walthall P.M. The solubility of aluminum in soils. In *The Environmental Chemistry of Aluminum*, 2nd Ed.; Sposito, G. Ed.; Lewis Publishers:

- Boca Raton, FL, 1996, pp. 333-357.
- 7 Su, C.; Harsh, J.B. Gibbs free energies of formation at 298 K for imogolite and gibbsite from solubility measurements. *Geochimica et Cosmochimica Acta*, 1994, 58(6), 1667-1677.
- 8 Hemingway, B.S.; Sposito, G. Inorganic aluminum-bearing solid phases. In *The Environmental Chemistry of Aluminum*, 2nd Ed.; Sposito, G. Ed.; Lewis Publishers: Boca Raton, FL, 1996, pp. 82-116.
- 9 Bohn, H.L.; Peech M. Phosphato-iron(III) and phosphato-aluminum complexes in dilute solutions. *Soil Science Society of America Proceedings*, 1969, 33, 873-876.
- 10 Langmuir, D. Techniques of estimating thermodynamic properties for some aqueous complexes of geochemical interest. In *Chemical Modeling in Aqueous Systems*; Jenne, E.A. Ed.; ACS Symposium Series 93; American Chemical Society: Washington, DC, 1977, pp. 353-387.
- 11 Martin, R.B. Fe³⁺ and Al³⁺ hydrolysis equilibria. Cooperativity in Al³⁺ hydrolysis reactions. *Journal of Inorganic Biochemistry*, 1991, 44(2), 141-147.
- 12 Stumm W. *Aquatic Chemistry: Chemical Equilibria and Rates in Natural Waters*; John Wiley & Sons: New York, NJ, 1996.
- 13 Lindsay, W.L.; Vlek, P.L.G.; Chien, S.H. Phosphate minerals. In *Minerals in soil environment*, 2nd Ed.; Dixon, J.B; Weed, S.B.; Eds.; Soil Science Society of America: Madison, WI, 1989, pp. 1089-1130.
- 14 Nordstrom, D.K.; May, H.M. Aqueous equilibrium data for mononuclear Aluminum species. In *The Environmental Chemistry of Aluminum*, 2nd Ed.; Sposito, G. Ed.; Lewis Publishers: Boca Raton, FL, 1996, pp. 39-79.
- 15 Nordstrom, D.K.; Plummer, L.N.; Langmuir, D.; Busenberg, E.; May, H.M.; Jones, B.F.; Parkhurst, D.L. Revised chemical-equilibrium data for major water-mineral reactions and their limitations. In *Chemical Modeling in Aqueous Systems II*; Melchior, D.C.; Bassett, R.L. Eds.; ACS Symposium Series 416; American Chemical Society: Washington, DC, 1990, pp. 398-413.
- 16 Robins, R.G.; Twidwell, L.G.; Dahnke, D.R.; McGrath, S.F.; Khoe, G.H. The

- solubility of metal phosphates. In *EPD Congress 1991*; Gaskell, D.R.; Hager, J.P., Eds.; The Minerals, Metals & Materials Society: Warrendale, PA, 1991, pp. 3-26.
- 17 Bache, B.W. Aluminum and iron phosphate studies relating to soils: I. Solution and hydrolysis of variscite and strengite. *Journal of Soil Science*, 1963, 14(1), 113-123.
- 18 Wagman, D.D; Evans, W.H; Parker, V.B; Schumm, R.H.; Halow, I.; Bailey, S.M.; Churney, K.L.; Nuttall, R.L. The NBS tables of chemical thermodynamic properties: Selected values for inorganic and C1 and C2 organic substances in SI units, *Journal of Physical and Chemical Reference Data*, 1982, 11(2).
- 19 Lindsay, W.L. *Chemical Equilibria in Soils*; John Wiley & Sons: New York, NJ, 1980; Chapter 8; pp. 163-209.
- 20 Viellard, P.; Tardy, Y.; Thermochemical properties of phosphates. In *Phosphate Minerals*; Nriagu, J.O.; Moore, P.B.; Eds.; Springer Verlag: Berlin, 1984, pp. 171-198.
- 21 May, H.M.; Helmke, P.A.; Jackson, M.L. Determination of mononuclear dissolved aluminum in near-neutral waters. *Geochimica et Cosmochimica Acta*, 1979, 24(3-4), 259-269.
- 22 May, H.M.; Helmke, P.A.; Jackson, M.L. Gibbsite solubility and thermodynamic properties of hydroxy-aluminum ions in aqueous solution at 25 °C. *Geochimica et Cosmochimica Acta*, 1979, 43(6), 861-868.

Chapter 5. Synthesis and stability of selected calcium phosphates

5.1 Introduction

In this chapter, the synthesis by reactive crystallisation of two calcium phosphates is described, namely dicalcium phosphate dihydrate and hydroxyapatite (calcium-deficient). It is the scope of this work to elaborate a method of synthesis of these salts from chloride media at room temperature based on the concept of supersaturation control. The effects of supersaturation, residence time, and seeding on the stoichiometry and crystallinity of these compounds are reported. In addition, this chapter seeks to define the conditions for controlled deposition of these salts on scorodite particles. Following their synthesis, these two materials were subjected to dissolution studies as a function of pH in order to determine their dissolution behaviour in terms of phase transformation and stability.

5.2 Synthesis

5.2.1 Materials and methods

Experimental set up: The experimental set-up used in this work was the same as the one described in Chapter 3 (Section 3.2).

Metastable zone determination: The precipitation of calcium phosphates in chloride media was investigated by homogeneous and seed-assisted precipitation under controlled supersaturation conditions. However, given the fact that the critical supersaturation conditions, for the $\text{CaCl}_2\text{-NaH}_2\text{PO}_4\text{-H}_2\text{O}$ system have not been reported in literature preliminary experiments were performed to identify the metastable zone

width as was done with the aluminium phosphate system (Chapter 4).

Acidified solutions (pH ~ 2.0) of NaH_2PO_4 (2 to 90 mmol/L) and CaCl_2 (2 to 150 mmol/L) were prepared at room temperature (the preparation considered two different Ca to P molar ratios in solution, 1.0 and 1.67 which are the stoichiometric ratios for dicalcium phosphate dihydrate and hydroxyapatite respectively) and stirred for 30 min. All initial solutions were undersaturated with respect to all modifications of calcium phosphate. The supersaturation in solution was built up by slow addition of 100 mmol/L NaOH solution in a step-wise fashion, in order to reach the critical supersaturation point. This point was determined by means of the evolution of pH, i.e., either the pH began to decrease spontaneously, due to acid generation, or remained constant for more than 5 min. If the former were the case, the point was registered as a critical supersaturation point. When the pH was constant longer than five min the pH was increased again. The extent of each pH step was 0.1 pH units.

Crystallisation of dicalcium phosphate dihydrate: The reactive crystallisation of dicalcium phosphate dihydrate was achieved via step-wise neutralisation of an acidic solution of $\text{CaCl}_2\text{-NaH}_2\text{PO}_4\text{-HCl}$ ($[\text{Ca(II)}] = 100 \text{ mmol/L}$ (4.0 g/L), $[\text{P(V)}] = 100 \text{ mmol/L}$ (3.1 g/L) and pH ~ 3.0). The solution matrix and composition were chosen as per previous work published by Arifuzzaman and Rohani [1]. For the preparation of the feed solution analytical-grade sodium phosphate monohydrate ($\text{NaH}_2\text{PO}_4\cdot\text{H}_2\text{O}$), calcium chloride dihydrate ($\text{CaCl}_2\cdot 2\text{H}_2\text{O}$) and hydrochloric acid (HCl) were used. The solution was then placed in the reactor and the pH was slowly raised (using NaOH 100 mmol/L) with the purpose of building-up supersaturation.

In homogeneous precipitation tests, the above feed was neutralised with 100 mmol/L NaOH to pH 5.40, which was above the critical concentration at which homogeneous nucleation occurs (the critical pH was determined to be 4.85 according to Figure 5.1(a))

In a seed-assisted precipitation test, the above solution was diluted to $[\text{Ca(II)}] \sim 37.5 \text{ mmol/L}$ (Ca:P of 1:1) and neutralised once more with 100 mmol/L NaOH, until the

precipitation pH of 5.0 was reached (just 0.2 units of pH before the pH for homogeneous nucleation); the solution was allowed to stabilise for 30 min in order to assure uniform supersaturated conditions. At this point, 10 g/L of seed produced by homogeneous precipitation (as per the experimental procedure described above) was used to begin the precipitation process.

In both homogeneous and seed-assisted precipitation tests, the pH was kept constant during the course of precipitation using NaOH (100 mmol/L) as base. Each test lasted 2.0 h. All experiments were carried out in duplicate runs. The experiments were carried out under open air; in other words, the presence of atmospheric CO₂ was not excluded.

Crystallisation of (Ca-deficient) hydroxyapatite: The precipitation of hydroxyapatite via stepwise neutralisation is not feasible, since when an acidified solution is neutralised, the formation of metastable phases, such as dicalcium phosphate dihydrate or octacalcium phosphate, is favoured instead. Hence, a different approach was chosen to produce hydroxyapatite. This approach is an adaptation of the method reported by Rodríguez-Lorenzo et al. [2].

In a typical hydroxyapatite precipitation test, 1 L of a metastable supersaturated solution of CaCl₂-NaH₂PO₄-NaOH ([Ca(II)] ~ 1.5 mmol/L (Ca:P = 1.67) was prepared by slowly adding 500 mL of calcium chloride solution ([Ca(II)] = 3 mmol/L) to a 500 mL of sodium dihydrogen phosphate ([P(V)] = 1.8 mmol/L). The pH was then adjusted with 100 mmol/L NaOH to the precipitation pH of 7.6 (just 0.2 pH units below the pH for homogeneous nucleation) and the solution was allowed to stabilise for 30 min.

Homogeneous precipitation was induced by controlling the build up of supersaturation via simultaneous addition of calcium chloride (50 mmol/L) and sodium dihydrogen phosphate (30 mmol/L) at a rate of 20 mL/h (using one peristaltic pump with two pump heads). The pH was maintained at 7.6. After 6.0 h of reaction, the addition of reagents was stopped and the final product was collected.

The seed-assisted precipitation tests were initiated by adding hydroxyapatite solids homogeneously produced into the metastable calcium phosphate solution previously defined. Right after the seed was added to the reactor, the simultaneous addition of calcium chloride and sodium dihydrogen phosphate (50 mmol/L and 30 mmol/L respectively) was started along with 100 mmol/L NaOH containing-solutions to control pH and supersaturation. During seed-assisted precipitation two different addition rates were investigated 40 mL/h and 80 mL/h for periods of 3 and 6 h respectively. All experiments were carried out in duplicate runs. The experiments were carried out under open air; in other words, the presence of atmospheric CO₂ was not excluded.

Characterisation and analysis: At predetermined times, samples were taken, filtered using 0.25 µm pore size membranes (Corning), diluted with HNO₃ solution ($w_{\text{HNO}_3} \sim 5\%$) and analysed. At the end of each test, the entire suspension was filtered. The final filtrate together with the filtrates of the intermediate samples were analysed for P and Ca. The final slurry was filtered and the solids washed by repulping 3 times with 1000 mL of deionised hot water (60 °C). The final solids were subjected to a number of characterisation techniques including X-ray Diffraction (XRD) analysis, chemical analysis by digestion, SEM examination and infrared spectroscopy analysis (more details on these techniques can be found in Chapter 3).

5.2.2 Metastable region of calcium phosphate precipitation

Critical supersaturation curves of calcium phosphate as determined by the homogeneous precipitation experiments are shown in Figure 5.1. This figure shows the metastable zone width, which is defined by the critical homogeneous nucleation line and the solubility line for the Ca:P = 1 (a) and Ca:P = 1.67 (b). The solubility data shown in these figures were determined experimentally by dissolution as reported in section 5.3 of this chapter.

It has been reported that different calcium phosphate phases form at different pH

regions. Thus, dicalcium phosphate dihydrate (brushite) is reported to be kinetically favoured when the precipitation pH is kept below 6.0 [1]; the formation of octacalcium phosphate, $\text{Ca}_8(\text{HPO}_4)_2(\text{PO}_4)_4 \cdot 5\text{H}_2\text{O}$, is favoured when precipitation is carried out in the solution pH range between 6.0 and 7.0 [3]; and for pH values exceeding 7.0, hydroxyapatite is the expected final phase [4,5].

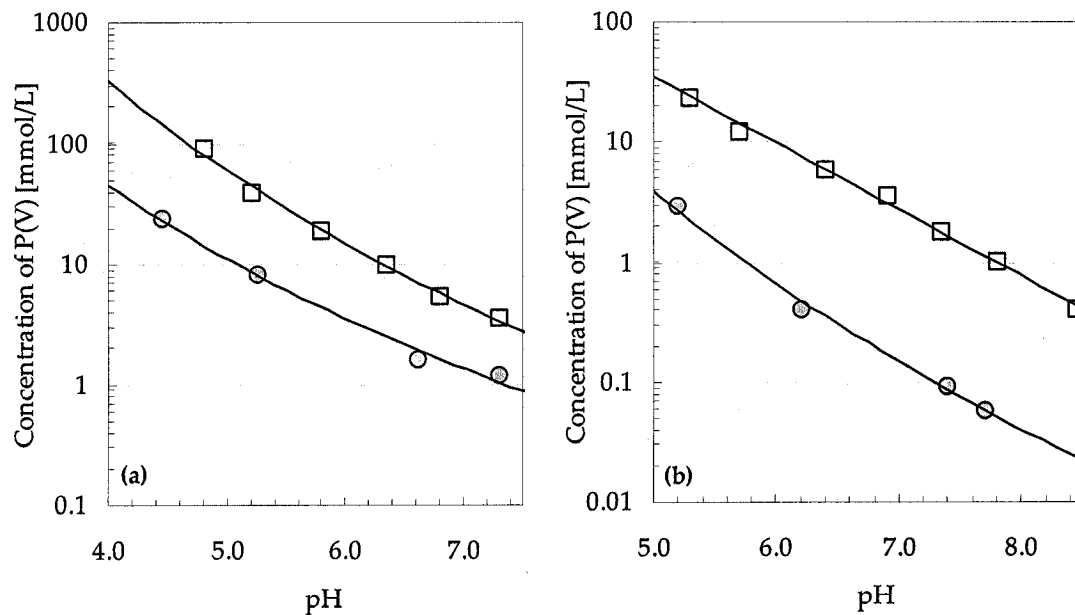


Figure 5.1. Metastable zone width for the $\text{CaCl}_2\text{-H}_3\text{PO}_4\text{-NaOH}$ system at 22 °C: (a) $\text{Ca:P} = 1$; (b) $\text{Ca:P} = 1.67$.

By incorporating the data of Figure 5.1(a,b) and the pH region of stability mentioned above the generalised precipitation diagram of Figure 5.2 was created. The boundaries between each phase, at pH 6.0 and 7.0, are only approximate and they help only to define the precipitation strategy selected for the synthesis of dicalcium phosphate dihydrate and hydroxyapatite. On this diagram, the reported solubility of octacalcium phosphate is also shown [6] (broken line), although, the synthesis of this phase was not investigated here.

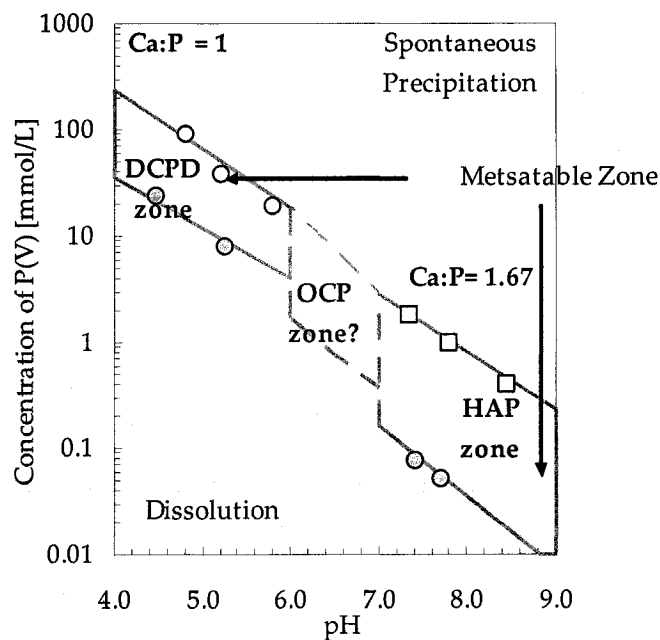


Figure 5.2. Generalised precipitation diagram for the synthesis of calcium phosphate phases. DCPD: $\text{CaHPO}_4 \cdot 2\text{H}_2\text{O}$; OCP: $\text{Ca}_8(\text{HPO}_4)_2(\text{PO}_4)_4 \cdot 5\text{H}_2\text{O}$; and HAP: $\text{Ca}_{10}(\text{PO}_4)_6(\text{OH})_2$.

5.2.3 Crystallisation of dicalcium phosphate dihydrate

The variation of calcium and phosphorus concentration in solution during homogeneous precipitation of $\text{CaHPO}_4 \cdot 2\text{H}_2\text{O}$ is plotted in Figure 5.3(a). It can be seen that the precipitation rate is reasonably high at the very beginning of the test with the reaction reaching apparent equilibrium after 30 min. The attainment of equilibrium was confirmed by making thermodynamic calculations using PHREEQC [7] and the thermodynamic data listed in Table 5.1. Compare $[\text{Ca(II)}]_{\text{actual}} = 8.68 \text{ mmol/L}$ (after 30 min) to $[\text{Ca(II)}]_{\text{eq}} = 8.73 \text{ mmol/L}$ obtained from PHREEQC. Moreover, calcium and phosphorus precipitation progressed at equivalent rates confirming the stoichiometry of the reaction (i.e. $\text{Ca:P} = 1$).

Figure 5.3(b) shows the precipitation kinetics of a typical test ran within the determined metastable zone in the presence of seed and at constant pH. Both the variation of Ca(II) and P(V) concentration is plotted. It can be seen that only ~65% of the Ca and P were removed in 2 h, moreover, the system did not reach equilibrium during the course of the

experiment: $[\text{Ca(II)}](t=2 \text{ h}) = 13.6 \text{ mmol/L}$ vs. $[\text{Ca(II)}]_{\text{eq}} = 12.4 \text{ mmol/L}$ (calculated with the aid of PHREEQC). The discrepancy can be explained by the fact that for homogeneous nucleation the initial saturation ratio (S) was very high (calculated at 77.8) but it was only 7.9 in seed-assisted precipitation. S was calculated with the aid of PHREEQC as the ratio of the initial ion activity product ($IAP = a(\text{Ca}^{2+}) \cdot a(\text{HPO}_4^{2-})$) to the solubility product of dicalcium phosphate dihydrate.

Table 5.1. Equilibria and constants considered in the present PHREEQC study

Reaction	Log K	Reference
$\text{H}_3\text{PO}_4 \leftrightarrow \text{H}_2\text{PO}_4^- + \text{H}^+$	-2.15	[8]
$\text{H}_2\text{PO}_4^- \leftrightarrow \text{HPO}_4^{2-} + \text{H}^+$	-7.20	[8]
$\text{HPO}_4^{2-} \leftrightarrow \text{PO}_4^{3-} + \text{H}^+$	-12.35	[8]
$\text{Ca}^{2+} + \text{H}_2\text{PO}_4^- \leftrightarrow \text{CaH}_2\text{PO}_4^+$	0.93	[27]
$\text{Ca}^{2+} + \text{HPO}_4^{2-} \leftrightarrow \text{CaHPO}_4(\text{aq})$	2.42	[27]
$\text{Ca}^{2+} + \text{PO}_4^{3-} \leftrightarrow \text{CaPO}_4^-$	6.46	[27]
$\text{Ca}^{2+} + \text{OH}^- \leftrightarrow \text{CaOH}^+$	1.30	[27]
$\text{CO}_2(\text{g}) \leftrightarrow \text{CO}_2(\text{aq})$	-1.468	[9]
$\text{CO}_3^{2-} + 2 \text{H}^+ \leftrightarrow \text{CO}_2(\text{aq}) + \text{H}_2\text{O}$	16.681	[9]
$\text{CO}_3^{2-} + \text{H}^+ \leftrightarrow \text{HCO}_3^-$	10.329	[9]
$\text{Ca}^{2+} + \text{HCO}_3^- \leftrightarrow \text{CaHCO}_3^+$	1.106	[9]
$\text{Ca}^{2+} + \text{CO}_3^{2-} \leftrightarrow \text{CaCO}_3(\text{aq})$	3.224	[9]
$\text{CaHPO}_4 \cdot 2\text{H}_2\text{O} \leftrightarrow \text{Ca}^{2+} + \text{HPO}_4^{2-} + 2 \text{H}_2\text{O}$	-6.59	[24]
$\beta\text{-Ca}_3(\text{PO}_4)_2 \leftrightarrow 3 \text{Ca}^{2+} + 2 \text{PO}_4^{3-}$	-28.92	[25]
$\text{Ca}_4\text{H}(\text{PO}_4)_3 \cdot 2.5\text{H}_2\text{O} \leftrightarrow 4 \text{Ca}^{2+} + \text{H}^+ + 3 \text{PO}_4^{3-} + 2.5 \text{H}_2\text{O}$	-48.40 @ 23.5 °C	[27]
$\text{Ca}_5(\text{PO}_4)_3\text{OH} \leftrightarrow 5 \text{Ca}^{2+} + 3 \text{PO}_4^{3-} + \text{OH}^-$	-58.52	[26]

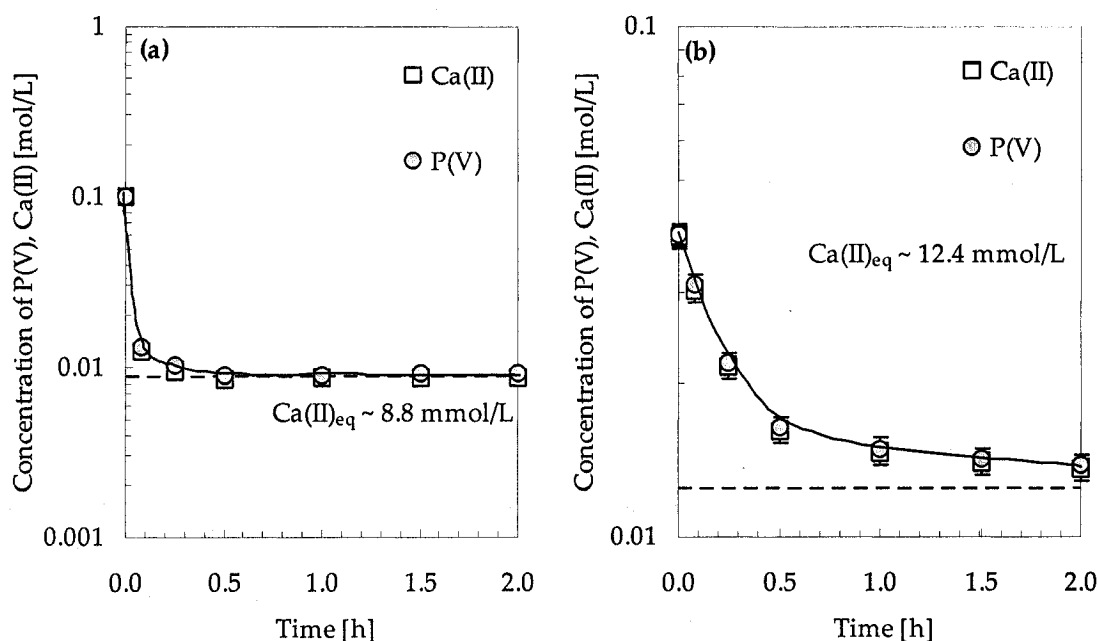


Figure 5.3. One-stage dicalcium phosphate dihydrate crystallisation. (a) Homogeneous precipitation (precipitation pH 5.4); (b) Seed-assisted precipitation using homogeneously produced seed (precipitation pH 5.0 and seed concentration, 10 [g/L]); NaOH as base.

5.2.4 Crystallisation of calcium-deficient hydroxyapatite

Homogeneous precipitation: Figure 5.4 shows the precipitation of hydroxyapatite via the application of the well-known LaMer diagram [10,11], along with the variation of the calcium to phosphorus molar ratio during the course of precipitation. It can be seen that the crystallisation of hydroxyapatite can be divided in four well-defined stages.

In stage I the supersaturation, as was mentioned above, was built up by slow addition of $CaCl_2$ (50 mmol/L) and NaH_2PO_4 (30 mmol/L) solutions, whereas the pH is kept constant at 7.6 by addition of NaOH (100 mmol/L). During this period no precipitation took place and no change in the Ca:P molar ratio was observed. When the phosphorus concentration reached a critical phosphorus concentration level, $C_{cr,homo} \sim 1.22 \text{ mmol/L}$ (see Figure 5.1(b)) homogeneous nucleation occurred (stage II). Following homogeneous nucleation bulk precipitation occurs in stage III.

At the beginning of stage III (this period is associated with growth, i.e., deposition on the

homogeneously nucleated material) a sharp positive change in the slope of the Ca(II) to P(V) molar ratio in solution was detected (Figure 5.4(right)) which suggests the formation of a calcium phosphate material with calcium to phosphate molar ratio less than 1.67. This change on Ca:P molar ratio may be associated with the formation of a metastable calcium phosphate phase (as was the amorphous phase reported to form via spontaneous precipitation of hydroxyapatite with a Ca to P molar ratio of 1.45 ± 0.05 [12]). This is rather awkward, as the formation of a metastable phase is known to be favoured [13] when homogeneous nucleation dominates (i.e. stage II) and not when precipitation proceeds via surface nucleation and growth (stage III).

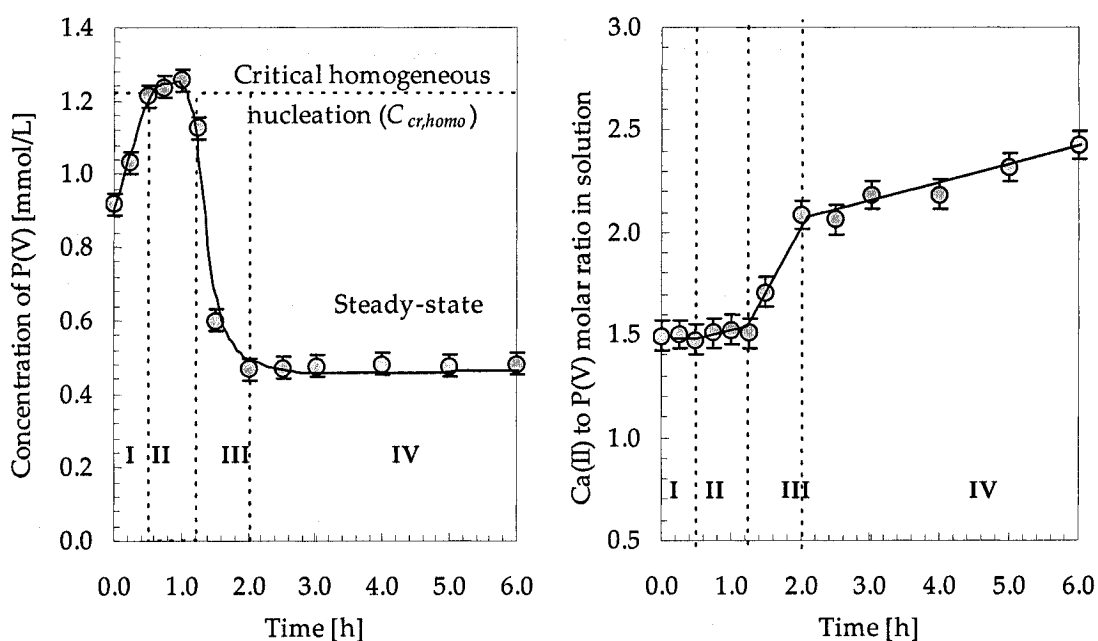


Figure 5.4. Homogeneous precipitation (spontaneous) of hydroxyapatite: LaMer diagram (left); evolution of calcium to phosphorus molar ratio (right).

Finally, it can be seen from Figure 5.4(left) that a steady state is reached after ~2.5 h (stage IV) meaning that the addition rate of phosphate matches the rate of phosphate precipitation. The precipitated calcium phosphate appears to be calcium-deficient hydroxyapatite judging from the increase of the Ca:P molar ratio in solution during this stage (the precipitation of stoichiometric hydroxyapatite would produce no change in the calcium to phosphorus molar ratio). Chemical analysis of the final precipitate by

digestion yielded indeed a ratio Ca to P of 1.48 ± 0.06 confirming the formation of a calcium-deficient hydroxyapatite. More on the characterisation of the produced material is reported in Section 5.2.5.

Seed-assisted precipitation: The semi-batch precipitation of (Ca-deficient) hydroxyapatite using two different reagent addition rates are shown in Figure 5.5 and Figure 5.6 for addition rates of 40 mL/h and 80 mL/h respectively. It can be seen from these Figures that during the course of the experiments the critical homogeneous nucleation was not reached for both addition rates.

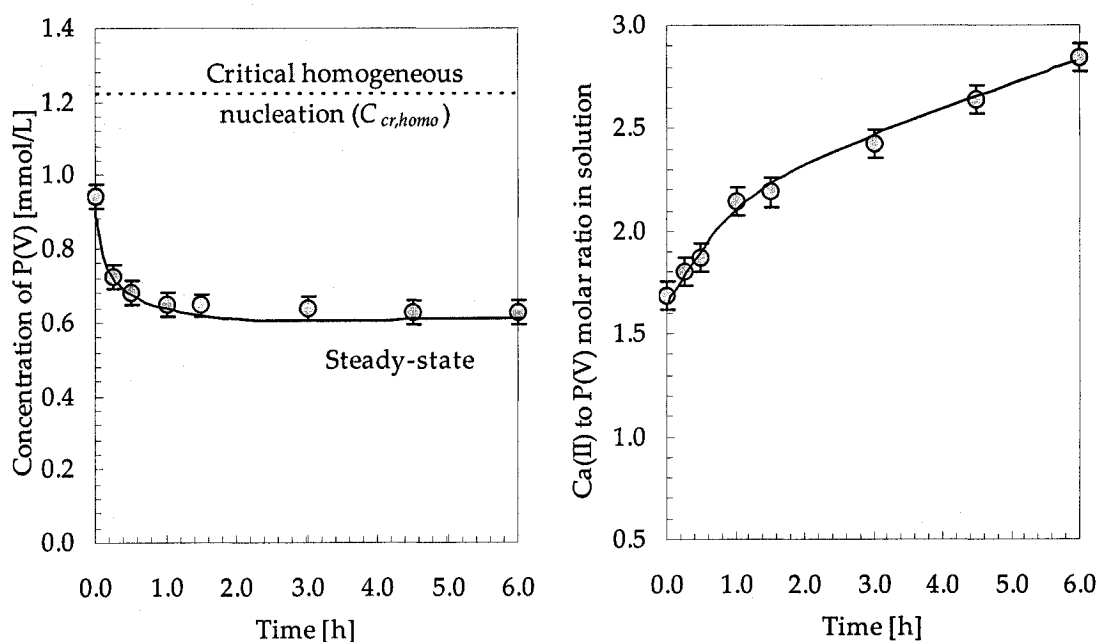


Figure 5.5. Semi-batch seed-assisted precipitation of (calcium-deficient) hydroxyapatite. Concentration of phosphorus in solution (left); evolution of calcium to phosphorus molar ratio (right). Reagent solution addition rate 40 mL/h.

However, the calcium to phosphorus molar ratio in solution increased with time, due to the apparent formation of calcium-deficient instead of stoichiometric hydroxyapatite. This was once more confirmed by digestion of ~ 100 mg of precipitate in 100 mL of HNO_3 solutions (~ 0.1 mol/L). This analysis yielded ratios Ca to P of 1.58 ± 0.07 and 1.50 ± 0.06 for the low and the high addition rates respectively. This calcium deficiency appears to be due to the low pH of the synthesis solutions adopted in this work. According to

Nancollas et al. [14], seeded crystallisation of calcium-deficient hydroxyapatite yields calcium to phosphate molar ratio ranging from 1.49 to 1.65 as the pH changes from 6.0 to 9.0.

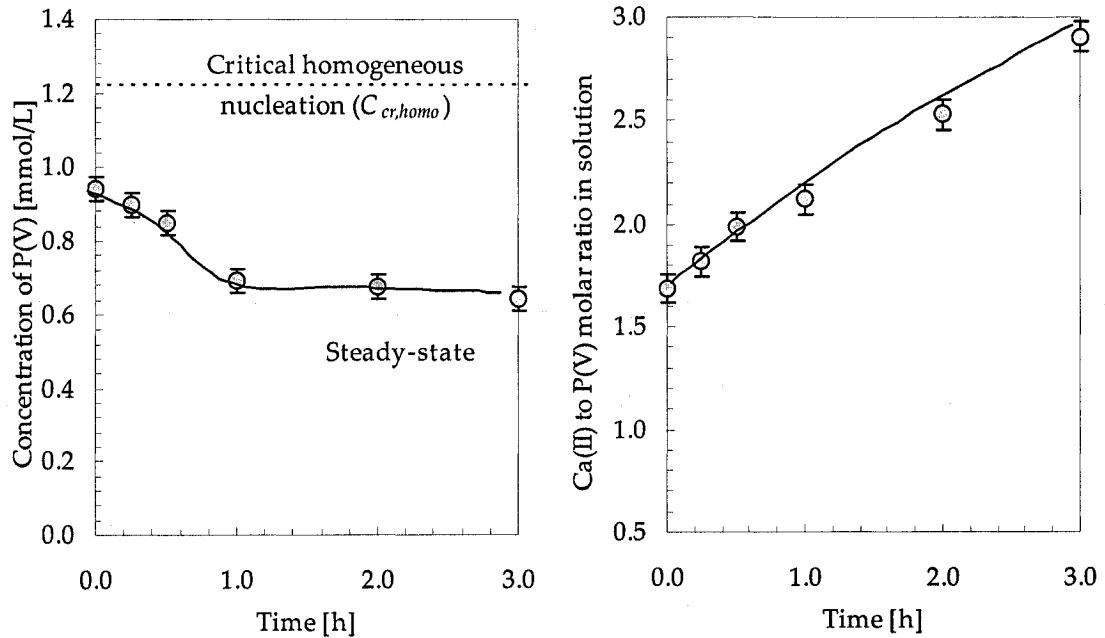


Figure 5.6. Semi-batch seed-assisted precipitation of (calcium-deficient) hydroxyapatite. Concentration of phosphorus in solution (left); evolution of calcium to phosphorus molar ratio (right). Reagent solution addition rate 80 mL/h.

5.2.5 Product characterisation

Dicalcium phosphate dihydrate: Figure 5.7 shows SEM images of the produced dicalcium phosphate dihydrate (brushite) at magnification of 500. It can be seen that the solids produced by homogeneous nucleation and seed-assisted precipitation are similar in shape, with the latter one being generally larger than the former one ($\sim 80 \mu\text{m}$ vs. $\sim 40 \mu\text{m}$). Crystals have the characteristic plate-like morphology of synthetic brushite ($\text{CaHPO}_4 \cdot 2\text{H}_2\text{O}$) produced in aqueous media [1].

XRD analysis confirmed the presence of $\text{CaHPO}_4 \cdot 2\text{H}_2\text{O}$ (brushite) as the dominant phase, with high degree of crystallinity (Figure 5.8). The stoichiometry of the precipitate was confirmed after digestion and analysis to be Ca to P molar ratio equal to 1.02 ± 0.08 . No

sodium nor chloride were detected.

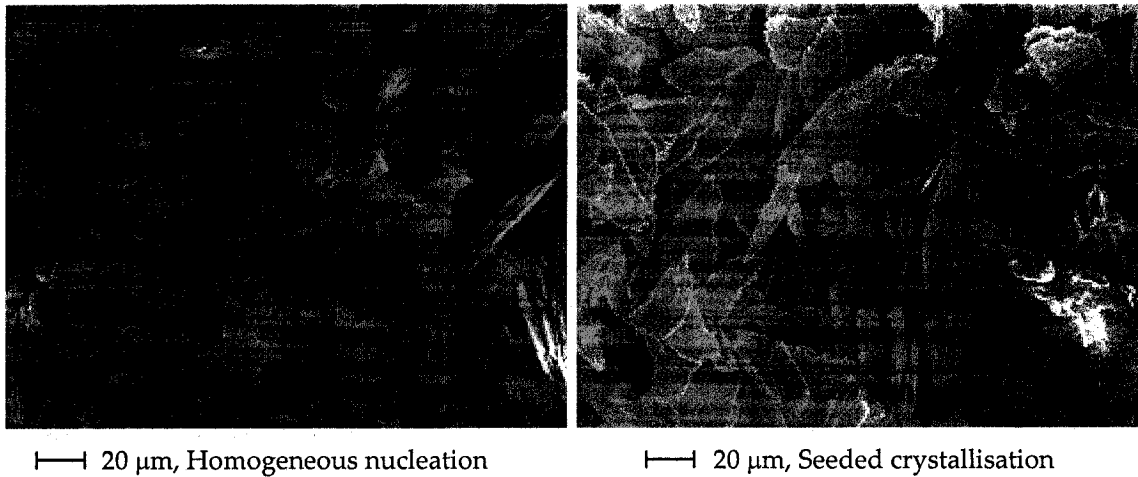


Figure 5.7. Scanning electron micrographs of dicalcium phosphate dihydrate produced by homogeneous precipitation (left) and seed-assisted precipitation (right).

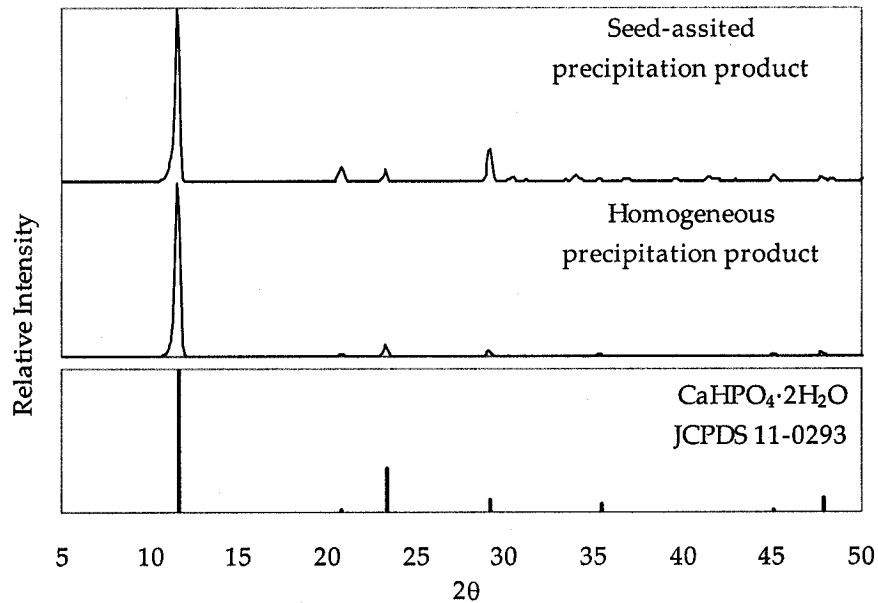


Figure 5.8. XRD pattern of products obtained by homogeneous precipitation and seed-assisted precipitation compared to $\text{CaHPO}_4 \cdot 2\text{H}_2\text{O}$ (brushite).

Calcium-deficient hydroxyapatite: Figure 5.9 and Figure 5.10 show SEM images of the precipitate produced by homogeneous and seed-assisted precipitation respectively at different magnifications. It appears from this examination that the homogeneously produced material consisted of irregularly shaped agglomerates of the order of 5-15 μm made up of primary crystallites smaller than 1 μm .

It can be seen that the product obtained by seed-assisted precipitation (Figure 5.10) was undoubtedly coarser than the solids produced by homogeneous precipitation. Moreover, the SEM photographs show that the crystals have grown through a combination of surface nucleation and agglomeration.

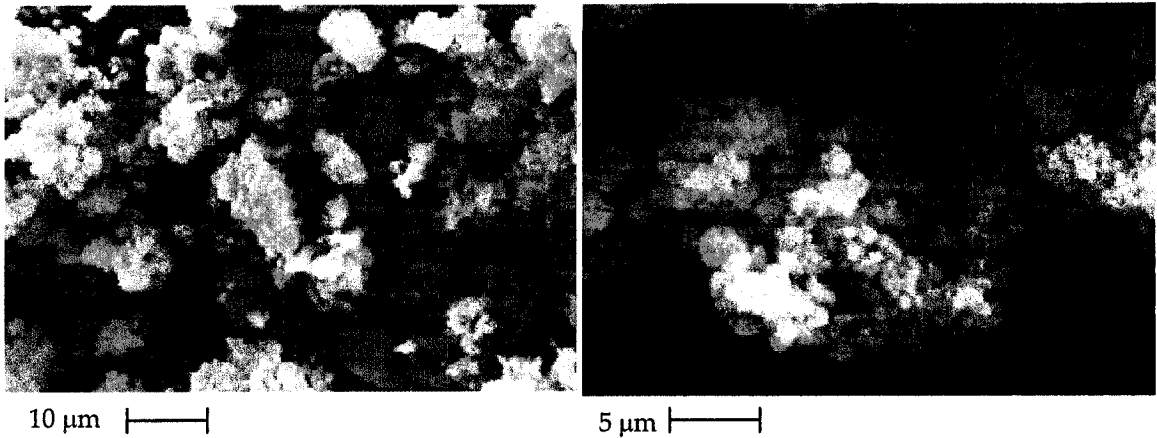


Figure 5.9. Scanning electron micrographs of hydroxyapatite produced by homogeneous precipitation.

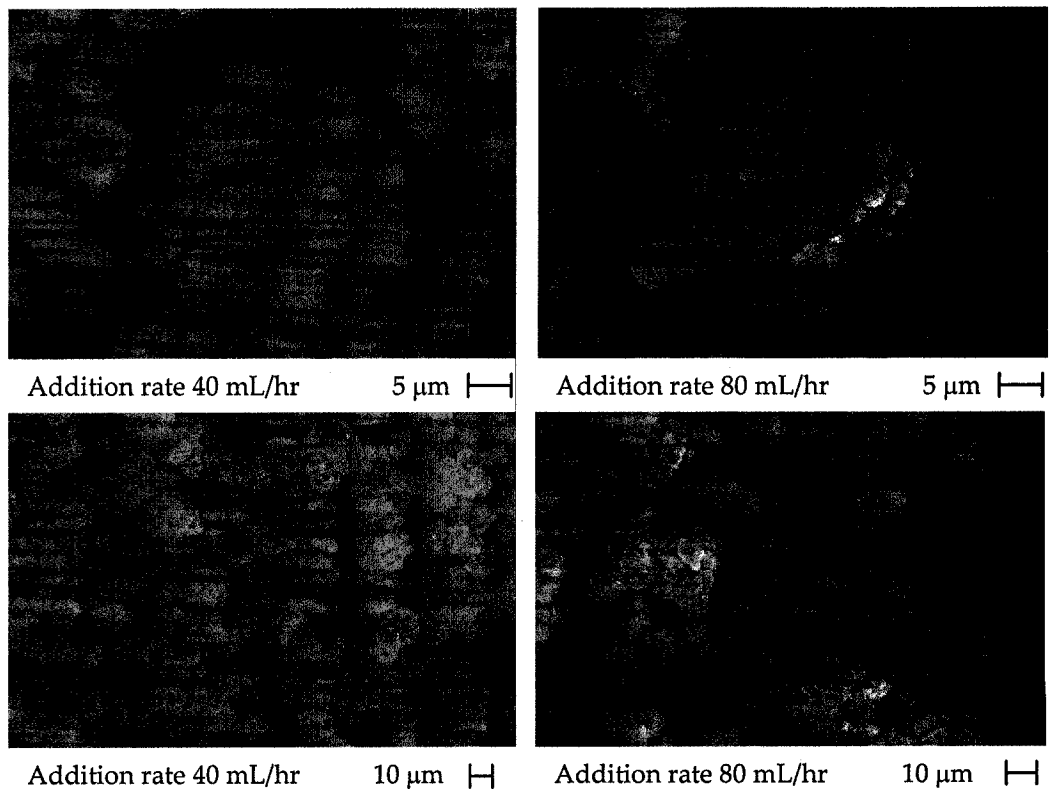


Figure 5.10. Scanning electron micrographs of hydroxyapatite produced by seed-assisted precipitation.

The XRD patterns of synthesised (Calcium-deficient) hydroxyapatites are shown in Figure 5.11. They are in good agreement with the pattern for hydroxyapatite with no apparent evidence of the presence of other calcium phosphates. The broad peaks are an indication of that synthesised material is of nano-crystalline nature [15].

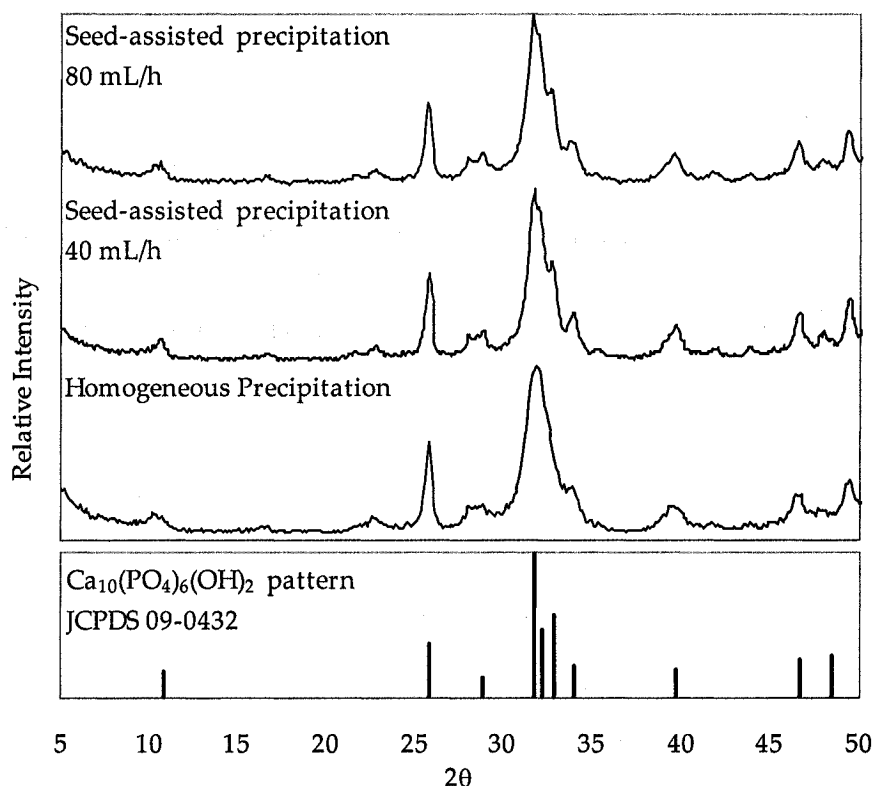


Figure 5.11. XRD patterns of hydroxyapatites produced with different precipitation strategies compared to $\text{Ca}_{10}(\text{PO}_4)_6(\text{OH})_2$ (hydroxyapatite).

The average crystallite size of the powder was estimated using the Scherrer equation [16]:

$$t = \frac{K\lambda}{B \cdot \cos \theta} \quad (5.1)$$

where t is the average crystallite size (nm); K is the shape factor ($K = 0.9$); λ is the wavelength of the X-rays ($\lambda = 0.15406$ nm for Cu-K α radiation); B is the full width at half maximum (rad) and θ is the Bragg's diffraction angle.

The values of t were calculated from the peak corresponding to (002) Miller plane family

with $2\theta = 25.80^\circ$; this diffraction peak was chosen since it is isolated from the other ones. This calculation yielded 19.0 nm for the homogeneously nucleated material and 20.4 and 17.4 nm for the product obtained by seed-assisted precipitation at the low and the high addition rates respectively. In comparison, the crystallite size for stoichiometric hydroxyapatite has been reported to be ~ 80 nm [17].

From the data of the X-ray diffraction pattern the crystallographic characteristics of the crystals can be determined. For the hexagonal $P6_3/m$ crystallographic system, in which hydroxyapatite belongs to, the relationship between the distance, d , of two adjacent planes and the (hkl) Miller indices of the reflection planes, is given by the following equation [18]:

$$\frac{1}{d^2} = \frac{4}{3} \left(\frac{h^2 + hk + l^2}{a^2} \right) + \frac{l^2}{c^2} \quad (5.2)$$

The calculated crystallographic characteristics of the c axis obtained by the (002) Miller index at $2\theta = 25.88^\circ$ along the a and b axes obtained by the (310) Miller index at $2\theta = 39.82^\circ$ are reported in Table 5.2.

Table 5.2. Lattice parameters and stoichiometry of produced solids

Sample	a=b (nm)	c (nm)	Ca:P	Na(%wt.)
Hydroxyapatite (JCPDS 09-0432)	94.18	68.84	1.67	-
Ca-deficient hydroxyapatite [19]	94.38	68.66	1.40-1.67	-
Homogeneous precipitation	95.1	69.0	1.48 \pm 0.06	0.11%
Seed-assisted precipitation (40 mL/h)	94.5	69.0	1.58 \pm 0.07	0.05%
Seed-assisted precipitation (80 mL/h)	94.7	69.3	1.50 \pm 0.06	0.08%

As is seen in Table 5.2, the values are similar to the reported values of calcium-deficient apatites [19]. The increase in a axis value as compared to the stoichiometric hydroxyapatite may be due to lattice substitution of HPO_4^{2-} ions [16]. The presence of HPO_4^{2-} ions was indeed confirmed by IR analysis (as discussed in the next paragraph). A

small amount of Na was incorporated (not removable by extensive washing) into the crystal structure of the products most likely via substitution for calcium.

The FT-IR spectra of produced Ca-deficient hydroxyapatites are shown in Figure 5.12. The presence of HPO_4^{2-} is associated with the bands at 1094, 961 and 868 cm^{-1} [18]. The solids show the characteristic bands of OH^- ions at 3572 cm^{-1} and phosphate ions at 1032, 602, and 561 cm^{-1} in hydroxyapatite [18].

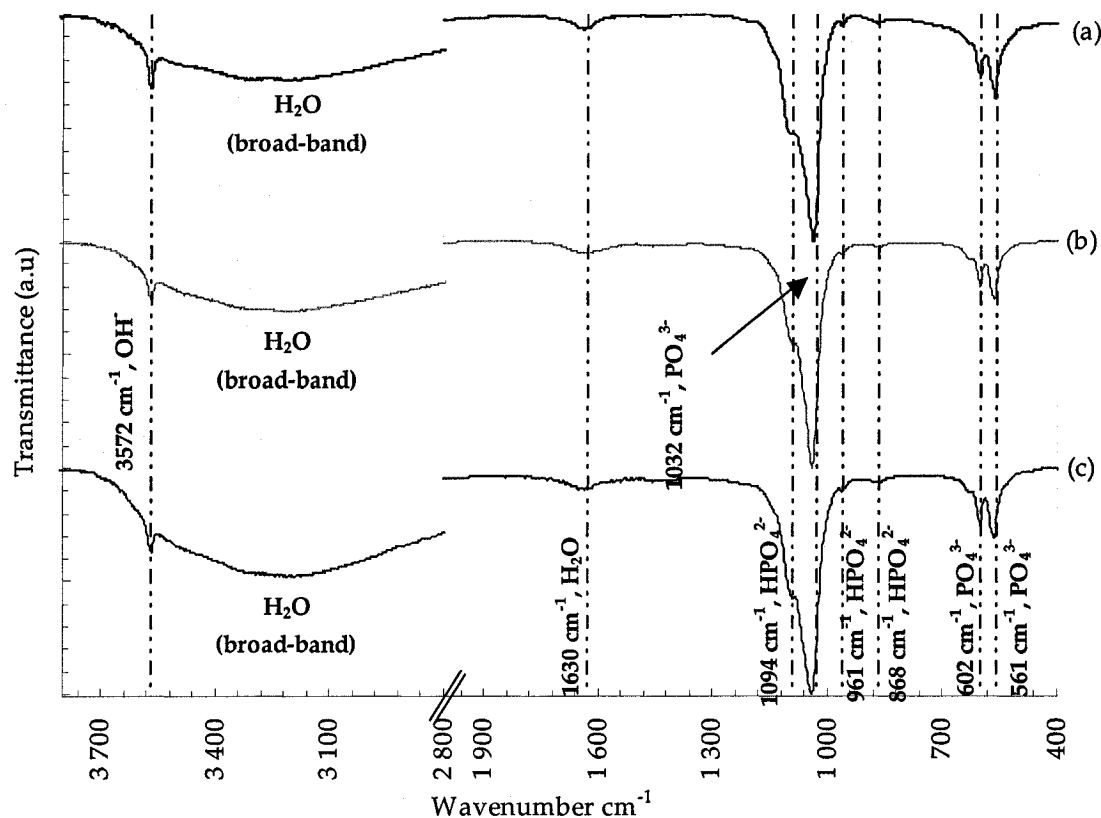


Figure 5.12. IR spectra of calcium-deficient hydroxyapatites. (a) homogeneous precipitation product; (b) seed-assisted precipitation product (40 mL/h); (c) seed-assisted precipitation product (80 mL/h).

The characteristic peaks of dicalcium phosphate at 3539, 3487, 3280, and 3155 cm^{-1} [20]) or octacalcium phosphate (1270, and 917 cm^{-1} [20]) were not found in the spectra. Moreover, water was found in the precipitates as adsorbed water molecules (broad-band from 3600 to 2800 and at 1630 cm^{-1} , [18]). No significant evidence of CO_3^{2-} was present in the precipitate (small peaks at 1452-1455 and 1415 cm^{-1} [18]).

5.3 Stability

In this section, the dissolution and stability of the two calcium phosphate materials, the synthesis of which was reported in the previous section, were investigated with the purpose of selecting the more appropriate one as candidate for the encapsulation of scorodite particles. In addition, the work reported here sought to evaluate the experimental results with PHREEQC [7] and to determine the solubility products of the two synthetic minerals in order to compare them with previously reported values.

5.3.1 Methods

Stability measurements: The $\text{CaHPO}_4 \cdot 2\text{H}_2\text{O}$ solids were subjected to a special leaching procedure before actual solubility measurements were made in order to remove any soluble non-crystalline material that could have distorted the measurements. This leaching procedure involved stirring 30 g of solids in 500 mL of HNO_3 -containing at pH 5.0 solutions for 5 periods of 24 h each. At the end of each 24 h period, the slurry was filtered and the solids washed by repulping 3 times with 500 mL of deionised hot water (60 °C) before proceeding with the subsequent 24 h leaching period. For the stability tests, 100 mL of deionised water was placed in 150 mL Erlenmeyer flasks, stoppered and agitated with magnetic stirrer. In each flask, 2.0 g of solids were added followed by pH adjustment. The pH of the slurry was measured and adjusted initially to defined pH values using HNO_3 solution (4.5, 5.5, and 6.7). The pH was not adjusted during the dissolution tests.

For hydroxyapatite, this leaching procedure was found inadequate, since the first solubility experiments performed yielded calcium to phosphate molar ratio in solution ranging from 10 to 0.05 for pH values from 5 to 8. This behaviour was attributed to the presence of a surface layer with a chemical composition different from that of the bulk.

Bell et al. [21] reported similar behaviour during the dissolution of stoichiometric hydroxyapatite with solution pH between 4.90 and 9.94. The authors reported that

freshly prepared hydroxyapatite possesses a surface layer of extremely high solubility, however, after removal of this surface layer, the behaviour of hydroxyapatite was reproducible. This surface layer of one atom-layer thickness or less was believed to have formed during the preparation of the solid [22].

The presence of a small amount of a highly soluble material can lead to completely erroneous solubility results. In order to remove this material, Bell et al. [21] suggested that each leaching procedure has to be conducted at the same pH values with pH in which the actual stability test to be carried out. In view of this behaviour a modified leaching procedure was used as described in the next paragraph.

The first step was performed at pH 7 for 24 h using a solid/liquid ratio of 2.0 g /100 mL calcium-deficient hydroxyapatite solids in pure water. The pH was adjusted to 7.0 with a HNO₃. The mixture was stirred with a magnetic stirrer bar at a constant speed. The pH was frequently adjusted with HNO₃ solution. After 24 h, a 10 mL sample was taken with a syringe and filtered on 0.25 µm pore size membrane (Corning). The solution was acidified and analysed for phosphorus and calcium concentration. The slurry was filtered on a 0.1 µm pore size membrane (Millipore) and the solid was washed with pure water using 3X the volume of filtrate.

After this first "cleaning" step at pH 7, the solids underwent several 24 h equilibration steps at the pH adjusted initially to 5.0, 6.0, 7.0, 8.0 and 9.0. At the end of each 24 h period, the slurry was filtered and the solids washed by repulping 3 times with 100 mL of deionised hot water (60 °C) before proceeding with the subsequent 24 h leaching period. The actual stability test was started when molar ratio Ca:P for the step "k" was similar ($\pm 10\%$) to the one in the step "k-1". If the latter were the case, the slurry was not filtered and the equilibration was allowed to continue for 30 d. The pH was not adjusted during the dissolution test.

At predetermined times, samples were taken, filtered through a membrane filter (Corning 0.25 µm), diluted with HNO₃ solution ($w_{\text{HNO}_3} \sim 5\%$) and analysed. The pH was

measured using a Ross™ combination electrode with a reported accuracy of ± 0.02 pH units ($\pm 4.5\%$ in H^+ activities). The pH electrode was standardised versus buffer pH solutions 4.0, 7.0 and 10.0. All experiments were carried out in duplicate runs. Stability tests were performed at room temperature (22 °C).

Characterisation and analysis: solutions and solids were characterised using the techniques described in 5.2.1.

5.3.2 Thermodynamic considerations

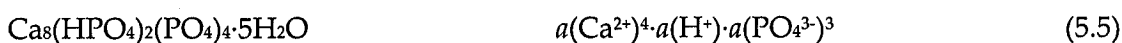
Under proper physical and chemical environment, different kinds of calcium phosphate phases may form, depending on the solution supersaturation. They are, in the order of decreasing solubility: Amorphous calcium phosphate (ACP), dicalcium phosphate dihydrate ($CaHPO_4 \cdot 2H_2O$), anhydrous calcium phosphate ($CaHPO_4$), octacalcium phosphate ($Ca_8(HPO_4)_2(PO_4)_4 \cdot 5H_2O$), β -tricalcium phosphate (β - $Ca_3(PO_4)_2$), calcium-deficient hydroxyapatite ($Ca_{10-x}(HPO_4)_x(PO_4)_{6-x}(OH)_{2-x}$, $x < 2$), and hydroxyapatite ($Ca_{10}(PO_4)_3(OH)_2$) [23].

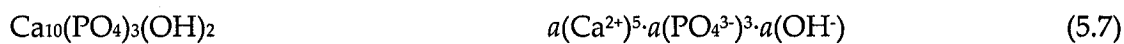
The saturation ratio (S) of a system with respect to a given calcium phosphate phase is defined as (see Eq. (2.1) in section 2.31 of Chapter 2):

$$S = \left(\frac{a(A)^\alpha \cdot a(B)^\beta}{a(A)_{eq}^\alpha \cdot a(B)_{eq}^\beta} \right) = \left(\frac{IAP}{K_{sp}} \right) \quad (5.3)$$

Where subscript eq refers to equilibrium conditions, a denotes the activity of the respective ion. IAP is the ion activity product in the supersaturated solution and K_{sp} is the solubility product.

In this work, the solubility product and the ion activity product for the main calcium phosphate salts of interest are calculated according to equations (5.4) to (5.7):





Moreover, a saturation index (SI) is defined as $SI = \text{Log } S$ to facilitate further discussion. For the calculation of the ion activity product of calcium phosphate salts the aqueous speciation equilibria and thermodynamic data reported by Brown and co-workers [24,25,26,27] were used. The experiments were carried out in air; therefore, the presence of CO_2 was included in the modelling with PHREEQC. Thermodynamic data used in this study are given in Table 5.1.

The activity coefficients were calculated according to Davies equation [28].

$$\text{Log } \gamma_k = -Az_k^2 \left(\frac{\sqrt{I}}{1 + \sqrt{I}} - 0.3I \right) \quad (5.8)$$

where γ_k is the activity coefficient of ion k , z_k its valency, I the ionic strength and A the Debye–Hückel constant. The calculated values for saturation help to understand and interpret the dissolution mechanism of these calcium phosphate salts.

5.3.3 Experimental data

Dissolution of dicalcium phosphate dihydrate: The variation of the solution concentration, in terms of Ca(II) and P(V) along with pH, as a function of time for the experiments performed, is shown in Figure 5.13. It is observed that solutions reached equilibrium in less than 5 d, the stability tests were allowed to last longer in order to evaluate solid phase transformations. The final (after 20 d) Ca(II) and P(V) concentrations are plotted as a function of equilibrium pH in Figure 5.14. The data presented in Figure 5.14(left) indicate the dissolution process was congruent in nature, that is, no transition from dicalcium phosphate dihydrate to more stable calcium phosphate salts is evident. This is better seen if the data of Figure 5.14(left) are replotted as a final (i.e. equilibrium) Ca(II) to P(V) molar ratio versus pH (Figure 5.14(right)).

According to this figure, the molar ratio calcium to phosphorus in solution was around 1.0.

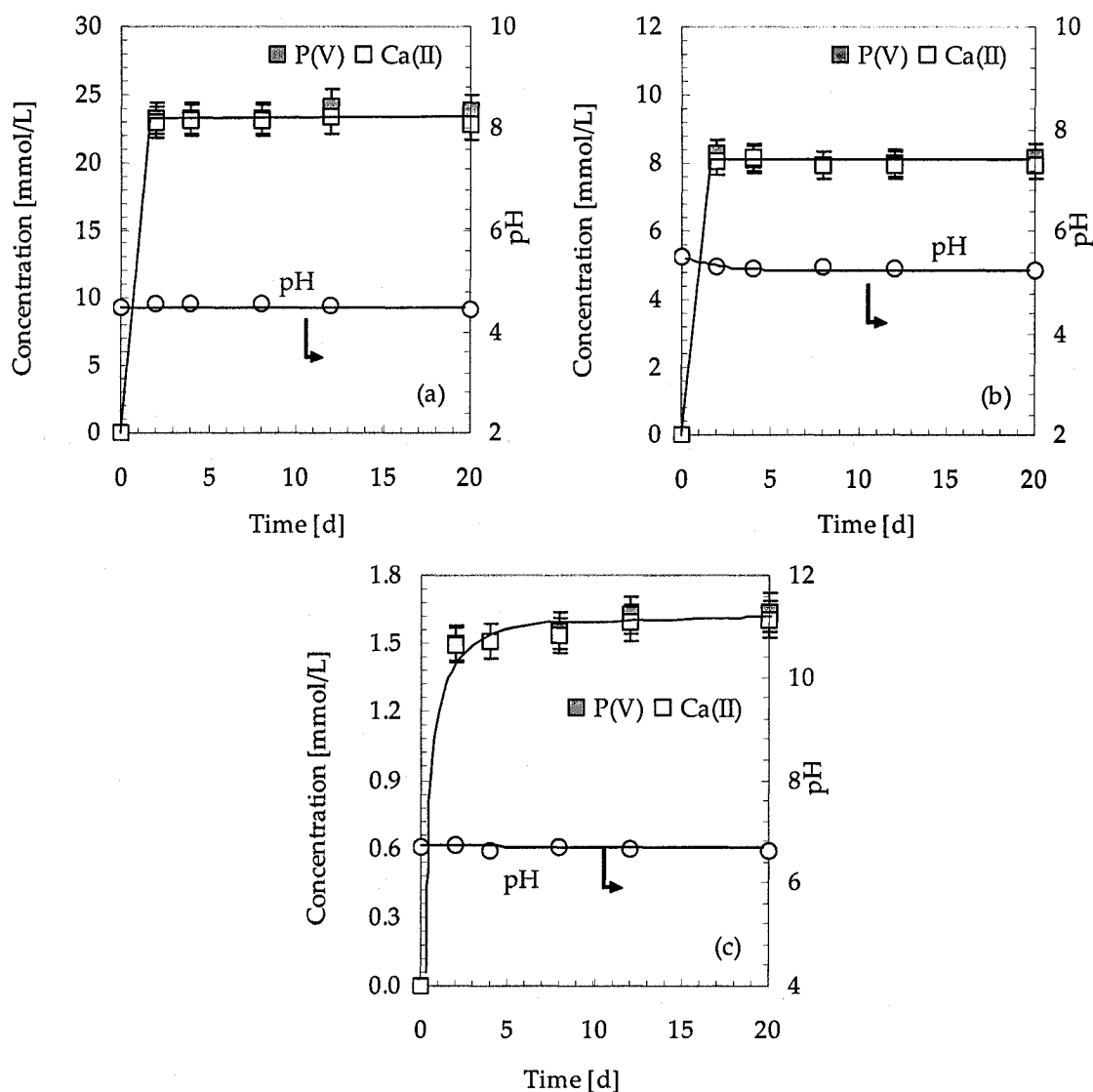


Figure 5.13. P(V) and Ca(II) concentrations and pH as a function of time at 22 °C. (a) initial pH of 4.5; (b) initial pH of 5.50 (c) initial pH of 6.70.

The equilibrated solids (after 20 d) were characterised by XRD in order to confirm the absence of hydrolysed products. The data are shown in Figure 5.15. The XRD analysis revealed the presence of dicalcium phosphate dihydrate as the sole phase. Transformation to octacalcium phosphate, β -tricalcium phosphate, or hydroxyapatite was not detected whatsoever.

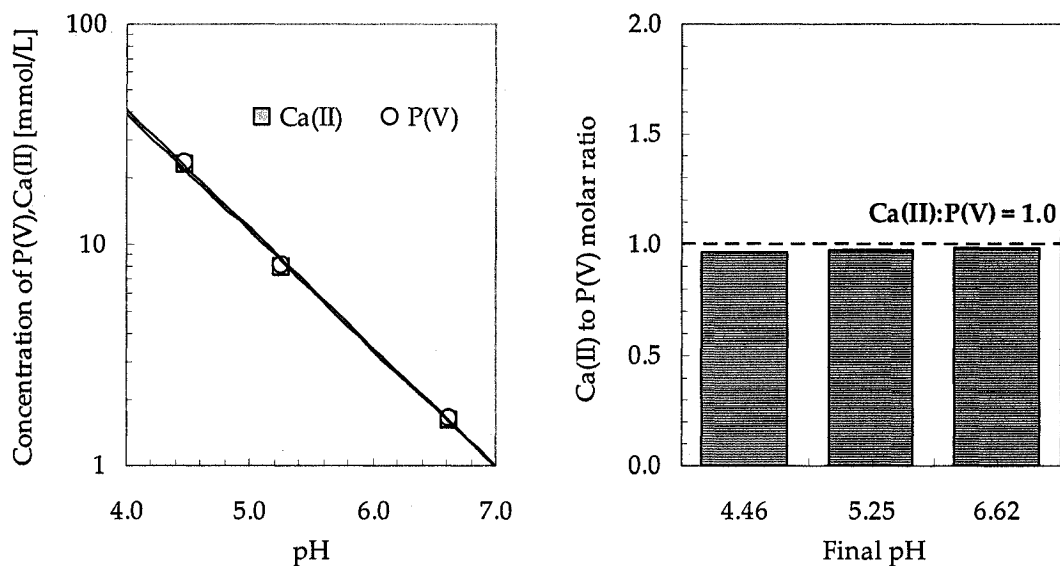


Figure 5.14. Experimental solubility determined for $\text{CaHPO}_4 \cdot 2\text{H}_2\text{O}$ at 22 °C. (equilibration time 20 d). Final concentrations of Ca(II) and P(V) as a function of pH (left). Calcium to Phosphorus molar ratio in solution after 20 d of dissolution (right).

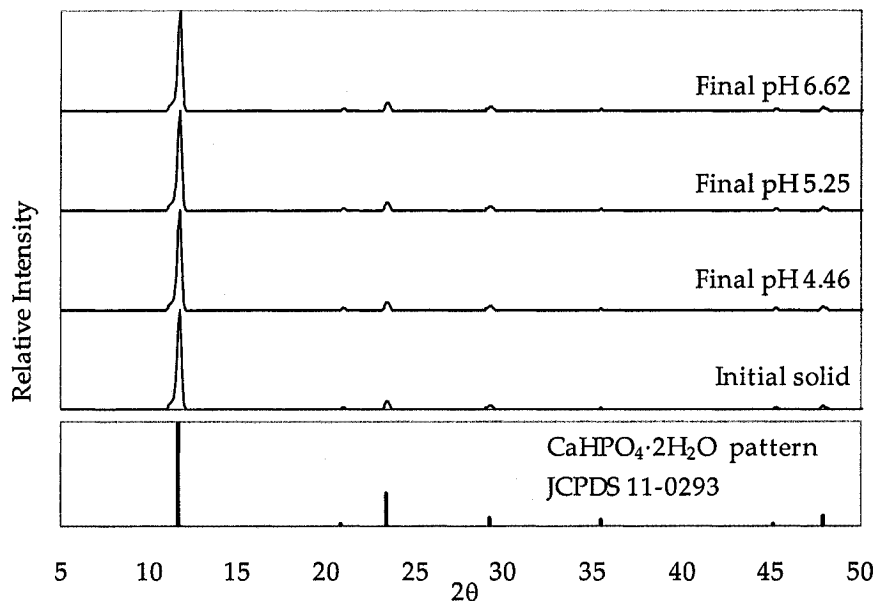


Figure 5.15. XRD pattern of solids before and after equilibration at various pH compared to $\text{CaHPO}_4 \cdot 2\text{H}_2\text{O}$.

Dissolution of calcium-deficient hydroxyapatite: The Ca:P molar ratio obtained from the repeated leaching of the solids prior to the stability test is shown in Figure 5.16. It can be seen that constant calcium to phosphorus molar ratio was obtained at the sixth

preparation step. A constant Ca:P molar ratio of ~ 1.58 was observed corresponding to the ratio of the original solids. The small variation is attributed to experimental error. For example, an experimental error of 5% in the measurement of Ca(II) and P(V) in solution would yield an error in Ca:P of 0.12 units, hence, any molar ratio ranging from 1.46 to 1.70 might be considered as congruent dissolution (this is the case of initial pH 5 to 8).

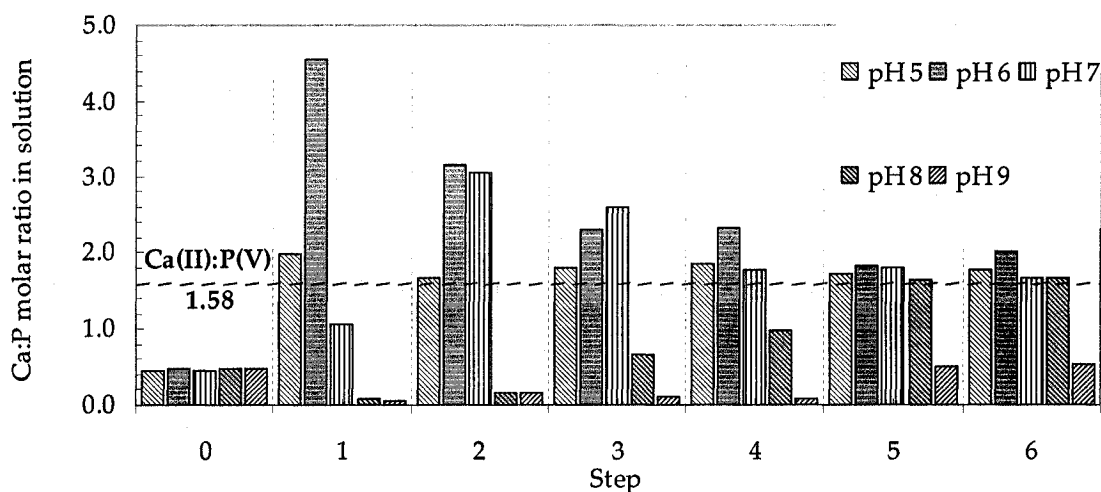


Figure 5.16. Ca(II) to P(V) molar ratio during solids preparation steps; (step 0 was performed at pH = 7.0).

The variation of the solution concentration, in terms of Ca(II) and P(V) along with pH, as a function of time for the experiments performed, are shown in Figure 5.17. It is observed that the calcium and phosphorus concentration reached equilibrium at around 10 d of dissolution, with the exception of the test with initial pH 9.0, which attained equilibrium after about 15 d of equilibration (Figure 5.17(e)).

The final (after 30 d) Ca(II) and P(V) concentrations and Ca:P in solution are plotted as a function of equilibrium pH in Figure 5.18 and Figure 5.19 respectively. The data presented in these figures reveal that the dissolution process is near congruent with a slight excess in calcium release for all pH values except for final pH 8.10 (corresponding to initial pH 9.0). In the latter case, the calcium to phosphorus molar ratio in solution is well below the stoichiometric value, so, revealing incongruent dissolution behaviour at $\text{pH} > 8$.

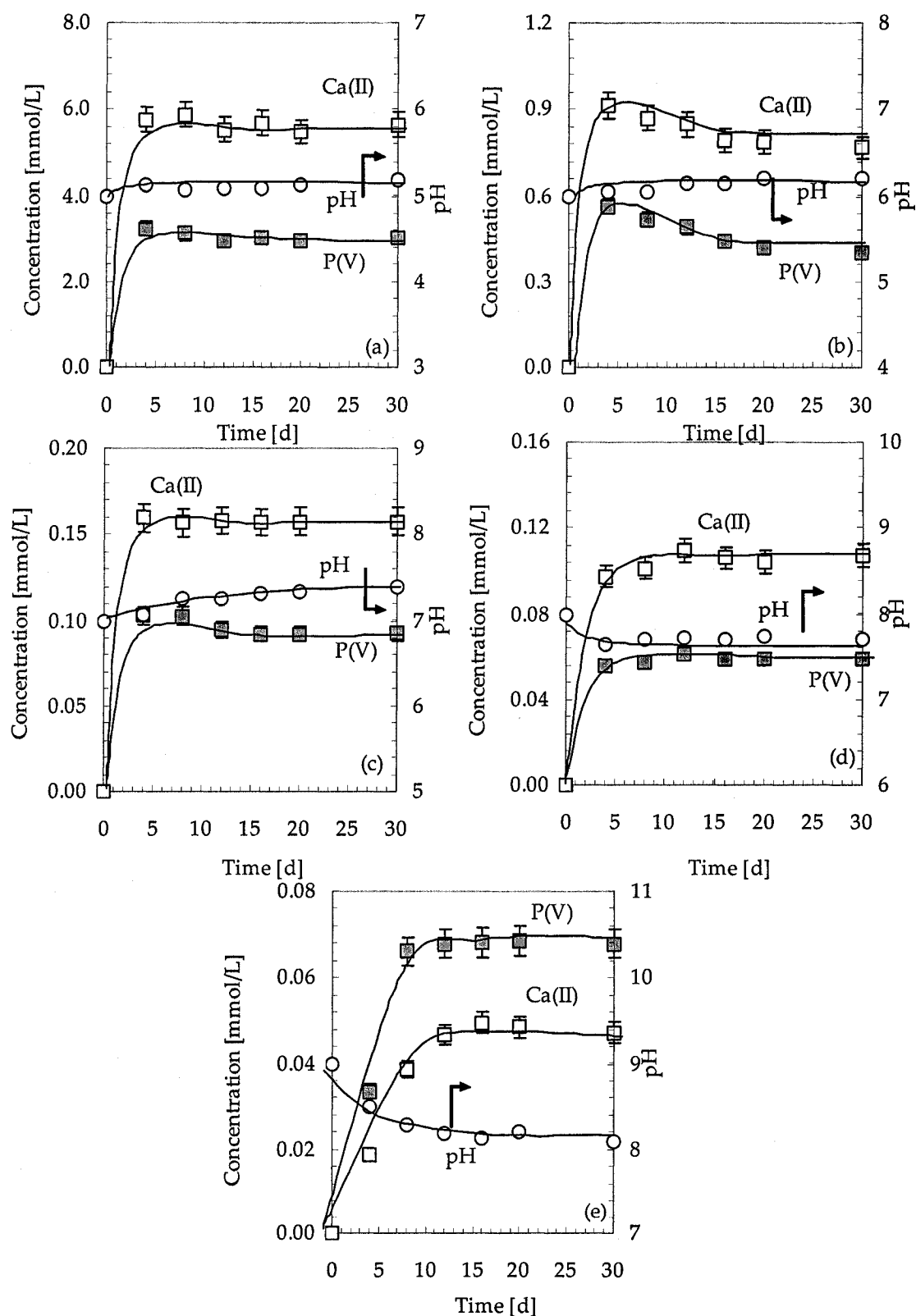


Figure 5.17. P(V) and Ca(II) concentrations and pH as a function of time at 22 °C. (a) initial pH of 5.0; (b) initial pH of 6.0; (c) initial pH of 7.0; (d) initial pH of 8.0; (e) initial pH of 9.0.

The lack of perfect congruent dissolution behaviour (i.e. Ca:P slightly above 1.58) has been reported by others as well for the case of hydroxyapatite. For example, the best cited studies that of McDowell et al. [26] reports a Ca:P molar ratio of up to 2.32 after 21 d of dissolution. This has been attributed to other phenomena taking place such as preferential adsorption of phosphate ions or a change on the surface layer of hydroxyapatite particles [29].

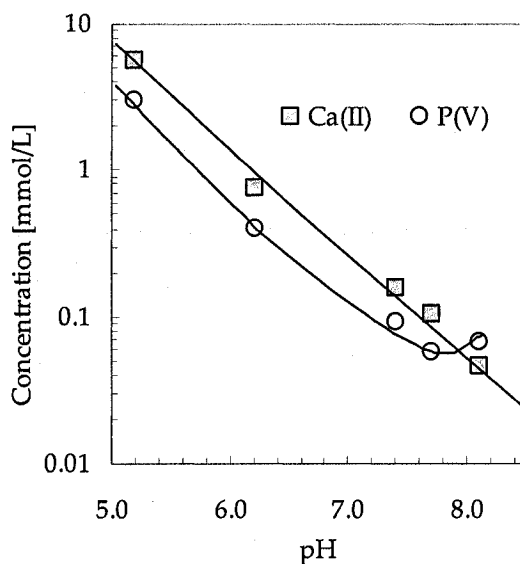


Figure 5.18. Experimental solubility determined for calcium-deficient hydroxyapatite at 22 °C (equilibration time 30 d).

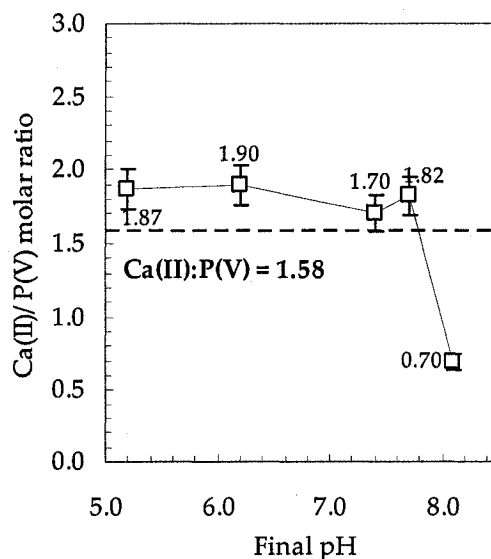


Figure 5.19. Calcium to phosphorus molar ratio in solution after 30 d of dissolution.

The XRD analysis of the equilibrated solids (after 30 d) revealed no-presence of another calcium phosphate phase (Figure 5.20) except the original calcium-deficient hydroxyapatite.

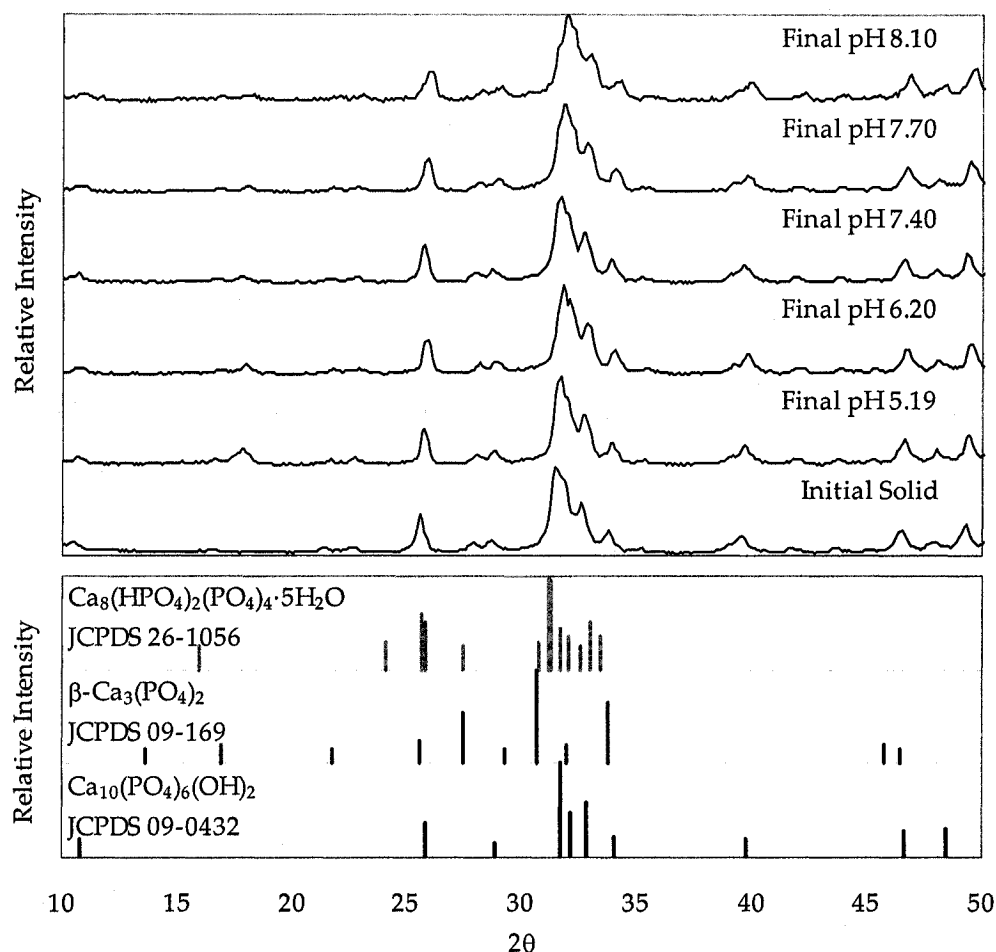


Figure 5.20. XRD pattern of solids before and after equilibrium at various pH compared to $\text{Ca}_8(\text{HPO}_4)_2(\text{PO}_4)_4 \cdot 5\text{H}_2\text{O}$; $\beta\text{-Ca}_3(\text{PO}_4)_2$ and $\text{Ca}_{10}(\text{PO}_4)_6(\text{OH})_2$ (hydroxyapatite).

5.3.4 Evaluation of the dissolution mechanism with PHREEQC

Dicalcium phosphate dihydrate: Using the variation of Ca(II) and P(V) concentration and pH during the dissolution of $\text{CaHPO}_4 \cdot 2\text{H}_2\text{O}$ along with the equilibrium and thermodynamic data listed in Table 5.1 the evolution of the ion activity product determined with the aid of PHREEQC was considered. The estimates are plotted in Figure 5.21. It can be seen that equilibrium was obtained rapidly as it was observed with

the precipitation tests (Section 5.2.3). Moreover, the constancy of the ion activity product means that no transformation to a more stable calcium phosphate salt occurs within the 20 d of dissolution period.

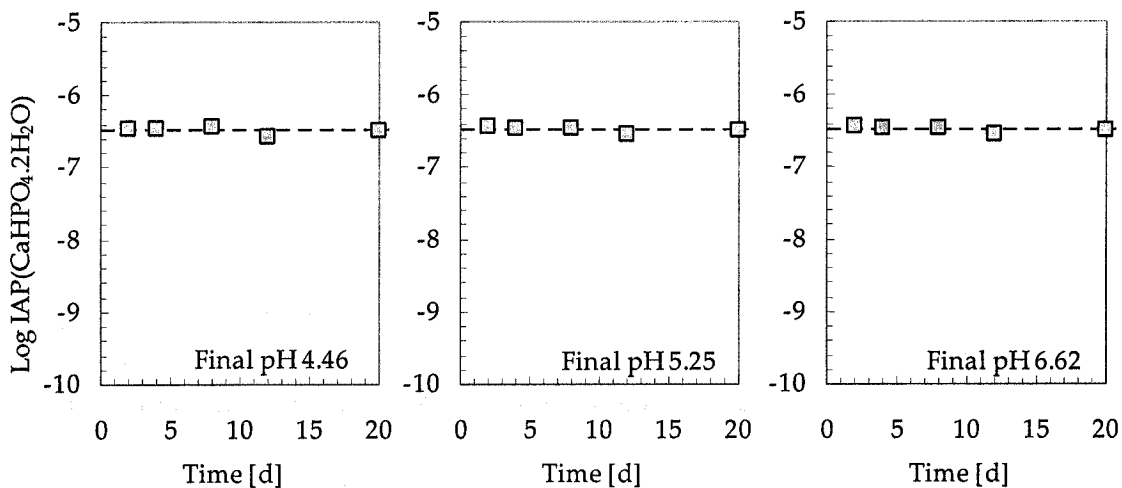


Figure 5.21. Ion activity product of $\text{CaHPO}_4 \cdot 2\text{H}_2\text{O}$ as a function of time at 22 °C at different equilibration pHs. Ion activity product expressed as equation (5.4).

The final ion activity product $\text{CaHPO}_4 \cdot 2\text{H}_2\text{O}$ (DCPD) values after 20 d of dissolution are in effect the K_{sp} . These K_{sp} values are shown in Table 5.3 along with the ion activity product that correspond to octacalcium phosphate (OCP), β -tricalcium phosphate (β -TCP), and hydroxyapatite (HAP). It is interesting to note that the estimated K_{sp} values for DCPD are very close to each other over the whole pH range revealing that the equilibrium with dicalcium phosphate dihydrate was attained and the calculation is good. From this calculation, the solubility product was determined to be $\text{Log}K_{sp} = -6.49 \pm 0.02$.

It can be further deduced from the data in Table 5.3 that the solutions were supersaturated versus hydroxyapatite at all pH values as well as at pH = 6.62 versus octacalcium phosphate, and β -tricalcium phosphate. These findings confirms that $\text{CaHPO}_4 \cdot 2\text{H}_2\text{O}$ is kinetically stabilised when pH is lower than 7.0 [30].

The standard Gibbs free energy of formation ($\Delta G_{f,0}$) for $\text{CaHPO}_4 \cdot 2\text{H}_2\text{O}$ was subsequently estimated using the determined solubility product and the following thermodynamic

values: $\Delta G_{f,0} = -552.86 \pm 1.0 \text{ kJ}\cdot\text{mol}^{-1}$ for Ca^{2+} [31], $\Delta G_{f,0} = -237.141 \pm 0.040 \text{ kJ}\cdot\text{mol}^{-1}$ for H_2O [32] and $\Delta G_{f,0} = -1089.09 \pm 1.5 \text{ kJ}\cdot\text{mol}^{-1}$ for HPO_4^{2-} [31]. This calculation determined the standard Gibbs free energy of formation ($\Delta G_{f,0}$) for $\text{CaHPO}_4\cdot 2\text{H}_2\text{O}$ to be $-2153.3 \pm 1.8 \text{ kJ}\cdot\text{mol}^{-1}$. The estimated K_{sp} and $\Delta G_{f,0}$ compare closely with the values reported in literature, namely $\text{Log}K_{sp} = -6.59 \pm 0.02$ [24] and $\Delta G_{f,0} = 2154.75 \text{ kJ}\cdot\text{mol}^{-1}$ [33] reported for dicalcium phosphate dihydrate, revealing that the experimental data and the estimation method are correct.

Table 5.3. Solubility data, K_{sp} , and ion activity product estimates using PHREEQC for the dissolution of $\text{CaHPO}_4\cdot 2\text{H}_2\text{O}$

Final pH	Conc. [mmol/L]		K_{sp}	Ion activity Product		
	Ca(II)	P(V)		DCPD	OCP	β -TCP
4.46	22.878	23.823	-6.49	-49.91 (-1.51)	-30.97 (-2.05)	-43.02 (15.5)
5.25	7.925	8.181	-6.50	-48.57 (-0.17)	-29.66 (-0.74)	-40.43 (18.1)
6.62	1.605	1.637	-6.49	-46.40 (2.00)	-27.50 (1.42)	-36.11 (22.4)

DCPD: dicalcium phosphate dihydrate; OCP: octacalcium phosphate; β -TCP: β -tricalcium phosphate; and HAP: hydroxyapatite. Saturation index values are shown in bracket

Calcium-deficient hydroxyapatite: Similarly to the calculation for $\text{CaHPO}_4\cdot 2\text{H}_2\text{O}$, the $\text{Log}(IAP)$ for $\text{Ca}_{10}(\text{PO}_4)_3(\text{OH})_2$ was estimated with the aid of PHREEQC as a function of time. The calculated $\text{Log}(IAP)$ values are presented in Figure 5.22. It can be seen that for each pH a steady state value for the ion activity product was obtained in around 10 d. However, this steady-state value cannot be considered the equilibrium value for hydroxyapatite dissolution because the ion activity product showed a strong dependence with pH.

The latter is better visualised when the final calculated IAP for hydroxyapatite is replotted versus final pH (Figure 5.23). According to this figure, the final ion activity product follows a linear trend versus pH; in fact regression by the least squares method, gave the relation:

$$\text{Log}[IAP(\text{hydroxyapatite})] = 1.11 \cdot \text{pH} - 62.33; r^2 = 0.99 \quad (5.9)$$

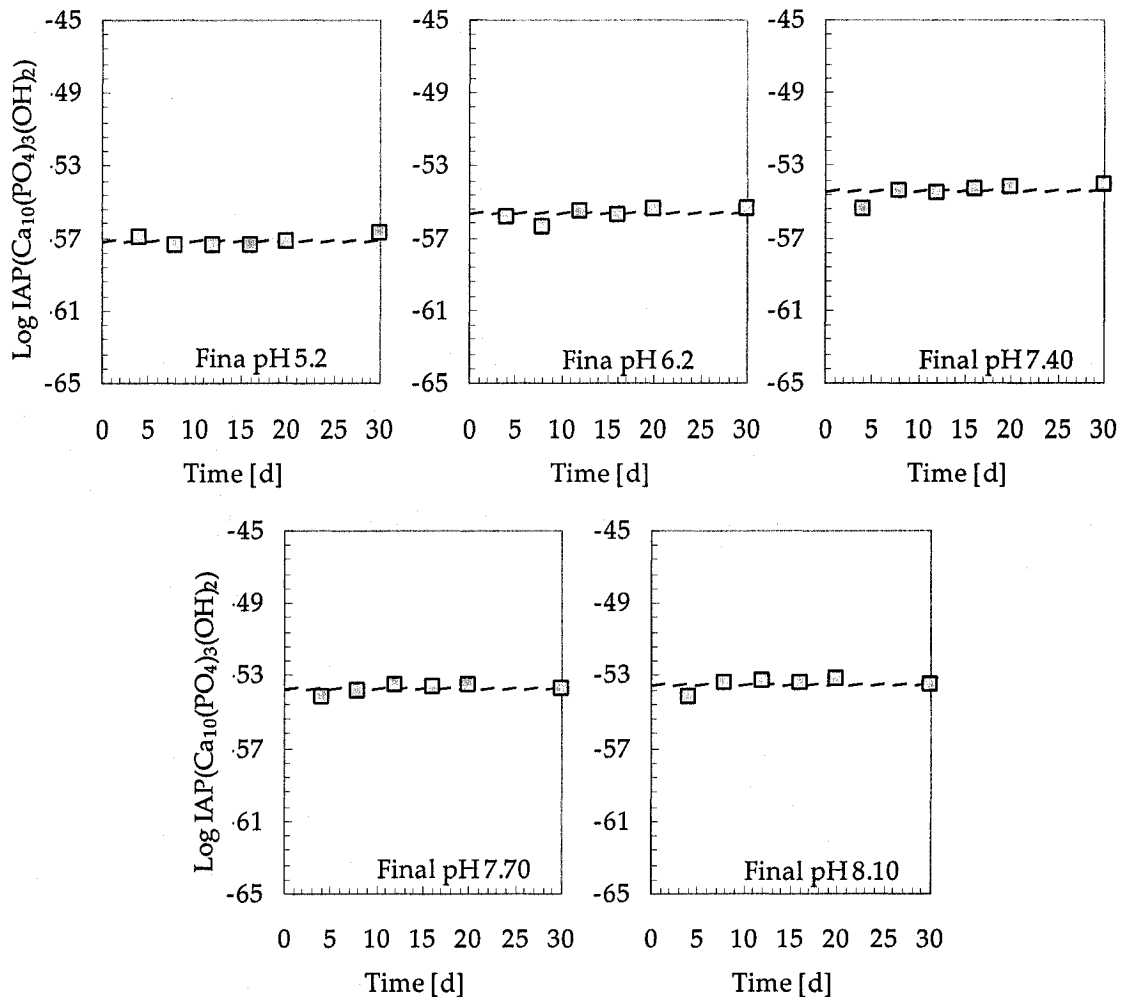


Figure 5.22. Ion activity product of $\text{Ca}_{10}(\text{PO}_4)_3(\text{OH})_2$ as a function of time at 22 °C at different equilibration pHs. Ion activity product expressed as equation (5.7).

This behaviour is apparently an artifact of the made assumption that stoichiometric hydroxyapatite is involved. Larsen and Jensen [34] reported a similar behaviour for the dissolution of dental enamel, a biological calcium-deficient hydroxyapatite, [35]. The authors reported the following relation for the ion activity product of their calcium-deficient hydroxyapatite in the range of pH from 4.6 to 7.6:

$$\text{Log}[IAP(\text{hydroxyapatite})] = 1.42 \cdot \text{pH} - 63.10; r^2 = 0.880 \quad (5.10)$$

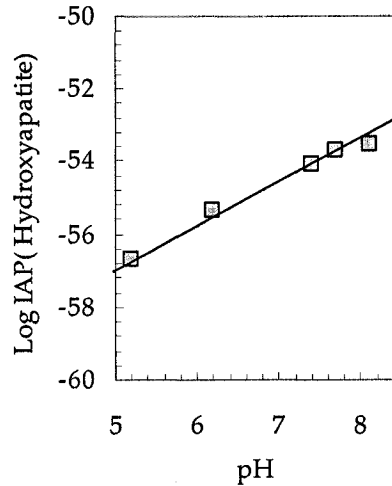


Figure 5.23. Final Ion activity product (expressed as hydroxyapatite) versus final pH.

In order to visualise if other calcium phosphate salts such octacalcium phosphate or β -tricalcium phosphate are controlling the calcium and phosphorus concentration in solution the so-called potential line was calculated. According to thermodynamics equilibrium between a calcium phosphate solid phase and an aqueous solution in the $\text{Ca}(\text{OH})_2 + \text{H}_3\text{PO}_4 + \text{H}_2\text{O}$ system is defined by the potential line [36]:

$$\text{Log } a(\text{H}^+)^3 \cdot a(\text{PO}_4^{3-}) = Q - q \text{Log } a(\text{Ca}^{2+}) \cdot a(\text{OH}^-)^2 \quad (5.11)$$

The logarithms of $a(\text{H}^+)^3 \cdot a(\text{PO}_4^{3-})$ and $a(\text{Ca}^{2+}) \cdot a(\text{OH}^-)^2$ are proportional to the chemical potentials of the components $\text{Ca}(\text{OH})_2$ and H_3PO_4 in solution. In this equation, q represents the molar calcium to phosphorus ratio in the saturated solid, whereas Q is indirectly related to the free energy of the stability-controlling phase. They are constant as long as the free energy of the controlling phase and that of water are constant.

In Figure 5.24, the negative logarithms of $a(\text{H}^+)^3 \cdot a(\text{PO}_4^{3-})$ and $a(\text{Ca}^{2+}) \cdot a(\text{OH}^-)^2$ are plotted for the experimental data along with potential lines defined by equation (5.11) for hydroxyapatite, octacalcium phosphate; β -tricalcium phosphate, and dicalcium phosphate dihydrate. Weighted least squares analysis shows that the data fall on a straight line with a slope q of 1.37 ± 0.03 . This slope approaches the theoretical value of 1.33 for octacalcium phosphate very well, hence, the possibility that this material is

controlling the solubility behaviour in these dissolution tests cannot be ruled out.

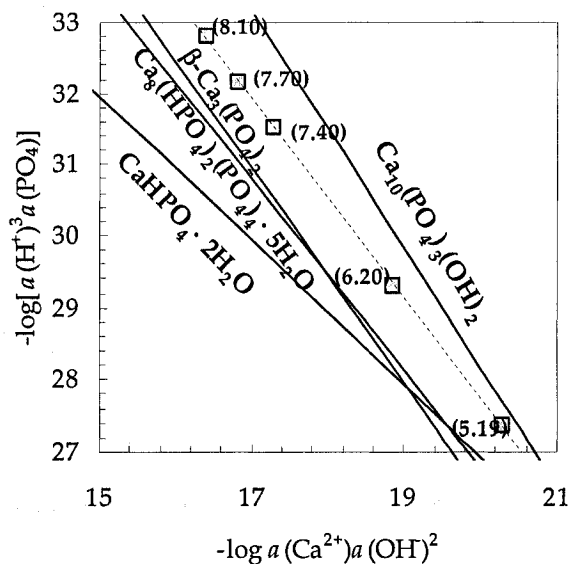


Figure 5.24. Potential lines of hydroxyapatite, octacalcium phosphate; β -tricalcium phosphate, and dicalcium phosphate dihydrate in the system $\text{Ca}(\text{OH})_2 + \text{H}_3\text{PO}_4 + \text{H}_2\text{O}$ at 22°C . Points represent experimental data after 30 d of equilibration. (Final pHs are shown in bracket).

However, it can be seen from Figure 5.24 that all experimental points are between the potential lines of hydroxyapatite and octacalcium phosphate. This means that the solutions are undersaturated with respect to all calcium phosphates but hydroxyapatite. Hence, the presence of octacalcium phosphate or β -tricalcium phosphate is not plausible.

As is seen in Figure 5.24, the experimental data obtained at $\text{pH} < 7.0$ seem to lie closer to the hydroxyapatite potential line than those obtained at higher pHs values. In order to investigate if this behaviour is due to the formation (via hydrolysis, for example) of some colloidal phase it was decided to filter the final solutions with a $0.02 \mu\text{m}$ pore size membrane instead of the standard one of $0.25 \mu\text{m}$. Figure 5.25 shows the effect of filter size on Ca and P concentration; it can be seen that the difference between the two sets of calcium and phosphorus levels is negligible proving that the formation of colloidal particles of hydroxyapatite is not the source of this behaviour. For the period of 30 d the dissolution study revealed no evidence of transformation of the calcium-deficient

hydroxyapatite phase towards stoichiometric hydroxyapatite

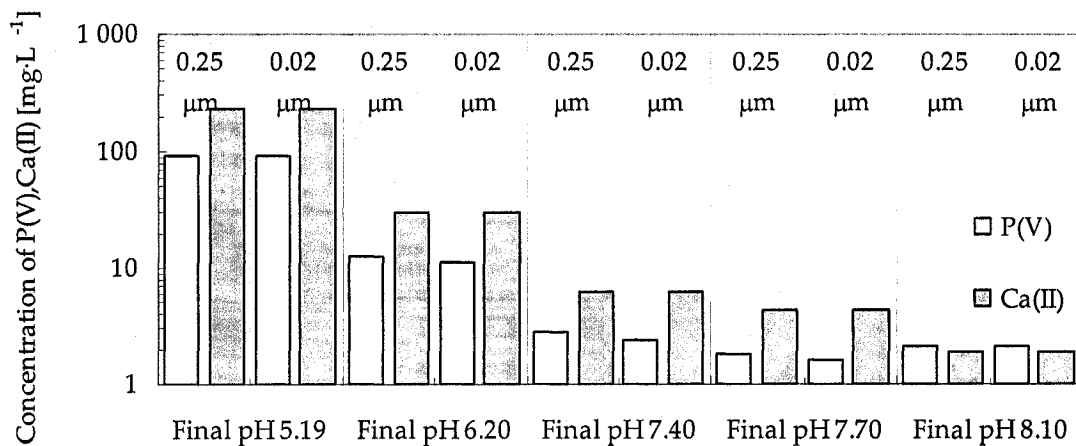


Figure 5.25. Ca and P concentrations in solution vs. pore size membrane used.

5.4 Conclusions

Two calcium phosphates were synthesised at ambient temperature: (1) dicalcium phosphate dihydrate (brushite) and (2) calcium-deficient hydroxyapatite. The synthesis of dicalcium phosphate dihydrate involved controlled neutralisation of a starting solution with Ca:P molar ratio equal to one. Homogeneous precipitation at pH 5.4 was found to be very fast, reaching equilibrium within 30 min. Seed-assisted precipitation, on the other hand, at pH 5 was slow. Nevertheless, in both cases well crystalline plate-like particles matching the stoichiometry of brushite ($\text{CaHPO}_4 \cdot 2\text{H}_2\text{O}$) were produced

The dissolution of $\text{CaHPO}_4 \cdot 2\text{H}_2\text{O}$ was studied under the following experimental conditions: 22 °C, 20 d, 20 g/L and initial pH of 4.5, 5.5, and 6.7. It was determined the dissolution to be congruent at every pH studied; this behaviour was confirmed by XRD analysis and thermodynamic analysis of the dissolution process with the aid of PHREEQC. Finally, the K_{sp} of $\text{CaHPO}_4 \cdot 2\text{H}_2\text{O}$ was determined to be $10^{-649 \pm 0.02}$ at 22 °C and one atm (101.325 kPa). The calculated standard Gibbs free energy of formation ($\Delta G_{f,0}$) for $\text{CaHPO}_4 \cdot 2\text{H}_2\text{O}$ was $-2153.3 \pm 1.8 \text{ kJ} \cdot \text{mol}^{-1}$. Both values in good agreement with previous published data.

The production of hydroxyapatite was effected via mixing of CaCl_2 and NaH_2PO_4

solutions at constant pH of 7.6. Supersaturation was controlled by the addition rate. The produced hydroxyapatite was found to be calcium-deficient with nano-crystalline structure. The crystallite size was found to be in the order of 20 nm. The best material (Ca:P = 1.58) was obtained with seed-assisted precipitation at slow addition rate. The overall stoichiometry of this material was estimated to be $(\text{Ca}_{9.48}\text{Na}_{0.02}(\text{HPO}_4)_{0.51}(\text{PO}_4)_{5.41}(\text{OH})_{1.49}, \text{Ca:P} = 1.58)$.

The dissolution of this synthetic calcium-deficient hydroxyapatite (Ca:P = 1.58) was studied at initial pH of 5.0, 6.0, 7.0, 8.0, and 9.0. It was found this material to be metastable versus stoichiometric hydroxyapatite and more stable than all other calcium phosphate phases commonly found under aqueous precipitation conditions, such as, dicalcium phosphate dihydrate or octacalcium phosphate. Furthermore, it was determined the dissolution to be congruent at initial pH 5.0, 6.0, 7.0, and 8.0 and becoming incongruent when initial pH was 9.0. Finally, analysis of the final Ca and P concentration levels with PHREEQC revealed the following relationship:

$$\text{Log}[IAP(\text{hydroxyapatite})] = 1.11 \cdot \text{pH} - 62.33; r^2 = 0.99$$

References

- 1 Arifuzzaman, S. M.; Rohani, S. Experimental study of brushite precipitation, *Journal of Crystal Growth*, **2004**, 267(3-4), 624-634
- 2 Rodríguez-Lorenzo, L.M.; Vallet-Regí, M. Controlled crystallization of calcium phosphate apatites. *Chemistry of Materials*, **2000**, 12, 2460-2465.
- 3 Paraskeva, C.A.; Charalambous, P.C.; Stokka, L-E; Klepetsanis, P.G.; Koutsoukos, P.G.; Read, P.; Ostvold, T; Payatakes, A.C. Sandbed Consolidation with Mineral Precipitation *Journal of Colloid and Interface Science*, **2000**, 232(2), 326-339.
- 4 Koutsoukos, P.G.; Amjad, Z.; Tomson, M.B.; Nancollas, G.H.; Crystallization of calcium phosphates. A constant composition study, *Journal of the American Chemical Society*, **1980**, 102(5), 1553-1557.
- 5 Graham, S; Brown, P.W. Reactions of octacalcium phosphate to form

- hydroxyapatite, *Journal of Crystal Growth*, **1996**, 165(1-2), 106-115.
- 6 Tung, M.S.; Eidelman, N.; Sieck, B.; Brown, W.E. Octacalcium Phosphate Solubility Product from 4 to 37 °C. *Journal of Research of the National Bureau of Standards*, **1988**, 95(3), 613-624.
 - 7 Parkhurst, D.L.; Appelo, C.A.J. *User's Guide to PHREEQC (Version 2)-A Computer Program for Speciation, Batch-Reaction, One-Dimensional Transport, and Inverse Geochemical Calculations; Water-Resources Investigations Report 99-4259; U.S. Geological Survey: Reston, VA, 1999; <http://wwwbrr.cr.usgs.gov/>.*
 - 8 Lindsay, W.L.; Vlek, P.L.G.; Chien, S.H. Phosphate minerals. In *Minerals in soil environment*, 2nd Ed.; Dixon, J.B; Weed, S.B.; Eds.; Soil Science Society of America: Madison, WI, **1989**, pp. 1089-1130.
 - 9 Plummer, L.N.; Bussenberg, E. The solubilities of calcite, aragonite and vaterite in CO₂-H₂O solutions between 0 and 90 °C, and an evaluation of the aqueous model for the System CaCO₃-CO₂-H₂O. *Geochimica et Cosmochimica Acta*, **1982**, 46, 1011-1040.
 - 10 LaMer, V.K.; Dinegar, R.H. Theory, production and mechanism of formation of monodispersed hydrosols. *Journal of the American Chemical Society*, **1950**, 72, 4847-4854.
 - 11 Sugimoto, T. Preparation of monodispersed colloidal particles. *Advances in Colloid and Interface Science*, **1987**, 28, 65-108.
 - 12 Nancollas, G.H.; Mohan, M.S. The growth of hydroxyapatite crystals, *Archives of Oral Biology*, **1970**, 15(8), 731-745.
 - 13 Feenstra, T.P.; De Bruyn, P.L. The Ostwald rule of stages in precipitation from highly supersaturated solutions: a model and its application to the formation of the nonstoichiometric amorphous calcium phosphate precursor phase. *Journal of Colloid and Interface Science*, **1981**, 84(1), 66-72 .
 - 14 Nancollas, G.H.; Lore, M.; Perez, L.; Richardson, C.; Zawacki S.J. Mineral phases of calcium phosphate. *The Anatomical Record*, **1989**, 224(2), 234-241.
 - 15 Eanes, E.D. Amorphous calcium phosphate: thermodynamic and kinetic

- considerations. In *Calcium Phosphates in Biological and Industrial Systems*; Amjad, Z; Ed., Kluwer Academic Publishers: Boston, MA, 1998, pp. 21-39.
- 16 Siddharthan, A; Seshadri S.K.; Kumar, T.S.S. Microwave accelerated synthesis of nanosized calcium-deficient hydroxyapatite. *Journal of Materials Science-Materials in Medicine*, 2004, 15(12), 1279-1284.
- 17 Gómez-Morales, J.; Torrent-Burgués, J.; Boix, T.; Fraile, J.; Rodríguez-Clemente, R. Precipitation of stoichiometric hydroxyapatite by a continuous method. *Crystal Research and Technology*, 2001, 36(1), 15-26.
- 18 Koutsopoulos, S. Synthesis and characterization of hydroxyapatite crystals: A review study on the analytical methods. *Journal of Biomedical Materials Research*, 2002, 62(4), 600-612.
- 19 Young, R.A., Holcomb, D.W. Variability of hydroxyapatite preparations. *Calcified Tissue International*, 1982, 34(Suppl 2), S17-S32.
- 20 Chair, H.; Heughebaert, J.C.; Heughebaert, M. Precipitation of stoichiometric tricalcium phosphate prepared by continuous process. *Journal of Materials Chemistry*, 1995, 5(6), 895-899.
- 21 Bell, L.C.; Mika, H.; Kruger, B.J. Synthetic hydroxyapatite-solubility product and stoichiometry of dissolution. *Archives of Oral Biology*, 1978, 23(5), 329-336.
- 22 Dorozhkin, S.V. A review on the dissolution models of calcium apatites. *Progress in Crystal Growth and Characterization of Materials*, 2002, 44, 45-61
- 23 Koutsoukos, P.G. Growth of calcium phosphates on different substrates: Epitaxial considerations. In *Calcium Phosphates in Biological and Industrial Systems*; Amjad, Z; Ed., Kluwer Academic: Boston, MA, 1998, pp. 41-66.
- 24 Moreno, E.C.; Gregory, T.M.; Brown, W.E. Solubility of $\text{CaHPO}_4 \cdot 2\text{H}_2\text{O}$ and formation of ion pairs in the system $\text{Ca}(\text{OH})_2\text{-H}_3\text{PO}_4\text{-H}_2\text{O}$ at 5, 15, 25, and 37 °C. *Journal of Research of the National Bureau of Standards*, 1970, 74A(4), 461-475.
- 25 Gregory, T.M.; Moreno, E.C.; Patel, J.M.; Brown, W.E. Solubility of $\beta\text{-Ca}_3(\text{PO}_4)_2$ in the system $\text{Ca}(\text{OH})_2\text{-H}_3\text{PO}_4\text{-H}_2\text{O}$ at 5, 15, 25, and 37 °C. *Journal of Research of the National Bureau of Standards*, 1974, 78A(6), 667-674.

- 26 McDowell, H.; Gregory, T.M.; Brown, W.E. Solubility of $\text{Ca}_5(\text{PO}_4)_3\text{OH}$ in the system $\text{Ca}(\text{OH})_2\text{-H}_3\text{PO}_4\text{-H}_2\text{O}$ at 5, 15, 25, and 37 °C. *Journal of Research of the National Bureau of Standards*, 1977, 81A, 273-281.
- 27 Tung, M.S.; Eidelman, N.; Sieck, B.; Brown, W.E. Octacalcium Phosphate Solubility Product from 4 to 37 °C. *Journal of Research of the National Bureau of Standards*, 1988, 95(3), 613-624.
- 28 Stumm W. *Aquatic Chemistry: Chemical Equilibria and Rates in Natural Waters*; Wiley: New York, NJ, 1996.
- 29 Driessens, F.C.M.; Verbeeck, R.M.H. Metastable states in calcium phosphate - aqueous phase equilibrations. *Journal of Crystal Growth*, 1981, 53(1), 55-62
- 30 Morden, G.W; Racz, G.J. Effect of pH, calcium concentration and temperature on the hydrolysis of dicalcium phosphate dihydrate, *Canadian Journal of Soil Science*, 1989, 69(3), 689-693
- 31 Wagman, D.D; Evans, W.H; Parker, V.B; Schumm, R.H.; Halow, I.; Bailey, S.M.; Churney, K.L.; Nuttall, R.L. The NBS tables of chemical thermodynamic properties: Selected values for inorganic and C1 and C2 organic substances in SI units, *Journal of Physical and Chemical Reference Data*, 1982, 11(2).
- 32 Nordstrom, D.K.; Plummer, L.N.; Langmuir, D.; Busenberg, E.; May, H.M.; Jones, B.F.; Parkhurst, D.L. Revised chemical-equilibrium data for major water-mineral reactions and their limitations. In *Chemical Modeling in Aqueous Systems II*; Melchior, D.C.; Bassett, R.L. Eds.; ACS Symposium Series 416; American Chemical Society: Washington, DC, 1990, pp. 398-413.
- 33 Viellard, P.; Tardy, Y.; Thermochemical properties of phosphates. In *Phosphate Minerals*; Nriagu, J.O.; Moore, P.B.; Eds.; Springer Verlag: Berlin, 1984, pp. 171-198.
- 34 Larsen, M.J.; Jensen, S.J. The hydroxyapatite solubility product of human dental enamel as a function of pH in the range 4.6-7.6 at 20 °C. *Archives of Oral Biology*, 1989, 34(12), 957-961.
- 35 Cazalbou, S.; Combes, C.; Eichert, D; Rey, C. Adaptative physico-chemistry of

- bio-related calcium phosphates. *Journal of Materials Chemistry*, **2004**, *14*, 2148-2153.
- 36 Verbeek, R.M.H.; Steyaer, H.; Thun, H.P.; Verbeek, F. Solubility of synthetic calcium hydroxyapatites, *Journal of the Chemical Society, Faraday Transactions*, **1980**, *76*, 209-219.

Chapter 6. Scorodite encapsulation with phosphate coatings

6.1 Introduction

In this chapter, the development of a novel method of arsenic fixation is investigated. This is based on the encapsulation of scorodite particles via direct crystallisation on them of aluminium and calcium phosphate coatings.

The directed deposition of phosphate on scorodite particles was achieved via the control of supersaturation. For the directed deposition of aluminium phosphate, the supersaturation was controlled via pH adjustment. Thus, heterogeneous nucleation and crystal growth were favoured against homogeneous nucleation. On the other hand, for the controlled deposition of calcium-deficient hydroxyapatite on scorodite substrate supersaturation was controlled via regulated mixing of two Ca(II) and P(V) solutions at constant pH of 7.6.

6.2 Encapsulation with aluminium phosphate

6.2.1 Materials and methods

Experimental set up: The experimental set-up used in this work was the same as the one described in Chapter 3 (Section 3.2).

Deposition method: This procedure follows closely the seed-assisted precipitation of aluminium phosphate described in Section 4.2.1 of Chapter 4. 1.5 L of an acidic sulphate solution containing ~0.16 mol/L of P(V) and Al(III):P(V) of 1:1 was heated to 95 °C and then neutralised with 1 mol/L NaOH, until the precipitation pH of 1.7 was reached (just before the critical supersaturation level was attained); the solution was allowed to stabilize for 30 min in order to assure uniform supersaturated conditions. At this point,

50 g/L (wet basis) of scorodite solids produced by the procedure described in Chapter 3 (section 3.5) was added to initiate the precipitation process; pH was kept constant using NaOH (1 mol/L) as base, and after 6.0 h of precipitation, the product was collected.

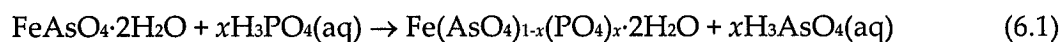
During the course of the deposition process, samples of slurry were taken at regular time intervals, filtered through a membrane filter (GE Osmonics Cameo 0.22 μm pore size) and diluted with acidified ($w_{\text{HNO}_3} \sim 5\%$) deionised water.

Characterisation and analysis: At the end of each test, the entire suspension was filtered. The final filtrate together with the filtrates of the intermediate samples were analysed for As, Fe, P, and Al. The final slurry was filtered and the solids washed by repulping 3 times with 1000 mL of acidified deionised hot water (60 $^{\circ}\text{C}$). The final solids were subjected to a number of characterisation techniques, such as XRD, SEM-EDX examination, TOF-LIMS, and TOF-SIMS analysis (more details on these techniques can be found in Chapter 3).

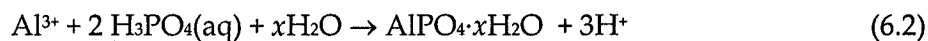
6.2.2 Deposition kinetics

Kinetics and stoichiometry: Figure 6.1(a) and (b) shows the precipitation kinetics of a typical deposition test in terms of P(V) and Al(III) removal and As(V) and Fe(III) dissolution with time respectively. According to the shape of P(V) and Al(III) removal and As(V) and Fe(III) dissolution curves the deposition process can be divided into two main stages:

The first stage corresponds to an induction period, of approximately 3 h of duration, during which very slow precipitation of P(V) took place (with almost no precipitation of Al(III)), accompanied by the release of arsenic from scorodite and no iron release was observed. This behaviour can be explained by an "ion exchange"-type reaction between As(V) and P(V) according to:



In stage 2, simple precipitation of aluminium phosphate apparently took place with no simultaneous dissolution of arsenic:



Aluminium and phosphorus precipitation proceeds at the same rate indicating the production of stoichiometric aluminium phosphate (1:1). In terms of overall kinetics, around 50% of P(V) was removed from the solution after 6 h (or 3 h if induction period is excluded).

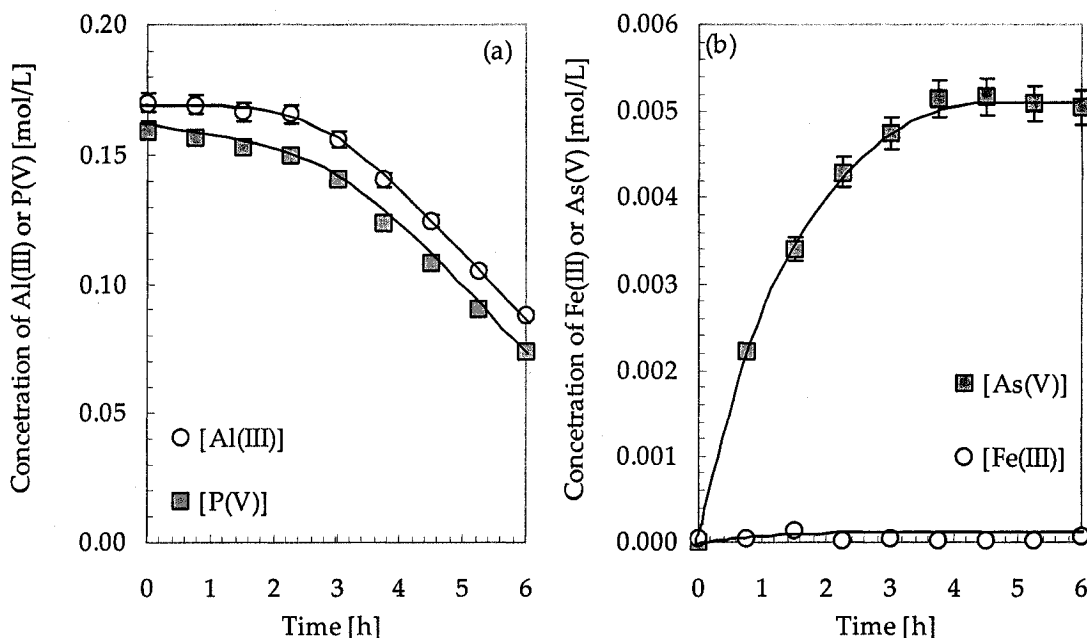


Figure 6.1. Controlled deposition of aluminium phosphate on scorodite. (a) Variation of P(V) and Al(III) with time; (b) Variation of As(V) and Fe(III) with time. Experimental conditions: P(V)=0.16 mol/L, Al:P=1, T=95 °C, precipitation pH 1.7.

The data of Figure 6.1 were further analysed in an effort to establish the reaction stoichiometry of the precipitation stages. Thus, in Figure 6.2 the molar quantities of aluminium and phosphorus removed along with the quantity of arsenic dissolved over consecutive periods of 1.5 h each are plotted. According to Figure 6.2 during the first 1.5 h of reaction there were 3.8 ± 0.3 mmol/L and 6.3 ± 0.8 mmol/L of Al(III) and P(V) removed respectively, whereas the amount of arsenic released during the same period was 3.4 ± 0.3 mmol/L. This implies that roughly 50% of the phosphate was removed due to

aluminium phosphate precipitation and 50% due to ion exchange with arsenate. During the next 1.5 h (1.5-3.0 h), the amount of arsenic released was reduced to 1.3 ± 0.1 mmol/L while the amounts of aluminium and phosphorus precipitated were 10.0 ± 2.5 mmol/L and 12.3 ± 1.6 mmol/L respectively. In other words, only ~10% of phosphorus removed was due to ion exchange with arsenate. The subsequent 3-6 h period the release of arsenic was effectively stopped and the removal of aluminium and phosphate proceeded apparently according to the stoichiometry of the precipitation reaction (6.2). Thus, between 3.0 and 4.5 h the ratio aluminium precipitated to phosphorus precipitated was found to be 0.97 ± 0.02 while the same ratio during the last 1.5 h of reaction was 1.07 ± 0.06 , i.e. for all practical purposes equal to one.

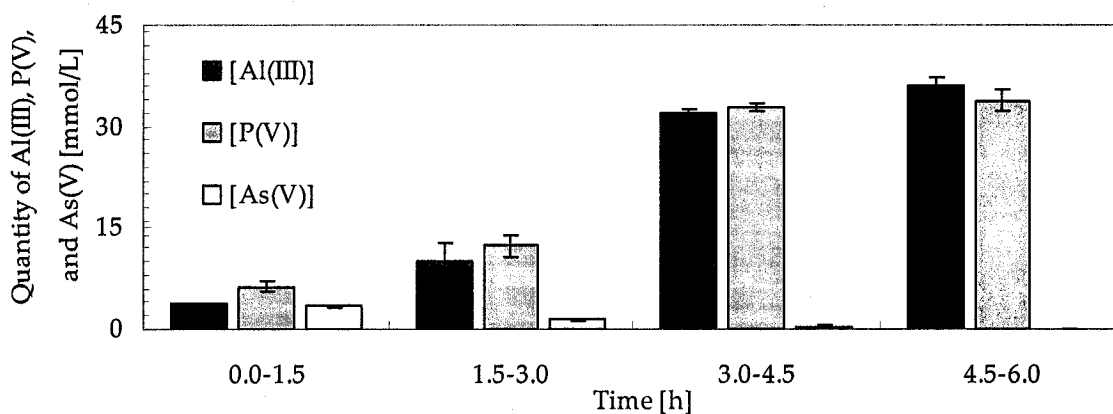


Figure 6.2. Quantity of aluminium and phosphorus removed and arsenic release as a function of 1.5 h periods during controlled crystallisation-deposition of $\text{AlPO}_4 \cdot x\text{H}_2\text{O}$ on scorodite particles.

Recycling-deposit growth: With the intention of evaluating the growth kinetics of aluminium phosphate deposits on scorodite surface, the solids produced from the first deposition run were recycled two more times using the same approach described above. Figure 6.3 shows the kinetics in terms of P(V) precipitation (a), and As(V) release (b). The precipitation kinetics were found to proceed at faster rates when recycled product was used rather than scorodite. In the former, the induction period was effectively eliminated reflecting the faster nucleation kinetics on a surface of material of the same kind, i.e. aluminium phosphate, than on a foreign surface, that is scorodite, $\text{FeAsO}_4 \cdot 2\text{H}_2\text{O}$. As it is

seen in Figure 6.3(b) the release of arsenic stopped after the second deposition run indicating complete coverage of scorodite surfaces by aluminium phosphate.

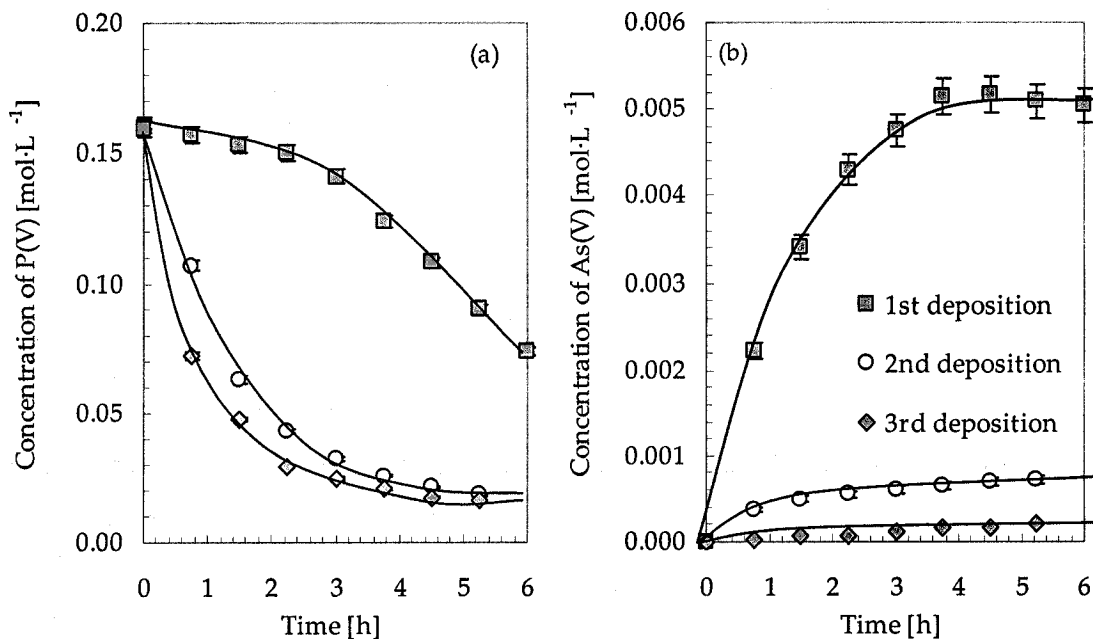


Figure 6.3. Controlled crystallisation-deposition of aluminium phosphate on scorodite followed by two recycles. Experimental conditions: P(V)= 0.16 mol/L, Al:P =1, T=95 °C, precipitation pH 1.7.

Similar to the calculations made above for the first controlled deposition test, the average quantities of phosphorus and aluminium removed over periods of 1.5 h for the two recycling tests are shown in Figure 6.4. It can be seen from Figure 6.4 that the precipitation of aluminium and phosphorus proceeded at the same rate during the course of the experiments confirming the stoichiometry (1:1) of the encapsulating material (refer to reaction (6.2)). Chemical analysis of the products following digestion yielded aluminium to phosphorus molar ratio of 0.96 ± 0.02 , 1.04 ± 0.05 , and 1.02 ± 0.05 for the first, second and third directed deposition tests. The molar ratio obtained for the solids produced using pure scorodite as substrate confirms that some phosphorus precipitated via ion exchange with arsenic (arsenate) rather than chemical precipitation (refer to reaction (6.1)).

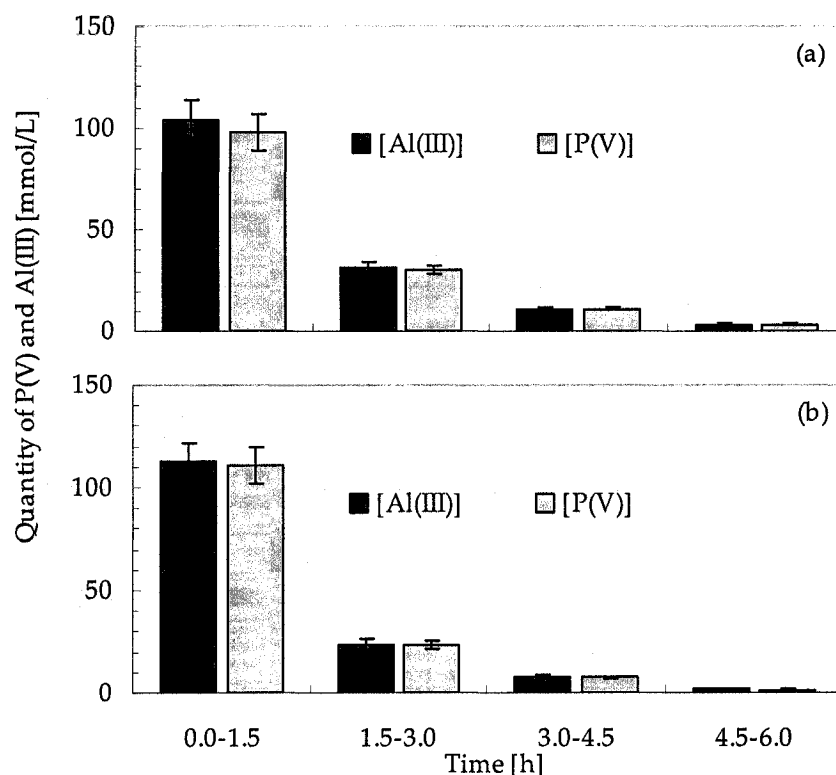


Figure 6.4. Quantity of aluminium and phosphorus removed and arsenic release as a function of 1.5 h periods during controlled crystallisation-deposition of $\text{AlPO}_4 \cdot x\text{H}_2\text{O}$ on previously coated scorodite particles. (a) One recycle; (b) two recycles.

Effect of base: In metallurgical industries, $\text{Ca}(\text{OH})_2$ is the neutralising agent of choice. However, the use of $\text{Ca}(\text{OH})_2$ will inevitably lead to the formation of gypsum that might act as substrate for the heterogeneous nucleation of aluminium phosphate, hence, resulting in the encapsulation process not being efficient. This is the reason that NaOH was used as base. However, MgO could be better suited, from an industrial point of view, as base due to cost advantage. The effectiveness of MgO as neutralising agent (tested as slaked MgO , $w_{\text{MgO}} \sim 10\%$) in this application can be evaluated from the results presented in Figure 6.5.

It can be seen that the use of MgO did not have an adverse impact on the kinetics of the precipitation reaction. Both NaOH and MgO yielded similar amounts of phosphorus precipitation, although, as is seen in Figure 6.5(b) the final As concentration in solution

for the test carried out with MgO was slightly higher than the standard test.

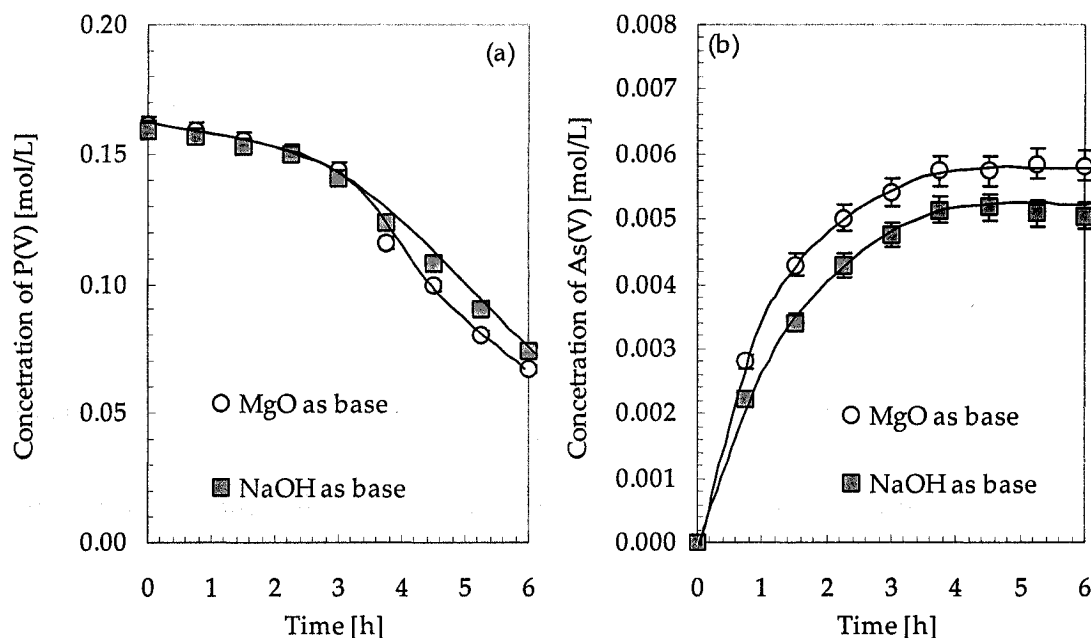


Figure 6.5. Effect of base on the precipitation kinetics. (a) Variation of P(V) with time; (b) Variation of As(V) with time. Experimental conditions: P(V) = 0.16 mol/L, Al:P = 1, T = 95 °C, precipitation pH 1.7.

6.2.3 Heterogeneous nucleation mechanism

As was reported in Section 6.2.2, during the controlled deposition of aluminium phosphate, an induction period (~3 h), apparently relating to the slow heterogeneous nucleation kinetics of aluminium phosphate on scorodite surface, was observed. The analysis of the amounts of P(V) and Al(III) removal and As(V) released suggested the simultaneous occurrence of two reactions during this induction period: a " $\text{PO}_4 \leftrightarrow \text{AsO}_4$ ion exchange" (reaction (6.1)) and an " AlPO_4 -precipitation" (reaction (6.2)). In order to get a better understanding of this behaviour a number of additional tests were performed.

Ion exchange: in the first test the postulated " $\text{PO}_4 \leftrightarrow \text{AsO}_4$ ion exchange" reaction was investigated by removing Al(III) from the system. In this test, an acidic solution containing ~0.16 mol/L of P(V) was first prepared from analytical-grade sodium phosphate monohydrate ($\text{NaH}_2\text{PO}_4 \cdot \text{H}_2\text{O}$), sodium sulphate (Na_2SO_4 , added to maintain

the same sulphate as in the standard test) and sulphuric acid (H_2SO_4). The solution was heated to 95 °C and then neutralised until the precipitation pH of 1.7. At this point, 50 g/L (wet basis) of scorodite solids was added to the reactor. The pH was kept constant using NaOH (1 mol/L) as base and after 3 h the product was collected. The final slurry was filtered and the solids were kept unwashed to be used as a substrate material in a subsequent controlled deposition test (described later).

The variation of the concentration of P(V) and As(V) in solution for this "ion exchange" test is compared to that of a standard test in Figure 6.6. The obtained data clearly confirmed the exchange between P(V) (removed from solution) and As(V) (released from scorodite particles). After 3 h of equilibration, the concentration of arsenic in solution was 19.0 ± 0.8 mmol/L as compared to 17.9 ± 1.5 mmol/L of P(V) removed suggesting stoichiometric substitution of phosphate for arsenate as per reaction (6.1).

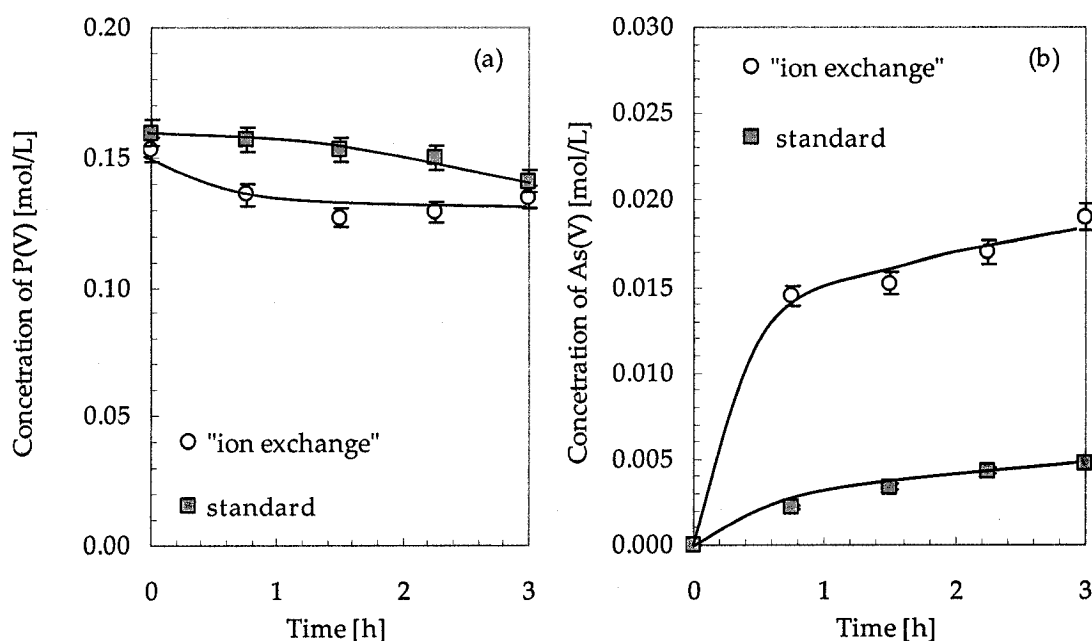


Figure 6.6. "Ion exchange" between scorodite and PO_4 -containing solution. (a) Variation of P(V) with time; (b) Variation of As(V) with time. Experimental conditions: P(V)= 0.16 mol/L, Al:P =0 in "ion exchange" test, Al:P=1 in standard test, T=95 °C, precipitation pH 1.7.

Moreover, the release of arsenic was higher than during the course of the direct

deposition of aluminium phosphate (19.0 ± 1.5 mmol/L versus 4.7 ± 0.4 mmol/L of As(V) after 3 h). The difference might be attributed to the effect of Al(III) on free phosphate ion activity. According to reaction (6.1) the extent of arsenic release should be proportional to the activity of " H_3PO_4 ", where " H_3PO_4 " encompasses all PO_4 species obtained from the dissociation of orthophosphoric acid. Figure 6.7(b) shows the predominant " H_3PO_4 " species at the pH region (around 1.7) of interest to this work are the species H_3PO_4^0 and H_2PO_4^- . On the other hand, when Al(III) is present a number of Al(III)- PO_4 complexes form (refer to Figure 6.7(a)) that effectively lower the activity of free PO_4 , i.e. H_3PO_4^0 and H_2PO_4^- , hence, resulting in lower release of arsenate. Note that the speciation of Figure 6.7 refers to 25 °C and not the temperature of reaction (95 °C), as no thermodynamic data were found in the databank of PHREEQC [1] (refer to Table 4.1 of Chapter 4) to allow extrapolation to the reaction temperature. Nevertheless, this comparison permits a qualitative basis to explain the observed behaviour.

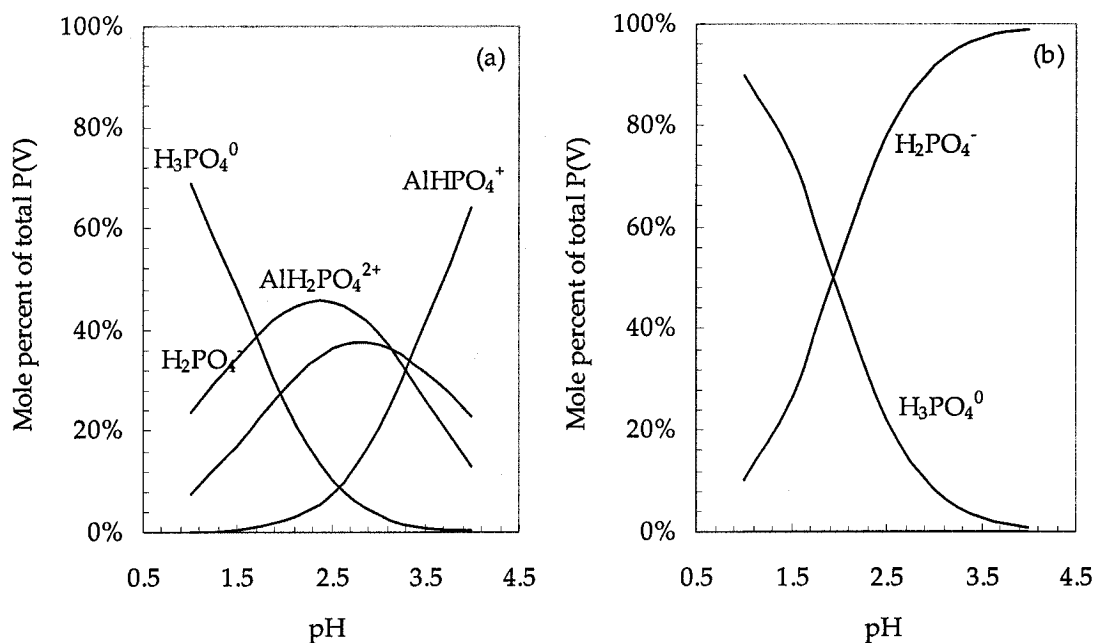


Figure 6.7. Distribution of phosphate complexes (at 25 °C) as a function of pH. (a) In the presence of Al^{3+} ions, (b) in a solution without Al^{3+} ions.

Use of PO_4 -surface substituted scorodite as substrate: The solids produced in the "ion exchange" experiment were used as substrate for an aluminium phosphate deposition test using the same experimental conditions as described in 6.2.1. The obtained precipitation kinetics from this test are presented in comparison to standard deposition test in Figure 6.8. It can be seen from Figure 6.8 that the same precipitation pattern was obtained following "ion exchange" as in the case of deposition on unreacted scorodite surface. This suggests that the formation of a $\text{Fe}(\text{AsO}_4)_{1-x}(\text{PO}_4)_x \cdot 2\text{H}_2\text{O}$ surface phase via ion exchange is not related to the heterogeneous nucleation of aluminium phosphate.

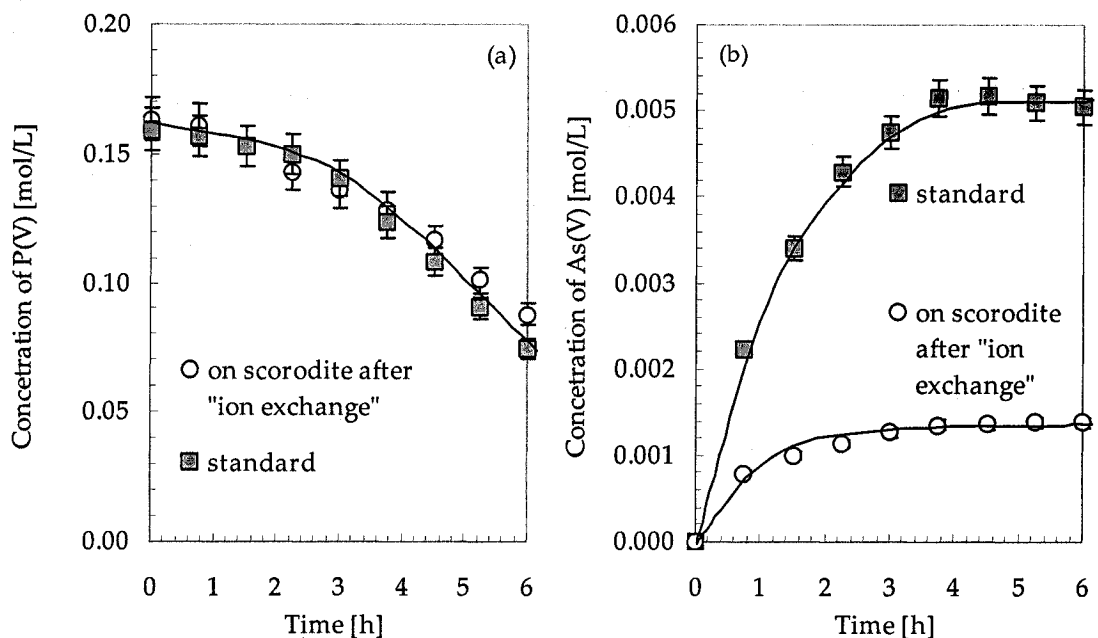


Figure 6.8. Deposition of aluminium phosphate on scorodite following "ion exchange". (a) Variation of P(V) with time; (b) Variation of As(V) with time. Experimental conditions: $\text{P(V)} = 0.16 \text{ mol/L}$, $\text{Al:P} = 1$, $T = 95 \text{ }^\circ\text{C}$, precipitation pH 1.7.

Use of gypsum as substrate: In addition, deposition of aluminium phosphate on gypsum ($\text{CaSO}_4 \cdot 2\text{H}_2\text{O}$) as substrate (instead of scorodite) was examined. It can be seen from Figure 6.9 that the deposition process proceeded at similar rates whether scorodite or gypsum was used as substrate confirming that the formation of a PO_4 -substituted scorodite surface layer (i.e. $\text{Fe}(\text{AsO}_4)_{1-x}(\text{PO}_4)_x \cdot 2\text{H}_2\text{O}$) does not influence the heterogeneous nucleation kinetics of $\text{AlPO}_4 \cdot x\text{H}_2\text{O}$. The nucleation of hydrated aluminium phosphate

clusters on the surface of gypsum crystals can be seen in Figure 6.10. It may be concluded, that the induction period seems to relate to the time necessary for the formation of aluminium phosphate hetero-nuclei rather than the formation of a $\text{Fe}(\text{AsO}_4)_{1-x}(\text{PO}_4)_x \cdot 2\text{H}_2\text{O}$ layer via "ion exchange".

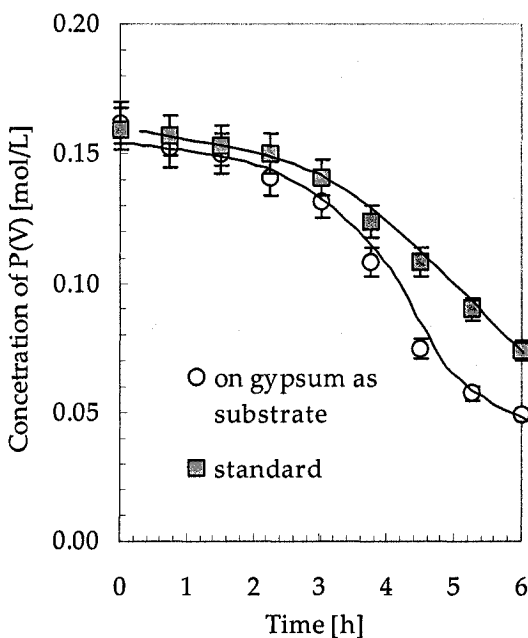


Figure 6.9. Effect of substrate material on the precipitation kinetics of aluminium phosphate Experimental conditions: $\text{P(V)} = 0.16 \text{ mol/L}$, $\text{Al:P} = 1$, $T = 95 \text{ }^\circ\text{C}$, precipitation pH 1.7. ($\text{CaSO}_4 \cdot 2\text{H}_2\text{O}$ 50 g/L).

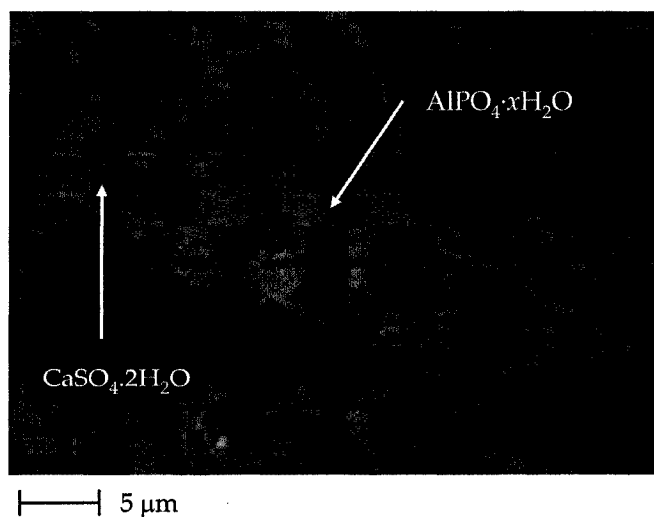


Figure 6.10. Scanning electron micrograph of hydrated aluminium phosphate precipitated heterogeneously on gypsum crystals.

6.2.4 Characterisation of the coating

Morphology: Figure 6.11 shows a scanning electron micrograph of a coated scorodite particle obtained with a variable pressure scanning electron microscope along with the associated X-ray elemental maps. This figure clearly shows the aluminium phosphate coating surrounding the original scorodite particle.

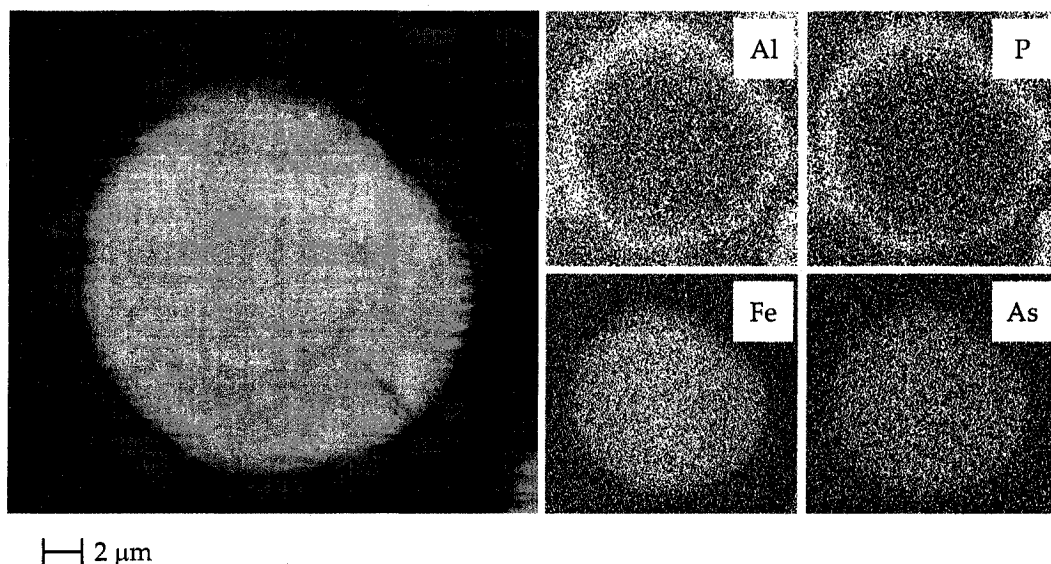


Figure 6.11. Back-scattered electron (BSE) image of a scorodite particle coated with aluminium phosphate material (left) and elemental X-ray maps.

The encapsulated scorodite particles (after one controlled deposition cycle) were separated by screening in three size fractions: $+40\ \mu\text{m}$, $-40+20\ \mu\text{m}$, and $-20\ \mu\text{m}$ in order to further evaluate their coating. Figure 6.12 shows BSE micrographs of the solids after screening. Via image analysis of the particles depicted in Figure 6.12 it was determined the thickness of the $\text{AlPO}_4 \cdot x\text{H}_2\text{O}$ coating to decrease from an average of $3.5 \pm 0.2\ \mu\text{m}$ for $+40\ \mu\text{m}$ particles, to $3.2 \pm 0.4\ \mu\text{m}$ for the $-40+20\ \mu\text{m}$ particles and finally to $2.5 \pm 0.2\ \mu\text{m}$ for the particles smaller than $20\ \mu\text{m}$.

It was further determined, following screening, the $\text{AlPO}_4 \cdot x\text{H}_2\text{O}$ to partially detach from scorodite surface and dislodge into small fragments, visible in Figure 6.12 ($-20\ \mu\text{m}$ fraction) as grey dark particles. The fragmentation and dislodging of the coating is likely

to have been caused because of the drying of the particles prior to screening. Apparently mechanical stress and shrinkage experienced by the coating upon drying led to this fragmentation. Obviously, such fragmentation/dislodging of the coating is undesirable and drying should be avoided, which likely is the case for the generation and disposal of hydrometallurgical waste solids.

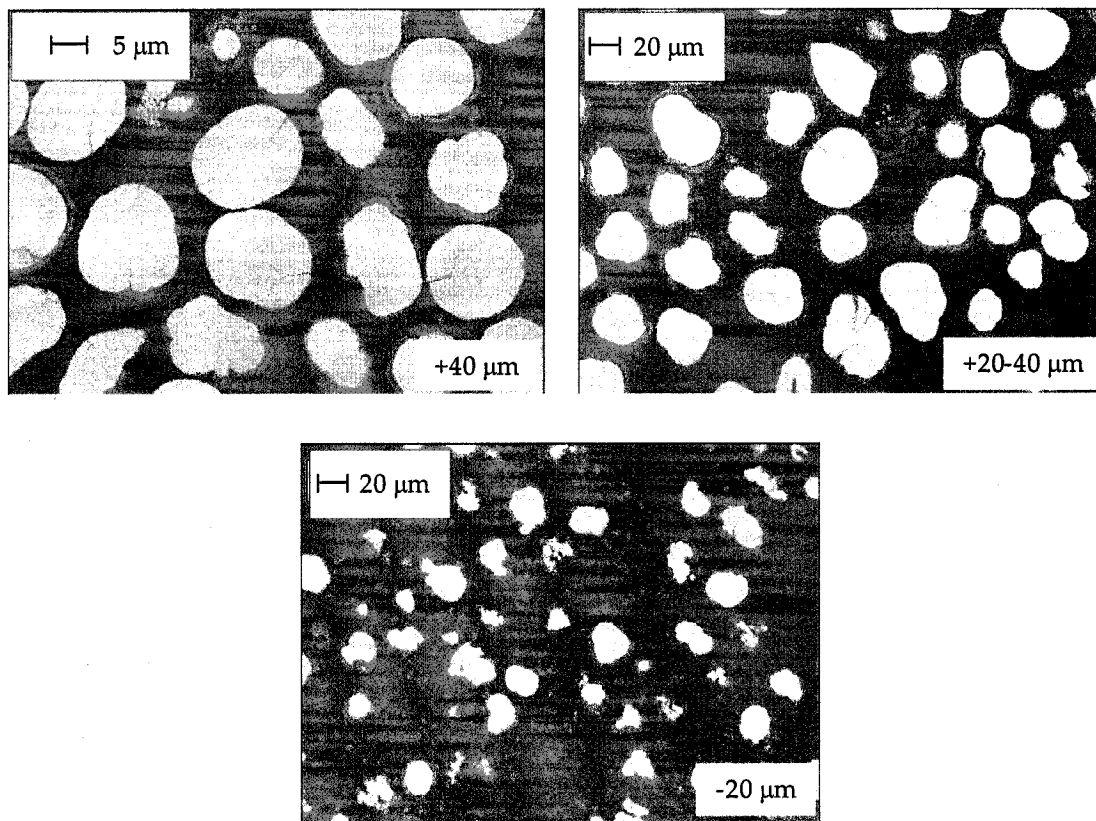


Figure 6.12. Back-scattered electron (BSE) images of encapsulated scorodite particles of different size fractions.

Scorodite particles encapsulated via repetitive deposition of aluminium phosphate were also studied using scanning electron microscopy as is shown in Figure 6.13. It can be seen that the morphology of the coating changes with repetitive deposition. Thus, the deposition process appears to begin with an epitaxial growth layer-by-layer mode (1st deposition) and switching with further deposition (2nd and 3rd) to 3D-island growth mode.

But the mode of growth of the aluminium phosphate coating was also found to be

affected when slaked MgO was used as base instead the standard NaOH (see BSE images in Figure 6.14). The use of slaked MgO appears to favour the 3D-island growth mode. This may be due to adsorption of Mg^{2+} on the surface of the scorodite substrate or the aluminium phosphate nucleation layer having as a result modification of the interfacial energy between substrate and solution (γ_{sl}), or between nuclei and solution (γ_{el}) or even between the substrate surface and the nuclei (γ_{se}). A change in interfacial energy causes then a change in the wetting condition $\Delta\gamma$ (see Eq. (2.26) of Chapter 2). This ultimately interferes with the growth process.

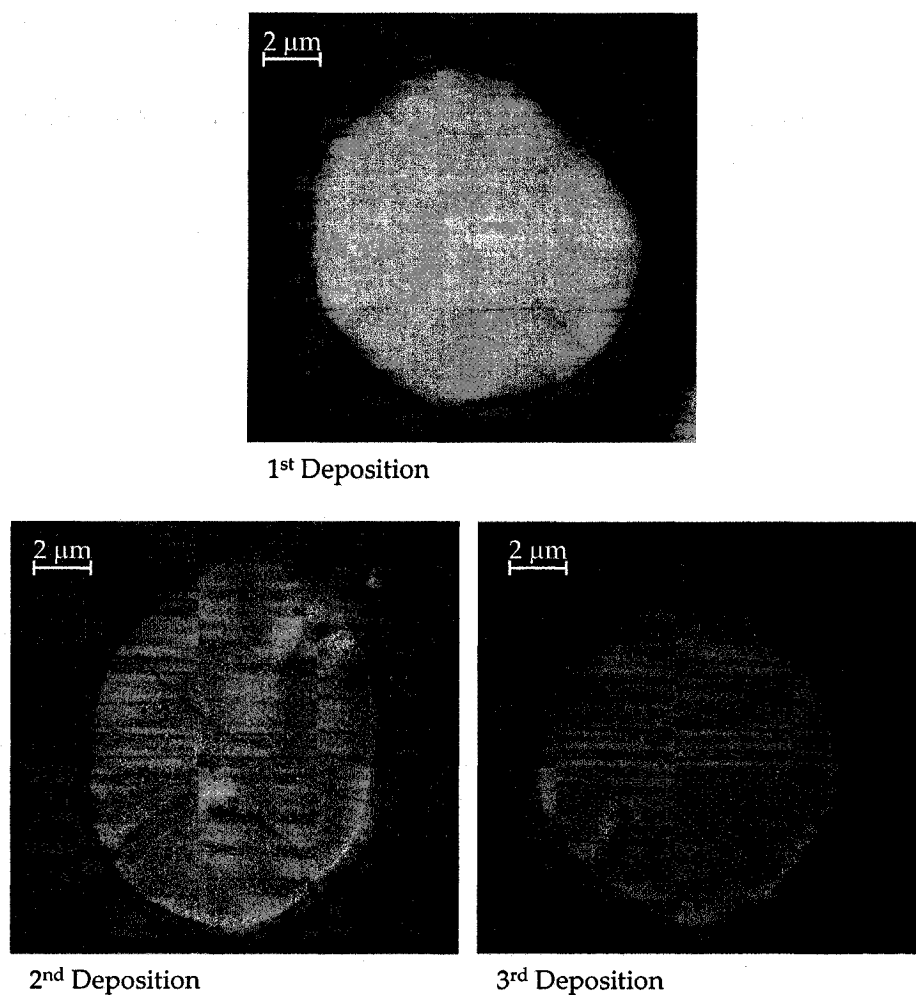


Figure 6.13. Cross section scanning electron micrographs of scorodite particles coated with aluminium phosphate material after one-, two-, and three-deposition cycles.

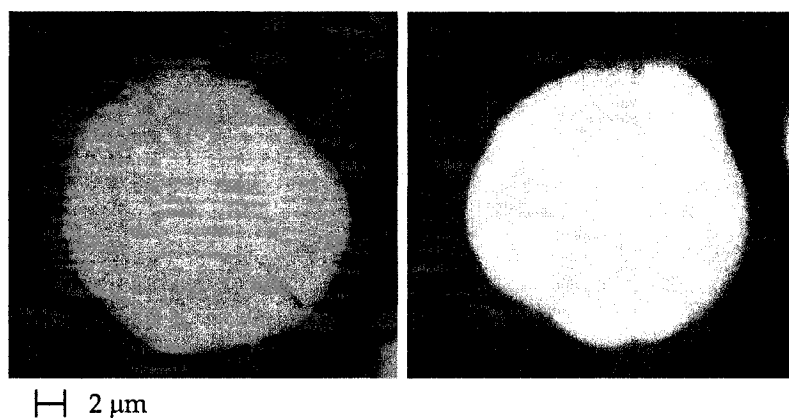


Figure 6.14. Back-scattered electron images of a scorodite particles coated with aluminium phosphate material. The particle on the left was obtained by deposition using NaOH as base, while the particle on the right was obtained with MgO as base.

X-ray diffraction analysis: In order to confirm that the deposited hydrated aluminium phosphate coating was $\text{AlPO}_4 \cdot 1.5\text{H}_2\text{O}$ (i.e. $\text{AlPO}_4 \cdot \text{H}_3$, refer to Chapter 4), the solids produced after three directed deposition cycles were subjected to XRD analysis. The XRD pattern of the coated scorodite material along with the patterns of reference materials, scorodite, $\text{FeAsO}_4 \cdot 2\text{H}_2\text{O}$, and hydrated aluminium phosphate, $\text{AlPO}_4 \cdot 1.5\text{H}_2\text{O}$, are shown in Figure 6.15. It can be seen from Figure 6.15 that the solids produced have good crystallinity and is a mixture of scorodite and the hydrated aluminium phosphate H_3 , ($\text{AlPO}_4 \cdot 1.5\text{H}_2\text{O}$) [2].

Compositional analysis and depth profiling: An encapsulated particle with aluminium phosphate scorodite particle was subsequently characterised with the aid of scanning electron microscope equipped with an energy dispersive X-ray analyser with the purpose of determining its radial composition. For this analysis, a particle that had lost almost all of the aluminium phosphate layer upon drying and screening (refer to earlier section) was used to better characterise the transition from scorodite to aluminium phosphate (Figure 6.16). In the backscattered electron image 12 different white spots are shown and each spot is a burn mark where EDX analysis was done. Only the analysis at point #12 represents the aluminium phosphate coating, while analysis at points 9, 10, and 11 appears to represent the phase formed at the very beginning of the deposition

process. The SEM-EDX analytical results (semi-quantitative) are shown in Figure 6.17.

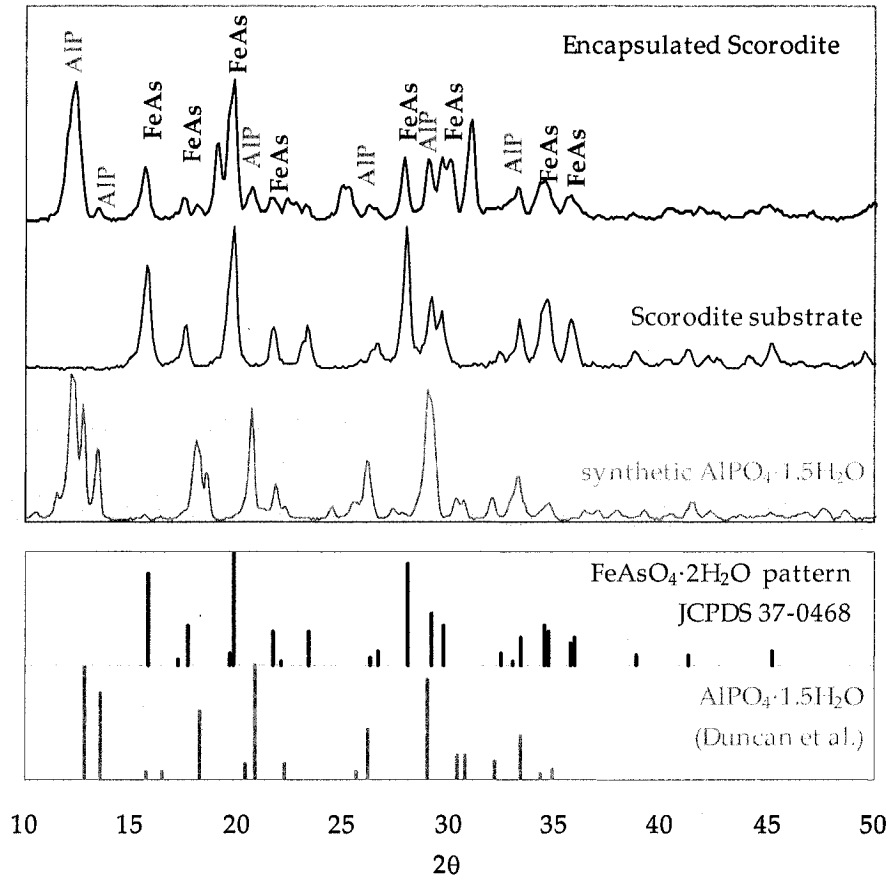


Figure 6.15. XRD pattern of product obtained by directed deposition of aluminium phosphate after two consecutive recycles. Scorodite substrate (Chapter 3) and AlPO₄·1.5H₂O produced by seed-assisted precipitation (Chapter 4) are also shown. The AlPO₄·H₃ pattern is from reference [3].

At the contact zone between the scorodite mantle and Al-phosphate layer (points 9, 10, and 11) there is clear decrease in all scorodite components (Fe, As) with a simultaneous appearance of sulphur and phosphorus. The phosphorus appearance is believed to be explained by the presence of the phase surface $\text{Fe}(\text{AsO}_4)_{1-x}(\text{PO}_4)_x \cdot 2\text{H}_2\text{O}$ that was stipulated earlier to form as a result of the ion exchange between AsO_4 and PO_4 .

Based on the average SEM-EDX analyses from the spots 9, 10, and 11 the following composition was calculated for this phase: $\text{Fe}_{0.99}\text{Al}_{0.01}\text{H}_{0.43}(\text{AsO}_4)_{0.94}(\text{PO}_4)_{0.15}(\text{SO}_4)_{0.08} \cdot x\text{H}_2\text{O}$ (H^+ is used solely for charge balance purposes). The SEM-EDX analysis also revealed that

some of arsenic, sulphur, and iron were incorporated into the structure of the adjacent aluminium phosphate layer (analysis 12), most likely via substitution. The composition of this layer was estimated to be $\text{Al}_{0.93}\text{Fe}_{0.07}\text{H}_{0.01}(\text{AsO}_4)_{0.05}(\text{PO}_4)_{0.94}(\text{SO}_4)_{0.02} \cdot x\text{H}_2\text{O}$.

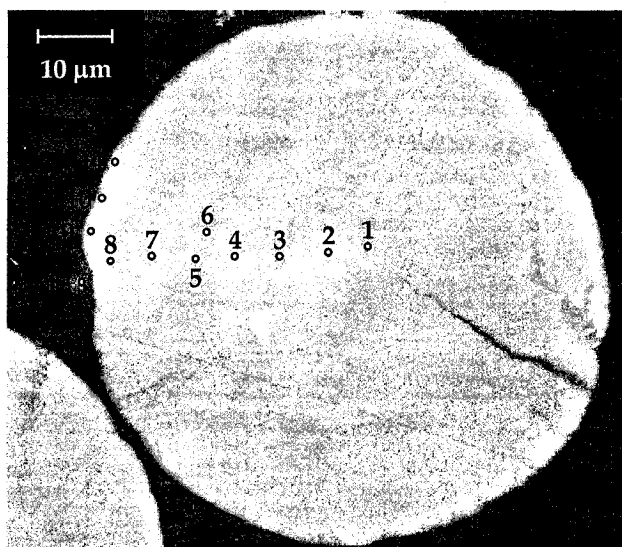


Figure 6.16. Backscattered electron image of a scorodite particle coated with aluminium phosphate material after the bulk of the coating was dislodged.

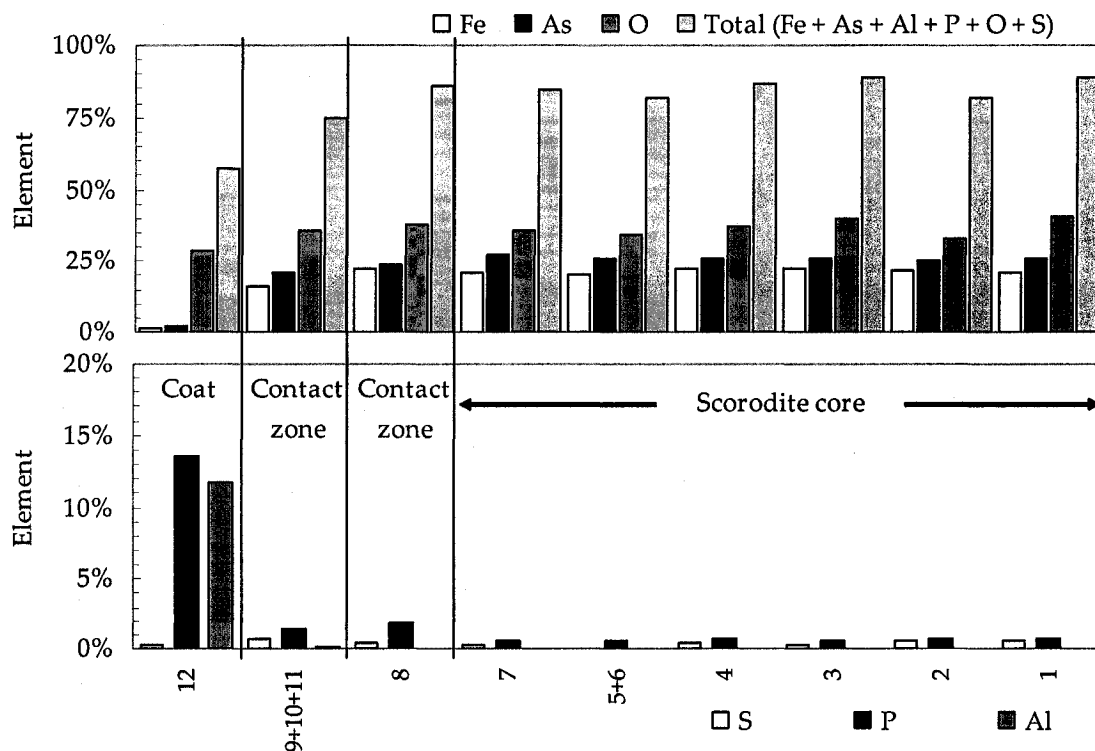


Figure 6.17. SEM-EDX radial compositional analysis of coated scorodite particle shown in Figure 6.16.

To get more insight into the deposition process, further analysis was made this time using the TOF-LIMS and TOF-SIMS techniques. Fast TOF-LIMS (Time of Flight Laser Ionisation Mass Spectrometry) was used to establish the depth profiling through an encapsulated scorodite particle. In this procedure repeated analysis on the same point of a particle was made by sequentially ablating through the aluminium phosphate coating (see Figure 6.18). In this manner, TOF-LIMS spectra were collected from the very surface region, a sub-surface region within the $\text{AlPO}_4 \cdot 1.5\text{H}_2\text{O}$ coating, and from the scorodite core.

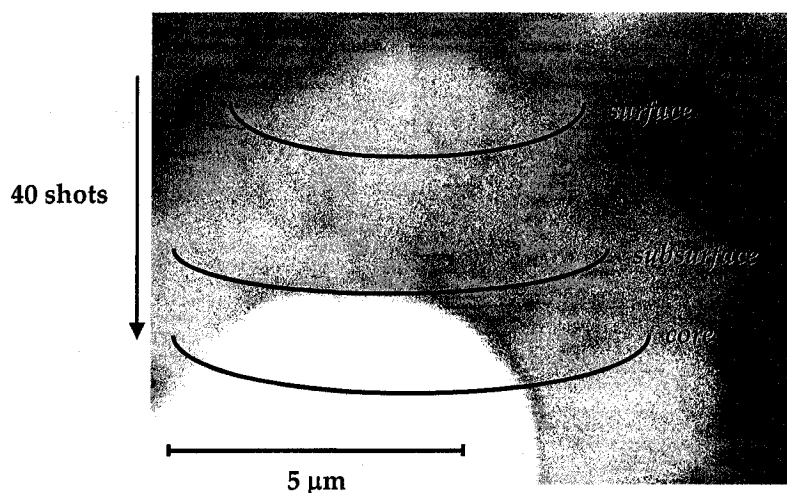


Figure 6.18. Depth Profiling through the encapsulated scorodite by TOF-LIMS.

The "surface" layer refers to the surface of the aluminium phosphate coating (first "slice" in Figure 6.18); the "subsurface" layer refers to the aluminium phosphate coating-scorodite interfacial zone (second "slice" in Figure 6.18). Finally "core" refers to the scorodite particle itself. The spectra were collected with a sampling depth of $<0.1\mu\text{m}$, hence, it took ~ 40 ablator laser "shots" to reach the scorodite. The analytical results are plotted in Figure 6.19. The concentrations are given in arbitrary units (counts in relevant peak over total counts in spectrum). On the left-hand side plot the concentration of positive ions (Al and Fe) is given while on the right-hand side the concentration of negative ions (AsO_4 and PO_4) is shown. More than twenty encapsulated scorodite particles were analysed.

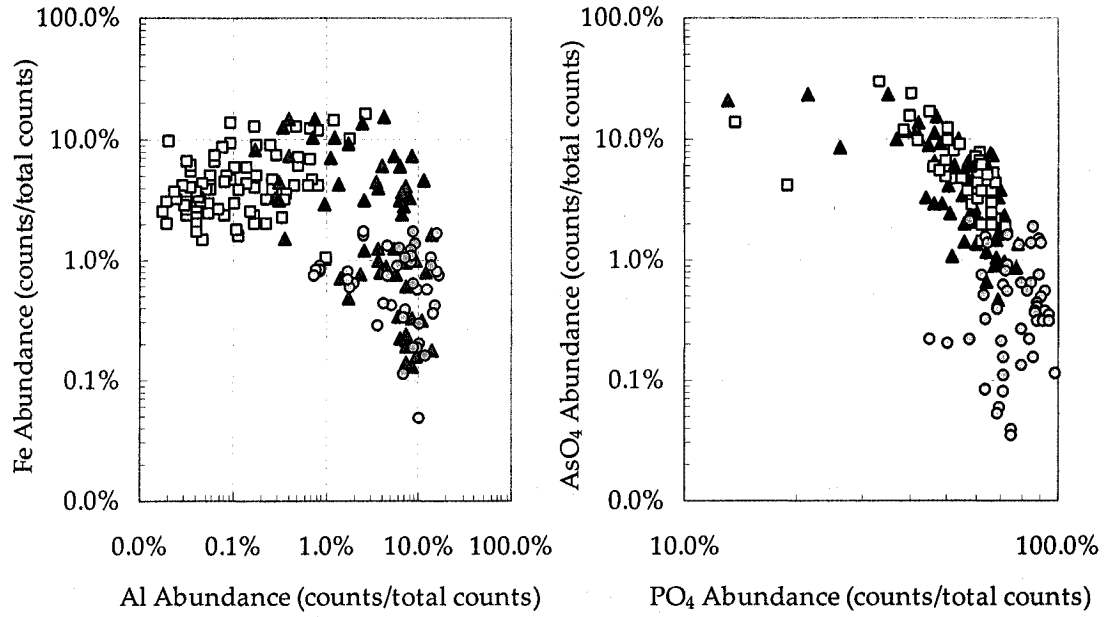


Figure 6.19. In depth profiling through AlPO₄ coated scorodite. Scatterplot of positive ion (+ve, left) and negative ion (-ve, right). TOF-LIMS data collected at moderate ablator laser energies. Symbols: □ Core, ▲ Subsurface, and ○ Surface.

It can be seen from Figure 6.19(left) the iron concentration to be high in the core, intermediate in the subsurface region and low in the surface. Exactly the reverse happens with aluminium. As far the distribution of phosphate (PO₄) and arsenate (AsO₄) is concerned (Figure 6.19(right)) it can be seen, as expected, the phosphate concentration to decrease whereas arsenate concentration to increase with depth analysis. However, the analysis shows significant amount of phosphate present in the core which is believed to be related to the ablation process that resulted in certain amount of the coating to have been analysed with the core (see ablation front in Figure 6.18).

Finally encapsulated scorodite particles were imaged by TOF-SIMS (Time of Flight Secondary Ion Mass Spectrometry) to display spatial distribution of aluminium and iron after various ablation times. It can be seen from Figure 6.20 that at time zero (surface; no sputtering) there is practically only aluminium with virtually no iron evident.

Variation in aluminium across the image is topographically controlled, i.e., dark areas represent surface depressions. After 20 s sputtering, an increase in iron can be seen in

about 2 regions, where the core is partially exposed. Images at 180 s and 240 s sputtering are very similar and represent the scorodite core. The aluminium phosphate coating remains only in surface depressions.

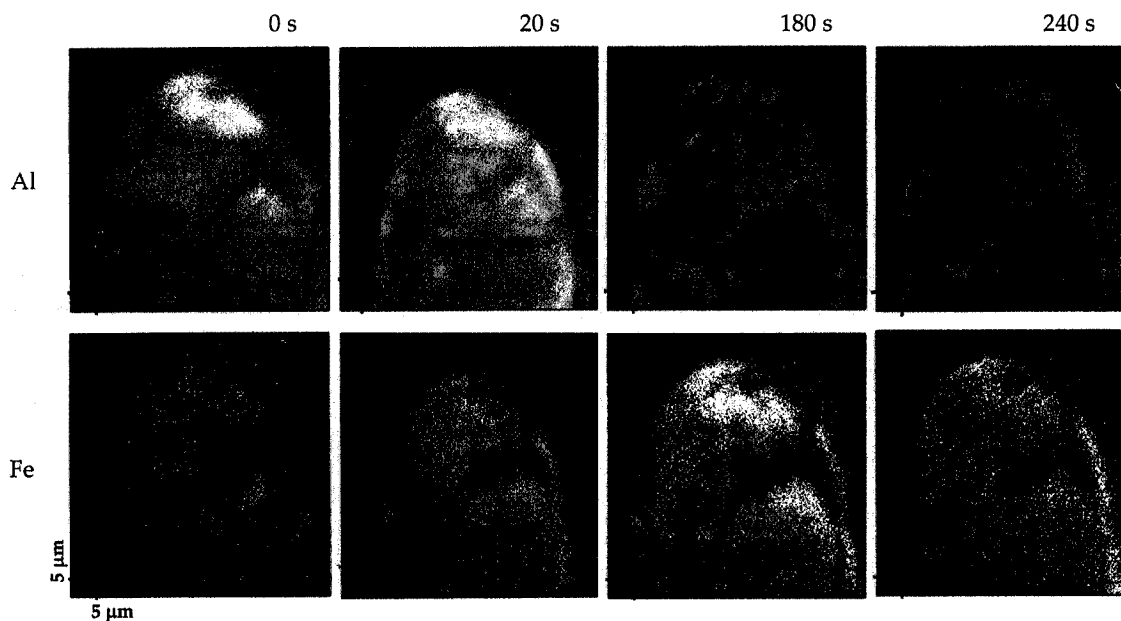


Figure 6.20. Spatial distribution of Al and Fe after various ablation times.

6.3 Encapsulation with calcium phosphate

This section is devoted to the study of controlled deposition of Calcium-deficient hydroxyapatite on scorodite particles. This material was selected as a candidate for the encapsulation of scorodite because of its low solubility under neutral to alkaline environment. The synthesis of this material was discussed in Chapter 5. In addition to the encapsulation of scorodite with calcium-deficient hydroxyapatite, deposition of dicalcium phosphate dihydrate was attempted but with poor results. A brief report summarising the deposition of $\text{CaHPO}_4 \cdot 2\text{H}_2\text{O}$ on scorodite is given in Appendix A.

6.3.1 Materials and methods

Experimental set up: The experimental set-up used in this work was the same as the one described in Chapter 3 (Section 3.2).

Deposition method: The controlled deposition procedure adopted was similar to the one described in Chapter 5 (Section 5.2.1) for the semi-batch seeded crystallisation of Ca-deficient hydroxyapatite. Prior to the main semi-batch controlled deposition work some preliminary batch tests were designed to gain insight into the precipitation kinetics of the system. These batch tests were carried as described below:

A metastable (as determined in Chapter 5) supersaturated solution of $\text{CaCl}_2\text{-NaH}_2\text{PO}_4\text{-NaOH}$ having $[\text{Ca(II)}] = 1.5 \text{ mmol/L}$, $\text{Ca:P} = 1.67$, and $\text{pH} = 7.6$ ($[\text{Ca(II)}] = 60 \text{ mg/L}$ and $[\text{P(V)}] = 28 \text{ mg/L}$) was prepared by slowly adding 500 mL of calcium chloride solution (CaCl_2 3 mmol/L) to a 500 mL of sodium dihydrogen phosphate (NaH_2PO_4 0.9 mmol/L) and the pH was then adjusted with 100 mmol/L NaOH. The solution was allowed to stabilise for 30 min to ensure uniform supersaturated conditions. Hereafter, 10 g/L (wet basis) of scorodite substrate material was used to begin the precipitation process. The pH was kept constant using NaOH (100 mmol/L) as base and after 4 h of precipitation the product was collected.

For the main deposition work, the experimental procedure consisted of two parts. In part one, the procedure was identical to that of batch precipitation procedure just described. Batch precipitation from a metastable solution (of the same composition as the one already described) on scorodite particles was allowed to proceed for 30 min. Subsequently to that, in part two, there was simultaneous addition (semi-batch mode) of two solutions of P(V) and Ca(II) (60 and 100 mmol/L respectively) at fixed rate into the slurry resulting from part one. The pH was maintained constant during the whole experiment using 100 mmol/L NaOH solution. Three different addition rates were investigated, namely 6 mL/h, 10 mL/h and 20 mL/h, with corresponding addition rates of 24 h, 14 h and 7 h respectively. All experiments were carried out in duplicate runs. The experiments were carried out under open air; in other words, the presence of atmospheric CO_2 was not excluded.

Characterisation and analysis: During the course of the deposition process, samples of slurry were taken at regular time intervals, filtered through membrane filter (Corning 0.25 μm pore size) and diluted with acidified ($w_{\text{HNO}_3} \sim 1\%$) deionised water. At the end of each test, the entire suspension was filtered. The final filtrate together with the filtrates of the intermediate samples were analysed for As, Fe, P and Ca. The final slurry was filtered and the solids washed by repulping 3 times with 1000 mL of deionised hot water (60 $^{\circ}\text{C}$). The final solids were subjected to SEM examination (see Chapter 3 for more details).

6.3.2 Deposition kinetics

Batch deposition: The precipitation kinetics of a typical batch test involving addition of scorodite substrate particles in a metastable Ca-PO_4 solution at constant pH is shown in Figure 6.21(a). It can be seen that around 30% of Ca(II) was removed from solution whereas the concentration of P(V) remained almost constant during the course of the test while a minor quantity of As(V) (0.07 mmol/L or 5 mg/L) appeared in solution. Fe(III) was found to be below the detection limit (0.01 mg/L). In Figure 6.21(b) the evolution of the Ca(II) to P(V) molar ratio versus time is presented. According to this figure, the Ca:P molar ratio in solution dropped to 1.21 after 1 h and remained constant thereafter until the end of the experiment.

Apparently, a calcium-containing phase other than calcium phosphate formed that hindered the nucleation of the latter. Alternatively it may be thought that heterogeneous nucleation of calcium phosphate was not energetically favoured. In other words, despite the solution being metastable, to all practical purposes, the supersaturation might have been less than $S_{\text{cr,net}}$ in the cases of nucleation on the surface of scorodite or the induction time for the nucleation of calcium phosphate may have been in this case much longer than 4 h. The latter appears very plausible, as it is known from literature the induction periods associated with the crystallisation of calcium phosphate phases on foreign surfaces varied with supersaturation and type of substrate [3]. For example, Wu and

Nancollas [4] have reported the induction period prior the heterogeneous nucleation of hydroxyapatite on anatase and rutile to last around 8 h and 12 h respectively at $SI_{HAP} = 10.60$ (as compared to this work where the initial saturation index for hydroxyapatite, SI_{HAP} , for the above batch precipitation was 10.76).

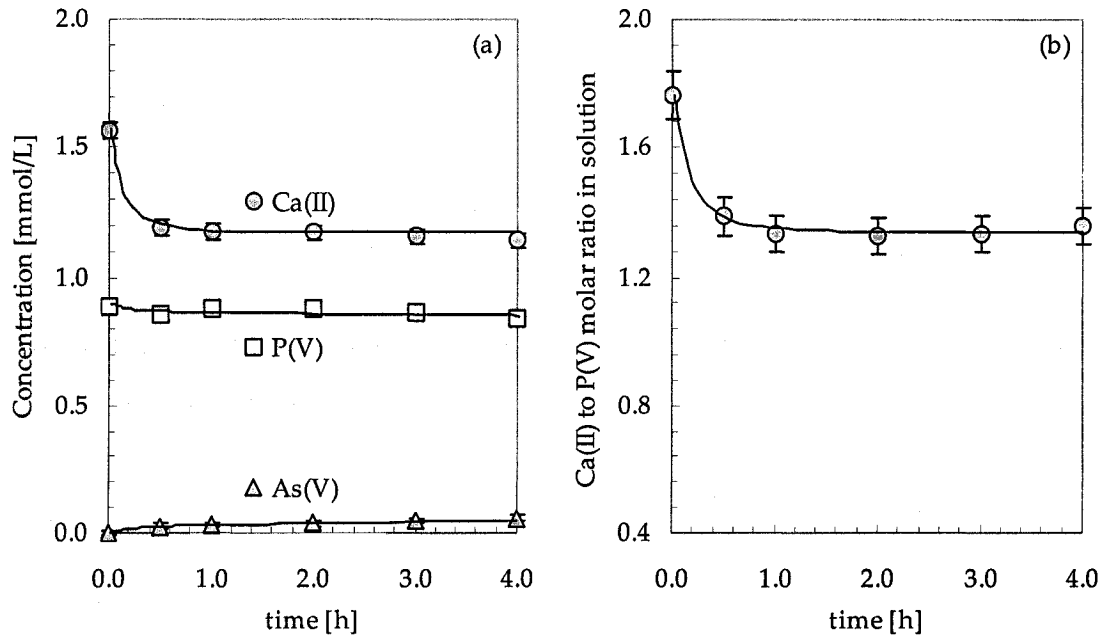


Figure 6.21. Batch precipitation of (Ca-deficient) hydroxyapatite at controlled pH on scorodite particles (10 g/L); NaOH as base; precipitation pH 7.60. a) Variation of P(V), Ca(II), and As(V) with time; b) Variation of Ca:P molar ratio in solution with time.

In an attempt to modify the surface characteristics of the substrate material, hence facilitate the nucleation of calcium phosphate, the scorodite particles were equilibrated for 15 min in a solution at pH 7.6 (using NaOH) before added into the Ca-PO₄ metastable solution. It is reminded that as mentioned in section 3.5 of Chapter 3 the scorodite solids were stirred at pH=2 for 24 h (three times) to remove amorphous material followed by washing involving repulping the solids 3 times with 1000 mL of acidified deionised hot water (pH ~3, 60 °C).

Figure 6.22(a) presents the progression of precipitation (using the pre-equilibrated at pH 7.6 scorodite as substrate). It can be seen; in this case, that calcium phosphate did indeed take place over the first hour with this time the calcium to phosphorus molar ratio

decreasing to 0.9. A minor amount of arsenic was once more released into the solution.

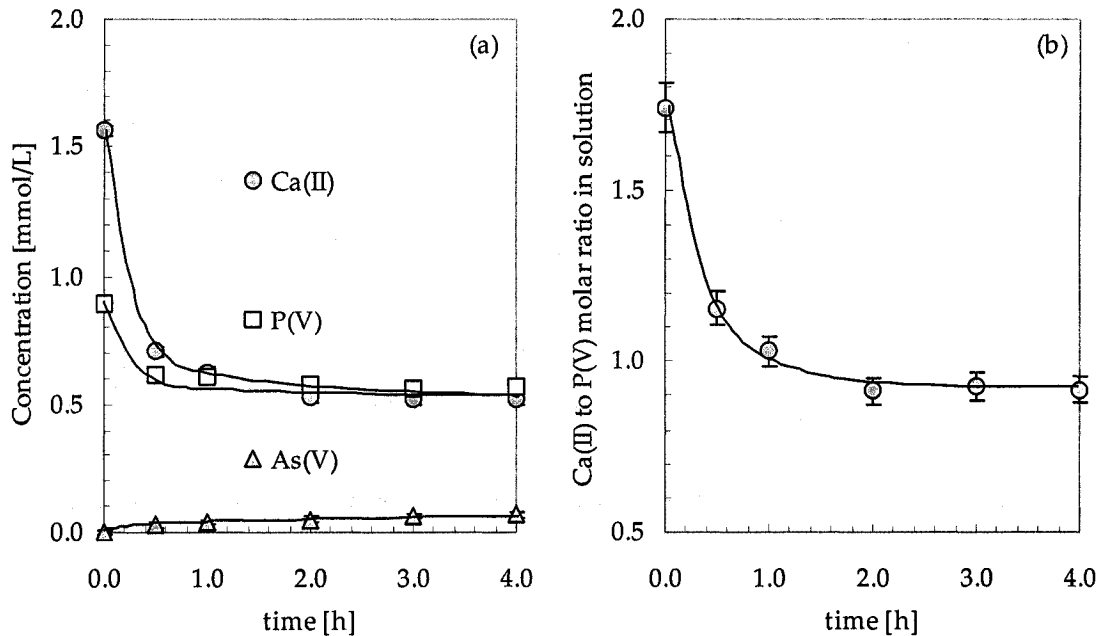


Figure 6.22. Batch precipitation of (Ca-deficient) hydroxyapatite at controlled pH on scorodite previously equilibrated at pH 7.6 (10 g/L); NaOH as base; precipitation pH 7.60. a) Variation of P(V), Ca(II), and As(V) with time; (b) Variation of Ca:P molar ratio in solution with time.

Analysis of the amount of calcium and phosphorus removed from solution and arsenic released after 30 min of reaction (Figure 6.21 and Figure 6.22) generated the data plotted in Figure 6.23. This reveals that the amount of calcium removed was higher when pre-equilibrated scorodite was used (0.37 ± 0.02 mmol vs. 0.86 ± 0.03 mmol) whereas arsenic dissolution reached similar values for both tests. In the case when pre-equilibrated scorodite was used as substrate material, 50% of the calcium was removed due to calcium phosphate precipitation whereas the other 50% due to precipitation of another calcium-containing phase. The question is what other type of calcium phase had precipitated. One possibility is that some calcium arsenate phase formed. There exist several calcium arsenates, most notably (in a descending pH order of stability): $\text{Ca}_4(\text{OH})_2(\text{AsO}_4)_2 \cdot 4\text{H}_2\text{O}$, $\text{Ca}_5(\text{AsO}_4)_3\text{OH}$ (arsenate-apatite), $\text{Ca}_3(\text{AsO}_4)_2 \cdot 3.66\text{H}_2\text{O}$, $\text{Ca}_3(\text{AsO}_4)_2 \cdot 4.25\text{H}_2\text{O}$, and $\text{CaHAsO}_4 \cdot \text{H}_2\text{O}$ [5,6,7].

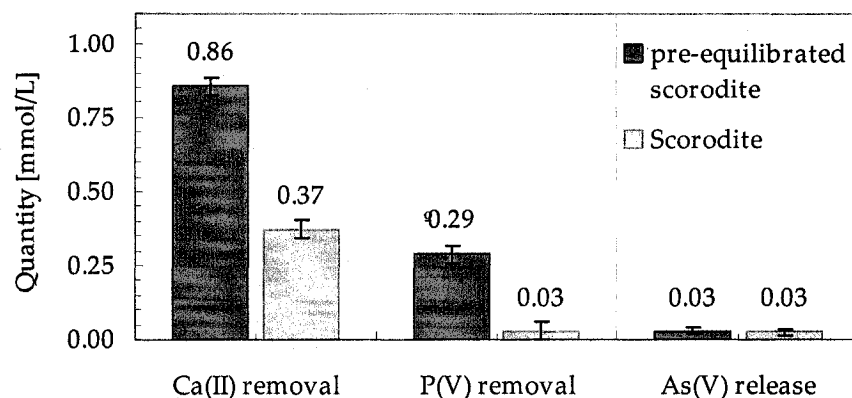


Figure 6.23. Quantity of calcium and phosphorus removal and arsenic release after 30 min of batch deposition of Ca-deficient hydroxyapatite on scorodite with and without pre-equilibration at pH 7.6.

To verify if any of these phases were thermodynamically feasible to form under the conditions employed in this part of the work, PHREEQC was used to calculate their saturation index (*SI*). For these calculations, the equilibrium data listed in Table 6.1 and Table 5.1 (refer to Chapter 5) were used.

The calculations revealed that in all cases the system was undersaturated (see Figure 6.24) in terms of all calcium arsenate phases listed in Table 6.1. Thus, the excess removal of calcium cannot be attributed to the formation of a calcium arsenate phase. Another possibility is that calcium was removed because of the atmospheric CO_2 in the form of calcium carbonate. Once more PHREEQC was used to assess this possibility assuming fast equilibrium between atmospheric CO_2 ($p_{\text{CO}_2(\text{g})} = 0.000316 \text{ atm}$), and the Ca-PO_4 metastable solutions. Three modifications of calcium carbonate were considered, namely, aragonite, calcite, and vaterite. In this case the equilibrium data listed in Table 6.1 was used as well. The calculation showed (once more) that in all cases the system was undersaturated (Figure 6.25) vis-à-vis these phases. If no calcium arsenate or carbonate had precipitated then adsorption may have been (at least in part) responsible for the small fraction of calcium removed from solution.

Table 6.1. Equilibria and constants considered in the present PHREEQC study.

Reaction	Log K	Reference
$\text{H}_3\text{AsO}_4 \leftrightarrow \text{H}_2\text{AsO}_4^- + \text{H}^+$	-2.30	[8]
$\text{H}_2\text{AsO}_4^- \leftrightarrow \text{HAsO}_4^{2-} + \text{H}^+$	-6.99	[8]
$\text{HAsO}_4^{2-} \leftrightarrow \text{AsO}_4^{3-} + \text{H}^+$	-11.80	[8]
$\text{Ca}^{2+} + \text{H}_2\text{AsO}_4^- \leftrightarrow \text{CaH}_2\text{AsO}_4^+$	1.30	[7]
$\text{Ca}^{2+} + \text{HAsO}_4^{2-} \leftrightarrow \text{CaHAsO}_4$	2.66	[7]
$\text{Ca}^{2+} + \text{AsO}_4^{3-} \leftrightarrow \text{CaAsO}_4^-$	4.36	[7]
$\text{CO}_2(\text{g}) \leftrightarrow \text{CO}_2(\text{aq})$	-1.468	[9]
$\text{CO}_3^{2-} + 2 \text{H}^+ \leftrightarrow \text{CO}_2(\text{aq}) + \text{H}_2\text{O}$	16.681	[9]
$\text{CO}_3^{2-} + \text{H}^+ \leftrightarrow \text{HCO}_3^-$	10.329	[9]
$\text{Ca}^{2+} + \text{HCO}_3^- \leftrightarrow \text{CaHCO}_3^+$	1.106	[9]
$\text{Ca}^{2+} + \text{CO}_3^{2-} \leftrightarrow \text{CaCO}_3(\text{aq})$	3.224	[9]
$\text{CaCO}_3 \text{ (vaterite)} \leftrightarrow \text{Ca}^{2+} + \text{CO}_3^{2-}$	-7.91	[9]
$\text{CaCO}_3 \text{ (aragonite)} \leftrightarrow \text{Ca}^{2+} + \text{CO}_3^{2-}$	-8.34	[9]
$\text{CaCO}_3 \text{ (calcite)} \leftrightarrow \text{Ca}^{2+} + \text{CO}_3^{2-}$	-8.48	[9]
$\text{Ca}_4(\text{OH})_2(\text{AsO}_4)_2 \cdot 4\text{H}_2\text{O} \leftrightarrow 4 \text{Ca}^{2+} + 2 \text{AsO}_4^{3-} + 2 \text{OH}^- + 4 \text{H}_2\text{O}$	-29.20	[7]
$\text{Ca}_5(\text{AsO}_4)_3\text{OH} \text{ (As-apatite)} \leftrightarrow 5 \text{Ca}^{2+} + 3 \text{AsO}_4^{3-} + \text{OH}^-$	-38.04	[7]
$\text{Ca}_3(\text{AsO}_4)_2 \cdot 3.66\text{H}_2\text{O} \leftrightarrow 3 \text{Ca}^{2+} + 2 \text{AsO}_4^{3-} + 3.66 \text{H}_2\text{O}$	-21.00	[7]
$\text{Ca}_3(\text{AsO}_4)_2 \cdot 4.25\text{H}_2\text{O} \leftrightarrow 3 \text{Ca}^{2+} + 2 \text{AsO}_4^{3-} + 4.25 \text{H}_2\text{O}$	-21.00	[7]
$\text{CaHAsO}_4 \cdot \text{H}_2\text{O} \leftrightarrow \text{Ca}^{2+} + \text{HAsO}_4^{2-} + \text{H}_2\text{O}$	-4.79	[7]

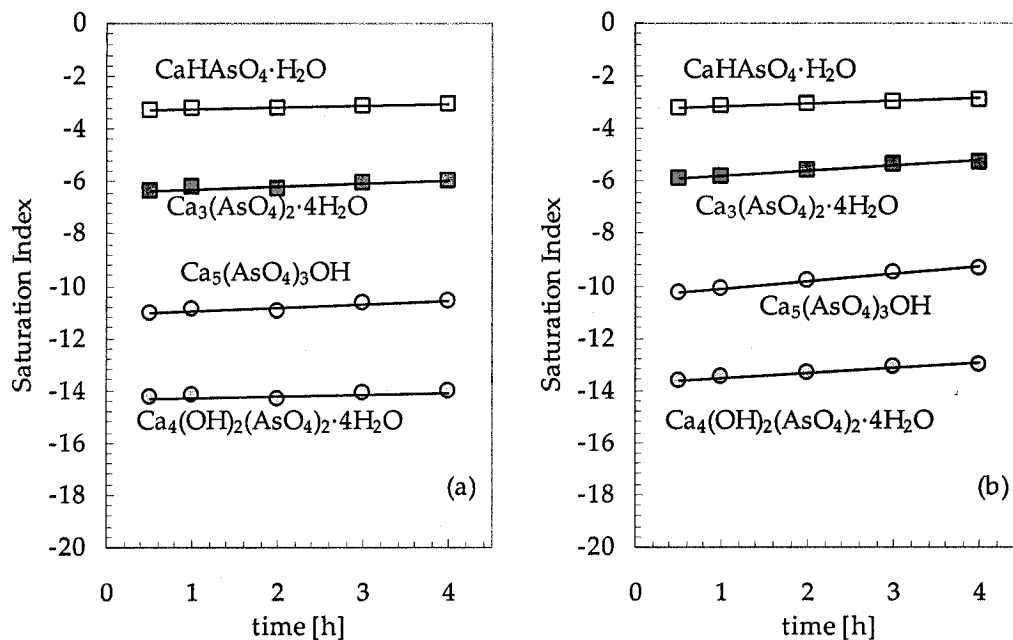


Figure 6.24. Evolution of the saturation index for some crystalline calcium arsenate compounds as a function of time during batch precipitation. (a) Using pre-equilibrated scorodite at pH 7.6 particles as substrate; (b) using "as is" scorodite particles as substrate.

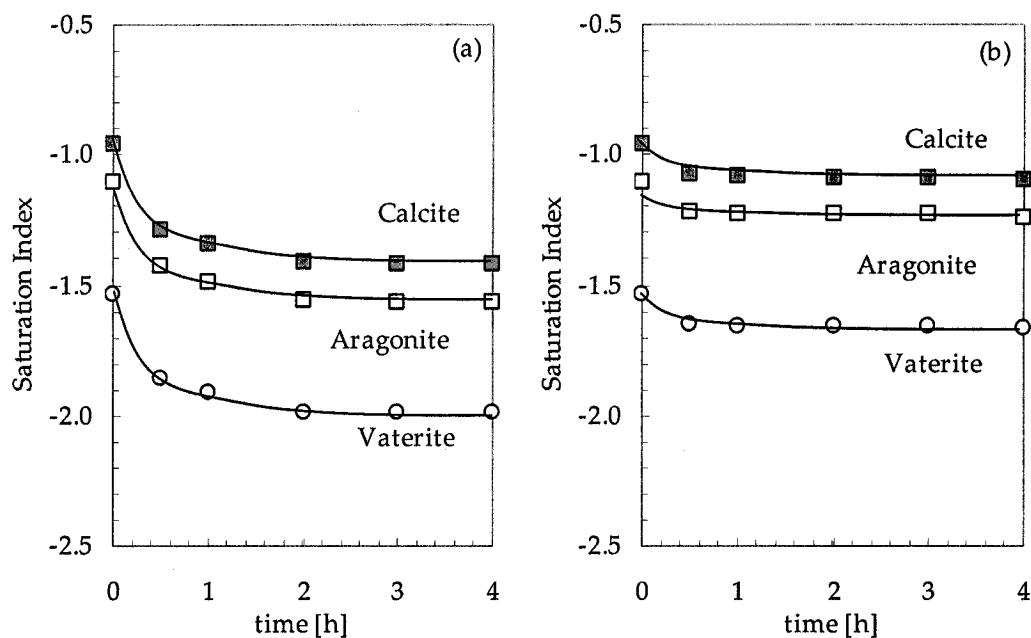


Figure 6.25. Evolution of the saturation index for some crystalline calcium carbonate compounds as a function of time during batch precipitation. (a) Using pre-equilibrated scorodite at pH 7.6 particles as substrate; (b) using "as is" scorodite particles as substrate.

Semi-batch deposition: In this type of test, different addition rates were explored. As it can be deduced from the data of Figure 6.23 the PO_4 removal rate was $\sim 0.6 \text{ mmol}\cdot\text{L}^{-1}\cdot\text{h}^{-1}$ when pre-equilibrated at pH 7.6 scorodite was used as substrate. Therefore, if all this phosphate were precipitated as hydroxyapatite the P(V) solution addition rate would be 10 mL/h. Thus, the addition rates were selected, to be 6 mL/h, 10 mL/h, and 20 mL/h. The scorodite substrate material used here had been previously pre-equilibrated at pH 7.6 to enhance its activity as per findings reported in previous section.

The progress of semi-batch deposition of Ca-deficient hydroxyapatite in the presence of scorodite substrate is depicted in Figure 6.26, Figure 6.27, and Figure 6.28 for addition rates of 6 mL/h, 10 mL/h, and 20 mL/h respectively. The figures on the left-hand side show the evolution of phosphorus and arsenic concentration with time; while, on the right-hand side the figures shown the variation of calcium to phosphorus molar ratio.

On each Figure, three well defined stages can be distinguished. **Stage I** represents the initial (batch) period of precipitation (30 min). During this stage no addition of reagent solutions was made and the Ca:P molar ratio decreased exactly in the same way as it was observed previously (Figure 6.22). During this stage a small amount of phosphorus ($\sim 9.3 \text{ mg}$ or 0.3 mmol) and calcium ($\sim 36 \text{ mg}$ or 0.9 mmol) precipitated on the surface (most likely) of scorodite substrate.

Stage II corresponds to initial built up of supersaturation (by the addition of CaCl_2 (100 mmol/L) and NaH_2PO_4 (60 mmol/L) solutions) and the release of the excess of supersaturation until the attainment of a "steady-state" is reached. It can be seen that at some point in stage II the concentration of phosphate reached a maximum value meaning the attainment of a critical value that signified the onset of primary nucleation (either homogeneous or heterogeneous). **Stage III** corresponds to the steady-state period or growth period, i.e. deposition on the nucleated material. In this period, no further nucleation was expected.

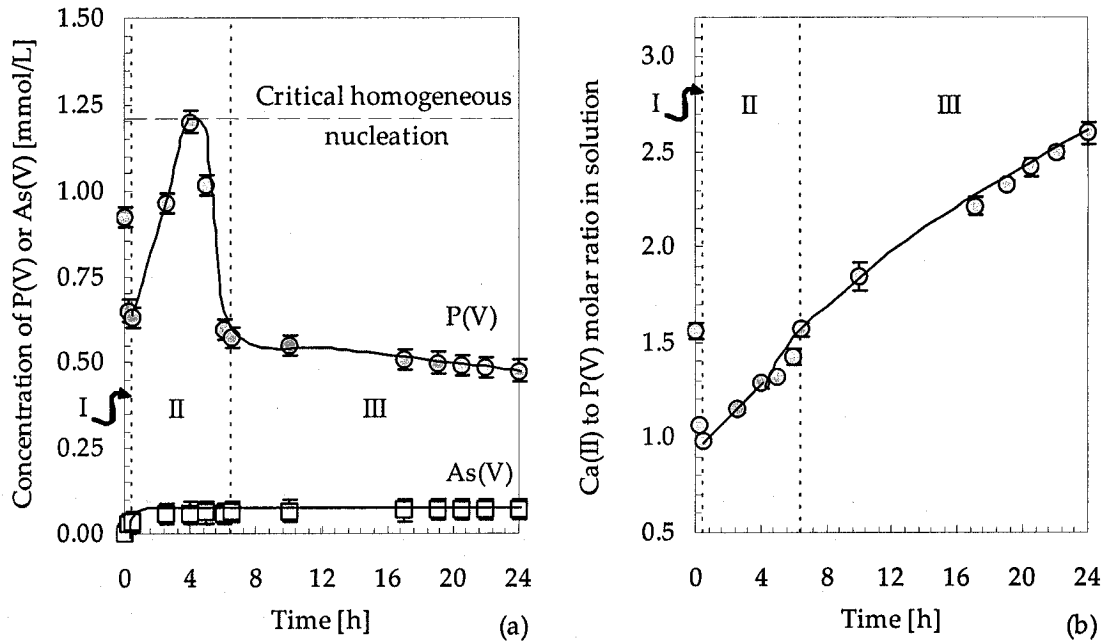


Figure 6.26. Semi-batch crystallisation of Ca-deficient hydroxyapatite using scorodite particles as substrate (10 g/L) (a) Concentration of P and As in solution; (b) Ca:P molar ratio. Reagent solution addition rate 6 mL/h.

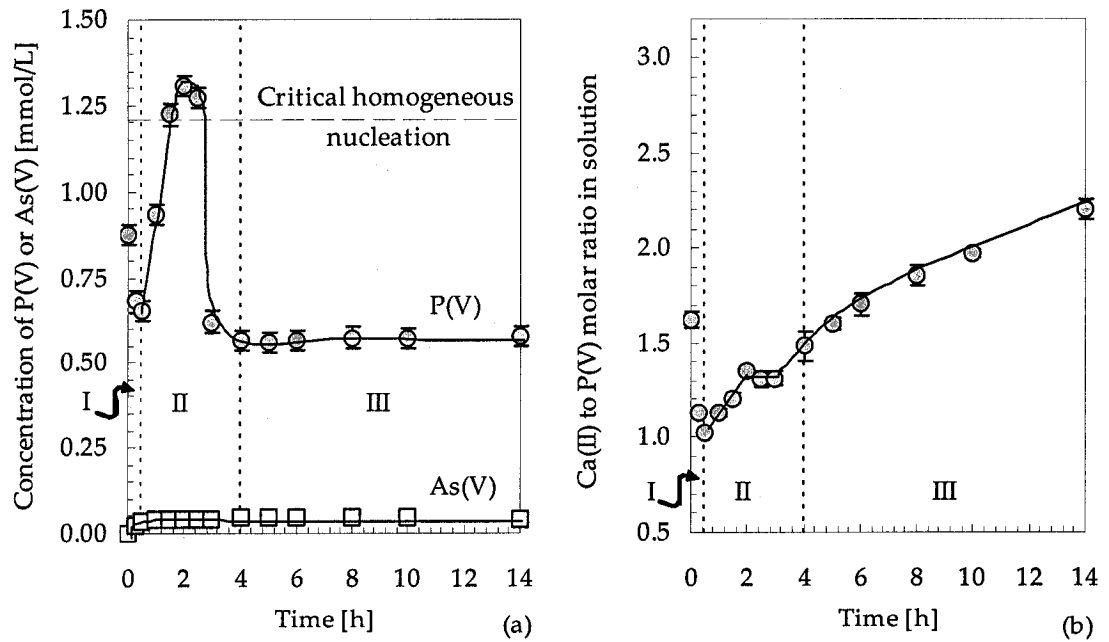


Figure 6.27. Semi-batch crystallisation of Ca-deficient hydroxyapatite using scorodite particles as substrate (10 g/L) (a) Concentration of P and As in solution; (b) Ca:P molar ratio. Reagent solution addition rate 10 mL/h.

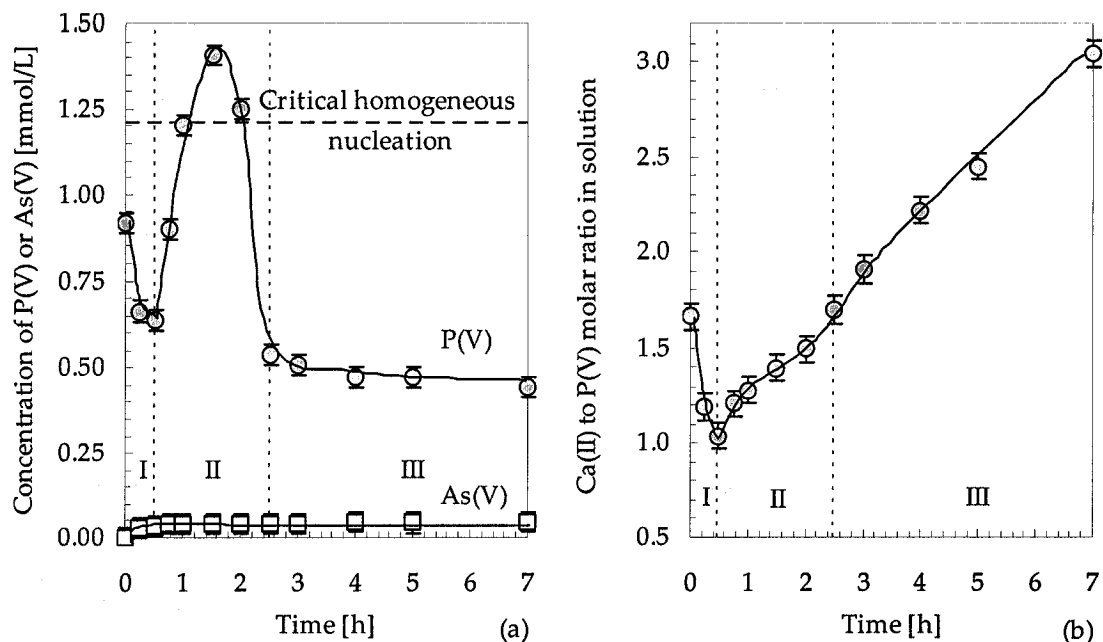


Figure 6.28. Semi-batch crystallisation of Ca-deficient hydroxyapatite using scorodite particles as substrate (10 g/L) (a) Concentration of P and As in solution; (b) Ca:P molar ratio. Reagent solution addition rate 20 mL/h.

The data reported in Figure 6.26, Figure 6.27, and Figure 6.28 reveal that the maximum phosphorus concentration reached in each test was not the same. Thus; for the slowest addition rate (Figure 6.26(a) at 6 mL/h) the maximum P(V) concentration was lower than the critical phosphorus concentration for homogeneous nucleation (~ 1.22 mmol/L or 38 mg/L of P(V)) as determined in Chapter 5. On the other hand, for addition rates of 10 and 20 mL/L this level was surpassed (Figure 6.27(a) and Figure 6.28(a) respectively).

Moreover, during stage I the calcium to phosphate molar ratio in solution decreased from 1.6 to around 1.0, whereas during stages II and III this ratio increased, although, at different rates in each stage. This change in Ca:P ratio with stage implies that Ca was preferentially removed from solution during stage I while during stages II and III PO_4 precipitation took place preferentially to calcium (apparently) due to deposition of a Ca-deficient hydroxyapatite phase.

Stoichiometry of Ca-deficient hydroxyapatite: A mass balance was attempted with the intention of determining the Ca:P molar ratio of the precipitating solid on each of the stages reported above. Considering that the amount of Ca(II) and P(V) added are known as well as the concentration of them in the solution, the average precipitation rate of Ca(II) or P(V) in a period of time Δt can be calculated as follows:

$$C(t) \cdot V(t) = C(t-\Delta t) \cdot V(t-\Delta t) + Q \cdot M \cdot \Delta t + (-\mathfrak{R}(t)) \cdot V(t) \cdot \Delta t \quad (6.3)$$

where $C(t)$ being the bulk concentration of Ca(II) or P(V) at time t (C in mmol/L and t in h); $V(t)$ the volume of solution at time t [L]; Q the reagent addition rate ($6 \cdot 10^{-3}$, $10 \cdot 10^{-3}$ or $20 \cdot 10^{-3}$ L/h); M the reagent molarity (100 mmol/L and 60 mmol/L for Ca(II) and P(V) respectively) and $-\mathfrak{R}(t)$ the precipitation rate [$\text{mmol} \cdot \text{L}^{-1} \cdot \text{h}^{-1}$]. Then, equation (6.3) can be rewritten as:

$$-\mathfrak{R}(t) = \left[\frac{C(t) \cdot V(t) - C(t-\Delta t) \cdot V(t-\Delta t)}{V(t) \cdot \Delta t} \right] - \frac{Q \cdot M}{V(t)} \quad (6.4)$$

Therefore, the stoichiometric Ca:P ratio of the calcium deficient hydroxyapatite precipitated in a period of time Δt will be:

$$\left. \frac{\mathfrak{R}_{\text{Ca}}}{\mathfrak{R}_{\text{P}}} \right|_t = \left. \frac{\text{Ca}}{\text{P}} \right|_{\Delta t} = \frac{C_{\text{Ca}}(t) \cdot V(t) - C_{\text{Ca}}(t-\Delta t) \cdot V(t-\Delta t) - Q \cdot M_{\text{Ca}} \cdot \Delta t}{C_{\text{P}}(t) \cdot V(t) - C_{\text{P}}(t-\Delta t) \cdot V(t-\Delta t) - Q \cdot M_{\text{P}} \cdot \Delta t} \quad (6.5)$$

The determined Ca:P ratios for the three stages I, II and III that correspond to each addition rate are shown in Figure 6.29. It can be seen that during stage I the Ca:P molar ratio was ~ 3.0 (no calcium phosphate has been reported with that molar ratio) for all the experiments, being in agreement with the result found during one-stage (batch) precipitation of Ca-deficient hydroxyapatite (refer to Figure 6.23 in previous section).

During stage II (nucleation period), no matter what reagent addition rate was used the precipitated solid seems to have a Ca:P molar ratio around 1.50. Finally, during the growth period (stage III) this molar ratio was found to be 1.56 ± 0.01 , 1.57 ± 0.01 , and 1.52 ± 0.01 when the addition rates were 6, 10, and 20 mL/h respectively. From the above analysis it can be concluded that the precipitated calcium phosphates phases (with the

exception of stage I) were indeed Ca-deficient hydroxyapatite (refer to Chapter 5).

In order to check the above calculation the solids obtained via semi-batch deposition were subjected to chemical analysis after digestion in HCl solution. The comparison is shown in Table 6.2. It can be observed that the measured and calculated values are reasonably close to each other hence rendering the estimation reliable.

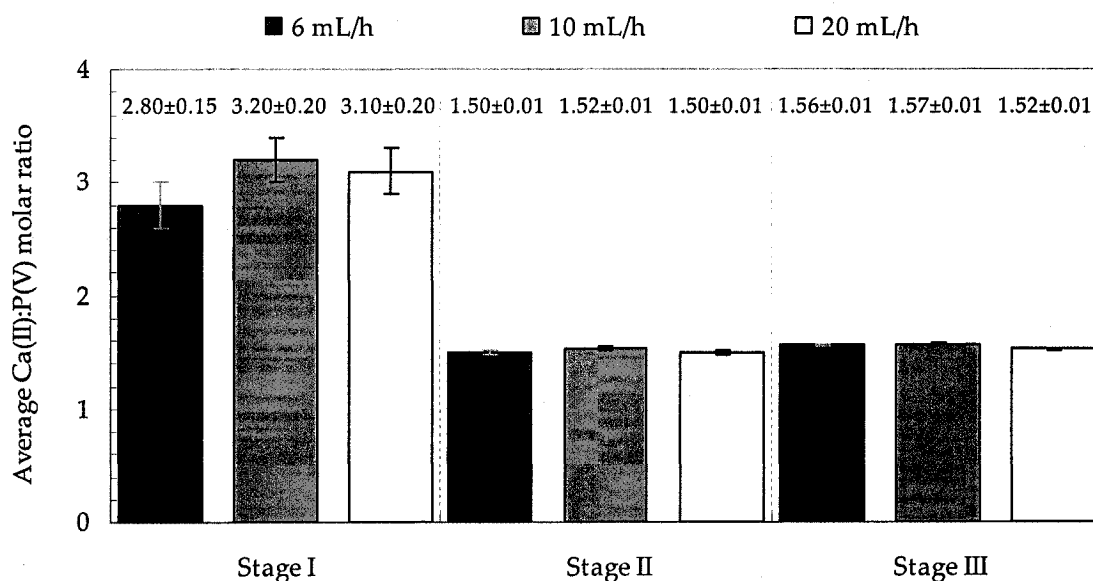


Figure 6.29. Calculated calcium to phosphate molar ratio in the precipitated product during the course of the semi-batch precipitation of Ca-deficient hydroxyapatite in the presence of scorodite substrate.

Table 6.2. Calculated and measured stoichiometry of produced coated solids

Sample	Calculated Ca:P	Measured Ca:P
Low addition rate (6 mL/h)	1.59±0.01	1.58±0.02
Medium addition rate (6 mL/h)	1.62±0.01	1.60±0.04
High addition rate (6 mL/h)	1.57±0.01	1.57±0.03

At this point it is not clear which phase or phases deposited during stage I (batch deposition). As was mentioned earlier, neither calcium arsenate nor calcium carbonate appears to have formed during the early stages of precipitation. One possibility (beyond

the adsorption scenario) is the formation of a surface compound consisting of $\text{Ca-Fe-PO}_4\text{-AsO}_4$. During the study of aluminium phosphate deposition, it was determined ion exchange led to the formation of a $\text{Fe-Ca-PO}_4\text{-AsO}_4$ with composition: $\text{Fe}(\text{AsO}_4)_{1-x}(\text{PO}_4)_x \cdot 2\text{H}_2\text{O}$ (refer to section 6.2.2). On the other hand, it is known that Ca-Fe-AsO_4 secondary phases form as a result of natural [10] or simulated [11] weathering (decomposition) of scorodite at $\text{pH} > 7$. One of these phases is yukonite (a poorly crystalline Ca-Fe-AsO_4 phase of composition approaching $\text{Ca}_2\text{Fe}_3(\text{AsO}_4)_4\text{OH} \cdot 12\text{H}_2\text{O}$). Due to the isostructural resemblance of arsenate and phosphate minerals the formation of a Ca-Fe-PO_4 or for that matter $\text{Ca-Fe-PO}_4\text{-AsO}_4$ phase cannot be ruled out. A surface reaction during the early stages of precipitation between the scorodite particles and the solution may have indeed led to the formation of such phase that explains the high Ca:P ratio observed.

Evaluation of the precipitation mechanism with PHREEQC: Considering the results from the semi-batch tests (in particular stage II) the following questions becomes relevant: was the formation of Ca-deficient hydroxyapatite via primary homogeneous or via primary heterogeneous nucleation? A cursory examination of Figure 6.26(a), Figure 6.27(a), and Figure 6.28(a) suggests that with the exception of addition rate 6 mL/h (Figure 6.26(a)) primary homogeneous nucleation occurred since the critical $P(V)$ concentration level was exceeded. Such evaluation of supersaturation, however, is not accurate as it ignores the role of Ca(II). Saturation ratio, as reminder, is defined as the ion activity product over the solubility product, as is shown in Eq. (6.6). Thus, it was decided to reevaluate the data with the aid of PHREEQC.

$$S = \left(\frac{IAP}{K_{sp}} \right) = \left(\frac{a(\text{PO}_4^{3-})^\alpha \cdot a(\text{Ca}^{2+})^\beta}{a(\text{PO}_4^{3-})_{eq}^\alpha \cdot a(\text{PO}_4^{3-})_{eq}^\beta} \right) \quad (6.6)$$

For this analysis, the precipitation of an "amorphous" calcium phosphate with composition $\text{Ca}_3(\text{PO}_4)_2$ was assumed. The critical IAP for the onset of homogeneous nucleation (using the data from Chapter 5), i.e., $IAP_{cr,homo}$ of this compound was estimated to be $\sim 10^{-24.80}$ (refer to Chapter 5). This critical IAP was used to evaluate the data of

Figure 6.26(a), Figure 6.27(a), and Figure 6.28(a) by calculating $\text{Log}[IAP(\text{Ca}_3(\text{PO}_4)_2)]$. In all three cases, the thermodynamic data listed in Table 5.1 (refer to Chapter 5) and Table 6.1 were used. The respective evolution of $\text{Log}[IAP(\text{Ca}_2(\text{PO}_4)_3)]$ for each of the three stages is presented in Figure 6.30(a,b,c). On the same figure the $\text{Log}(IAP_{cr,hom})$ is also shown. It can be seen from Figure 6.30 that for the addition rate of 20 mL/h, the calculated ion activity product exceeded the critical value. For an addition rate of 10 mL/h this critical point was very close to the critical value ($IAP_{max} = 10^{-24.84}$ vs. $IAP_{cr,homo} = 10^{-24.86}$); and when the reagent addition rate was 6.0 mL/h this critical point was never reached. Thus, this calculation suggests that the mechanism in which Ca-deficient hydroxyapatite formed was clearly homogeneous for an addition rate of 20 mL/h, border-line for addition rate of 10 mL/h, and undoubtedly heterogeneous for 6 mL/h addition rate confirming the earlier postulation.

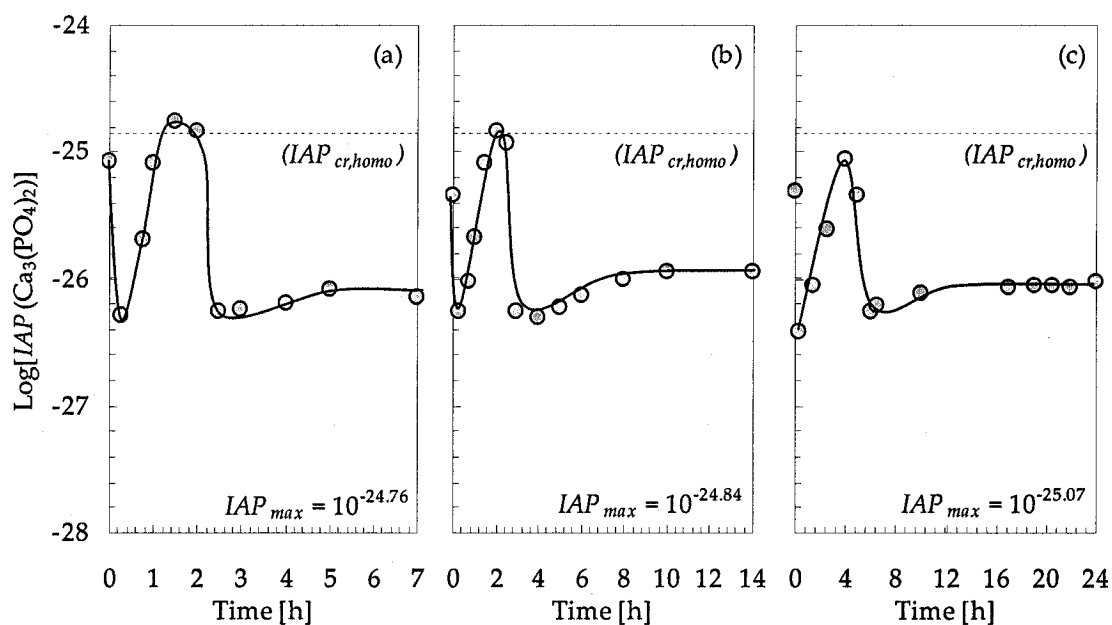


Figure 6.30. Ion activity product for $\text{Ca}_3(\text{PO}_4)_2$ during the semi-batch precipitation of Ca-deficient hydroxyapatite in presence of scorodite particles as a function of time. (a). Reagent solution addition rate 20 mL/h; (b). Reagent addition rate 10 mL/h; and (c). Reagent addition rate 6 mL/h. (Critical IAP is shown in broken lines).

6.3.3 Analysis of the deposition process using SEM

To facilitate the evaluation of the deposition process, a cross section of the material produced by the semi-batch tests was analysed by variable pressure scanning electron microscopy (VP-SEM). Figure 6.31 shows scanning electron micrographs of a scorodite particle coated with calcium phosphate. Since the brightness of each zone in SEM-BSE (Back-Scattered Electron) images is proportional to the average atomic number (Z) of the material. The scorodite (heavy) and calcium phosphate (light) are clearly distinguishable. It can be seen different types of deposit to have been produced as a function of the reagent addition rate.

As it is seen in Figure 6.31(a,b) that for addition rate of 20 mL/h resulted mainly in crystallisation of hydroxyapatite via primary homogeneous nucleation-dominated precipitation, not desirable from a deposition-encapsulation point of view. In the case of addition rate of 10 mL/h the crystallisation process was a mixture of homogeneous precipitation and deposition in the form of 3D-island growth (Figure 6.31(c,d)). Finally, with the slow addition rate (6 mL/h) no distinct formation of calcium phosphate was evident (Figure 6.31(e and f)). Therefore, elemental information produced by X-Ray diffraction (XRD) was collected. This analysis revealed the presence of scorodite particles coated with a layer of calcium phosphate material.

6.4 Stability

This section examines the stabilising effect of phosphate coatings on scorodite particles. Two different stability tests were performed either under oxic or anoxic conditions.

6.4.1 Materials and methods

Materials: Six different materials were studied; the first one was the scorodite substrate material itself used in the encapsulation studies. In addition to the original material, scorodite particles coated with aluminium and calcium phosphates, namely scorodite

coated by one controlled crystallisation-deposition of $\text{AlPO}_4 \cdot 1.5\text{H}_2\text{O}$, (hereafter, AIP(1)); scorodite coated with $\text{AlPO}_4 \cdot 1.5\text{H}_2\text{O}$ after one recycle of the coated substrate (hereafter, AIP(2)); and scorodite after two recycles of the coated substrate (hereafter, AIP(3)). Ca-deficient hydroxyapatite coatings produced at addition rates of 6 mL/h and 10 mL/h (hereafter dHAP(low) and dHAP(med) respectively) were studied.

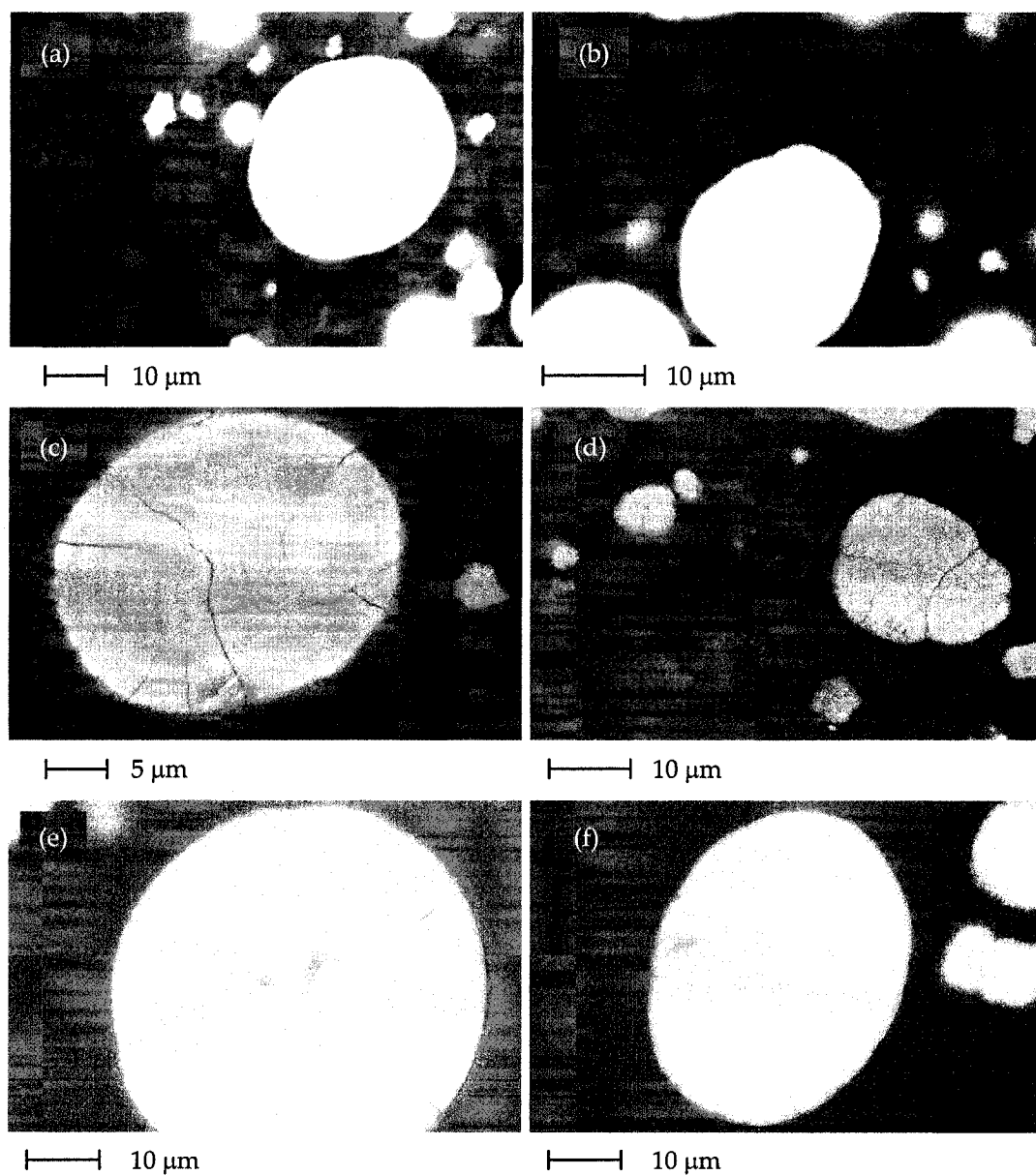


Figure 6.31. Back-scattered electron images of scorodite particles coated with calcium phosphate material. (a),(b) Reagent addition rate 20 mL/h; (c),(d). Reagent addition rate 10 mL/h; and (e),(f) Reagent addition rate 6 mL/h.

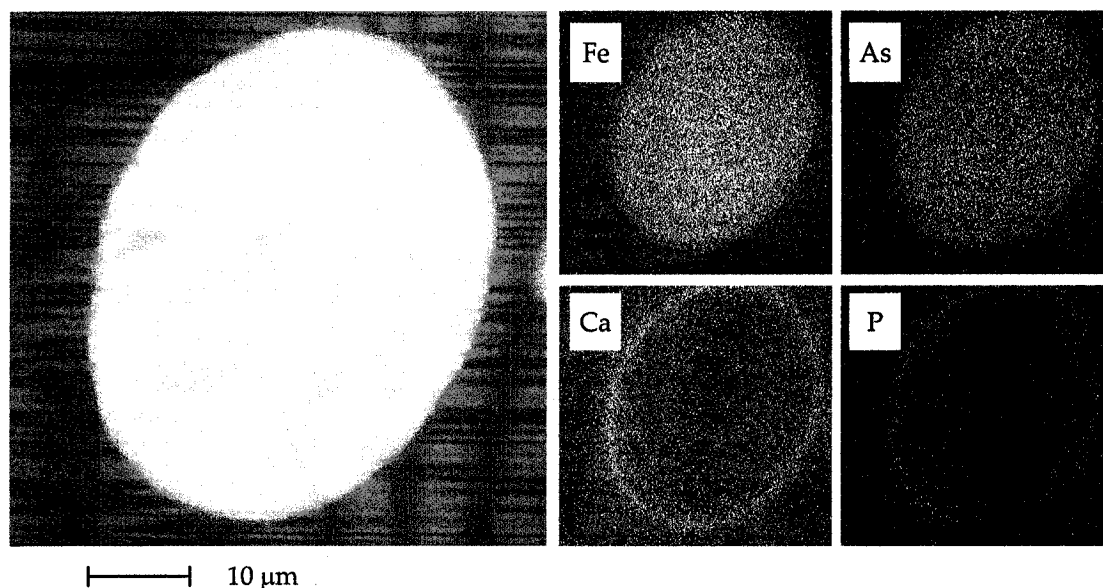


Figure 6.32. Back-scattered electron image of a scorodite particle coated with calcium phosphate material produced under reagent addition rate 6 mL/h(left). X-ray maps confirming the presence of CaPO_4 -material deposited on scorodite (right).

Oxic stability test: The stability of scorodite coated with phosphate minerals was studied as a function of pH under oxic conditions at room temperature: pH 4.0, 6.0 and 8.0 for aluminium phosphate coatings and pH 6.0 and 8.0 for calcium phosphate coatings.

Similar to the stability tests for aluminium and calcium phosphate reported in Chapter 4 and Chapter 5, the solids were subjected to a special leaching procedure before actual stability measurements were made in order to remove any soluble non-crystalline material that could have distorted the measurements. This cleaning procedure involved stirring at the pH at which the oxic stability experiments were carried out for 24 h. For this procedure, 100 mL of deionised water was placed in 125 mL Erlenmeyer flasks, stoppered and agitated with the aid of an orbital shaker. In each flask, 3 g of solids were then added followed by pH adjustment. The pH of the solution was monitored and periodically adjusted by the addition of NaOH or HNO_3 solutions to assure the pH remains ± 0.2 of the set point value. The experiments were performed at room temperature (22 °C). After 24 hours, a 10 mL sample was taken with a syringe and

filtered on 0.25 μm pore-size membrane (Corning). The solution was acidified and analysed for As, P, Fe, and Ca (or Al) concentrations. The slurry was filtered on a 0.1 μm pore size membrane (Millipore) and the solids were washed with pure water using 4X the volume of filtrate. The solids were immediately repulped to undergo another similar test. The procedure was repeated three times.

The oxic stability test was in fact very similar to this cleaning procedure. The only difference resides in the fact that these preparation steps were performed for 24 h only, whereas, the stability test lasted 10 d. At the end of the test, the solids were filtered on 0.1 μm pore size membrane and washed with pure water using 4X the volume of filtrate. The solids were kept wet in a bag.

Anoxic stability test: This test was conducted at controlled oxidation-reduction potential (E_h) conditions (100 ± 20 mV, adjusted twice a day) via addition of NaHS-containing solution (0.5 mol/L). The pH of the solution was monitored and periodically adjusted by the addition of NaOH or H_2SO_4 solutions to assure the pH remains ± 0.2 of the set point value 7.0. Prior to the anoxic stability test the solids were subjected to a leaching procedure as well.

For each oxic stability test, 100 mL of deionised water was placed in 250 mL Erlenmeyer flasks, stoppered and agitated with the aid of an orbital shaker. The experiments were performed at room temperature (22 °C). In each flask, 5 g of solids were then added followed by pH and E_h adjustment. The anoxic stability test lasted 6 weeks.

For both, anoxic and oxic tests, samples were taken at predetermined times, filtered using 0.25 μm pore size membranes (Corning) acidified with 3 drops of concentrated H_2SO_4 solution ($w_{\text{H}_2\text{SO}_4} \sim 96\%$) and analysed. The pH was measured using a Ross™ combination electrode with a reported accuracy of ± 0.02 pH units ($\pm 4.5\%$ in H^+ activities). The pH electrode was standardised versus buffer pH solutions 4.0, 7.0 and 10.0. For anoxic stability test the E_h was measured using a Cole-Parmer® ORP platinum combination electrode (Ag/AgCl) with a reported accuracy ± 20 mV. The ORP electrode

was standardised versus Thermo-Orion ORP standard solution. All experiments were carried out in duplicate runs and performed at room temperature (22 °C).

Characterisation and analysis: Solutions and solids were characterised using some of the techniques described in Chapter 3.

6.4.2 Stability in oxic environment

Aluminium phosphate coatings: The variation of the solution concentration, in terms of As(V) as a function of time for the experiments performed, is shown in Figure 6.33. It is observed that the arsenic release kinetics were indeed reduced when the scorodite particles were covered with an aluminium phosphate layer. Naturally, the release kinetics were better affected when the solids were coated after two and three recycles of the scorodite substrate material. The final arsenic concentration (after 10 d of equilibration) was reduced one order of magnitude with the AIP(3) coating.

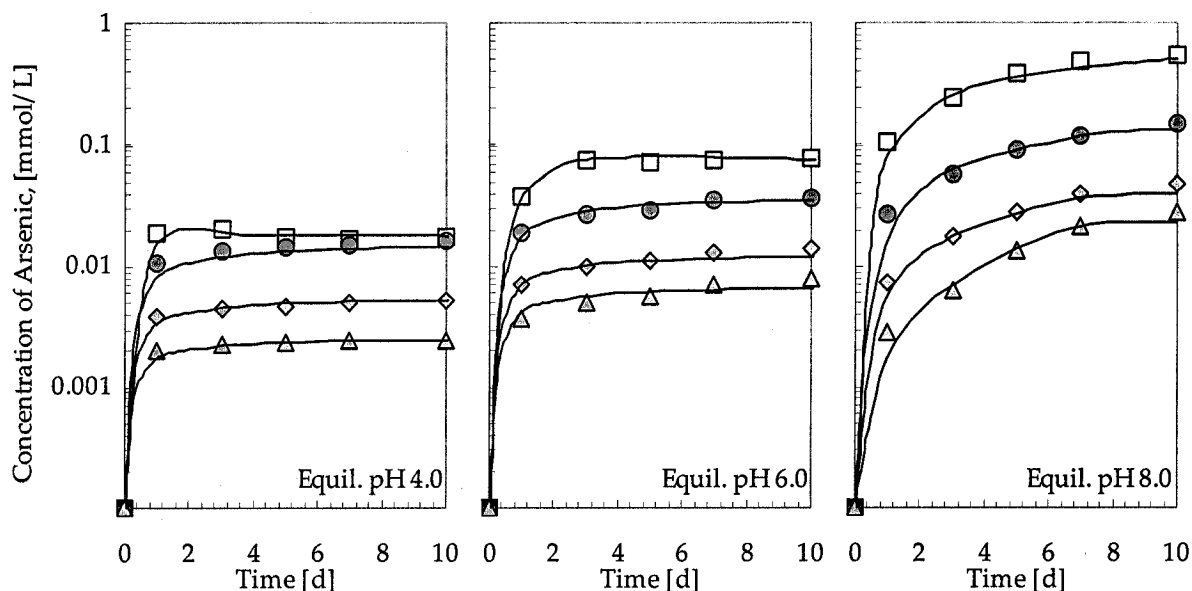


Figure 6.33. Dissolution kinetics of Arsenic(V) versus time at different equilibration pH at oxic conditions. Symbols: \square Scorodite substrate; \bullet AIP(1); \diamond AIP(2); and \triangle AIP(3).

The latter is better seen when the final As concentration is plotted as a function of pH for each material studied. It can be seen from Figure 6.34 that the final arsenic concentration

is increasingly reduced, with consecutive number of deposition cycles. In Figure 6.35, the final concentrations of P and Al are shown. It is revealed from the observation of these figures that the dissolution of aluminium phosphate is incongruent in nature (as expected according to the stability test reported in Chapter 4). But equilibrium had not been attained after 10 days as the comparison with the solubility data indicates.

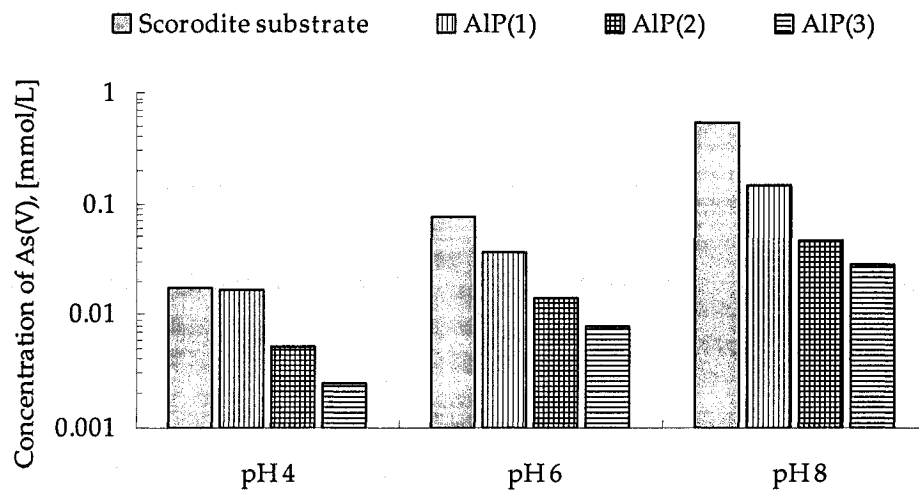


Figure 6.34. Arsenic concentration in solution after 10 d of dissolution for scorodite particles coated with an aluminium phosphate material.

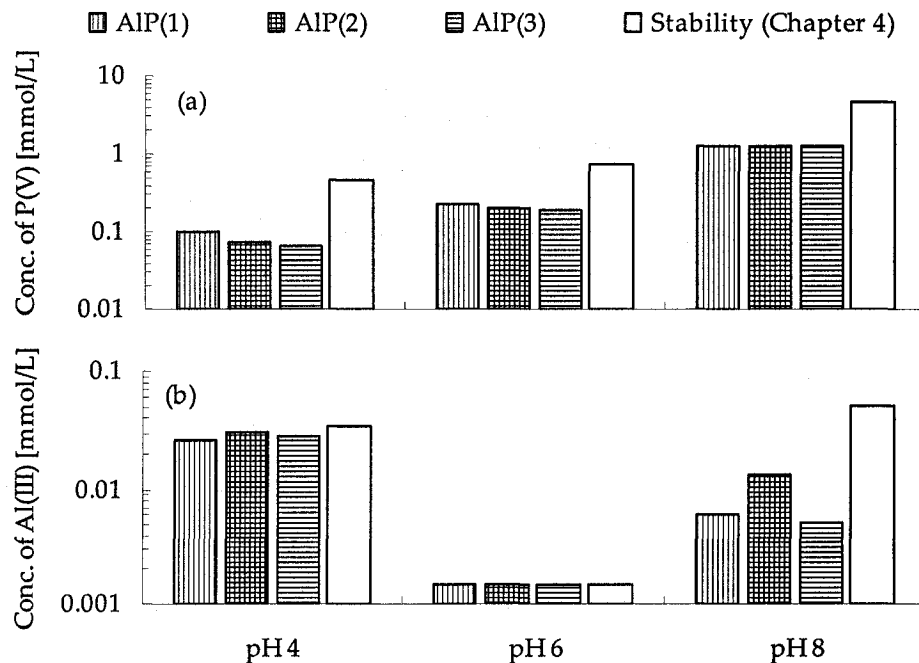


Figure 6.35. Concentration after 10 d of equilibration compared to respective solubilities. (a) phosphorus concentration; (b) aluminium concentration.

Calcium phosphate coatings: Similar to the previous reported results, the variation of the solution concentration, in terms of As(V) along with pH, as a function of time for the scorodite particles coated with calcium phosphate (calcium-deficient hydroxyapatite) is shown in Figure 6.36 and the final As concentration is plotted as a function of pH in Figure 6.37. Upon observation of those figures it is revealed that at pH 8 the arsenic release kinetics were slowed down when the scorodite particles were covered with a calcium-deficient hydroxyapatite coating.

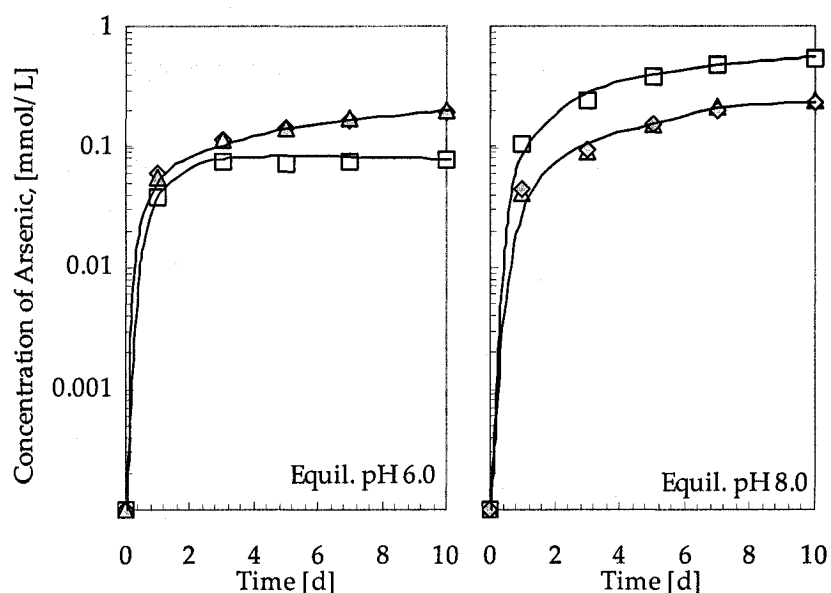


Figure 6.36. Dissolution kinetics of As(V) versus time at different equilibration pH at oxidic conditions. Symbols: \square Scorodite substrate; \diamond dHAP(low); and \triangle dHAP(med)

The encapsulation effect, though, was not as effective as in the case of aluminium phosphate. For example, at pH 8 after 10 days of equilibration the final arsenic concentration was 0.15 mmol/L (11.2 mg/L) when scorodite was encapsulated with $\text{AlPO}_4 \cdot 1.5\text{H}_2\text{O}$ after one controlled deposition test (AIP(1)) as compared to 0.24 mmol/L (18 mg/L) for Ca-deficient hydroxyapatite encapsulation (dHAP(low) and dHAP(med)). The latter appears to be related to the thickness of the coating; AIP(1) coating thickness was $\sim 3 \mu\text{m}$ whereas the Ca-deficient hydroxyapatite coating was clearly thinner. In Figure 6.38(a,b) the final concentrations of P and Ca are shown. It is revealed from the observation of these figures that the levels of calcium and phosphorus in solution were

similar to those obtained from stability test of calcium-deficient hydroxyapatite reported in Chapter 5.

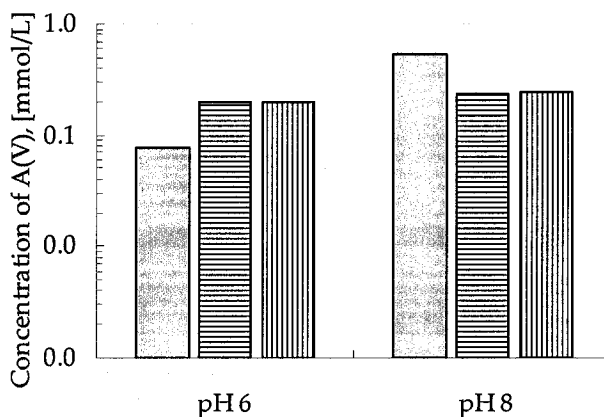


Figure 6.37. Arsenic concentration after 10 d of equilibration for scorodite particles coated with a calcium phosphate material.

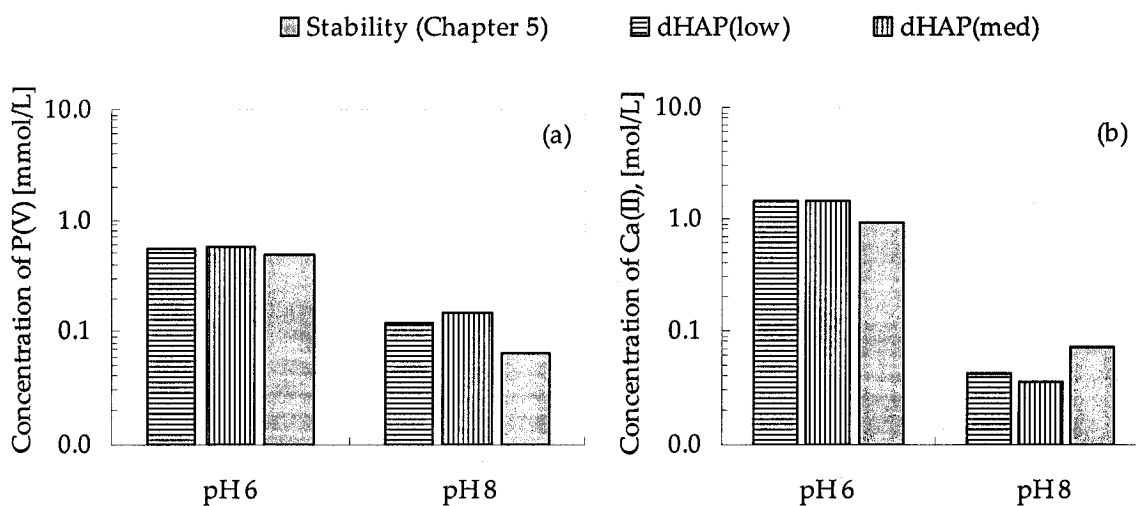


Figure 6.38. Concentration after 10 d of equilibration compared to respective solubilities. (a) phosphorus concentration; (b) calcium concentration.

However, the encapsulation of scorodite with Ca-deficient hydroxyapatite coating seems to have a negative effect on the "solubility" of scorodite at pH 6.0. As is seen in Figure 6.36 and Figure 6.37 the concentration of arsenic in solution reached higher values when scorodite was coated with Ca-deficient hydroxyapatite!

The latter is better seen when the variation of the solution concentration, in terms of

Ca(II), P(V), and As(V) as a function of time for the experiments performed at pH 6 is considered (Figure 6.39(a,b)). It can be seen that the phosphorus concentration reached a maximum value after 1 d of equilibration, thereafter followed by a decrease whereas calcium concentration remained reasonably constant during the course of the stability test.

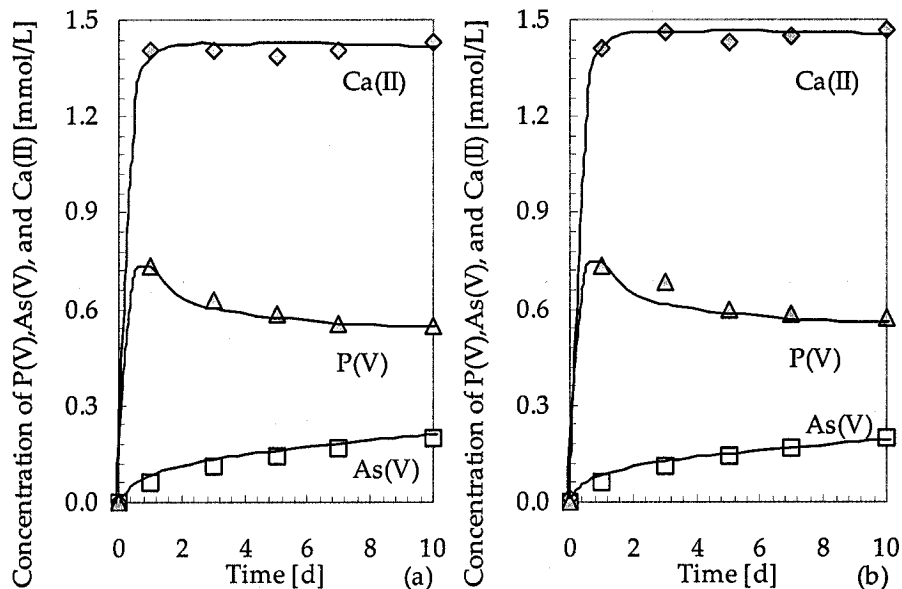
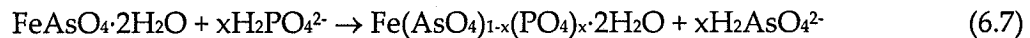


Figure 6.39. Dissolution kinetics of As(V), P(V) and Ca(II) versus time at pH 6.0. (a) dHAP(low); (b) dHAP(med).

This reduction in phosphorus concentration in conjunction with the release of arsenic from scorodite may be related to an "ion exchange" reaction between As(V) and P(V) (as determined in the case of aluminium phosphate) according to:



In Figure 6.40(a,b), the variation of calcium to phosphorus molar ratio along with calcium to phosphorus plus arsenic in solution are shown. It can be seen that Ca:P gradually increase during the course of the tests, whereas the Ca:(P+As) remained constant after 4 d of dissolution, confirming the above reaction.

Moreover, during those oxic stability tests the phosphorus concentration reached very high levels of P. According to the US EPA, in order to prevent the development of

eutrophication total phosphorus (P) should not exceed 0.05 mg/L (1.6 $\mu\text{mol/L}$) in any stream at the point where it enters a lake or reservoir [12]. In this regard, therefore, this coating material will not be suitable for industrial application.

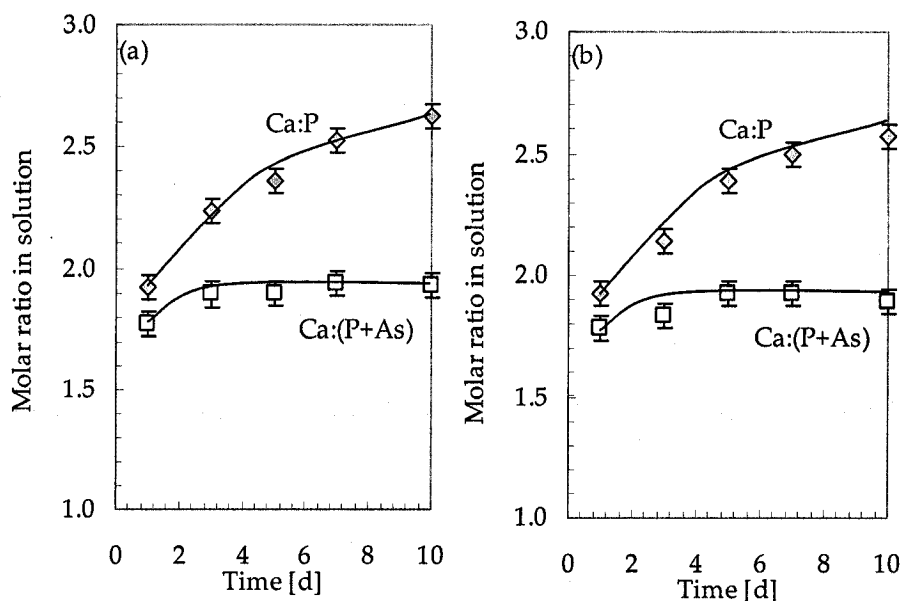


Figure 6.40. Ca:P and Ca:(P+As) in solution as a function of time at pH 6. (a) dHAP(low); (b) dHAP(med).

6.4.3 Stability in anoxic environment

Figure 6.41 shows the variation of the solution composition as a function of time for the experiments performed (duplicate runs) under anoxic conditions in terms of total arsenic (left) and total iron (right). It can be observed that the dissolution kinetics of arsenic and iron were indeed suppressed with the aid of these phosphate coatings.

In terms of effectiveness, the best results were obtained for aluminium phosphate coating (AIP(1) and AIP(3)). This is better seen when the final concentrations of total arsenic and total iron are replotted in Figure 6.42. It can be observed that the final concentration of total iron and total arsenic were reduced, at least, one order of magnitude. On the same Figure, the final concentrations of phosphorus, aluminium, and calcium are also shown.

The relative high "noise" of the concentration data reported is attributed to the lack of precise E_h control. In Figure 6.43 the variation of pH and E_h is plotted (along with their standard deviation). It can be seen that the pH control was indeed more precise than the E_h control.

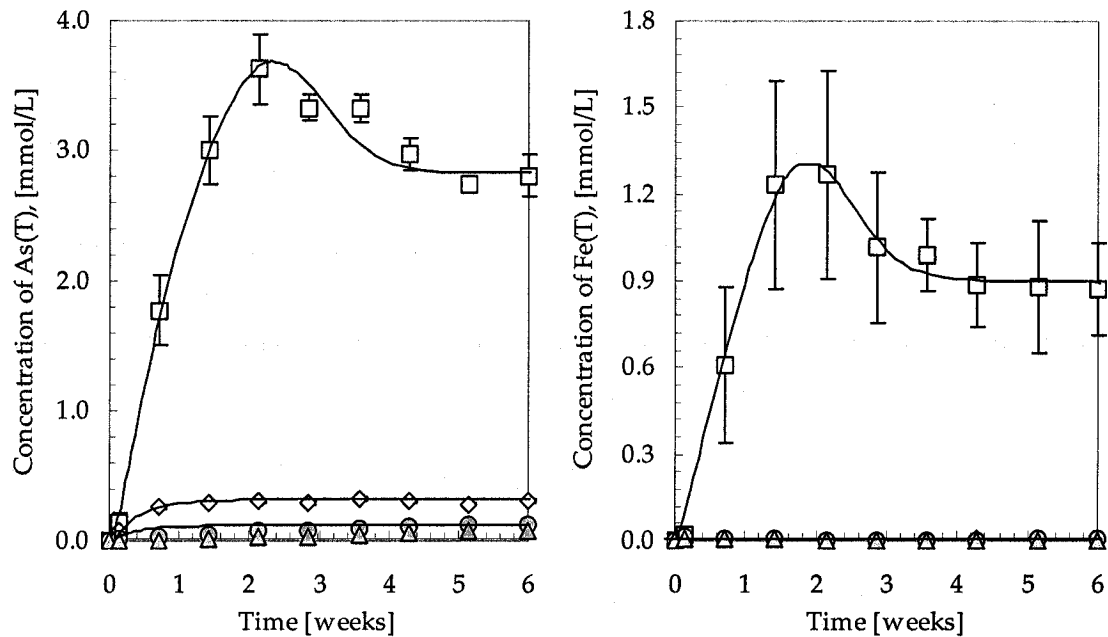


Figure 6.41. Dissolution kinetics of total arsenic(left) and total iron(right) versus equilibration time at under chemically generated anoxic conditions. Symbols: \square Scorodite substrate; \bullet AIP(1); \triangle AIP(3); and \diamond dHAP(low).

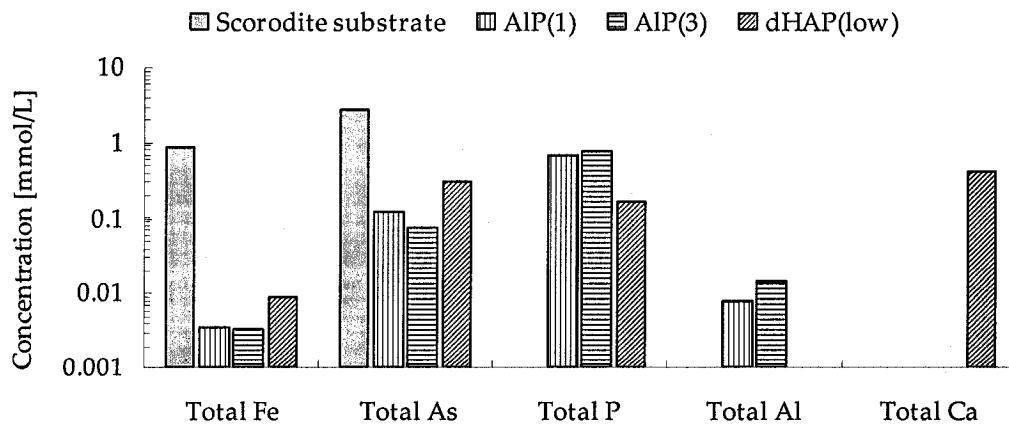


Figure 6.42. Final concentration levels of elements from anoxic dissolution of scorodite substrate, AIP(1), AIP(3) and dHAP(low) at pH 7, E_h 100 mV, and 22 °C (equilibration time 6 weeks).

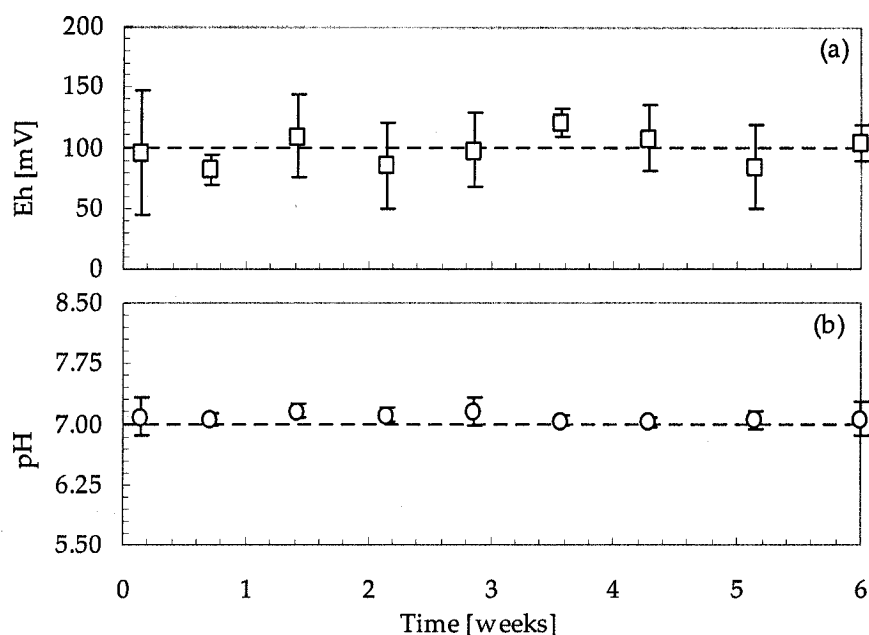
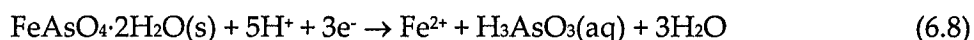


Figure 6.43. Daily average values of pH and E_h during anoxic stability test. (a) E_h variation; (b) pH variation. Set-point values are also shown in broken lines.

Further analysis determined the arsenic and iron speciation. The evolution of iron (ferrous and ferric ions) and arsenic (arsenate and arsenite species) is presented in Figure 6.44. It can be seen from Figure 6.44 that during the anoxic dissolution of scorodite the predominant forms of iron and arsenic were Fe(II) and As(III) confirming that scorodite underwent reductive decomposition to Fe(II) and As(III) according to:



6.4.4 Analysis of the coating stability with SEM

The solids AIP(1), AIP(3) and dHAP(low) after the oxic stability test at pH 8 and after the anoxic stability test were analysed by variable pressure scanning electron microscopy in order to investigate morphological changes on phosphate coating and mechanical adhesion between the coating and the scorodite substrate. Figure 6.45 shows scanning electron micrographs of scorodite particles coated with aluminium and calcium phosphate before and after those stability tests. Upon observation of these micrographs it becomes clear that the coating remains on the surface of scorodite confirming the

adhesion between the scorodite substrate and the phosphate coating. However, as the dissolution tests indicated the coating does not provide complete sealing of the scorodite surface, hence allowing arsenic to be released to the environment albeit at reduced rate.

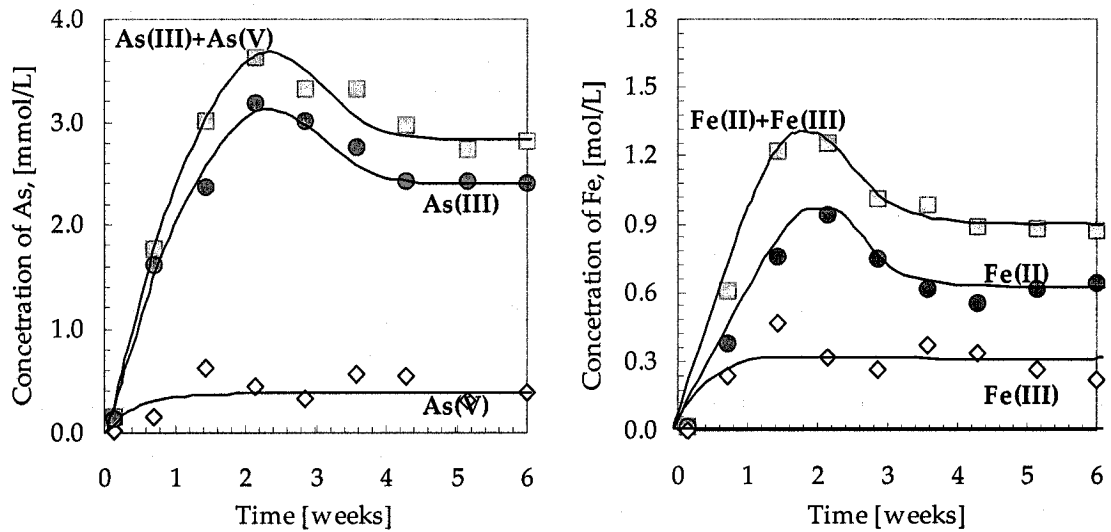


Figure 6.44. Dissolution kinetics and speciation of scorodite dissolution under chemically generated anoxic conditions. Arsenic speciation (left); iron speciation (right).

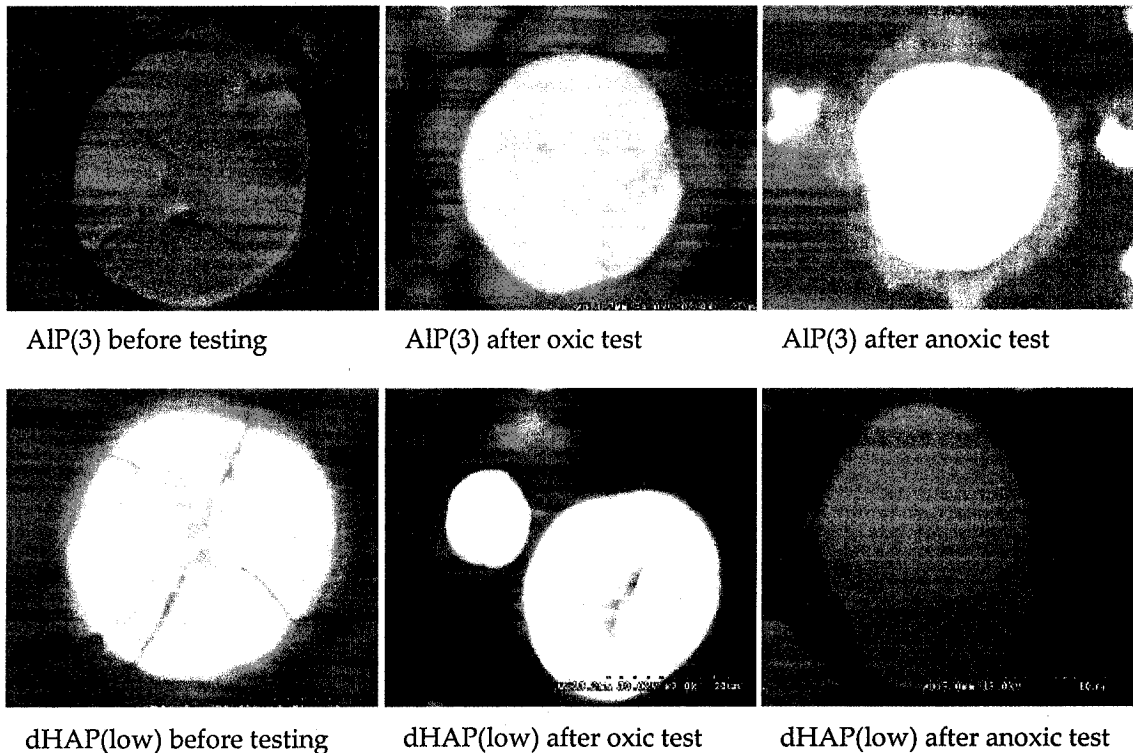


Figure 6.45. Back-scattered electron images of scorodite particles coated with calcium and aluminium phosphate before and after oxidic and anoxic stability tests.

6.5 Conclusions

Encapsulation with aluminium phosphate: A new encapsulation concept for scorodite was investigated for the first time. The encapsulation method involved directed deposition of $\text{AlPO}_4 \cdot 1.5\text{H}_2\text{O}$ ($\text{AlPO}_4\text{-H}_3$) as coating on the surface of scorodite under controlled supersaturation conditions from a sulphate-matrix solution with Al(III):P(V) molar ratio equal to one at 95 °C.

The controlled deposition of $\text{AlPO}_4 \cdot 1.5\text{H}_2\text{O}$ on scorodite particles began with an induction period characterised by an "ion exchange" reaction between PO_4 and AsO_4 . This "ion exchange" process led to the formation of a solid solution surface layer with the following composition: $\text{Fe}_{0.99}\text{Al}_{0.01}\text{H}_{0.43}(\text{AsO}_4)_{0.94}(\text{PO}_4)_{0.15}(\text{SO}_4)_{0.08} \cdot 2\text{H}_2\text{O}$. An investigation of the induction period using gypsum as substrate instead of scorodite revealed to be still present suggesting that it relates to the heterogeneous nucleation of $\text{AlPO}_4 \cdot 1.5\text{H}_2\text{O}$ rather than to the "ion exchange" process. The induction period was eliminated when AlPO_4 -coated scorodite particles were recycled.

The aluminium phosphate coating was characterised by XRD, SEM-EDX, TOF-LIMS and TOF-SIMS. The coating was crystalline $\text{AlPO}_4 \cdot 1.5\text{H}_2\text{O}$. After one controlled deposition procedure a uniform in thickness coating, typically ranging from 2.5-3.5 μm was obtained. The coating thickness decreased or increased with the substrate particle size. Further deposition of $\text{AlPO}_4 \cdot 1.5\text{H}_2\text{O}$ made the coating thicker changing its morphology according to 3D-island type growth.

Encapsulation with calcium phosphate: The directed deposition of Ca-deficient hydroxyapatite on scorodite particles was achieved via mixing of CaCl_2 and NaH_2PO_4 solutions a constant pH of 7.6. Supersaturation was controlled by the addition rate. It was found that for an addition rate of 20 mL/h the crystallisation process was mainly by homogeneous nucleation; whereas, for addition rates of 10 mL/h the crystallisation process was a mixture of homogeneous crystallisation and deposition in the form of 3D-

island growth. The best results were obtained with addition rate of 6 mL/h.

The deposition of calcium-deficient hydroxyapatite begun with the formation of a calcium phosphate phase with Ca:P ~ 1.5, as determined by mass balance calculation, followed by growth of a Ca-deficient hydroxyapatite with Ca:P average molar ratio equal to 1.56 ± 0.01 , 1.57 ± 0.01 , and 1.52 ± 0.01 when the addition rates were 6, 10 mL/h respectively.

Stability: Encapsulation of scorodite particles with hydrated aluminium phosphate and calcium-deficient hydroxyapatite appears to be able to control (partially only) the release of arsenic under both oxic and anoxic conditions. The best results were obtained with aluminium phosphate reflecting most likely the thickness of the respective coating. The more interesting results by far are those obtained under the anoxic stability test since the release of arsenic was decreased in more than one order of magnitude. The high level of phosphorus release, though, is of concern. Hence, further work is necessary to improve this type of encapsulation process.

References

- 1 Parkhurst, D.L.; Appelo, C.A.J. *User's Guide to PHREEQC (Version 2)-A Computer Program for Speciation, Batch-Reaction, One-Dimensional Transport, and Inverse Geochemical Calculations; Water-Resources Investigations Report 99-4259; U.S. Geological Survey: Reston, VA, 1999; <http://wwwbrr.cr.usgs.gov/>.*
- 2 Duncan, B.; Stocker, M.; Gwinup, D.; Szostak, R.; Vinje, K. Template-Free Synthesis of the Aluminophosphates H₁ through H₄. *Bulletin de la Société Chimique de France*, **1992**, 129, 98-110.
- 3 Koutsoukos, P.G. Growth of calcium phosphates on different substrates: Epitaxial considerations. In *Calcium Phosphates in Biological and Industrial Systems*; Amjad, Z; Ed., Kluwer Academic: Boston, MA, **1998**, pp. 41-66.
- 4 Wu, W.; Nancollas, G.H. Kinetics of heterogeneous nucleation of calcium phosphates on anatase and rutile surfaces. *Journal of Colloid and Interface Science*,

- 1998, 199(2), 206-211.
- 5 Bothe, J.V. Brown, P.W. Mechanism of arsenic immobilization by calcium arsenate formation, *Environmental Science and Technology*, **1999**, 33, 3806-3811.
 - 6 Nishimura, T.; Robins, R.G. A re-evaluation of the solubility and stability regions of calcium arsenites and calcium arsenates in aqueous solution at 25 °C, *Mineral Processing and Extractive Metallurgy Review*, **1998**, 18, 283-308.
 - 7 Bothe, J.V. Brown, P.W. The stabilities of calcium arsenates at 23±1°C. *Journal of Hazardous Materials*, **1999**, 69(2), 197-207.
 - 8 Nordstrom, D.K.; Archer. D.G. Arsenic thermodynamic data and environmental geochemistry. In *Arsenic in Ground Water*; Welch, A.H.; Stollenwerk, K.G. Eds.; Kluwer Academic: Boston, MA, **2003**, pp. 1-25.
 - 9 Plummer, L.N.; Bussenberg, E. The solubilities of calcite, aragonite and vaterite in CO₂-H₂O solutions between 0 and 90 °C, and an evaluation of the aqueous model for the System CaCO₃-CO₂-H₂O. *Geochimica et Cosmochimica Acta*, **1982**, 46(6), 1011-1040.
 - 10 Paktunc,D; Foster, A. Heald, S.; Laflamme, G. Speciation and characterization of arsenic in gold ores and cyanidation tailings using X-ray absorption spectroscopy. *Geochimica et Cosmochimica Acta*, **2004**, 68(5), 969-983.
 - 11 Bluteau, M-C. The incongruent dissolution of scorodite- solubilities, kinetics and mechanisms. *M.Eng. Thesis*, McGill University, QC, **2004**.
 - 12 US Environmental Protection Agency. Quality criteria for water 1986, Office of Water Regulations and Standards: Washington, DC, **1986**. <http://www.epa.gov/waterscience/criteria/goldbook.pdf>

Chapter 7. Synopsis

Key findings from each component of this work have already been summarised at the end of each Chapter. In this Chapter, global conclusions are given by considering the whole of the work rather than the individual parts. Subsequently, what is considered as an original contribution to knowledge is outlined, and finally ideas for continuation of this work are presented.

7.1 Global conclusions

The encapsulation of scorodite particles with phosphate coatings was studied in the present research work as a novel method of arsenic fixation. The encapsulation method involved direct crystallisation of phosphate coatings on scorodite particles potentially not prone to oxic and anoxic decomposition. The major findings of this study are summarized below.

1. A new synthesis method for hydrated aluminium phosphate $\text{AlPO}_4 \cdot 1.5\text{H}_2\text{O}$ ($\text{AlPO}_4\text{-H}_3$) was developed that involves precipitation from a sulphate-matrix solution with aluminium to phosphorus molar ratio equal to one at 95 °C. Homogeneous precipitation tests led to the definition of the metastable zone of aluminium phosphate. This zone was used to design the supersaturation-controlled seeded tests. The homogeneously formed product consisted of aggregates of sub-micron size crystallites of 3.5 μm average size that have grown to 16.5 μm after three cycles of seed-assisted precipitation.
2. $\text{AlPO}_4 \cdot 1.5\text{H}_2\text{O}$ was found to be more soluble than the better known dihydrate (variscite, $\text{AlPO}_4 \cdot 2\text{H}_2\text{O}$). This material was determined to undergo incongruent dissolution at pH around 3.0 and higher producing initially amorphous $\text{Al}(\text{OH})_3$

which gradually (within 30-day dissolution period) converted to the stable gibbsite phase. Upon evaluation of the experimental data with PHREEQC it was possible to calculate the solubility product ($\text{Log } K_{sp}$) and the standard Gibbs free energy of formation ($\Delta G_{f,0}$) for $\text{AlPO}_4 \cdot 1.5\text{H}_2\text{O}$ to be respectively -20.46 ± 0.40 and $-1980.5 \pm 2.0 \text{ kJ} \cdot \text{mol}^{-1}$ at 22°C

3. A synthesis method for the production of calcium-deficient hydroxyapatite was described. This method involved controlled mixing of CaCl_2 and NaH_2PO_4 solutions at a constant pH of 7.6 and ambient temperature. The produced hydroxyapatite was found to be calcium-deficient with nano-crystalline structure having crystallite size in the order of 20 nm.
4. The synthetic calcium-deficient hydroxyapatite (Ca:P~1.58) was determined to be metastable versus stoichiometric hydroxyapatite and more stable than all other calcium phosphate phases commonly formed under aqueous precipitation conditions. Furthermore, it was determined the dissolution to be congruent at initial pH 5.0, 6.0, 7.0, and 8.0 and becoming incongruent when initial pH was 9.0.
5. By controlling supersaturation it was possible to form either an aluminium phosphate coating or calcium phosphate coating on scorodite. This coating of scorodite particles with aluminium or calcium phosphates was found to significantly reduce the release of arsenic under both oxic and anoxic conditions. Aluminium phosphate coatings seemed to provide better coverage of scorodite than hydroxyapatite coatings but further work is required for these coatings to prove effective in meeting arsenic and phosphorus acceptable release levels.

7.2 Claims to originality

Several aspects of the present work constitute, according to the opinion of the author, original contributions to knowledge. The most important of them are outlined below:

1. A novel synthesis method for hydrated aluminium phosphate $\text{AlPO}_4 \cdot 1.5\text{H}_2\text{O}$ ($\text{AlPO}_4\text{-H}_3$) was developed. The new synthesis method developed here differs from the ones previously reported in literature as it involves direct crystallisation in a sulphate solution rather than long-term ageing or hydrothermal-based synthesis routes in chloride or nitrate media.
2. Equally novel is the study of the dissolution of $\text{AlPO}_4 \cdot 1.5\text{H}_2\text{O}$ via experimental and thermodynamic modelling. Moreover, the sequence of formation of Al(III) (oxy)hydroxides phases was found to conform to Stranski's rule, i.e., the least stable phase forming first followed by its transformation to next stable Al(III) (oxy)hydroxide.
3. The finding that the dissolution of a synthetic calcium-deficient hydroxyapatite (Ca:P = 1.58) was metastable versus stoichiometric hydroxyapatite and more stable than all other calcium phosphate phases commonly found under aqueous precipitation conditions has never been reported previously.
4. It is the first time that a systematic study on the heterogeneous crystallisation of aluminium and calcium phosphates, as it applies to the encapsulation of scorodite particles was undertaken, both from a fundamental perspective and from the standpoint of its application to arsenic fixation.

7.3 Recommendations for future work

Future work of both fundamental and practical nature is proposed below that may help for better understanding and development of the scorodite encapsulation process:

1. Further work is required to optimise the properties of the phosphate coatings in terms of thickness, adhesion, and complete coverage of the scorodite surface. Hence, the role of additives has to be explored and the formation of stoichiometric hydroxyapatite promoted.

2. Investigate the encapsulation of scorodite particles with other stable phosphate minerals such as fluoroapatite, $\text{Ca}_{10}(\text{PO}_4)_6\text{F}_2$, or partially fluoride substituted hydroxyapatite, $\text{Ca}_{10}(\text{PO}_4)_6\text{F}_x(\text{OH})_{2-x}$, since both are known to be the most stable of all members of the hydroxyapatite mineral family.
3. Finally, encapsulation using other stable minerals not prone to reductive decomposition, for example, calcium carbonate coatings (calcite, CaCO_3) or aluminium (oxy)hydroxide coatings (gibbsite, $\gamma\text{-Al}(\text{OH})_3$) are worthy to be investigated as well.

Appendix A. Deposition of $\text{CaHPO}_4 \cdot 2\text{H}_2\text{O}$

Introduction

In this appendix, the exploratory work aimed to encapsulate scorodite particles with dicalcium phosphate dihydrate is reported. The controlled deposition of this material on the surface of scorodite, as is shown below, was not successful under the experimental conditions studied. However, it was decided report the results in this section since they could prove useful if some future work in this field is attempted.

Materials and methods

Experimental set up: The experimental set-up used in this work was the same as the one described in Chapter 3 (Section 3.2).

Deposition test: The experimental tests aimed to deposit dicalcium phosphate dihydrate on scorodite were similar to the experimental procedure described in Section 5.2.1 of Chapter 5 for the seeded crystallisation of $\text{CaHPO}_4 \cdot 2\text{H}_2\text{O}$, i.e., an initial acidic solution of CaCl_2 - NaH_2PO_4 - HCl (~1.5 g/L (37.5 mmol/L) of Ca(II) and Ca(II):P(V) of 1:1) was neutralised with 100 mmol/L NaOH , until the precipitation pH of 5.0 was reached (just 0.2 units of pH before the critical supersaturation level was attained). The solution was allowed to stabilise for 30 min in order to assure uniform supersaturated conditions. At this point, 10 g/L of scorodite substrate material produced by atmospheric precipitation (see Chapter 2) was used to begin the precipitation process.

Characterisation and analysis: During the course of the precipitation process, samples of slurry were taken at regular time intervals, and were filtered through membrane filter (Corning 0.25 μm pore size) and diluted with acidified ($w_{\text{HNO}_3} \sim 5\%$) deionised water. At the end of each test, the entire suspension was filtered. The final filtrate together with the

filtrates of the intermediate samples were analysed for As, Fe, P and Ca. The final slurry was filtered and the solids washed by repulping 3 times with 1000 mL of deionised hot water (60 °C). The final solids were subjected to SEM examination (see Chapter 3 for more details).

Results

Figure A.1 shows the precipitation kinetics of a typical test run within the determined metastable zone in the presence of scorodite particles as seed and at constant pH. The variation of Ca(II) and P(V) is plotted in Figure A.1(a), whereas, the variation of Fe(III) and As(V) is shown in Figure A.1(b).

It can be seen the precipitation of $\text{CaHPO}_4 \cdot 2\text{H}_2\text{O}$ followed similar behaviour with the one reported for the precipitation of $\text{AlPO}_4 \cdot 1.5\text{H}_2\text{O}$ on the surface of scorodite (refer to Section 6.2.2 of Chapter 6). Initially an induction period was observed, which lasted less than 1 h, during which very slow precipitation of P(V) and Ca(II) took place accompanied by the release of arsenic from scorodite; no iron release was observed. Following this induction period, rapid precipitation of $\text{CaHPO}_4 \cdot 2\text{H}_2\text{O}$ took place. However, the continuation of the dissolution of arsenic indicates that the scorodite particles were not covered with calcium phosphate.

The latter is better seen when the solids produced with this procedure were characterised by scanning electron microscopy as is shown in Figure A.2. It can be seen from Figure A.2 that plate-like $\text{CaHPO}_4 \cdot 2\text{H}_2\text{O}$ particles formed in the bulk of the solution rather on the scorodite substrate. In other words, precipitation took place homogeneously.

This unsuccessful approach suggests that keeping supersaturation in solution below the critical supersaturation level for homogeneous nucleation ($S_{cr,homo}$) is not a sufficient condition for directing deposition (nucleation) of this material on the surface of scorodite. This apparently relates to the induction period. In essence, the solution was

not in a "truly" metastable state and given enough time (in this case ~ 1.15 h, 30 min for initial equilibration plus 45 min in presence of scorodite) homogeneous nucleation developed.

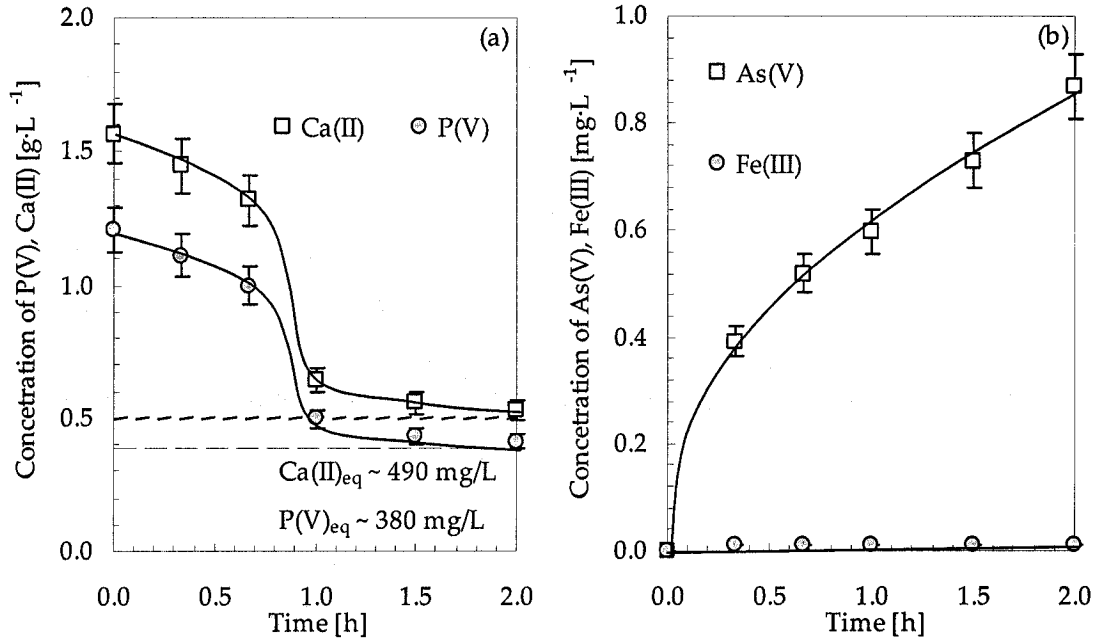


Figure A.1 One-stage $\text{CaHPO}_4 \cdot 2\text{H}_2\text{O}$ precipitation kinetics with pH control using scorodite particles as substrate. (a) Variation of P(V) and Ca(II) with time; (b) Variation of As(V) and Fe(III) with time. Seed concentration, 20 g/L ; NaOH as base; precipitation pH 5.0.

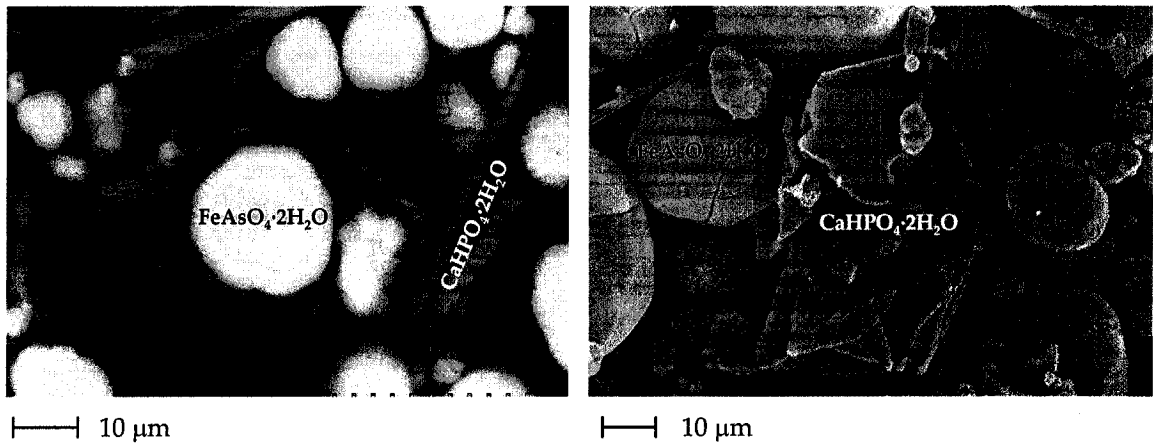


Figure A.2 Cross section back-scattered electron micrographs of scorodite and brushite particles after precipitation of dicalcium phosphate dihydrate (left); Scanning electron micrograph of scorodite substrate along with dicalcium phosphate dihydrate (right).

Hence, to directly deposit $\text{CaHPO}_4 \cdot 2\text{H}_2\text{O}$ on scorodite particles the supersaturation has to be lower than the value used during this test. As reported in Chapter 5 (Section 5.3.2) the initial saturation ratio in solution was ~ 7.9 when S is expressed as the ratio of the initial ion activity product ($IAP = a(\text{Ca}^{2+}) \cdot a(\text{HPO}_4^{2-})$) to the solubility product of dicalcium phosphate dihydrate or only 3.2 (expressed as $C_{\text{Ca(II)}}/C_{\text{Ca(II),eq}}$). This value is very low, so, if this value were reduced the yield of the process would be lowered as well. Thus, it was decided to end the study on this material in favour of controlled deposition of hydroxyapatite on scorodite particles. This was also driven by the realisation that the latter is more stable than the former at the pH region of interest to arsenic disposal.